Dynamics of Feshbach molecule production

Thomas Mark Hanna

A thesis submitted in partial fulfilment
of the requirements for the degree of
Doctor of Philosophy at the University of Oxford

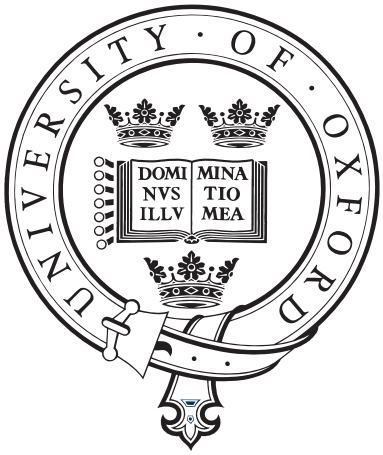

Merton College
University of Oxford
Hilary Term, 2008

Abstract

The variation of a magnetic field in the vicinity of a zero-energy resonance allows highly vibrationally excited molecules ('Feshbach molecules') to be produced from an ultracold atomic gas. In this thesis, we study the dynamics of this process. We begin by studying the dissociation of Feshbach molecules, showing that in the limit of a sudden jump the shape of the spectrum of dissociated atoms can act as a probe of the zero-energy resonance. For some resonances, such jumps are within reach of current experiments. We also study the intermediate region between sudden jumps and asymptotically wide, linear ramps. It is shown from a precise derivation how the latter limit leads to a universal spectrum with a shape independent of the implementation of the two-body physics, provided that the near-resonant scattering properties are correctly modelled.

We then turn to the dynamics of Feshbach molecule production from thermal and condensed gases. Our microscopic quantum dynamics approach includes the exact two-body evolution as an input to the many-body calculations. We show that in the long-time limit, and the Markov limit for the interactions, the non-Markovian Boltzmann equation (NMBE) we derive for the one-body density matrix reduces to the normal Boltzmann equation. In the limit of short times and small depletion of the atomic gas, the molecule production efficiency can be calculated by thermally averaging the two-body transition probability density. This thermal averaging technique is applied to studies of the formation of Feshbach molecules using a magnetic field modulation that is near-resonant with the molecular bound state energy. The continuum is shown to have a significant effect on both the dynamics and efficiency of this process. We examine the dependence of the molecule production efficiency on the duration, amplitude and frequency of the modulation, as well as the temperature and density of the gas. This method of producing molecules is effective for a wide range of bound state energies, but requires sufficient variation of the two-body energy levels with magnetic field.

Lastly, we implement the NMBE for the case of a fast linear ramp across a Feshbach resonance. The solution of this equation is made feasible by including a large part of the required computation in the kernel, which is calculated in advance. The NMBE allows predictions of the molecule production efficiency which go beyond the thermal averaging technique by accounting for the depletion and rethermalisation of the continuum. In the limit of small depletions, the two approaches give the same results.

As the depletion increases, the two approaches differ due to many-body effects limiting the maximum possible molecule production efficiency. We have observed this in our simulations by considering higher-density gases. We have therefore shown the suitability and practicability of this beyond mean-field approach for application to further problems in the production of Feshbach molecules from ultracold gases.

For Zsófi

Acknowledgements

The assistance of several people is acknowledged, and due displays of gratitude are made. People from a variety of places and situations are mentioned, as are some computers. As is customary for the acknowledgements section of a thesis, bad jokes and unnecessarily obscure remarks are included.

Big thanks to Thorsten for his generosity with both his time and his vast knowledge of physics. Working with Thorsten has taught me a lot and been great fun. I also thank Keith for his wise advice, encouragement, and demonstrations of how to make molehills out of mountains. Anything seems possible after a chat with Keith.

I've been lucky to work with many very excellent people in the Clarendon. Professor Góral (the physicist, formerly referred to as BigBoss) was a huge source of good advice on physics and physics life in general. I thank Marzena and Slawek for their good ideas while I was developing the Boltzmann equation code, and Ian Walmsley for his help over these last few months. I also thank those attached to the Keith Burnett Memorial Group during my time here: Mark Lee (now there's a man with one seriously retarded Green's function*), David Sm-err, Hallwood (who took a 3 month 'working trip' so that I could catch up and finish my DPhil at the same time as him), J-ordi Mur Petit (who spotted a lot of erroneous minus signs in this thesis), Hugo Martay, Lord Dunningham, Chairman Ma (who taught me the value of long lunch breaks), Ho-Tsang Ng, Andreas Nunnenkamp, Robert Schumann, Josh Milstein, James Douglas, *et* (concluding with that great academic cop-out in full chorus, the much-cited) *al.*

I've also been lucky with the many very excellent people I've known outside the Clarendon. Zsófi, now and always to remain first, who has never let me forget that there is life apart from physics, and that it can actually be a lot of fun. I thank her for keeping me happy and keeping me going, particularly over these last few months. Érdekes krumpli, eh? Dad, Mum, Julia, Jo and Em have been great also and I thank them for all their support over the last few years. When I remember my time here I'll remember Merton College, St Andrew's, the Globe cafe, and the Gatehouse. I thank all who've made me so glad to have shared those things with them.

*It seems somehow appropriate that my DPhil thesis should contain the geekiest joke I've ever told. Nonetheless, I apologise.

I gratefully acknowledge financial support from the General Sir John Monash Foundation, and Universities UK through the Overseas Research Student Award Scheme. Much of the intensive computation for the non-Markovian Boltzmann equation and resonant association parts of this thesis was done using the facilities of the Oxford e-Science Research Centre and the UK National Grid Service. I thank David Wallom for helping me get started with using these.

And now here's the thing. You can never stay where you came from. The challenge of modern freedom, or the combination of isolation and freedom which confronts you, is to make yourself up. There was only one catch...[†]

[†]Since this is a thesis, and all non-original material must be cited... this last paragraph is misquoted from the works of Saul Bellow, the Idea of North, and Joseph Heller.

Contents

List of Figures

Chapter 1

Introduction

1.1 Ultracold gases

In 1924, Bose published a derivation of Planck's law treating black-body radiation in terms of a gas of identical photons, considering the total number in each mode rather than allocating a mode to each individually [1]. This quantum-statistical idea of the indistinguishability of particles is in contrast to classical statistics, where it is assumed that each particle can in principle be identified. Einstein extended the work of Bose to the case of an ideal gas of atoms in which number is conserved, predicting that a macroscopic number of atoms would accumulate in the ground state at a sufficiently low temperature, or sufficiently high density [2, 3]. This phenomenon became known as Bose-Einstein condensation (BEC), and the statistics of such a gas are referred to as Bose-Einstein statistics. Although there was initial scepticism about the practical significance of BEC, it was found to explain several properties of superfluid liquid ^{4}He, despite the interatomic interactions in this system [4, 5]. In 1926, Fermi-Dirac statistics were suggested for an ideal gas in which no two particles can have identical quantum numbers [6, 7, 8]. This followed on from Pauli's work on the exclusion principle in the context of electron shell orbitals [9], and was quickly applied to phenomena such as white dwarf stars, properties of metals, and electron distributions in heavy atoms (see [10] and references therein). Pauli later found that Bose-Einstein (Fermi-Dirac) statistics apply to particles with a spin equal to an integer (half an odd integer) [11].

Production of a BEC in a dilute atomic gas requires cooling it to degeneracy, where the de Broglie wavelength of the atoms, λ_{deB}, becomes comparable to the interatomic

spacing, i.e. $n\lambda_{\mathrm{deB}}^3 \sim 1$, where n is the density. In current BEC experiments, typical densities and temperatures are of order $10^{13} - 10^{15}$ cm^{-3} and $0.1 - 1\,\mu$K. The study of atomic gases at cold (≤ 1 mK) and ultracold ($\leq 1\,\mu$K) temperatures was made possible by the development of laser cooling techniques in the 1970s and 1980s, and the magneto-optical trapping of atoms at cold temperatures. From this starting point, ultracold gases can be produced through evaporative cooling of atoms in magnetic or optical dipole traps [12], in which the most energetic atoms are selectively removed from the gas while those remaining rethermalise. Bose-Einstein condensates of atomic gases were achieved using ^{87}Rb [13], ^{23}Na [14] and ^{7}Li [15, 16] in 1995. Condensates have also been produced of H [17], ^{85}Rb [18], metastable helium (^{4}He*) [19, 20], ^{41}K [21], ^{133}Cs [22], ^{174}Yb [23], ^{52}Cr [24] and ^{39}K [25]. Early experiments in BEC focused on superfluid [26, 27] and coherence [28] properties. These experiments were well described by the theory of weakly interacting Bose gases developed by Bogoliubov [29] and discussed in several textbooks (e.g., Refs. [30, 31]). In particular, many experiments could be described using the mean-field equation derived by Gross and Pitaevskii [32, 33], commonly referred to as the Gross-Pitaevskii equation (GPE). Due to the Pauli exclusion principle, evaporative cooling of identical fermions becomes impossible as degeneracy is approached. This problem can be overcome using sympathetic cooling, in which collisions with another atomic species [21] or another spin component of the same species [34, 35] are used to maintain thermal equilibrium as the most energetic atoms are removed. To date, fermionic gases of ^{40}K [35] and ^{6}Li [36] have been cooled to degeneracy. Effects such as Cooper pairing, analogous to that observed in superconductors, have been studied [37, 38].

The interactions and confinement of cold atoms can be manipulated to a high degree of precision using electromagnetic fields, and these effects are well enough understood that many problems are theoretically tractable. Since the early studies of ultracold gases, a range of experiments has been made possible by the growing number of condensed atomic species and experimental configurations. Cold gases in optical lattices [39] provide an implementation of the Bose-Hubbard model [40] and are used for studying condensed matter systems, as well as being considered for quantum information processing [41]. Gases in quasi-1D [42, 43] and quasi-2D [43] traps have also been studied. The high ($\sim$20 eV) internal energy of metastable helium atoms provides the possibility of detecting small numbers of atoms with high spatial and temporal resolution, which has been applied to measurements of correlation functions and the Hanbury Brown-Twiss effect for bosons and fermions [44]. Yb is a rare earth atom with a ^{1}S$_0$ ground state and has

a number of abundant isotopes with no hyperfine structure and narrow transition lines, making it suitable for use as a time or frequency standard [23].

1.2 Resonance-enhanced collisions in ultracold gases

Resonance-enhanced collisions are those for which the relative kinetic energy of the interacting particles coincides closely with that of a metastable state, greatly increasing the collision cross-section. Significant early work was done on the problem by Fano [45, 46], who considered the autoionisation of atoms caused by tunnelling of electrons through a potential energy barrier into continuum modes of a resonant energy. In the context of the scattering of nucleons, Feshbach considered the coupling of an energy level of a subsystem to its environment resonantly enhancing the collision rate of free particles [47, 48]. Fano later pointed out the equivalence of the two pictures [46]. Resonance-enhanced interactions had been considered to some extent in earlier works. For example, the autoionisation of atoms was also considered by Rice [49].

The prospect of tuning the interactions in cold gases using a magnetic field was first raised by Stwalley, who suggested Zeeman splitting between hyperfine levels as the cause for decay due to resonant spin-flips of spin-aligned hydrogen, and that this mechanism would be suppressed by a suitable magnetic field [50]. At cold temperatures, *s*-wave collisions are dominant (except between identical fermions), and the collision energy is close to the dissociation threshold. At some magnetic field in the vicinity of that at which the dissociation threshold is degenerate with a bound state of another spin configuration, there is a singularity in the *s*-wave scattering length. This resonance coincides with the presence of an extra bound state on the side of positive scattering length. Consequently, such zero-energy resonances can be used to widely vary the scattering properties of atoms [51] and to produce molecules in their highest-excited vibrational state [52], which have become known as Feshbach molecules. The tuning of the interatomic potential allows the creation of interactions sufficiently strong that the scattering length is of the order of the interparticle separation. In this case, the theory of the weakly interacting Bose gas does not apply.

In ultracold gases, zero-energy resonances were observed in ^{23}Na [53], ^{85}Rb [54, 55] and ^{133}Cs [56] in 1998. In addition to the study of strong interactions and diatomic molecules, zero-energy resonances have been used to tune the scattering length to values

useful for other experiments. For some atomic species, such as ^{85}Rb, ^{133}Cs, and ^{39}K, the *s*-wave scattering length can be tuned to zero, producing an almost ideal gas. Cr atoms have a large magnetic dipole moment and a scattering length that can be magnetically tuned to a small value [24, 57]. This allows investigation of ultracold gases in which the long-range, anisotropic magnetic dipole-dipole interaction is dominant [57, 58, 59]. Also, varying the scattering length during the experiment was central to the achievement of BEC in ^{85}Rb [18] and ^{133}Cs [22]. Both of these experiments employed two stages of evaporative cooling, the first at a magnetic field chosen to maximise the elastic collision rate, and the second at a field chosen to provide sufficient elastic collisions with the minimum possible inelastic loss. Inelastic collisions, leading to the heating of the gas and loss of atoms, can also be enhanced in the vicinity of zero-energy resonances.

1.3 Ultracold diatomic molecules

Ultracold molecules provide an opportunity to study chemistry at low temperatures, where the interactions are well understood and widely tunable. Interactions between diatomic molecules, and between dimers and atoms, provide an entry to studies of few-body physics. Although an established technique for atoms, laser cooling is difficult to implement for molecules because of their more complicated internal structure. For this reason, samples of cold molecules are usually produced from atomic gases by photoassociation [60] or by varying a magnetic field in the vicinity of a zero-energy resonance [61]. Buffer gas cooling, in which an atomic or molecular cloud is cooled by thermalisation with a cryogenically cooled background gas, has been used to produce samples with temperatures of order 100 mK [62, 63, 64]. Photoassociation [60, 65] was the first method by which cold dimers were produced. Typically, photons are used to couple pairs of atoms to a metastable state of an excited potential, which then spontaneously decays into a bound state of the lower potential [66]. The first experiments in photoassociation produced $^{23}Na_2$ [66], $^{85}Rb_2$ [67], $^{133}Cs_2$ [68, 69], and $^{39}K_2$ [70] from magneto-optical traps. Wyner *et al.* produced $^{87}Rb_2$ starting from an atomic condensate [71].

Feshbach molecules were first produced by Wieman's group from a gas of ^{85}Rb [72], using a sudden jump in the magnetic field which projected some atom pairs onto the molecular state. Feshbach molecules have since been created of $^{133}Cs_2$ [73], $^{6}Li_2$ [74, 75, 76], $^{23}Na_2$ [77], $^{87}Rb_2$ [78], and $^{40}K_2$ using both *s*-wave [79] and *p*-wave [80] res-

onances. In addition, heteronuclear molecules of ^{85}Rb-^{87}Rb [81] and ^{40}K-^{87}Rb [82, 83] were recently produced. The majority of these experiments used a linear magnetic field ramp across the zero-energy resonance from negative to positive scattering length. For a trapped gas, the lowest trap state for a pair of atoms is adiabatically mapped onto the Feshbach molecular state as the resonance is crossed, and so some atom pairs are converted to molecules. This has remained the standard technique for producing Feshbach molecules [73, 74, 76, 77, 78, 79, 84, 85, 86, 87, 88]. Other techniques demonstrated include a magnetic field modulation resonant with the molecular bound state energy [80, 81, 89], and thermalisation of the atomic gas into a molecular cloud during a long hold time in the strongly interacting region around the resonance [75, 90, 91]. Bound molecule-like states of two particles have been found to form for negative scattering lengths in one-dimensional waveguides [92] and optical lattices [82, 93]. In contrast to photoassociation, molecules formed by magnetic field variation are typically in their highest excited vibrational bound state. Recently, however, efficient transfer of $^{87}Rb_2$ Feshbach molecules over avoided crossings with deeper bound states was achieved using rf radiation [94].

For magnetic fields sufficiently close to the resonance, the physics of an interacting pair of cold atoms is described solely by the scattering length, a phenomenon referred to as universality (see, e.g., Ref. [61]). Close to the resonance, the Feshbach molecular state has a large spatial extent [95]. Such molecules are an example of a quantum halo system, in which the wavefunction typically has a large admixture beyond the outer classical turning point of the interatomic potential [96]. Measurements of bound state energy [72, 79, 92, 97] and molecular lifetime [98, 99] have confirmed the long range, halo-like form of the molecular wavefunction in the universal regime. In the case of ^{85}Rb, the molecules are in an excited state and so decay due to inelastic spin relaxation [98, 99], a process which occurs at a higher rate for dimers of a small spatial extent. The long range wavefunction of molecules in the universal regime therefore enhances their stability. In the case of dimers formed from a gas of atoms of two different Zeeman states of a fermionic atom, atom-dimer relaxation is suppressed by the Pauli exclusion principle, as two of the three atoms must be identical and so can interact only via p-wave interactions [100, 101]. This allows molecular lifetimes on the order of seconds for the 830 G resonance of ^{6}Li [74, 75, 76]. Bosonic dimers, on the other hand, do not have this suppression.

Degenerate samples of molecules are difficult to produce by photoassociation, due to the population of several molecular states, or unwanted Raman processes in the case of Raman beam photoassociation, and to date have only been made using magnetic field variation. In the experiments of Wieman's group in ^{85}Rb [72], the application of a Ramsey-like pulse in the magnetic field showed coherent evolution between the molecular and atomic components, proving the coherence of the molecular sample. A degenerate sample of $^{23}Na_2$ was produced by Ketterle's group using a linear magnetic field sweep [77]. Molecular condensates, which also require the gas to be in thermal equilibrium, have been created from degenerate Fermi gases of ^{40}K [84] and ^{6}Li [90, 102]. The long lifetime of the dimers allowed thermalisation of the molecular sample and evaporative cooling into the degenerate regime. These experiments, in forming bosonic molecules from fermionic atoms, have given rise to a number of experiments investigating the crossover from BCS pairing to a BEC of molecules [37, 38], as well as associated theoretical work (see [61] and references therein).

Ultracold mixtures of different atomic species, as used in some sympathetic cooling experiments [21], have allowed the study of coexisting degenerate Bose and Fermi gases [42], the separation of bosonic and fermionic components [103], and the production of heteronuclear Feshbach molecules [81, 82, 83]. Heteronuclear molecules in low-lying vibrational states are predicted to have a large electric dipole moment, and are of interest for precision measurements such as the search for a permanent electron electric dipole moment [104]. The experiment of Ref. [82] was carried out in an optical lattice, a context in which heteronuclear molecules are also thought to hold potential as an implementation of quantum information processing [105]. Ultracold atoms and molecules are also used for studies of few-body physics. Zero-energy resonances between molecules of $^{133}Cs_2$ have been observed [106]. Evidence for resonant universal states of three atoms in the vicinity of zero-energy resonances has also been reported [107]. In addition to theoretical work on three-body bound states (see [108] and references therein), a number of studies have begun to look at the structure and dynamics of four-atom systems [109].

For isolated pairs of atoms in an optical lattice, the molecule production efficiency can be made close to 100% by using, for example, a sufficiently slow ramp across a zero-energy resonance [110]. In this case, the suppression of tunnelling by a sufficiently strong potential barrier between each site prevents many-body effects from playing a role. For the formation of diatomic molecules in a loosely trapped gas, however, many-

body effects become significant for times long enough that an interacting pair can be affected by interactions with a third atom. As well as changing the molecule production efficiency, many-body effects alter the velocity distribution of the remaining atoms, leading at long times to rethermalisation. Consequently, the question of the ultimate limits on the production efficiency of ultracold molecules from a loosely trapped gas requires consideration of the many-body effects occurring throughout the process. The maximum production efficiencies from atomic gases in loose harmonic traps achieved to date are 88% in ^{40}K [84] and 85% in ^{6}Li [74]. In the limit of slow ramps, the maximum production efficiency was found from measurements in ^{40}K and ^{85}Rb to be well described by a theory depending only on the phase-space density of the gas [111]. This implies a role for the thermalisation of the gas in limiting the production efficiency, as has been incorporated in theoretical work in a variety of ways [112, 113, 114, 115].

1.4 Structure of this thesis

In this thesis we study the dynamics of molecule association and dissociation using magnetically tuned zero-energy resonances. We begin in Chapter 2 by discussing the theory of resonance-enhanced ultracold collisions. We discuss the physics of atomic collisions at ultracold temperatures, and the physical origin of the resonant enhancement. We then describe the two- and single-channel approaches to modelling ultracold collisions, and the limits of their applicability. We also describe the hard core + van der Waals potential and the separable potential, which are the two models used throughout this thesis.

Chapter 3 concerns the dissociation of Feshbach molecules using linear magnetic field sweeps, and the manner in which the resulting spectrum of dissociated atoms may be used as a probe of the zero-energy resonance. In particular, the nature of the zero-energy resonance determines the shape of the dissociation spectrum in the case of a sufficiently fast ramp in the magnetic field. We also discuss the transfer of molecules into deeper bound states from fast ramps, and the way in which the dissociation spectrum approaches the normal, broad shape for a sufficiently slow, wide ramp. The work of Chapter 3 was published in Ref. [116].

We then turn, in Chapter 4, to the association of Feshbach molecules. After a summary of the dynamics and kinetics of cold gases, and the extension of early work on BEC dynamics to consider nonzero temperatures and strong interactions, we discuss the

theory of cumulants, the microscopic quantum dynamics technique we use in our studies of molecular association. In our approach, the exact two-body dynamics is used as an input to the many-body equation. We derive the non-Markovian, nonlinear Schrödinger equation, giving the evolution of a condensate that is initially at zero temperature, and the non-Markovian Boltzmann equation governing the dynamics of a thermal gas. We then show how these two equations lead to predictions of the molecule production efficiency. For a thermal gas, we show how the molecule production efficiency in the limit of short times and small depletions can be calculated from a thermal average over the two-body transition probability density. Lastly, we show how the non-Markovian Boltzmann equation reduces to the conventional Boltzmann equation in the limits of stationary interactions and long times.

In Chapter 5 we study in detail the association of molecules using a magnetic field modulation that is resonant with the molecular bound state energy, as developed in Wieman's group [81, 89]. The approaches derived in Chapter 4 are applied to study resonant association from both thermal and condensed gases. The continuum of states is found to have a significant effect on the dynamics and efficiency of the molecule production. We discuss the dependence of the molecule production efficiency on the frequency, amplitude and duration of the resonant modulation, and on the temperature and density of the gas. Our theory is applied to a range of bound state energies, and to different experimentally relevant zero-energy resonances, and the limits of the resonant association technique are discussed. The work of Chapter 5 was published in Ref. [117].

In Chapter 6 we apply the non-Markovian Boltzmann equation to studies of the production of molecules from a thermal gas. This goes beyond the approach of Chapter 5 by including many-body effects, such as the rethermalisation and depletion of the continuum. We detail the computationally intensive calculation of the kernel for the non-Markovian equation, and the implementation of the dynamical code. We have applied this technique to a linear ramp across a Feshbach resonance, and in the limit of small depletions obtain results equal to those calculated from the thermal averaging technique used in Chapter 5. As the density of the gas increases, the predicted efficiency of molecule production falls below the thermal averaging prediction due to the onset of many-body effects. In Chapter 7 we conclude and outline plans for further development of the work contained in this thesis.

Chapter 2

Resonance-enhanced ultracold collisions

In this chapter we discuss the physics and modelling of resonance-enhanced ultracold collisions. After a general discussion of the physical origins of the resonant enhancement of the collisions, we discuss the two-channel approach to modelling them. We then discuss the simpler but more limited single-channel approach. Lastly, we introduce the separable and hard core + van der Waals potential models which are used in this thesis.

2.1 Physical origin of resonance-enhanced ultracold collisions

The defining feature of collisions of atoms at cold temperatures is that the de Broglie wavelength of the atoms is much greater than the length scales associated with the interactions between them. This greatly simplifies the theoretical description of these interactions. For two S-state atoms, the long-range form of the potential is the $-C_6/r^6$ van der Waals interaction, where r is the relative position of the two atoms, and C_6 is the van der Waals coefficient. The van der Waals tail has a characteristic length of

$$l_{\mathrm{vdW}} = \frac{1}{2}\left(mC_6/\hbar^2\right)^{1/4}, \tag{2.1}$$

referred to as the van der Waals length, and an associated energy scale of $E_{\mathrm{vdW}} = \hbar^2/(ml_{\mathrm{vdW}}^2)$. As an example of the separation of length scales of the de Broglie wavelength and interatomic potential, ^{85}Rb atoms at 1 μK have $\lambda_{\mathrm{T}} = 9000a_0$, and $l_{\mathrm{vdW}} = 82a_0$, where $\lambda_{\mathrm{T}} = \hbar\sqrt{2\pi/(mk_{\mathrm{B}}T)}$ is the thermal de Broglie wavelength. The collisions between particles may be decomposed into partial waves, all but the lowest of which have a centrifugal barrier. Below approximately 1 mK, the collisions are dominated by the lowest partial wave, the s-wave, and so may be characterised by the s-wave scattering length, a.

In this section, we discuss the physical origin of the resonance-enhancement of ultracold collisions, and the way in which they can be controlled using electromagnetic fields. In Secs. 2.2 and 2.3 we discuss the two- and single-channel approaches to modelling ultracold collisions, and their respective regions of validity. Lastly, in Sec. 2.4 we introduce the hard core + van der Waals and separable potential models which are used throughout this thesis.

We consider two identical alkali atoms with single valence electrons, in the $^2\mathrm{S}_{1/2}$ state. Here, we use Russell-Saunders notation, $^{2s+1}l_j$, where $\mathbf{s}$ is the spin of the unpaired electron, $\mathbf{l}$ is its orbital angular momentum, and $\mathbf{j} = \mathbf{l} + \mathbf{s}$ is the total electronic angular momentum. The sum of the unpaired electron spins of the two atoms, $\mathbf{S} = \mathbf{s}_1 + \mathbf{s}_2$, gives rise to singlet ($S = 0$) and triplet ($S = 1$) states. The electronic interaction between the two atoms is described by the singlet and triplet Born-Oppenheimer potentials. The singlet potential has symmetries summarised by the symbols $^1\Sigma_g^+$, and the triplet by $^3\Sigma_u^+$. Here, the left superscript gives the value of $2S + 1$. Odd ('ungerade') and even ('gerade') symmetry of the wavefunction with respect to reflection through the geometric centre of the molecule are indicated by u and g, respectively. The '+' sign indicates that the electronic wavefunction is symmetrical with respect to reflection in a plane containing the atomic nuclei. There is a splitting between the two potentials created by the difference in chemical bonding interactions from the overlap of the charge clouds of the two atoms at $r \leq 1\,\mathrm{nm}$. The long-range form of this interaction is due to electron exchange, which decreases exponentially with r. For the singlet state, the spin wavefunction is anti-symmetric, leading to a symmetric wavefunction in configuration space. As a result of this, there is an excess of negative charge between the two (slightly positive) atoms, which makes electron exchange attractive. For the triplet state the wavefunction is antisymmetric in configuration space, creating a node in the wavefunction midway between the two atoms, and leading to repulsion from the electron exchange interaction. Consequently, the singlet wavefunction has a deeper attractive minimum than the corresponding triplet potential.

At zero magnetic field, the unpaired electrons in each atom, with total electronic angular momentum $\mathbf{j}$, interact with the nuclear spin $\mathbf{i}$ to produce the hyperfine levels of total angular momentum $\mathbf{f} = \mathbf{j} + \mathbf{i}$. Ground state atoms have $l = 0$, and so the total angular momentum is given by $f = i \pm 1/2$. For some separation r_u, referred to as the uncoupling radius, the splitting between the singlet and triplet potentials is equal to the

hyperfine energy. For ^{85}Rb, for example, $r_u \approx 22a_0$ [61], where a_0 is the Bohr radius. For separations smaller than this the unpaired electrons can be regarded as coupled to each other, whereas for larger separations they are more strongly coupled to their respective nuclei. Magnetic fields split each hyperfine state into its Zeeman components, defined by m_f, the projection of $\mathbf{f}$ in the direction of the magnetic field. Although f ceases to be a good quantum number for high fields at which the Zeeman energy E_Z is larger than the hyperfine splitting E_hf, symmetry demands that m_f remains a good quantum number. Since E_hf and E_Z are typically much larger than the kinetic energies of the atoms involved in a cold collision, collisional properties depend strongly upon the Zeeman levels.

For a pair of identical atoms, the relative and centre of mass coordinates separate. At the collision energies relevant to ultracold gases, it is sufficient to consider only the relative motion. The wavefunction of the relative motion of two identical atoms interacting through a spherically symmetric potential can be written as the sum of an incoming plane wave and an outgoing spherical wave:

$$\psi(\mathbf{r}) = \frac{1}{(2\pi\hbar)^{3/2}}\left(e^{ikz} + f(\theta, p)\frac{e^{ikr}}{r}\right). \tag{2.2}$$

Here, $f(\theta, p)$ is referred to as the scattering amplitude, $p = \hbar k$, and θ is defined with respect to the axis of the collision, $\hat{\mathbf{z}}$. The scattering amplitude is related to the scattering cross-section σ by

$$\frac{d\sigma}{d\Omega} = |f(\theta, p)|^2, \tag{2.3}$$

where $\frac{d\sigma}{d\Omega}$ is the derivative of σ with respect to the solid angle Ω. For the scattering of identical particles we must ensure the correct symmetry of the wavefunction to account for the two different outcomes of the scattering process, i.e. the two atoms swapping output paths. Eq. (2.2) then becomes

$$\psi(\mathbf{r}) = \frac{1}{\sqrt{2}(2\pi\hbar)^{3/2}}\left(e^{ikz} \pm e^{-ikz} + \left[f(\theta, p) \pm f(\pi - \theta, p)\right]\frac{e^{ikr}}{r}\right), \tag{2.4}$$

where the plus (minus) sign applies to bosons (fermions).

Scattering channels describe the state of two greatly separated atoms, and are important in the description of cold collisions, for which a colliding pair begin and end asymptotically far apart. Because of the symmetry of the collision with respect to rotation around the z-axis, it is convenient to perform a partial wave expansion of the stationary scattering wavefunction of the relative motion of the atom pair. A basis for

the separated atoms, and thus for the scattering channels, is then given by the channel index $\alpha = \{f_1 m_{f_1} f_2 m_{f_2} l m_l\}$, where $f_{1,2} m_{f_{1,2}}$ give the Zeeman states of the two atoms, and l and m_l are the quantum numbers of the angular momentum of the relative motion and its projection onto the magnetic field axis, respectively. The lowest three partial waves, $l = 0$, 1, and 2, are referred to as s, p, and d-waves, respectively. Only even (odd) l-states exist for 2 identical bosons (fermions). Channels with a dissociation threshold of energy less than that of the atom pair are described as open. Other channels are referred to as closed.

It is convenient to decompose the wavefunction and Hamiltonian into coupled channels [118], which provides a clear way of considering the component of the wavefunction in each spin configuration, and the interchannel coupling. This gives the equation

$$\frac{\partial^2}{\partial r^2} F_\alpha(r, E) + \frac{m}{\hbar^2} \sum_\beta \left[E\delta_{\alpha\beta} - V_{\alpha\beta}(r) \right] F_\beta(r, E) = 0 \,. \tag{2.5}$$

Here, $E = p^2/m$, m is the atomic mass, $F_\alpha(r, E) = r\psi_\alpha(r, E)$, and $\psi_\alpha(r, E)$ is the projection of the wavefunction onto the channel α. The potential matrix is given by

$$V_{\alpha\beta}(r) = \left[E_{f_1 m_{f_1}} + E_{f_2 m_{f_2}} + \frac{\hbar^2 l(l+1)}{m r^2} \right] \delta_{\alpha\beta} + V_{\text{int}}(r) \,. \tag{2.6}$$

The centrifugal barrier for nonzero l leads to the suppression of higher partial waves at sufficiently low energies. The Zeeman and hyperfine energy are given by the sum $E_{f_1 m_{f_1}} + E_{f_2 m_{f_2}}$. The interaction term in Eq. (2.6) can be written as the sum of two contributions [61]:

$$V_{\text{int}}(r) = V_{\text{el}}(r) + V_{\text{ss}}(r) \,. \tag{2.7}$$

The first component of $V_{\text{int}}(r)$ is the strong electronic interaction, $V_{\text{el}}(r)$, which arises from mixing between the singlet and triplet Born-Oppenheimer potentials, and is responsible for elastic scattering and inelastic spin-exchange collisions. The strong electronic interaction is diagonal in l, i.e. there is no coupling between partial waves, but is not diagonal in $f_1 m_{f_1} f_2 m_{f_2}$, and so couples different Zeeman states. The second contribution to $V_{\text{int}}(r)$ is the weak relativistic spin-spin potential, $V_{\text{ss}}(r)$, which arises from an anisotropic, dipolar interaction of the two electron spins. It is non-diagonal in l, and so couples partial waves. At large r, $V_{\text{ss}}(r) \propto \alpha^2/r^3$, where α is the fine-structure constant. Only blocks with l differing by 0 or 2 units have non-vanishing matrix elements of $V_{\text{ss}}(r)$. The spin-dipole interaction is modified at short-range by second order spin-orbit

contributions, which are significant for heavier atoms. It is responsible for weak inelastic spin-dipolar relaxation.

For a colliding pair of atoms that start and end asymptotically far apart, the evolution of the wavefunction at a sufficiently large relative position of the atoms is indistinguishable from their motion in the absence of an interaction potential. The wavefunction $|\psi\rangle$ at some small separation can therefore be formally written in terms of the in (out) asymptote $|\psi_{\text{in}}\rangle$ ($|\psi_{\text{out}}\rangle$) as

$$|\psi\rangle = \Omega_+|\psi_{\text{in}}\rangle = \Omega_-|\psi_{\text{out}}\rangle\,. \tag{2.8}$$

Here, the Møller operators $\Omega_\pm$ are defined by

$$\Omega_\pm = \lim_{t\to\mp\infty} U^\dagger(t)U_0(t)\,, \tag{2.9}$$

where $U(t)$ is the evolution operator associated with the full Hamiltonian, and $U_0(t)$ is that associated with the free Hamiltonian, H_0. The in and out asymptotes are related to each other by $|\psi_{\text{out}}\rangle = S\,|\psi_{\text{in}}\rangle$, where the S-matrix is defined as

$$S = \Omega_-^\dagger\Omega_+\,. \tag{2.10}$$

It is convenient to define a further quantity, the T-matrix, representing the difference between the S-matrix and the form it would take in the absence of a collision. Assuming elastic collisions, the ingoing and outgoing relative kinetic energies are the same, i.e. $p^2 = p'^2$. We refer to this as the on-shell T-matrix, defined by

$$\langle\mathbf{p}'|S\,|\mathbf{p}\rangle = \delta(\mathbf{p}'-\mathbf{p}) - 2\pi i\delta\left(\tfrac{p'^2}{m} - \tfrac{p^2}{m}\right)\langle\mathbf{p}'|T(z)|\mathbf{p}\rangle\,. \tag{2.11}$$

Here, $z = (p^2/m)+i0$, where '$+i0$' indicates that the energy p^2/m is approached from the upper half of the complex plane, ensuring the correct boundary conditions in Eq. (2.10), and also in the scattering wavefunction of Eq. (2.2). The T-matrix can also be defined for $p'^2 \neq p^2$ ('off-shell'), however only the on-shell T-matrix occurs in the S-matrix.

Decomposing the scattering amplitude and collision cross-section, $\sigma(p)$, in terms of partial waves allows all the information about a collision to be expressed in terms of the phase shifts $\xi_l(p)$ [119]:

$$f(\theta,p) = \frac{\hbar}{p}\sum_{l=0}^{\infty}(2l+1)e^{i\xi_l(p)}\sin(\xi_l(p))P_l(\cos\theta)\,, \tag{2.12}$$

$$\sigma(p) = \frac{4\pi\hbar^2}{p^2}\sum_{l=0}^{\infty}(2l+1)^2\sin^2\xi_l(p)\,. \tag{2.13}$$

Here, $P_l(\cos\theta)$ is the lth Legendre polynomial. We now focus on the s-wave phase shift, $\xi_0(p)$, and the corresponding scattering length and cross-section, which are dominant at cold temperatures. They have no angular dependence, since $P_0(\cos\theta) = 1$. The long-range form of the scattering wavefunction is given by a sine wave divided by r, with a phase shift due to the short-range interaction:

$$\psi_\alpha(r, p^2/m) \propto \sin[(p/\hbar)r + \xi_0(p)]/r\,. \tag{2.14}$$

The s-wave scattering phase shift and amplitude may be decomposed into background and resonance components, i.e.

$$\xi_0(p) = \xi_0^{\rm bg}(p) + \xi_0^{\rm res}(p)\,, \tag{2.15}$$

$$f_0(p) = f_0^{\rm bg}(p) + f_0^{\rm res}(p)\,, \tag{2.16}$$

where $f_0^{\rm bg}(p) = (\hbar/p)e^{i\xi_0^{\rm bg}(p)}\sin(\xi_0^{\rm bg}(p))$ and $f_0^{\rm res}(p) = e^{2i\xi_0^{\rm bg}(p)}(\hbar/p)e^{i\xi_0^{\rm res}(p)}\sin(\xi_0^{\rm res}(p))$. This separation is visible in the scattering phase shifts shown in Fig. 2.1. The background contribution is constant with magnetic field, and the resonance feature is visible at large enough collision energies, centred around the resonance energy $E_{\rm res}(B)$. The behaviour at low collision energies varies depending on the strength of the resonance, as will be discussed in Sec. 2.2.

The scattering amplitude may also be expressed in terms of the T-matrix of Eq. (2.11):

$$f_0(p) = -\frac{(2\pi\hbar)^3 m}{4\pi\hbar^2}\langle \mathbf{p}|T(p^2/m + i0)|\mathbf{p}\rangle\,. \tag{2.17}$$

In the limit of low momentum, $f_0(p) \underset{p\to 0}{\sim} -a$, where a is referred to as the s-wave scattering length. As this is independent of angle, after we apply the symmetrisation of Eq. (2.4) for identical particles, the s-wave cross section becomes $8\pi a^2$ for bosons, and 0 for fermions. The s-wave scattering length generally varies weakly with magnetic field. However, a bound state of a closed channel can be near in energy to that of the colliding atoms, in which case it is referred to as a resonance level. In the low energy limit where the resonance level is degenerate with the entrance-channel dissociation threshold, this gives rise to a so-called zero-energy resonance. The metastability of the resonance level leads to an enhancement of the scattering length of the following form [120]:

$$a(B) = a_{\rm bg}\left(1 - \frac{\Delta B}{B - B_0}\right). \tag{2.18}$$

Here, $a_{\rm bg}$ is the background scattering length, i.e. the s-wave scattering length far from the resonance where the resonance contribution to Eq. (2.16) is zero. The width and

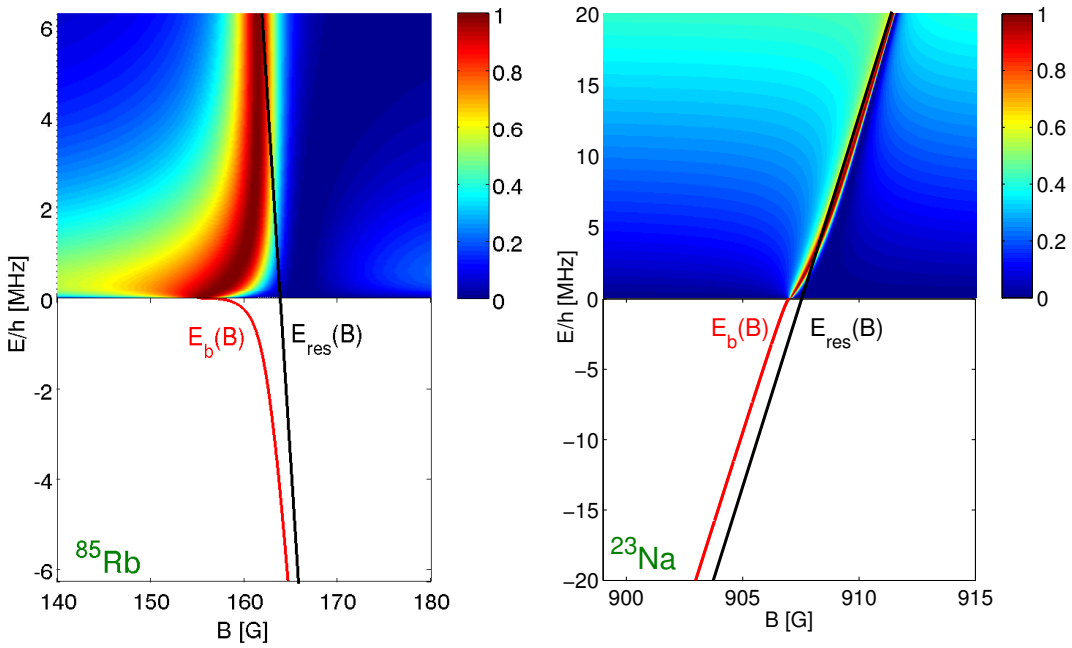

Figure 2.1: s-wave phase shift $\sin^2\xi_0$ for the 155 G resonance of ^{85}Rb (left), and the 907 G resonance of ^{23}Na (right). The resonance at small positive energies mirrors the bound state energy $E_\mathrm{b}(B)$ for the case of ^{85}Rb. A clear resonance feature, close to the energy of the resonance level $E_\mathrm{res}(B)$, only emerges for energies larger than $E_\mathrm{vdW} = h \times 6.3\,\mathrm{MHz}$, where E_vdW is the van der Waals energy, defined after Eq. (2.1). For ^{23}Na the resonance feature follows the energy of the resonance level at energies much smaller than $E_\mathrm{vdW} = h \times 78\,\mathrm{MHz}$. The distinction between the resonances of ^{85}Rb and ^{23}Na , leading to the different behaviours of the scattering phase-shift, is discussed in Sec. 2.2.

location of the resonance are given by ΔB and B_0, respectively. The interchannel coupling shifts B_0 from the field B_res at which the resonance level becomes degenerate with the entrance-channel dissociation threshold. We discuss the derivation and applicability of Eq. (2.18) in Sec. 2.2. The scattering length given by Eq. (2.18) is plotted for the case of ^{85}Rb atoms in the vicinity of the 155 G resonance in Fig. 2.2. The resonant enhancement of the scattering length can be interpreted as the capture of the atom pair into the metastable state, and a delay due to the decay time of that state which contributes to the phase-shift of Eq. (2.15). The width of the resonance is determined by the coupling strength between the channels, which sets the metastable state lifetime. The first correction to the relation of scattering phase shift and scattering length with increasing energy can be found from an asymptotic low-energy expansion known as effective range

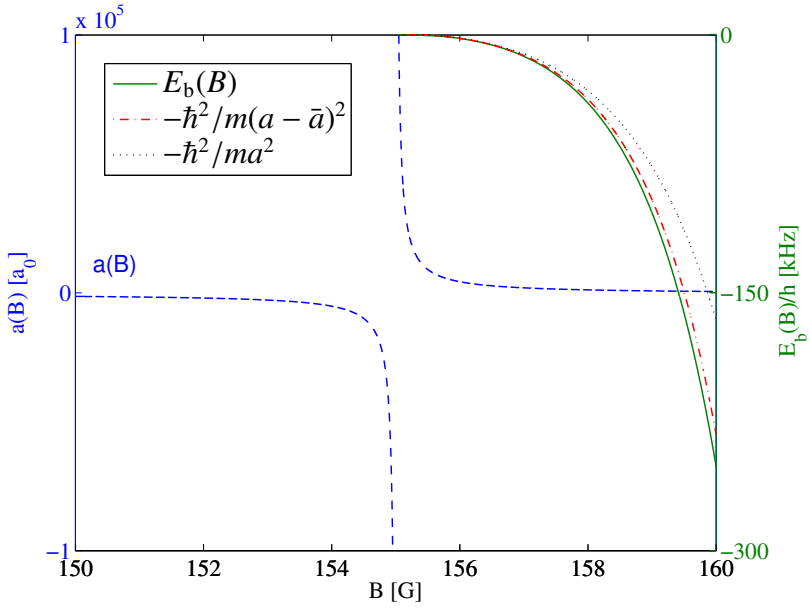

Figure 2.2: Variation of the scattering length (dashed line) and bound state energy around the 155 G resonance of ^{85}Rb. On the positive scattering length side of the resonance the highest vibrational bound state is referred to as the Feshbach molecule. The dotted line, dot-dashed line and solid line show the bound state energy given by the universal formula of Eq. (2.44), the Gribakin-Flambaum formula of Eq. (2.48), and the two-channel approach of Eq. (2.27), respectively.

theory [121]:

$$k\cot(\xi(\hbar k)) = -\frac{1}{a} + \frac{1}{2}k^2 r_{\text{eff}}\,, \tag{2.19}$$

where r_{eff} is a constant with units of length, referred to as the effective range. For the ultracold temperatures considered in this thesis, only the scattering length needs to be considered.

2.2 Two-channel approach

Expanding the Hamiltonian for an interacting pair of atoms in terms of coupled channels allows prediction of the properties of resonance-enhanced ultracold collisions [118, 122, 123], including the location of zero-energy resonances. This requires adjustment of the potential of each channel to recover the singlet and triplet scattering lengths of the Born-Oppenheimer potentials, and the long-range van der Waals interaction. For a wide range of problems, it is sufficient to use the parameters extracted from coupled-channels calculations to model a zero-energy resonance including only the entrance channel, defining

the initial Zeeman states of the atom pair, and one closed channel, containing the resonance level which becomes degenerate with the entrance-channel dissociation threshold [52, 120, 124, 125, 126, 127]. This is referred to as the two-channel approach, and leads to the Hamiltonian

$$H_{2B}(B) = |\mathrm{bg}\rangle H_{\mathrm{bg}}\langle \mathrm{bg}| + W|\mathrm{bg}\rangle\langle \mathrm{cl}| + |\mathrm{cl}\rangle\langle \mathrm{bg}|W + |\mathrm{cl}\rangle H_{\mathrm{cl}}(B)\langle \mathrm{cl}|\,. \tag{2.20}$$

Here, $H_{\mathrm{bg,cl}} = H_0 + V_{\mathrm{bg,cl}}$ are the bare Hamiltonians of the entrance and closed channels, respectively, $H_0 = -\hbar^2\nabla^2/m$ is the kinetic energy operator of the relative motion of an atom pair, and W represents the interchannel coupling. We choose the zero of energy to be at the dissociation threshold of the entrance channel. Consequently, all the magnetic field dependence of the Hamiltonian is contained in $H_{\mathrm{cl}}(B)$. The application of a magnetic field to an atom changes the relative energies of different channels due to the Zeeman effect. This can lead to the degeneracy of the resonance level with the dissociation threshold of the entrance channel, as discussed in the previous section. It can be shown that once coupling is included, there exists a bound vibrational molecular state that becomes degenerate with the entrance-channel dissociation threshold at B_0, as illustrated in Fig. 2.2. A pair of atoms in this molecular bound state is commonly referred to as a Feshbach molecule. This molecular state is an eigenstate of the two-channel Hamiltonian, and its degeneracy with the entrance-channel dissociation threshold coincides with the singularity in the scattering length given by Eq. (2.18).

Within magnetic field ranges normally of experimental relevance for single zero-energy resonances, only the Feshbach resonance level, ϕ_{res}, has an energy that can become near resonant with pairs of atoms in the entrance channel. Consequently, the closed-channel Hamiltonian $H_{\mathrm{cl}}(B)$ is well described by taking into account only ϕ_{res}, which fulfils the Schrödinger equation

$$H_{\mathrm{cl}}(B)\phi_{\mathrm{res}} = E_{\mathrm{res}}(B)\phi_{\mathrm{res}}\,. \tag{2.21}$$

Here, $E_{\mathrm{res}}(B) = \mu_{\mathrm{res}}(B - B_{\mathrm{res}})$ is the energy of the Feshbach resonance level, shown as a black line in Fig. 2.1, with μ_{res} the difference in magnetic moment between the two channels. The validity of Eq. (2.21) requires that the electronic degrees of freedom of the atoms adiabatically follow all changes in the magnetic field strength. The single-resonance approach to $H_{\mathrm{cl}}(B)$ consists of making the approximation

$$H_{\mathrm{cl}}(B) = |\phi_{\mathrm{res}}\rangle E_{\mathrm{res}}(B)\langle \phi_{\mathrm{res}}|\,. \tag{2.22}$$

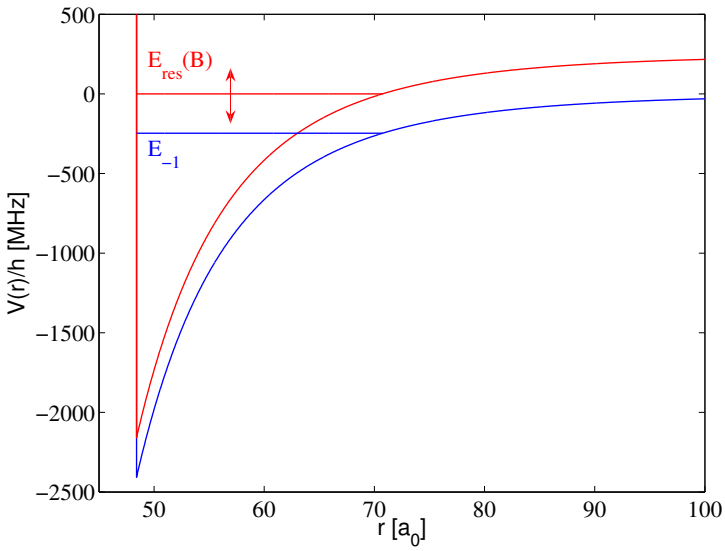

Figure 2.3: Representation of the entrance and closed channels with the hard core + van der Waals potential of Sec. 2.4.1, for the 155 G resonance of ^{85}Rb. At a field $B_{\rm res}$ close to the singularity in scattering length at B_0, the resonance level becomes degenerate with the dissociation threshold of the entrance channel, i.e. $E_{\rm res}(B_{\rm res}) = 0$. The highest vibrational bound state of the entrance channel has energy E_{-1}, and in this case is far enough below the dissociation threshold to play no role within the experimentally relevant range of magnetic fields.

The two-channel Hamiltonian of Eq. (2.20) then becomes

$$\begin{aligned} H_{\rm 2B}(B) = {} & |{\rm bg}\rangle H_{\rm bg}\langle{\rm bg}| + W|\phi_{\rm res},{\rm bg}\rangle\langle\phi_{\rm res},{\rm cl}| \\ & + |\phi_{\rm res},{\rm cl}\rangle\langle\phi_{\rm res},{\rm bg}|W + |\phi_{\rm res},{\rm cl}\rangle E_{\rm res}(B)\langle\phi_{\rm res},{\rm cl}|\,. \end{aligned} \tag{2.23}$$

On the side of B_0 where $a > 0$ the Hamiltonian of Eq. (2.23) supports the Feshbach molecular state, satisfying

$$H_{\rm 2B}(B)\phi_{\rm b}(B) = E_{\rm b}(B)\phi_{\rm b}(B)\,. \tag{2.24}$$

Here, $E_{\rm b}(B)$ is the magnetic-field dependent bound state energy, which vanishes at B_0. In the single-resonance approach, the Feshbach molecule assumes the two-component form [128]

$$\begin{pmatrix} \phi_{\rm b}^{\rm bg}(B) \\ \phi_{\rm b}^{\rm cl}(B) \end{pmatrix} = \frac{1}{\mathcal{N}_{\rm b}(B)} \begin{pmatrix} G_{\rm bg}(E_{\rm b}(B))W\phi_{\rm res} \\ \phi_{\rm res} \end{pmatrix}. \tag{2.25}$$

Here, $\phi_{\rm b}^{\rm bg}(B)$ and $\phi_{\rm b}^{\rm cl}(B)$ are the entrance- and closed-channel components of $\phi_{\rm b}(B)$, respectively, and the normalisation constant $\mathcal{N}_{\rm b}(B)$ is given by

$$\mathcal{N}_{\rm b}(B) = \sqrt{1 + \langle\phi_{\rm res}|WG_{\rm bg}^2(E_{\rm b}(B))W|\phi_{\rm res}\rangle}\,. \tag{2.26}$$

In Eqs. (2.25) and (2.26) the energy dependent Green's function $G_{\rm bg}(z)$, associated with the entrance-channel Hamiltonian by $G_{\rm bg}(z) = (z - H_{\rm bg})^{-1}$, is evaluated at the bound state energy $z = E_{\rm b}(B)$. The solution of Eq. (2.24) using the single-resonance Hamiltonian of Eq. (2.23) indicates that $E_{\rm b}(B)$ fulfils the condition

$$E_{\rm b}(B) = E_{\rm res}(B) + \langle \phi_{\rm res} | W G_{\rm bg}(E_{\rm b}(B)) W | \phi_{\rm res} \rangle \,. \tag{2.27}$$

We have plotted the bound state energy obtained in this manner for the case of ^{85}Rb dimers near the 155 G resonance in Fig. 2.2.

The continuum part of the spectrum of $H_{\rm 2B}(B)$ is represented by the scattering states $\phi_{\mathbf{p}}(B)$, which are labelled by the relative momentum $\mathbf{p}$ of an atom pair and satisfy

$$H_{\rm 2B}(B)\phi_{\mathbf{p}}(B) = E\phi_{\mathbf{p}}(B) \,, \tag{2.28}$$

where $E = p^2/m$. The scattering states have the following two-component form in the single-resonance approach [128]:

$$\begin{pmatrix} \phi_{\mathbf{p}}^{\rm bg}(B) \\ \phi_{\mathbf{p}}^{\rm cl}(B) \end{pmatrix} = \begin{pmatrix} \phi_{\mathbf{p}}^{(+)} + A(B,E) G_{\rm bg}(z) W \phi_{\rm res} \\ A(B,E)\phi_{\rm res} \end{pmatrix} . \tag{2.29}$$

Here, $z = E + i0$. The magnetic-field and energy dependent amplitude $A(B, E)$ is given by

$$A(B,E) = \frac{\langle \phi_{\rm res} | W | \phi_{\mathbf{p}}^{(+)} \rangle}{E - E_{\rm res}(B) - [\Delta(E) - i\gamma(E)]} \,, \tag{2.30}$$

where the real functions $\Delta(E)$ and $\gamma(E)$ satisfy

$$\Delta(E) - i\gamma(E) = \langle \phi_{\rm res} | W G_{\rm bg}(z) W | \phi_{\rm res} \rangle \,. \tag{2.31}$$

The function $\Delta(E)$ acquires the meaning of an energy shift, while $\gamma(E)$ gives the decay width of the metastable Feshbach resonance level. In the case of negative energies, as in Eq. (2.27), the decay width $\gamma(E)$ vanishes. The entrance-channel scattering state of relative momentum $\mathbf{p}$, $\phi_{\mathbf{p}}^{(+)}$, is associated with the entrance-channel Hamiltonian $H_{\rm bg}$ via $H_{\rm bg}\phi_{\mathbf{p}}^{(+)} = E\phi_{\mathbf{p}}^{(+)}$ [128]. It may be calculated from

$$|\phi_{\mathbf{p}}^{(+)}\rangle = |\mathbf{p}\rangle + G_0(z) T_{\rm bg}(z) |\mathbf{p}\rangle \tag{2.32}$$

The form of the s-wave scattering length may be calculated from the entrance-channel component of Eq. (2.29), the bound closed-channel contribution being negli-

gible at long distances. Substituting Eq. (2.32) we obtain

$$|\phi_{\mathbf{p}}^{\mathrm{bg}}\rangle = |\mathbf{p}\rangle + G_0(z)T(z)|\mathbf{p}\rangle \tag{2.33}$$

$$= |\mathbf{p}\rangle + G_0(z)T_{\mathrm{bg}}(z)|\mathbf{p}\rangle + G_0(z)[1 + T_{\mathrm{bg}}(z)G_0(z)]W|\phi_{\mathrm{res}}\rangle A(B,E)\,. \tag{2.34}$$

Here, we have used the following relation for the entrance-channel Green's function [119]:

$$G_{\mathrm{bg}}(z) = G_0(z) + G_0(z)T_{\mathrm{bg}}(z)G_0(z)\,. \tag{2.35}$$

Closing Eq. (2.33) and Eq. (2.34) with $\langle\mathbf{q}|$, we use the relation [61]

$$\frac{1}{z' - p^2/m} = -i\pi\delta\left(\tfrac{q^2}{m} - \tfrac{p^2}{m}\right) + \mathcal{P}\frac{1}{(q^2/m) - (p^2/m)}\,, \tag{2.36}$$

where $\mathcal{P}$ indicates the principal value of the integral, and obtain

$$\langle\mathbf{p}|T(z)|\mathbf{p}\rangle = \langle\mathbf{p}|T_{\mathrm{bg}}(z)|\mathbf{p}\rangle + \langle\phi_{\mathbf{p}}^{(-)}|W|\phi_{\mathrm{res}}\rangle A(B,E)\,. \tag{2.37}$$

Using Eq. (2.17) we can then identify the background and resonance parts of the scattering amplitude in Eq. (2.16):

$$f_0^{\mathrm{bg}}(p) = -2\pi^2 m\hbar\langle\mathbf{p}|T_{\mathrm{bg}}(z)|\mathbf{p}\rangle\,, \tag{2.38}$$

$$f_0^{\mathrm{res}}(p) = -2\pi^2 m\hbar\langle\phi_{\mathbf{p}}^{(-)}|W|\phi_{\mathrm{res}}\rangle A(B,E)\,. \tag{2.39}$$

In analogy to the zero-momentum limit of Eq. (2.17), the background scattering length a_{bg} is given by $f_0^{\mathrm{bg}} \underset{p\to 0}{\sim} -a_{\mathrm{bg}}$. Taking the zero-energy limit of Eq. (2.37), and using Eq. (2.29) and Eq. (2.30) gives the result of Eq. (2.18) for a in the vicinity of a zero-energy resonance. In this approach, the resonance width ΔB and shift $B_0 - B_{\mathrm{res}}$ are given by

$$\Delta B = \frac{m}{4\pi\hbar^2 a_{\mathrm{bg}}}\frac{(2\pi\hbar)^3|\langle\phi_{\mathrm{res}}|W|\phi_0^{(+)}\rangle|^2}{\mu_{\mathrm{res}}}\,, \tag{2.40}$$

$$B_0 - B_{\mathrm{res}} = -\frac{\langle\phi_{\mathrm{res}}|WG_{\mathrm{bg}}(0)W|\phi_{\mathrm{res}}\rangle}{\mu_{\mathrm{res}}}\,. \tag{2.41}$$

The manner in which the two-body energy spectrum varies in the vicinity of a zero-energy resonance depends on the admixtures in the open and closed channels. For the case of a closed-channel dominated resonance, the molecular state varies significantly from the resonance level only within a narrow range of magnetic fields around the resonance. Outside of this range, the resonance level has a clearly visible signature. Resonances which are dominated by the entrance channel have a wider range of magnetic

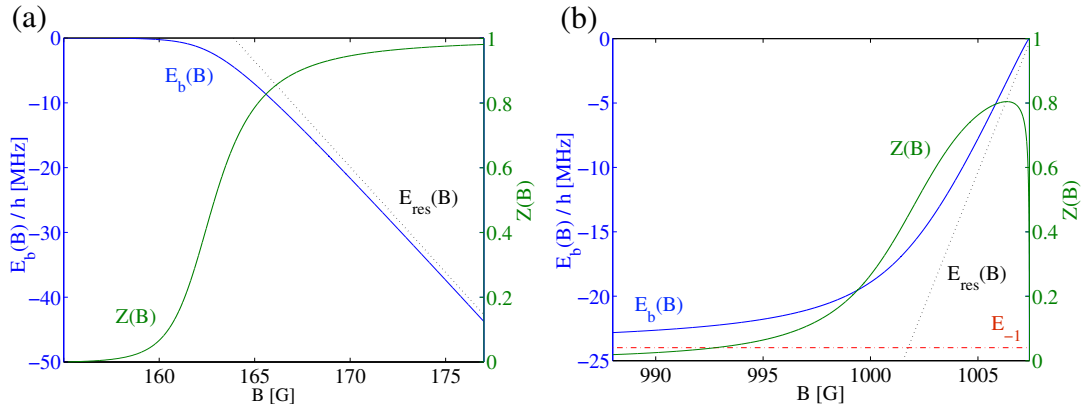

Figure 2.4: Bound-state energy $E_\mathrm{b}(B)$ and closed-channel admixture $Z(B)$ for (a) $^{85}Rb_2$ near the entrance-channel dominated 155 G resonance, and (b) $^{87}Rb_2$ near the closed-channel dominated 1007.4 G resonance. For the ^{85}Rb resonance, the closed-channel admixture is suppressed over a range of several Gauss. For the ^{87}Rb resonance, however, the closed-channel admixture quickly increases outside the narrow universal regime, before again being suppressed by an avoided crossing with the bare entrance-channel bound state at $E_{-1}/h = -24$ MHz. As the closed-channel admixture increases, $E_\mathrm{b}(B)$ approaches the energy of the resonance level, $E_\mathrm{res}(B)$.

field within which the Feshbach molecular state behaves differently to the resonance level, which can only become dominant at much larger energies [129, 130]. This contrast is shown by the comparison of the 155 G resonance of ^{85}Rb and the 907 G resonance of ^{23}Na in Fig. 2.1. The suppression of the resonance level is closely linked to the concept of universality and the capacity to describe a resonance using only a single channel.

2.3 Single-channel approach

The Feshbach molecular state has an admixture in the closed-channel of $Z(B) = \mathcal{N}_\mathrm{b}(B)^{-2}$, where $\mathcal{N}_\mathrm{b}(B)$ is given by Eq. (2.26). The closed-channel admixture can also be calculated from the ratio of the magnetic moment of the Feshbach molecular state to that of the resonance level:

$$Z(B) = \mu_\mathrm{res}^{-1}\left(\frac{\partial E_\mathrm{b}}{\partial B}\right). \tag{2.42}$$

This relation can be derived from Eqs. (2.26) and (2.27), using the identity

$$G_\mathrm{bg}^2(E_\mathrm{b}) = -\frac{\partial}{\partial E_\mathrm{b}} G_\mathrm{bg}(E_\mathrm{b}). \tag{2.43}$$

The closed-channel admixture is small for magnetic fields sufficiently close to the resonance. The molecular wavefunction then has a long-range form, with a large part of

its admixture beyond the outer classical turning point of the potential at the bound state energy. Such molecules are examples of quantum halo systems [96], and have a bound state energy given by

$$E(B) = -\frac{\hbar^2}{ma(B)^2}\,. \tag{2.44}$$

Differentiating this result with respect to B and substituting into Eq. (2.42) shows the suppression of the closed-channel admixture. This was directly measured by Partridge *et al.* [131]. In the close vicinity of a zero-energy resonance there exists a region in which the physics depends only on the scattering length. This is referred to as the Wigner threshold law regime for positive energies [132], and as the universal regime for negative energies (see, e.g., Ref. [61]). Suppression of the closed-channel admixture of the Feshbach molecular state occurs in the universal regime. The decay rate of the resonance level into the continuum in the Wigner threshold law regime, given by Fermi's golden rule, determines the width of the zero-energy resonance. The decay rate is given by the imaginary part of Eq. (2.31), evaluated in the limit of low energies [132]:

$$\langle\phi_{\rm res}|WG_{\rm bg}(z)W|\phi_{\rm res}\rangle \underset{k\to 0}{\sim} \mu_{\rm res}(B_{\rm res} - B_0 - ika_{\rm bg}\Delta B)\,. \tag{2.45}$$

Evaluating this quantity at $z = E_{\rm b}(B)$ and substituting into Eq. (2.27) gives the result of Eq. (2.44), showing the link between the Wigner threshold law and universal regimes.

When the closed-channel admixture is sufficiently small, the Feshbach molecular state can be described using only one channel [95, 114, 128]. The effective single-channel approach aims to recover the resonance-enhanced scattering properties by choosing the interaction potential as a perturbed background scattering potential. The potential is varied with magnetic field in order to reproduce the scattering length of Eq. (2.18). The two-body Hamiltonian is then given by

$$H_{\rm 2B} = H_0 + V_{\rm eff}(B)\,, \tag{2.46}$$

where $V_{\rm eff}(B)$ is the effective potential. The Feshbach molecular state is then modelled using the highest vibrational bound state of this varying potential, which satisfies

$$|\phi_{\rm b}\rangle = G_0(E_{\rm b}(B))V_{\rm eff}(B)|\phi_{\rm b}\rangle\,. \tag{2.47}$$

The scattering states are modelled in the single-channel approach by the bare scattering states of Eq. (2.32). For narrow, closed-channel dominated resonances, the single-channel approach is only valid in the universal regime. For such resonances, the universal regime can be narrow to the extent of being experimentally inaccessible. For

entrance-channel dominated resonances the closed-channel admixture is small over a wider range of fields, making the universal region wider. Furthermore, for these resonances the universal bound state energy of Eq. (2.44) is accurately extended beyond the universal regime by the entrance-channel Gribakin-Flambaum formula for the bound state energy [133, 134]:

$$E_{\mathrm{b}} \approx -\frac{\hbar^2}{m(a-\bar{a})^2}\,. \tag{2.48}$$

Here, $\bar{a} = \frac{1}{\sqrt{2}}\frac{\Gamma(3/4)}{\Gamma(5/4)} l_{\mathrm{vdW}}$ is the mean scattering length, which represents the correction due to the van der Waals tail of the potential. The van der Waals length, l_{vdW}, is given by Eq. (2.1). The Gribakin-Flambaum bound state energy of Eq. (2.48) is plotted for $^{85}Rb_2$ in Fig. 2.2. This extension to the universal bound state energy is made valid by the dominance of the van der Waals tail of the entrance-channel potential over the resonance level. Consequently, the single-channel approach is valid over a wider range of fields for entrance-channel dominated resonances. We discuss the manner in which closed-channel dominance can be measured in Chapter 3.

2.4 Modelling ultracold interactions

In 1935, Bethe introduced a model for the scattering of a neutron off a nucleus in which a short-range, WKB wavefunction for the neutron inside the nucleus was matched to the free stationary wavefunction at asymptotically large distances [135]. As the wavelength of the free motion is too great to resolve features at the length scale characteristic of the potential, the short-range physics can be approximated in a simple manner that provides the correct phase shift in Eq. (2.14). Quantum defect theory [136, 137, 138] applies the idea of matching short- and long-range wavefunctions to collisions of cold atoms, using the analytic properties of the van der Waals interaction to account for the long-range physics. This allows the energy dependence of the resonant enhancement to be analytically treated at millikelvin temperatures. In order to model resonance-enhanced ultracold collisions with energies of order microkelvin, however, theories can be made even simpler. For this case, it is only necessary that the chosen entrance-channel potential recover the correct background scattering length and asymptotic long range form (or equivalently the energy of the highest vibrational bound state), and that the interchannel coupling reproduce the resonance width and shift of Eqs. (2.40) and (2.41). The resonance width

Table 2.1: Parameters of the entrance channel for resonances studied in this thesis. Unless otherwise noted, data are taken from [61] and the references contained therein.

Species	(f, m_f)	B_0 [G]	a_{bg} [a_0]	C_6 [a.u.]	$\frac{1}{h}\lvert E_{-1}\rvert$ [MHz]
^{85}Rb	(2, -2)	155	-443	4703	218
^{23}Na	(1, 1)	907	62.8	1561	218
^{87}Rb	(1, 1)	1007.4	100.5	4703	24.0
^{87}Rb	(1, 1)	685 [87]	100.5	4703	24.0
^{133}Cs	(3, 3)	-11.2 [140]	1720 [140]	6890	0.011
^{133}Cs	(3, 3)	47.97	905	6890	0.045

Table 2.2: Interchannel coupling parameters of resonances studied in this thesis. Unless otherwise noted, data are taken from [61] and the references contained therein. The closed-channel dominance η is given by Eq. (3.8).

Species	B_0 [G]	ΔB [G]	μ_{res}/h [MHz/G]	η
^{85}Rb	155	10.71	-3.26	0.04
^{23}Na	907	1.0	5.24	11
^{87}Rb	1007.4	0.21	4.2	5.9
^{87}Rb	685 [87]	0.0062 [87]	1.76 [141]	479.6
^{133}Cs	-11.2 [140]	27.5 [140]	4.2 [141]	0.001
^{133}Cs	47.97	0.15	2.09	0.99

can be measured experimentally, while the shift must be deduced from the following equation, which can be derived from quantum defect theory [136, 137, 138, 139]:

$$B_0 - B_{\mathrm{res}} = (\Delta B)\frac{\frac{a_{\mathrm{bg}}}{\bar{a}}\left(1-\frac{a_{\mathrm{bg}}}{\bar{a}}\right)}{1+\left(1-\frac{a_{\mathrm{bg}}}{\bar{a}}\right)^2}. \tag{2.49}$$

The parameters of the entrance-channel potential and interchannel coupling for the resonances studied in this thesis are given in Tables 2.1 and 2.2.

In this section we describe the two potential models used throughout this thesis. In Sec. 2.4.1 we discuss the hard core + van der Waals potential, which assumes a $-C_6/r^6$ potential at all distances larger than a certain core radius, within which the potential is infinite. Several other potentials have also been described, which vary at small separations but recover the long-range van der Waals interaction (e.g. Refs. [95, 126, 127]). These have a clear motivation from the ideas of quantum defect theory and are able to accommodate arbitrarily many bound states in the bare entrance-channel potential. However, they can often be impractical for dynamical simulations, and in many cases

cover an unnecessarily wide energy range. Consequently, many studies use simpler effective potentials which recover the required properties of the low-energy collisions (e.g. Refs. [109, 128, 142, 143]). In Sec. 2.4.2 we discuss the separable potential, a simpler approach which allows analytic calculation of some matrix elements and is ideal as an input to many-body calculations.

2.4.1 Hard core + van der Waals potential

The hard core + van der Waals potential has the intuitive feature of retaining the physical form of the atomic interaction at long distances. At the short distances not resolved by the low-energy atoms, a hard core is used within a radius set to recover the correct scattering length. The entrance-channel potential has the form

$$V_{\mathrm{bg}}(r) = \begin{cases} \infty & r < R_{\mathrm{c}} \\ -C_6/r^6 & r > R_{\mathrm{c}} \end{cases} , \tag{2.50}$$

where R_{c} is the core radius. This potential is illustrated in Fig. 2.3. R_{c} is varied to recover the correct background scattering length for the known C_6 and m. There are typically several values of this radius which all recover the correct scattering length, each corresponding to a different number of bound states being included in the potential. The highest excited vibrational bound state of the entrance channel is denoted ϕ_{-1}, and its energy is denoted E_{-1}. The background scattering length is calculated from the long-range behaviour of the zero-momentum limit of the scattering wavefunction, according to the semiclassical approach of Gribakin and Flambaum [133]. For the potential of Eq. (2.50), the scattering length is given by

$$a_{\mathrm{bg}} = \bar{a}\left[1 - \tan\left(\Phi - \frac{3\pi}{8}\right)\right] . \tag{2.51}$$

Here, $\bar{a}$ is the mean scattering length defined after Eq. (2.48), representing the correction due to the long-range tail, and Φ is the semiclassical phase defined by

$$\begin{aligned} \Phi &= \frac{1}{\hbar}\int_{R_{\mathrm{c}}}^{\infty} dr\, \sqrt{2m(-V_{\mathrm{bg}}(r))} \\ &= \frac{\sqrt{mC_6}}{\sqrt{2}\hbar R_{\mathrm{c}}^2} . \end{aligned} \tag{2.52}$$

We model the potential of the closed channel by

$$V_{\mathrm{cl}}(r) = V_{\mathrm{bg}}(r) + \mu_{\mathrm{res}}(B - B_{\mathrm{res}}) + E_{\mathrm{shift}} , \tag{2.53}$$

where $E_{\rm shift}$ ensures that the resonance level crosses the dissociation threshold at $B_{\rm res}$. We also approximate the wavefunction of the Feshbach resonance level to be the same as that of the top vibrational bound state of the entrance-channel potential, and so $E_{\rm shift} = -E_{-1}$. As in the construction of $V_{\rm bg}$, this is permissible because of the long de Broglie wavelength of the ultracold atoms. In accordance with the discussion of Sec. 2.2, we make the single-resonance approximation, including only one bound state in the bare potential. There is also great flexibility in the modelling of interchannel coupling, which is taken to have the form

$$W(r) = \beta \exp(-r/r_{\rm off})\,. \tag{2.54}$$

Here, β is the amplitude and $r_{\rm off}$ is the range of the coupling. This form of the coupling is arbitrary, but by fitting the parameters β and $r_{\rm off}$ appropriately has been found to exactly recover ΔB and $B_0 - B_{\rm res}$ [95, 126]. Equations (2.40) and (2.41) show that the ratio $\frac{B_0 - B_{\rm res}}{\Delta B}$ is independent of β, and so we calculate this ratio, adjusting it to agree with the result given by Eq. (2.49) to find the correct $r_{\rm off}$. We then adjust β to give the correct values of the resonance shift and width. In this thesis, we use this approach for static calculations, and for some of the dissociation calculations in Chapter 3.

Basis set expansion of the Feshbach molecular state

In calculations using this approach, the Hamiltonian is expanded in terms of the eigenstates of the bare potential. For the applications we consider in this thesis, it is sufficient to include just one bound state in the entrance-channel potential. If the Feshbach molecular state is the initial state of the system, we may then expand it as

$$\phi_{\rm b}^{\rm bg}(r) = \int d\mathbf{p}\, \phi_{\mathbf{p}}^{(+)}(\mathbf{r}) \overbrace{\langle \phi_{\mathbf{p}}^{(+)} | \phi_{\rm b}^{\rm bg} \rangle}^{C_p(0)} + \phi_{-1}(r) \overbrace{\langle \phi_{-1} | \phi_{\rm b}^{\rm bg} \rangle}^{C_{-1}(0)}, \tag{2.55}$$

$$\phi_{\rm b}^{\rm cl}(r) = \phi_{\rm res}(r) \underbrace{\langle \phi_{\rm res} | \phi_{\rm b}^{\rm cl} \rangle}_{C_{\rm res}(0)}\,. \tag{2.56}$$

Here, $C_p(t)$, $C_{-1}(t)$ and $C_{\rm res}(t)$ are the population amplitudes of the scattering states, entrance-channel bound state, and resonance level, respectively. We detail the transformed grid method used for this potential model in Appendix A.

The coupling matrix elements are calculated between the resonance level and each eigenstate of the entrance-channel potential. The population of each level in the entrance channel has dynamics defined by its energy and coupling to the resonance level. The

dynamical equations for the system are

$$i\hbar\frac{\partial}{\partial t}C_p(t) = \frac{p^2}{m}C_p(t) + \langle\phi_{\mathbf{p}}^{(+)}|W|\phi_{\rm res}\rangle C_{\rm res}(t)\,, \tag{2.57}$$

$$i\hbar\frac{\partial}{\partial t}C_{-1}(t) = E_{-1}C_{-1}(t) + \langle\phi_{-1}|W|\phi_{\rm res}\rangle C_{\rm res}(t)\,, \tag{2.58}$$

$$i\hbar\frac{\partial}{\partial t}C_{\rm res}(t) = E_{\rm res}(B(t))C_{\rm res}(t) + \langle\phi_{\rm res}|W|\phi_{-1}\rangle C_{-1}(t) + \int d\mathbf{p}\langle\phi_{\rm res}|W|\phi_{\mathbf{p}}^{(+)}\rangle C_p(t)\,. \tag{2.59}$$

2.4.2 Separable potential

In the approach of the previous subsection, a potential model is constructed by reproducing the background scattering length and long-range form of the entrance-channel potential. Such models may be used to calculate the energy of the highest vibrational bound state of the entrance-channel potential, E_{-1}, which together with the background scattering length can be used to construct a simpler model of the zero-energy resonance. In the separable potential approach, the entrance-channel T-matrix is constructed to have a pole at E_{-1}, which can be ensured by the following expression [128]:

$$T_{\rm bg}(z) = \frac{|\chi_{\rm bg}\rangle\xi_{\rm bg}\langle\chi_{\rm bg}|}{1 - \xi_{\rm bg}\langle\chi_{\rm bg}|G_0(z)|\chi_{\rm bg}\rangle}\,. \tag{2.60}$$

The potential is taken to have the separable form,

$$V_{\rm bg} = |\chi_{\rm bg}\rangle\xi_{\rm bg}\langle\chi_{\rm bg}|\,, \tag{2.61}$$

where $\xi_{\rm bg} = 1/\langle\chi_{\rm bg}|G_0(E_{-1})|\chi_{\rm bg}\rangle$ is the amplitude of the potential, and $|\chi_{\rm bg}\rangle$ is referred to as the form factor. Equation (2.60) can be derived by using Eq. (2.61) to iteratively solve the general relation for the T-matrix,

$$T_{\rm bg}(z) = V_{\rm bg} + V_{\rm bg}G_0(z)T_{\rm bg}(z)\,. \tag{2.62}$$

For the case of a cold gas, the form factor is not resolved by the low energy collisions and so can have an arbitrary form. Here, we use a Gaussian profile in momentum [128, 144],

$$\langle\mathbf{p}|\chi_{\rm bg}\rangle = \frac{1}{(2\pi\hbar)^{3/2}}\exp\left(-\frac{p^2\sigma_{\rm bg}^2}{2\hbar^2}\right)\,, \tag{2.63}$$

where the length $\sigma_{\rm bg}$ gives the range of the potential in configuration space. In the single-resonance approximation, the interchannel coupling can be modelled using

$$W|\phi_{\rm res}\rangle = |\chi\rangle\zeta\,, \tag{2.64}$$

where $|\chi\rangle$ has the Gaussian form, analogous to $|\chi_{\rm bg}\rangle$, of

$$\langle \mathbf{p}|\chi\rangle = \frac{1}{(2\pi\hbar)^{3/2}} \exp\left(-\frac{p^2\sigma^2}{2\hbar^2}\right). \tag{2.65}$$

This approach to modelling the potential is simpler than the hardcore + van der Waals model, allowing the analytic calculation of commonly occurring matrix elements such as $\langle\chi|G_0(z)|\chi\rangle$. This makes it ideal for use in dynamical simulations on long (∼10 ms) timescales [116, 117] or many-body calculations [114, 128, 134, 145]. For this reason, it is used in many of the calculations presented in this thesis. A separable potential, in contrast to a contact interaction approach [146], allows the inclusion of bound states in the bare potential beyond the universal regime and does not lead to an ultraviolet divergence.

We now discuss the technique for deriving a form for the separable potential which recovers all the properties of a resonance relevant for ultracold collisions. The s-wave scattering length is related to the background potential through the evaluation of the T-matrix of Eq. (2.38) at zero energy. Together with Eq. (2.60), this gives

$$\xi_{\rm bg} = \frac{4\pi^{3/2}\hbar^2\sigma_{\rm bg}a_{\rm bg}}{m\left(\pi^{1/2}\sigma_{\rm bg} - a_{\rm bg}\right)}. \tag{2.66}$$

$\sigma_{\rm bg}$ can be found by substituting this into the following equation to eliminate $\xi_{\rm bg}$:

$$1 - \xi_{\rm bg}\langle\chi_{\rm bg}|G_0(E_{\text{-}1})|\chi_{\rm bg}\rangle = 0. \tag{2.67}$$

The matrix element in Eq. (2.67) can be calculated using the complementary error function $\mathrm{erfc}(x)$, according to the following formula [128]:

$$\langle\chi_{\rm bg}|G_0(E_{-1})|\chi_{\rm bg}\rangle = \frac{m}{4\pi^{3/2}\hbar^2\sigma_{\rm bg}}\left[\sqrt{\pi}xe^{x^2}\mathrm{erfc}(x) - 1\right], \tag{2.68}$$

where $x = \sqrt{-mE_{-1}}\sigma_{\rm bg}/\hbar$. This formula is also valid for positive energies E, for which it must be evaluated using the complex energy $z = E + i0$.

The parameters for the interchannel coupling, ζ and σ, are calculated from the resonance width and shift. Using Eqs. (2.32) and (2.38) in the limit of zero energy, we find that

$$\langle\phi_{\rm res}|W|\phi_0^{(+)}\rangle = \frac{\zeta}{(2\pi\hbar)^{3/2}}\left(1 - \frac{a_{\rm bg}}{\sqrt{\pi}\bar{\sigma}}\right). \tag{2.69}$$

Here, $\bar{\sigma} = \sqrt{(\sigma^2 + \sigma_{\rm bg}^2)/2}$. Substituting this into Eq. (2.40) gives

$$\Delta B = \frac{m}{4\pi\hbar^2 a_{\rm bg}} \frac{\zeta^2}{\mu_{\rm res}} \left(1 - \frac{a_{\rm bg}}{\sqrt{\pi}\bar{\sigma}}\right)^2 . \tag{2.70}$$

To calculate the resonance shift within the separable potential approach, we first calculate the matrix element in Eq. (2.41) using the relation for the entrance-channel Green's function in Eq. (2.35). For a separable potential, using the result for the T-matrix of Eq. (2.60), this leads to

$$\langle \phi_{\rm res}|WG_{\rm bg}(0)W|\phi_{\rm res}\rangle = -\frac{\zeta^2 m}{4\pi^{3/2}\hbar^2\sigma}\left(1 - \frac{\sigma}{\sqrt{\pi}\bar{\sigma}^2}a_{\rm bg}\right). \tag{2.71}$$

Substituting this into Eq. (2.41), we then have the following result for the resonance shift:

$$B_0 - B_{\rm res} = \frac{\zeta^2}{\mu_{\rm res}} \frac{m}{4\pi^{3/2}\hbar^2\sigma}\left(1 - \frac{\sigma}{\sqrt{\pi}\bar{\sigma}^2}a_{\rm bg}\right) \tag{2.72}$$

$$= (\Delta B)\frac{a_{\rm bg}}{\sqrt{\pi}\sigma}\frac{\left(1 - \frac{a_{\rm bg}\sigma}{\sqrt{\pi}\bar{\sigma}^2}\right)}{\left(1 - \frac{a_{\rm bg}}{\sqrt{\pi}\bar{\sigma}}\right)^2}. \tag{2.73}$$

As in the previous section, we calculate the ratio $(B_0 - B_{\rm res})/\Delta B$, which is independent of ζ, and so can be used to calculate σ by comparison to Eq. (2.49). The coupling strength ζ is then adjusted to reproduce ΔB.

Basis set expansion of the Feshbach molecular state

In Chapters 3 and 5 we apply the separable potential of this subsection to dynamical simulations, using a bare basis defined by the resonance level for the closed channel, and the bare bound states and scattering states for the entrance channel. We therefore calculate the matrix elements for the expansion of the Feshbach molecular state in terms of this basis. Here, we present the expansion for the association calculations of Chapter 5, in which the final molecular state is expanded, and evolved backwards in time. This allows all of the matrix elements to be calculated from a single simulation. The expansion for the dissociation calculations of Chapter 3, in which the molecular state is the initial state, is analogous.

Assuming the inclusion of one bound state in the entrance channel is sufficient, a complete basis set is $\left\{|\phi_{-1}, {\rm bg}\rangle, |\phi_{\mathbf{p}}^{(+)}, {\rm bg}\rangle, |\phi_{\rm res}, {\rm cl}\rangle\right\}$. The expansion of the Feshbach

molecular state in this basis is given by

$$\langle \phi_{\rm b}^{\rm f} | \phi_{\text{-1}}, {\rm bg} \rangle = \frac{\zeta}{\mathcal{N}_{\rm b}^{\rm f}} \frac{\langle \chi | G_{\rm bg}(E_{\rm b}^{\rm f}) G_0(E_{-1}) | \chi_{\rm bg} \rangle}{\sqrt{\langle \chi | G_0^2(E_{-1}) | \chi_{\rm bg} \rangle}}, \tag{2.74}$$

$$\langle \phi_{\rm b}^{\rm f} | \phi_{\mathbf{p}}^{(+)}, {\rm bg} \rangle = \frac{\zeta}{\mathcal{N}_{\rm b}^{\rm f}} \langle \chi | G_{\rm bg}(E_{\rm b}^{\rm f}) | \phi_{\mathbf{p}}^{(+)} \rangle, \tag{2.75}$$

$$\langle \phi_{\rm b}^{\rm f} | \phi_{\rm res}, {\rm cl} \rangle = \frac{1}{\mathcal{N}_{\rm b}^{\rm f}}. \tag{2.76}$$

Here, $\phi_{\rm b}^{\rm f}$, $E_{\rm b}^{\rm f}$ and $\mathcal{N}_{\rm b}^{\rm f}$ are the Feshbach molecular state, bound state energy, and normalisation constant of Eq. (2.26), respectively, all evaluated at the final magnetic field $B_{\rm f}$. We have also used the unit normalisation of $|\phi_{-1}\rangle$ together with the relation $|\phi_{-1}\rangle = G_0(E_{-1}) V_{\rm bg} |\phi_{-1}\rangle$. The matrix element of $G_{\rm bg}(E)$ may be calculated from Eq. (2.35). The matrix element of $G_0^2(E_{-1})$ can be calculated using $G_0^2(E) = -\frac{\partial}{\partial E} G_0(E)$, or from a spectral decomposition. Further bound states can be included in the entrance channel, however they are typically sufficiently far detuned to be neglected. For the ^{85}Rb calculations of Chapter 5, the highest vibrational bound state in the entrance channel is at $E_{-1}/h = -218\,{\rm MHz}$, and so also does not play a role and can be neglected from the above equations. The necessary matrix elements of the interchannel coupling are given by

$$\langle \phi_{\rm res} | W | \phi_{\mathbf{p}}^{(+)} \rangle = \zeta \left(\langle \chi | \mathbf{p} \rangle + \frac{\xi_{\rm bg} \langle \chi | G_0(z) | \chi_{\rm bg} \rangle \langle \chi_{\rm bg} | \mathbf{p} \rangle}{1 - \xi_{\rm bg} \langle \chi_{\rm bg} | G_0(z) | \chi_{\rm bg} \rangle} \right), \tag{2.77}$$

$$\langle \phi_{\rm res} | W | \phi_{-1} \rangle = \frac{\zeta \langle \chi | G_0(E_{-1}) | \chi_{\rm bg} \rangle}{\sqrt{\langle \chi | G_0^2(E_{-1}) | \chi_{\rm bg} \rangle}}, \tag{2.78}$$

where $z = (p^2/m) + i0$.

Conversion of bare amplitudes to dressed amplitudes

Having expanded the Feshbach molecular state in a bare basis, we can evolve it using the Schrödinger equation to obtain the bare amplitudes $\langle \phi_{\rm b}^{\rm f} | U_{\rm 2B}(t_{\rm f}, t_{\rm i}) | \phi_{\mathbf{p}}^{(+)} \rangle$, $\langle \phi_{\rm b}^{\rm f} | U_{\rm 2B}(t_{\rm f}, t_{\rm i}) | \phi_{-1} \rangle$, and $\langle \phi_{\rm b}^{\rm f} | U_{\rm 2B}(t_{\rm f}, t_{\rm i}) | \phi_{\rm res} \rangle$. Here, $U_{\rm 2B}(t_{\rm f}, t_{\rm i})$ is the two-body evolution operator of the relative motion, defined by

$$i\hbar \frac{\partial}{\partial t_{\rm f}} U_{\rm 2B}(t_{\rm f}, t_{\rm i}) = H_{\rm 2B}(B(t_{\rm f})) U_{\rm 2B}(t_{\rm f}, t_{\rm i}), \tag{2.79}$$

with $U_{\rm 2B}(t_{\rm f}, t_{\rm f}) = 1$. The physical states corresponding to atoms of relative momentum p are the dressed scattering states of Eq. (2.29). The conversion from bare to dressed

amplitudes is given by

$$\langle\phi_{\rm b}^{\rm f}|U_{\rm 2B}(t_{\rm f},t_{\rm i})|\phi_{\mathbf{p}}^{\rm i}\rangle = \langle\phi_{\rm b}^{\rm f}|U_{\rm 2B}(t_{\rm f},t_{\rm i})|\phi_{\mathbf{p}}^{(+)}\rangle + \left[\langle\phi_{\rm b}^{\rm f}|U_{\rm 2B}(t_{\rm f},t_{\rm i})G_{\rm bg}(z)W|\phi_{\rm res}\rangle + \langle\phi_{\rm b}^{\rm f}|U_{\rm 2B}(t_{\rm f},t_{\rm i})|\phi_{\rm res}\rangle\right]A(B_{\rm i},p^2/m)\,, \tag{2.80}$$

where $z = (p^2/m) + i0$, and $A(B_{\rm i}, p^2/m)$ is given by Eq. (2.30) evaluated at the initial magnetic field, $B_{\rm i}$. Here, the Feshbach molecular state and scattering states are evaluated at the final and initial magnetic fields, respectively. The first matrix element in the square brackets is calculated by spectral decomposition:

$$\langle\phi_{\rm b}^{\rm f}|U_{\rm 2B}(t_{\rm f},t_{\rm i})G_{\rm bg}(z)W|\phi_{\rm res}\rangle = \int d\mathbf{p}'\frac{\langle\phi_{\rm b}^{\rm f}|U_{\rm 2B}(t_{\rm f},t_{\rm i})|\phi_{\mathbf{p}'}^{(+)}\rangle\langle\phi_{\mathbf{p}'}^{(+)}|W|\phi_{\rm res}\rangle}{z-\frac{p'^2}{m}} + \frac{\langle\phi_{\rm b}^{\rm f}|U_{\rm 2B}(t_{\rm f},t_{\rm i})|\phi_{-1}\rangle\langle\phi_{-1}|W|\phi_{\rm res}\rangle}{\frac{p^2}{m}-E_{\text{-}1}}\,. \tag{2.81}$$

Here, $\langle\phi_{-1}|W|\phi_{\rm res}\rangle$ is given by Eq. (2.78). Changing the denominator to a time integral, the integral in Eq. (2.81) can be written

$$\frac{1}{i\hbar}\int_0^\infty dp' 4\pi p'^2\alpha(p')\int_{-\infty}^0 dt\exp\left[-\frac{it}{\hbar}\left(\frac{p^2}{m}-\frac{p'^2}{m}+i0\right)\right], \tag{2.82}$$

where $\alpha(p') = \langle\phi_{\rm b}^{\rm f}|U_{\rm 2B}(t_{\rm f},t_{\rm i})|\phi_{\mathbf{p}'}^{(+)}\rangle\langle\phi_{\mathbf{p}'}^{(+)}|W|\phi_{\rm res}\rangle$. The p'^2 term can be replaced by a partial derivative with respect to time. Reversing the order of integration and using integration by parts then gives

$$\langle\phi_{\rm b}^{\rm f}|U_{\rm 2B}(t_{\rm f},t_{\rm i})G_{\rm bg}(z)W|\phi_{\rm res}\rangle = -4\pi m\left(F(0)+\frac{ip^2}{m\hbar}\int_{-\infty}^0 dt e^{-ip^2t/(m\hbar)}F(t)\right) + \frac{\langle\phi_{\rm b}^{\rm f}|U_{\rm 2B}(t_{\rm f},t_{\rm i})|\phi_{-1}\rangle\langle\phi_{-1}|W|\phi_{\rm res}\rangle}{\frac{p^2}{m}-E_{\text{-}1}}\,. \tag{2.83}$$

Here, $F(t) = \int_0^\infty dp'\,\alpha(p')e^{ip'^2t/(m\hbar)}$. We evaluate the integral in Eq. (2.83) numerically until the time where $F(t)$ approaches its asymptotic form, given by the stationary phase approximation to be

$$F(t) \underset{t\to-\infty}{\sim} \frac{\alpha(0)}{2}\sqrt{\frac{m\pi\hbar}{|t|}}e^{-i\pi/4}\,. \tag{2.84}$$

Single-channel theory

In the single-channel separable potential approach, the scattering length and bound state energy are recovered by an appropriate variation of the amplitude ξ in Eq. (2.61) such

that the scattering length of Eq. (2.18) is recovered. The effective potential in Eq. (2.46) is then given by

$$V_{\text{eff}}(B) = |\chi\rangle\xi(B)\langle\chi| \,. \tag{2.85}$$

The range σ of the single-channel separable potential is defined analogously to σ_{bg} in Eq. (2.63). The magnetic-field dependence of $V_{\text{eff}}(B)$ is contained in $\xi(B)$ through its dependence on the scattering length $a(B)$, as given by [95]:

$$\frac{1}{\xi(B)} = \langle\chi|G_0(0)|\chi\rangle + \frac{m(2\pi\hbar)^3|\langle\chi|0\rangle|^2}{4\pi\hbar^2 a(B)} \,. \tag{2.86}$$

The bound state energy is calculated from the poles of the Green's function, in analogy to Eq. (2.67):

$$1 - \xi(B)\langle\chi|G_0(E_{\text{b}})|\chi\rangle = 0 \,. \tag{2.87}$$

The range of the potential, σ, is found as in Eq. (2.67), and kept constant as the magnetic field is varied. All resonance-enhanced properties are reproduced by the variations in amplitude in accordance with Eq. (2.86). The Feshbach molecular state of Eq. (2.47) may be expanded in terms of plane waves using the separable potential of Eq. (2.85), yielding

$$\langle\phi_{\text{b}}|\mathbf{p}\rangle = \frac{\langle\chi|\mathbf{p}\rangle}{\left(E_{\text{b}} - \frac{p^2}{m}\right)\sqrt{\langle\chi|G_0^2(E_{\text{b}})|\chi\rangle}} \,. \tag{2.88}$$

We apply this single-channel approach to our calculations for condensed gases in Chapter 5, and to the studies of the non-Markovian Boltzmann equation in Chapter 6.

Chapter 3

Classification of zero-energy resonances using Feshbach molecule dissociation

In this chapter we study the dissociation of Feshbach molecules by a magnetic field sweep across a zero-energy resonance. In the limit of an instantaneous magnetic field change, the distribution of atomic kinetic energy can have a peak indicating dominance of the molecular closed-channel spin configuration over the entrance channel. The extent of this dominance influences physical properties such as stability with respect to collisions, and so the readily measurable presence or absence of the corresponding peak provides a practical method of classifying zero-energy resonances. For some resonances, currently achievable ramp speeds, e.g. those demonstrated by Dürr *et al.* [87], are fast enough to provide magnetic field changes that may be interpreted as instantaneous. We study the transition from sudden magnetic field changes to asymptotically wide, linear ramps. In the latter limit, the predicted form of the atomic kinetic energy distribution is independent of the specific implementation of the two-body physics, provided that the near-resonant scattering properties are properly accounted for. The work of this chapter is published in Ref. [116].

3.1 Introduction

The detection of cold molecules often relies upon measuring the atomic gas produced by their dissociation. This is because the lasers used in experiments are typically tuned to the atomic transitions, which are detuned from those for the corresponding molecules. The atoms produced by dissociation can then be imaged using a resonant laser pulse. Molecular dissociation often involves applying radio-frequency radiation [79, 84], photodissociation [85], monitoring the loss of atoms [72, 89], or a linear ramp across the resonance [73, 74, 75, 76, 77, 78, 79, 86, 87, 90, 91]. Linear ramps for molecule detection are often slow in order to minimise the speed of the fragments to be imaged. Such sweeps have also been used to determine resonance widths [87]. Fast sweeps have been used to measure, e.g., the population of more than one partial wave [88, 147].

In this chapter we consider dissociation by linear ramps across zero-energy resonances over the whole range of possible ramp speeds. We show that the dissociation process can act as a probe of the resonance. In the limit of a sudden jump the distribution of atomic kinetic energy, referred to as the dissociation spectrum, can have a sharp peak at an energy dependent on the final magnetic field [87]. Our studies show that such spectra occur only for resonances with weak interchannel coupling. Consequently, resonances may be classified by measuring the peak, which can be done while little is known about the resonance other than its position. The shape of the dissociation spectrum is therefore a simple and useful tool for characterising a zero-energy resonance.

The strength of the interchannel coupling affects the suitability of the resonance for studying phenomena of current experimental interest. For example, long-range halo molecules are more easily created using strongly coupled, entrance-channel dominated resonances, whereas Feshbach molecules created with closed-channel dominated resonances are usually unstable with respect to collisions [61]. We study the transition from sudden jumps to asymptotically wide, linear ramps, as the ramp speed and initial and final fields are changed. We provide an analytic treatment of the time evolution for arbitrary ramp speeds and initial and final fields. Taking the limit of an asymptotic ramp produces a spectrum which has been studied both experimentally [86, 87] and theoretically [86, 128, 148, 149]. Two-channel and single-channel approaches provide the same asymptotic spectrum. This is because, for the special case of a linear ramp, the outcome depends only on the ramp speed through the strongly interacting region around the resonance.

3.2 Dissociation spectra

Feshbach molecules can be dissociated by changing the magnetic field strength to the side of the zero-energy resonance where the Feshbach molecular state does not exist. We consider linear magnetic field ramps of the form

$$B(t) = B_{\mathrm{res}} + \dot{B}\,(t - t_{\mathrm{res}})\,. \tag{3.1}$$

Here $\dot{B}$ is the ramp speed, and t_{res} is the time at which the resonance level crosses the entrance-channel dissociation threshold, i.e. $B(t_{\mathrm{res}}) = B_{\mathrm{res}}$. The ramp begins at the time t_{i} and ends at t_{f}, ranging between the magnetic fields $B(t_{\mathrm{i}}) = B_{\mathrm{i}}$ and $B(t_{\mathrm{f}}) = B_{\mathrm{f}}$. The ramp

of Eq. (3.1) corresponds to a linear time dependence of the resonance energy

$$E_{\rm res}(t) = \dot{E}_{\rm res}\,(t - t_{\rm res})\,, \tag{3.2}$$

where $\dot{E}_{\rm res} = \mu_{\rm res}\dot{B}$, and $\mu_{\rm res}$ is the difference in magnetic moment between the entrance and closed channels.

In typical experiments [86, 87] the atomic gas produced by the sweep is allowed to freely expand with the magnetic field strength held at $B_{\rm f}$, after which a measurement of the atomic momentum distribution is performed. We therefore analyse the diatomic state produced by the ramp in terms of the scattering states of Eq. (2.28) evaluated at $B_{\rm f}$, which then become stationary states. The transitions into these states due to the ramp determine the dissociation spectrum $n(E)$, in accordance with the general formula [128]

$$n(E)dE = p^2 dp \int d\Omega_{\mathbf{p}}\ |T_{\rm diss}(\mathbf{p})|^2\ . \tag{3.3}$$

Here, $\int d\Omega_{\mathbf{p}}$ denotes the integration over angles, $E = p^2/m$, and $T_{\rm diss}(\mathbf{p})$ is the transition amplitude, given by

$$T_{\rm diss}(\mathbf{p}) = \langle \phi^{\rm f}_{\mathbf{p}} | U_{\rm 2B}(t_{\rm f}, t_{\rm i}) | \phi^{\rm i}_{\rm b} \rangle\,. \tag{3.4}$$

Here, the two-body evolution operator $U_{\rm 2B}(t_{\rm f}, t_{\rm i})$ is given by Eq. (2.79), $\phi^{\rm i}_{\rm b} = \phi_{\rm b}(B_{\rm i})$ is the Feshbach molecular state of Eq. (2.25) at the initial magnetic field, and $\phi^{\rm f}_{\mathbf{p}} = \phi_{\mathbf{p}}(B_{\rm f})$ is the scattering state of momentum $\mathbf{p}$ at the final magnetic field, given by Eq. (2.29). In this thesis, we consider only resonances for which a spherically symmetric Feshbach resonance state is coupled to the entrance channel by spin exchange [61]. Consequently, the transition amplitude depends only on the modulus of the momentum.

3.3 Sudden jumps across resonances

In this section we discuss the limit of an infinitely fast ramp across a zero-energy resonance, corresponding to an instantaneous jump in the magnetic-field strength. This scenario is directly related to a recent experiment of Dürr *et al.* [87], where a sharply peaked dissociation spectrum was observed following a fast ramp across the 685 G resonance of ^{87}Rb. For a jump, the transition amplitude of Eq. (3.4) is completely determined by the overlap of the initial Feshbach molecular state and the final scattering state,

$$T_{\rm diss}(p) \underset{t_{\rm f}\to t_{\rm i}}{\longrightarrow} \langle \phi^{\rm f}_{\mathbf{p}} | \phi^{\rm i}_{\rm b} \rangle\,. \tag{3.5}$$

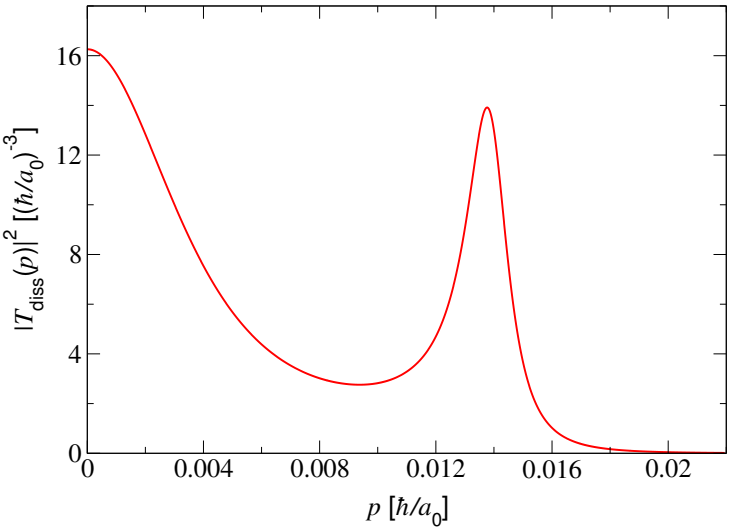

Figure 3.1: Transition probability density $|T_{\rm diss}(p)|^2$ for the dissociation of a $^{87}Rb_2$ Feshbach molecule into a pair of atoms with relative momentum p, due to a jump across the 1007.4 G resonance. The initial and final fields used here are $B_{\rm i} = 1007$ G and $B_{\rm f} = 1009.4$ G. The momentum $p_{\rm res} = 0.0140\,\hbar/a_0$, corresponding to the resonance energy $E_{\rm res}(B_{\rm f}) = p_{\rm res}^2/m$ at the end of the jump, gives the approximate position of the peak.

Evaluating this overlap using the two-channel approach of Chapter 2 reveals that the transition probability density $|T_{\rm diss}(p)|^2$ can have a two-peaked structure. An example of such a structure, for the 1007.4 G resonance of ^{87}Rb, is shown in Fig. 3.1. This particular form of $|T_{\rm diss}(p)|^2$ can be understood by considering the entrance-channel and closed-channel components of $\phi_{\rm b}^{\rm i}$ and $\phi_{\mathbf{p}}^{\rm f}$. The appearance of the peak at nonzero energies is controlled by the amplitude $A(B_{\rm f}, E)$, which determines the final scattering states $\phi_{\mathbf{p}}^{\rm f}$ through Eq. (2.30). Provided that the influence of $\Delta(E)$ and $\gamma(E)$ in Eq. (2.30) can be neglected, $|T_{\rm diss}(p)|^2$ tends to peak around $E \approx E_{\rm res}(B_{\rm f})$. This is the case for the example of Fig. 3.1. In general, though, the influence of $\Delta(E)$ and $\gamma(E)$ can be significant, leading to the broadening and possibly even disappearance of the nonzero-energy peak in the dissociation spectrum.

3.3.1 Analytic estimate

For small $E = (\hbar k)^2/m$, satisfying $|ka| \ll 1$, the two-body interactions can be completely characterised in terms of the scattering length. As discussed in Chapter 2, the regime where the physics depends only on the scattering length is referred to as the Wigner threshold law regime for positive energies, and the universal regime for negative ener-

gies. As shown by Eq. (2.45), the energy shift $\Delta(E)$ assumes its maximum value for $E \to 0$,

$$\Delta(E) \underset{k\to 0}{\sim} \mu_{\rm res}(B_{\rm res} - B_0)\,. \tag{3.6}$$

In this limit $\Delta(E)$ is proportional to the resonance shift, $B_0 - B_{\rm res}$, of Eq. (2.41). Similarly, from Eq. (2.45), the decay width $\gamma(E)$ in the Wigner threshold law regime assumes the form [132],

$$\gamma(E) \underset{k\to 0}{\sim} k a_{\rm bg} \mu_{\rm res} \Delta B\,, \tag{3.7}$$

where ΔB is the resonance width, and $a_{\rm bg}$ is the background scattering length. The resonance width and background scattering length are related to the scattering length a by Eq. (2.18). Equation (3.7) indicates that $\gamma(E)$ can be significant for broad resonances with large $|a_{\rm bg}|$, which will therefore have broad peaks in their dissociation spectra. The modulus of the resonance shift also tends to be large for these resonances.

For entrance-channel dominated resonances, the universal bound state energy of Eq. (2.44) is accurately extended beyond the universal regime by the Gribakin-Flambaum formula of Eq. (2.48). The accuracy of this extension depends on the degree to which the influence of the long range van der Waals tail of the entrance-channel potential dominates over that of the Feshbach resonance state. For closed-channel dominated resonances the influence of the Feshbach resonance state is dominant. The distinction is quantified by [100, 150]

$$\eta = \frac{\bar{a}}{a_{\rm bg}} \frac{\hbar^2/(m\bar{a}^2)}{\mu_{\rm res}\,\Delta B}\,, \tag{3.8}$$

which we term the closed-channel dominance. Values of η for the resonances studied in this thesis are given in Table 2.2. Equation 3.8 may be derived from the ratio $E_{\bar{a}}/\gamma(E_{\bar{a}})$, where $\gamma(E_{\bar{a}})$ is the decay width of Eq. (3.7) evaluated at $E_{\bar{a}}$, and $E_{\bar{a}} = \hbar^2/m\bar{a}^2$ is the energy associated with the mean scattering length defined after Eq. (2.48), differing only by a constant of order unity from the van der Waals energy defined by Eq. (2.1). It may also be derived by considering the relative size of the contributions to the bound state energy from the van der Waals tail and resonance level [150]. For entrance-channel dominated resonances the relation $\eta \ll 1$ is fulfilled, implying that $|a_{\rm bg}|$ and/or $|\mu_{\rm res}\Delta B|$ are large. The latter quantity being large indicates strong interchannel coupling [128], i.e. that the decay width is large. The opposite limit of weak coupling implies a closed-channel dominated resonance.

The relevance of the size of η to the structure of the dissociation spectrum can be revealed by analysing the position of the finite-energy peak, E_{peak}, relative to its spectral width, ΔE_{peak}. By using the Wigner threshold law expressions of Eqs. (3.6) and (3.7), it is possible to show that the finite-energy peak is approximately Lorentzian. Consequently, ΔE_{peak} will be taken as its half-width at half-maximum. A distinct peak appears in the jump dissociation spectrum when $E_{\mathrm{peak}}/\Delta E_{\mathrm{peak}} \gg 1$. Evaluating this quantity in the Wigner threshold law regime yields the expression for the peak clarity,

$$\frac{E_{\mathrm{peak}}}{\Delta E_{\mathrm{peak}}} = \eta \frac{[\mu_{\mathrm{res}}(B_{\mathrm{f}} - B_0)/E_{\bar{a}}] - 1/(2\eta^2)}{\sqrt{[\mu_{\mathrm{res}}(B_{\mathrm{f}} - B_0)/E_{\bar{a}}] - 1/(4\eta^2)}}, \tag{3.9}$$

The energy $E_{\bar{a}}$, which greatly exceeds the relative kinetic energies typical of cold atom pairs, gives the order of magnitude of the spacing between the highest excited vibrational bound states. It therefore sets the largest energy scale able to be experimentally accessed without other resonance phenomena arising, and limits the range of energies able to be considered within the single-resonance approach of Sec. 2.2. In the range of validity $\mu_{\mathrm{res}}(B_{\mathrm{f}} - B_0) \leq E_{\bar{a}}$, Eq. (3.9) gives the inequality

$$\frac{E_{\mathrm{peak}}}{\Delta E_{\mathrm{peak}}} \leq \eta \frac{1 - 1/(2\eta^2)}{\sqrt{1 - 1/(4\eta^2)}}, \tag{3.10}$$

with equality for $\mu_{\mathrm{res}}(B_{\mathrm{f}} - B_0) = E_{\bar{a}}$. It is evident from Eq. (3.10) that the condition for the existence of a distinct peak at a nonzero energy is $\eta \gg 1$, which is characteristic of closed-channel dominated resonances. An example of a resonance falling into this category is provided by the 1007.4 G resonance of ^{87}Rb, for which $\eta = 5.9$ (see Fig. 3.1). Entrance-channel dominated resonances, characterised by $\eta \ll 1$, exclude the possibility of a clear peak appearing at a nonzero energy in the dissociation spectrum. The presence or absence of a sharp peak in the dissociation spectrum is therefore an indicator of whether a zero-energy resonance is entrance-channel or closed-channel dominated.

We have verified the quality of the estimate given by Eq. (3.9) by comparing it to the results of exact, numerical calculations using the approach of Chapter 2. The comparison, shown in Fig. 3.2, confirms that Eq. (3.9) provides a good estimate of the ratio $E_{\mathrm{peak}}/\Delta E_{\mathrm{peak}}$. Moreover, the analytic expression of Eq. (3.9) slightly underestimates $E_{\mathrm{peak}}/\Delta E_{\mathrm{peak}}$, meaning that the peak clarity one would expect to see experimentally is always slightly greater than the analytic estimate. The preceding analysis treats the ideal case of an instantaneous change of the magnetic field strength. An experiment is described in Ref. [87] that actually operates in this regime. After an 80 G/ms ramp of

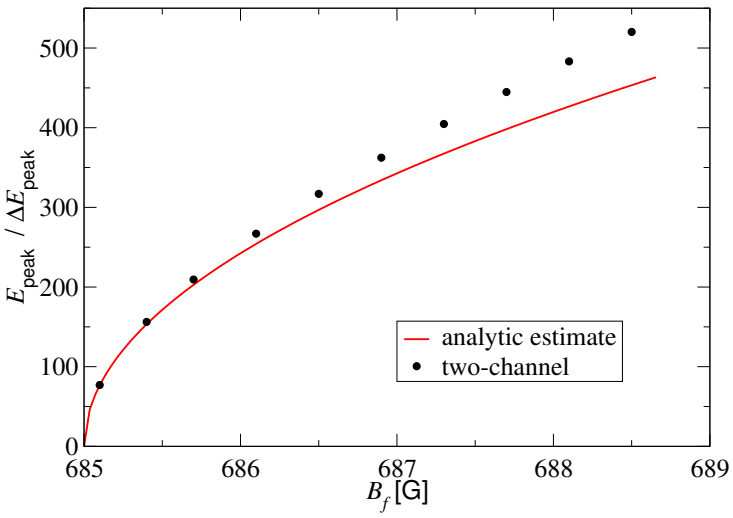

Figure 3.2: The measure of peak clarity $E_{\text{peak}}/\Delta E_{\text{peak}}$ in the dissociation spectrum of a $^{87}Rb_2$ molecule, using the 685 G resonance. This resonance has a high closed-channel dominance of $\eta = 463$. The initial field used is $B_i = 684.5$ G. The dots indicate values extracted from fits to the spectra obtained from full two-channel single-resonance calculations, while the solid line shows the approximate analytic predictions of Eq. (3.9). At $B \sim 688$ G, the single-resonance approach breaks down as the energy range covered starts to exceed the van der Waals energy.

the magnetic field across the 685 G resonance of ^{87}Rb, the atomic gas was found to expand outwards as a spherical shell, corresponding to a sharply peaked dissociation spectrum. In order to assess how closely the jump approximation follows the experimental observations of Ref. [87], we have performed an exact two-channel calculation of the dissociation spectrum of Eq. (3.3), for the experimental ramp speed of 80 G/ms. The comparison is shown in Fig. 3.3, and confirms that the 80 G/ms ramp is fast enough to produce a spectrum virtually indistinguishable from that of a jump. Consequently, the experiment of Ref. [87] provides a clear probe of the closed-channel admixtures of the initial bound and final scattering states, and of the strong closed-channel dominance ($\eta = 463$) of this particular resonance. We note that experiments reported in Ref. [87] using the less closed-channel dominated ($\eta = 5.9$) 1007.4 G resonance of ^{87}Rb did not produce such a peak for the 80 G/ms ramp-speed used. We have calculated that to be in the jump regime for this resonance would require a ramp speed of 5000 G/ms or above. The minimum ramp speed to be in the regime of a jump is different for each resonance, however ramp speeds of order 1000 G/ms are now possible [151].

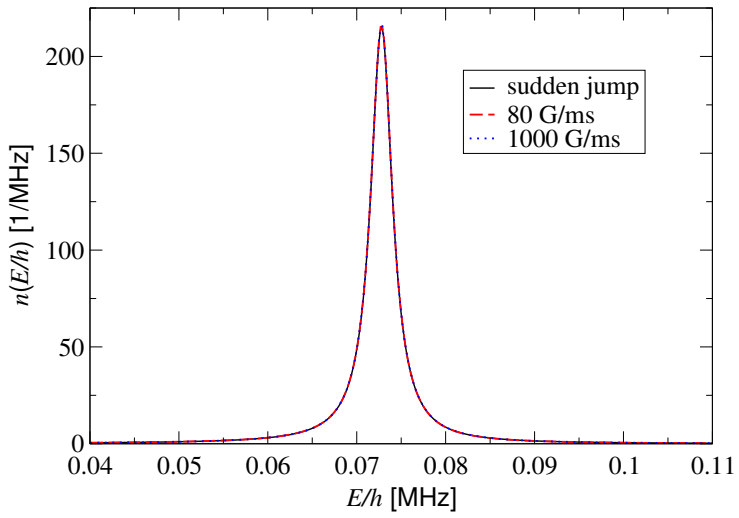

Figure 3.3: Dissociation spectrum of $^{87}Rb_2$ molecules produced in the vicinity of the 685 G resonance. The initial and final magnetic field strengths are $B_i = B_0 - 50\,\mathrm{mG}$ [151] and $B_f = B_0 + 40\,\mathrm{mG}$ [87]. 80 G/ms is the ramp speed reported in Ref. [87], while 1000 G/ms is approximately the maximum currently available [151]. The distinct peak is centred around $h \times 0.073$ MHz, corresponding to $3.5\,\mu$K, as compared to the $3.3\,\mu$K that can be deduced from Ref. [87].

3.3.2 Transfer into deeper bound states

At magnetic fields far from B_0, the highest excited vibrational bound state of $H_{2B}(B)$ often corresponds to the highest excited vibrational state of the entrance channel potential, ϕ_{-1}, as illustrated in Fig. 3.4. When the Feshbach molecular state is subjected to a magnetic field sweep across the resonance, some population can then be transferred to the highest excited vibrational bound state at the final field strength. Some Feshbach molecules will therefore not be dissociated during a ramp. We have calculated this effect for the 685 G resonance of ^{87}Rb and found it to be negligible. However, for the 48 G resonance of ^{133}Cs, the two-body energy level spectrum of which is plotted in Fig. 3.4, we have found that the transfer into the bound state can be as much as 10 %. In our calculations we have assumed sweep rates of no more than 1000 G/ms, which is currently achievable experimentally [151]. The transfer is unusually large for this particular resonance because the entrance-channel potential supports a state with an energy of only $E_{-1} = -h \times 45\,\mathrm{kHz}$ [61]. This makes the avoided crossing between the bound states narrow, as shown in Fig. 3.4, and so the wavefunctions of the Feshbach molecule and the final bound state converge to ϕ_{-1} quickly as B moves away from B_0. This increases the overlap between the initial and final bound states and so makes the transfer from a jump

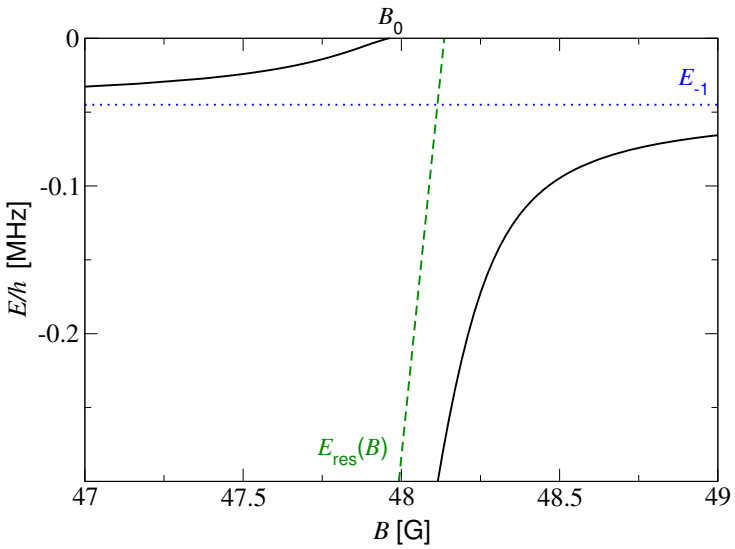

Figure 3.4: Energies of the two highest excited vibrational bound states near the 48 G resonance of ^{133}Cs. For fields far below the resonance, the Feshbach molecular state adiabatically correlates with the highest excited bound state ϕ_{-1} of the entrance channel (dotted line), while the next deeper bound state corresponds to the Feshbach resonance state (dashed line). Above B_0 the Feshbach molecule does not exist and the next deeper state converges to ϕ_{-1}. Due to this avoided crossing being narrow, the possible transfer into the final bound state from a jump can be as large as 10%.

larger.

3.4 Transition to asymptotic spectra

In this section we consider ramp speeds that are intermediate between the jumps of Sec. 3.3 and asymptotically wide, linear ramps. Keeping the initial and final magnetic fields used in Fig. 3.3 for all ramp speeds, we calculate the dissociation spectra including the full time evolution of Eq. (3.4). The resulting spectra have the characteristic double-peaked structure for jumps, but coincide with the asymptotic form for sufficiently slow ramps. This transition is shown in Fig. 3.5. For any given ramp speed, however, making the ramp wide enough will result in a spectrum of the asymptotic form.

For linear ramps of the form of Eq. (3.1), it is possible to derive an exact formula for the time-evolution operator $U_{2B}(t,t')$, associated with the two-body Hamiltonian $H_{2B}(B(t))$ by Eq. (2.79). Here we consider a continuum of positive energies as represented by the scattering states of Eq. (2.29), in contrast to the set of discrete levels

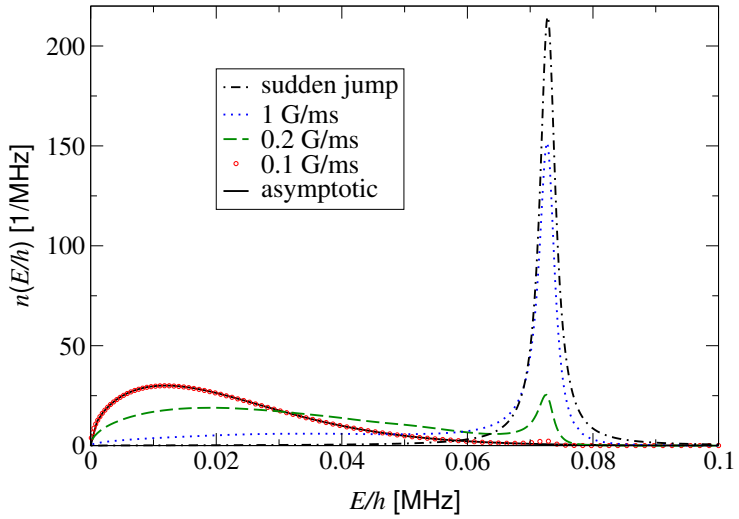

Figure 3.5: A sequence of dissociation spectra of $^{87}Rb_2$ molecules, produced near the 685 G resonance, for a range of ramp speeds. The initial and final magnetic field strengths are $B_i = B_0 - 50\,\mathrm{mG}$ and $B_f = B_0 + 40\,\mathrm{mG}$, respectively, and correspond to the conditions of Ref. [87]. The dash-dotted curve corresponds to a jump of the magnetic field strength and is identical to the curves shown in Fig. 3.3. The circles illustrate the spectrum obtained from an exact two-channel calculation for $\dot{B} = 0.1\,\mathrm{G/ms}$, and coincides with the evaluation of Eq. (3.15) indicated by the superimposed solid line.

examined in previous analytic treatments [61, 152, 153]. We separate Eq. (2.23) into its stationary and explicitly time dependent parts,

$$H_{2B}(B(t)) = H_{stat} + H_{cl}(t)\,, \tag{3.11}$$

where $H_{stat} = H_{2B}(B_{res})$, and we now express the single-resonance, closed-channel Hamiltonian of Eq. (2.22) as a function of time, i.e. $H_{cl}(B(t)) \to H_{cl}(t)$. Using the separability of $H_{cl}(t)$, the derivation of Appendix B.1 leading to Eq. (B.5) shows that $U_{2B}(t,t')$ can be calculated from only its closed-channel component,

$$g^{(+)}_{2B}(t,t') = \frac{1}{i\hbar}\theta(t-t')\langle\phi_{res},\mathrm{cl}|U_{2B}(t,t')|\phi_{res},\mathrm{cl}\rangle\,. \tag{3.12}$$

Here, $\theta(t-t')$ is the step function, which yields unity for $t-t' > 0$, and zero elsewhere. The linear variation of the resonance energy makes it possible to represent $g^{(+)}_{2B}(t,t')$ in terms of the following Fourier integrals:

$$g^{(+)}_{2B}(t,t') = \int dE \frac{e^{-iE(t-t')/\hbar}}{2\pi\hbar} \int_{-\infty}^{E} dE' \frac{e^{i[\varphi(z',t')-\varphi(z,t')]}}{i\hbar\dot{E}_{res}}\,. \tag{3.13}$$

Here $z = E + i0$, $z' = E' + i0$, and the phase $\varphi(z,t')$ is given in Eq. (B.8). This leads to the expression of Eq. (B.10) for the time-evolution operator, in which $U_{2B}(t_f,t_i)$ is expressed

solely in terms of the known energy dependent Green's function $G_{\mathrm{stat}}(z)$ associated with the stationary Hamiltonian H_{stat}, its closed-channel matrix element $g_{\mathrm{stat}}(z)$, and the phase $\varphi(z, t')$.

In Appendix B.2 we use Eq. (B.10) together with a stationary phase analysis to evaluate the transition amplitude of Eq. (3.4) in the limit of an asymptotically wide ramp. This shows the transition probability density to be

$$|T_{\mathrm{diss}}(p)|^2 = \frac{2\pi}{\hbar|\dot{E}_{\mathrm{res}}|}|\langle\phi_{\mathbf{p}}^{(+)}|W|\phi_{\mathrm{res}}\rangle|^2 \exp\left(-\frac{2\pi}{\hbar|\dot{E}_{\mathrm{res}}|}\int d\mathbf{p}'\theta(p-p')|\langle\phi_{\mathbf{p}'}^{(+)}|W|\phi_{\mathrm{res}}\rangle|^2\right). \quad (3.14)$$

Under typical experimental conditions the energies of the dissociated atoms do not exceed several μK, which is usually well within the Wigner threshold law domain. Consequently, the interchannel coupling matrix elements in Eq. (3.14) can be evaluated in the limit of zero relative momentum and related to the resonance width ΔB through Eq. (2.40). This constitutes a rigorous derivation of the asymptotic dissociation spectrum,

$$n(E) = -\frac{\partial}{\partial E}\exp\left(-\frac{4}{3}\sqrt{\frac{mE}{\hbar^2}}\left|a_{\mathrm{bg}}\right|\frac{E|\Delta B|}{\hbar\left|\dot{B}\right|}\right), \quad (3.15)$$

which was previously inferred in Refs. [86, 128] from Fermi's Golden Rule. The accuracy of this expression was confirmed by the experiments of Mukaiyama *et al.* [86] with ^{23}Na, and Dürr *et al.* [87] with ^{87}Rb. This led to the application of Eq. (3.15) to measuring the widths of previously unexplored resonances [87]. The dissociation spectrum of Eq. (3.15) is plotted in Fig. 3.5 as the asymptotic limit of slow ramps for the 685 G resonance of ^{87}Rb.

The dissociation spectrum of Eq. (3.15) does not depend on the magnetic moment μ_{res} of the Feshbach resonance level, but just on $|a_{\mathrm{bg}}\Delta B|$. This product characterises the scattering length in the close vicinity of a zero-energy resonance, as can be seen from Eq. (2.18). This suggests that it should be possible to arrive at Eq. (3.15) using different descriptions of the underlying two-body physics, the only condition being that the near-resonant scattering properties are correctly recovered. In Appendix B.3, we derive Eq. (3.15) using the single-channel approach of Sec. 2.3. Taking a separable form of the potential allows this relation to be derived analytically, just as in the two-channel case. The limitations of the single-channel approach when applied to closed-channel dominated resonances have no effect in the case of an asymptotic ramp. Consequently, for asymptotic ramps the physical description need only be accurate in the near-resonant

region. This is sufficient for recovering the near-resonant scattering properties, and therefore leads to the correct dissociation spectrum. For jumps or intermediate ramps, however, the physical description must apply over the entire range of magnetic fields.

3.5 Conclusions

In this chapter we have studied in detail the dissociation spectra produced by linear sweeps of the magnetic field strength across zero-energy resonances, for field ranges and ramp speeds varying from jumps to asymptotic ramps. A key finding of this chapter is that jumps in the magnetic field can be used to classify zero-energy resonances according to the dominance of their entrance and closed channels. Our scheme requires measuring whether a sharp peak occurs in the dissociation spectrum near the final resonance energy. The presence or absence of this peak allows a resonance to be classified as closed- or entrance-channel dominated, respectively. This may be measured before other properties of the resonance are studied. By comparing the spectrum of a jump to exact numerical calculations for the example of the 685 G resonance of ^{87}Rb, we have shown that the ramp speed required for such a measurement can be achieved by current experiments.

Our calculations of the dissociation spectrum for varying ramp speeds and fixed initial and final fields show that the spectrum approaches the asymptotic form as the ramp speed is lowered. Increasing the width of the ramp for a fixed ramp speed also brings the spectrum closer to the asymptotic result. We have analytically determined the time evolution for linear ramps using a two-channel approach. Evaluating this in the asymptotic limit rigorously produces the asymptotic spectrum of Eq. (3.15). Asymptotic ramps, however, only require a correct physical description of the near-resonant region, and so a single-channel approach is also valid.

Chapter 4

Microscopic quantum dynamics of Feshbach molecule production

In this chapter we detail the theory of cumulants, the microscopic quantum dynamics approach used in the following chapters. We begin by reviewing quantum kinetic theory and the dynamics of ultracold gases at nonzero temperatures. We then outline the theory of cumulants and its application to the production of Feshbach molecules from thermal and condensed gases. The non-Markovian, nonlinear Schrödinger equation for the dynamics of a zero-temperature condensed gas is derived within the first order cumulant approach. The second order cumulant approach is used to derive a non-Markovian Boltzmann equation, governing the dynamics of the one-body density matrix of a thermal gas. We show how these equations allow predictions of molecule production, and discuss the short-time limit for a thermal gas, in which case the molecule production is calculated from a thermal average of the two-body transition probability density. It is shown that the non-Markovian Boltzmann equation reduces to the normal, Markovian Boltzmann equation in the limit of long times and stationary interactions.

4.1 Introduction

The aim of kinetic theory is to calculate the macroscopic physical properties of a gas, including its thermodynamic properties, from the form of the microscopic interactions. In the late 19th century Boltzmann derived his famous transport equation [154], describing the dynamics of the distribution function for the phase-space density of particles, $f(\mathbf{r}, \mathbf{p}, t)$. By considering the flow of particles in and out of the phase-space element $d\mathbf{r}d\mathbf{p}$ surrounding $(\mathbf{r}, \mathbf{p})$, it can be shown that the evolution of $f(\mathbf{r}, \mathbf{p}, t)$ is given by

$$\left(\frac{\partial}{\partial t} + \frac{\mathbf{p}}{m} \cdot \nabla_{\mathbf{r}} + \mathbf{F}(\mathbf{r}) \cdot \nabla_{\mathbf{p}}\right) f(\mathbf{r}, \mathbf{p}, t) = \frac{\partial}{\partial t} f_{\text{coll}}(\mathbf{r}, \mathbf{p}, t)\,. \tag{4.1}$$

Here, $\mathbf{F}(\mathbf{r})$ is the force on each particle due to external potentials, and the right-hand side of the equation is the collision term. Specifying the collision term is the involved

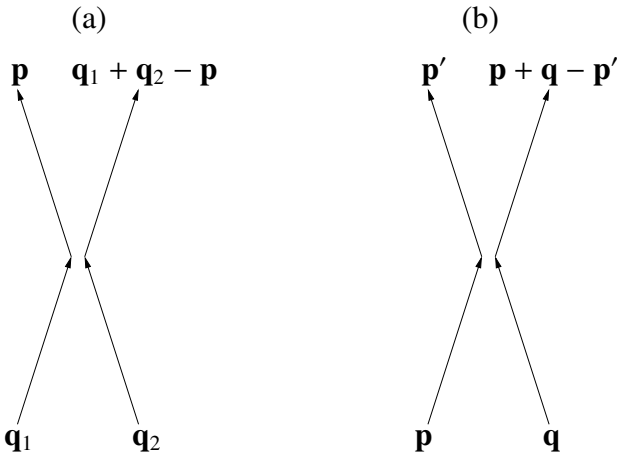

Figure 4.1: Scattering (a) in and (b) out of the phase-space element surrounding $(\mathbf{r}, \mathbf{p})$.

part in any kinetic theory. Assuming the gas to be sufficiently dilute that only pairwise interactions are significant, this can be shown to be [146]

$$\frac{\partial}{\partial t} f_{\text{coll}}(\mathbf{r}, \mathbf{p}, t) = \int d\mathbf{p}_2 d\mathbf{p}_3 d\mathbf{p}_4 \delta(\mathbf{p} + \mathbf{p}_2 - \mathbf{p}_3 - \mathbf{p}_4) \delta\left(\frac{p^2}{2m} + \frac{p_2^2}{2m} - \frac{p_3^2}{2m} - \frac{p_4^2}{2m}\right) |T_{\text{fi}}|^2 \times \left[f(\mathbf{r}, \mathbf{p}_3, t) f(\mathbf{r}, \mathbf{p}_4, t) - f(\mathbf{r}, \mathbf{p}, t) f(\mathbf{r}, \mathbf{p}_2, t)\right] . \tag{4.2}$$

Here $T_{\text{fi}} = \langle \mathbf{p}\mathbf{p}_2 | T(z) | \mathbf{p}_3 \mathbf{p}_4 \rangle$ is the two-body T-matrix, with $z = (p^2/2m) + (p_2^2/2m) + i0$. The first product in the square brackets represents the scattering into the phase-space element surrounding $(\mathbf{r}, \mathbf{p})$, and the second represents the scattering out of it. These are sketched in Fig. 4.1. In the limit of low collision energy, Eq. (4.2) reduces to

$$\frac{\partial}{\partial t} f_{\text{coll}}(\mathbf{r}, \mathbf{p}, t) = \frac{a^2}{m^2 (2\pi\hbar)^3} \int d\mathbf{p}_2 d\mathbf{p}_3 d\mathbf{p}_4 \delta(\mathbf{p} + \mathbf{p}_2 - \mathbf{p}_3 - \mathbf{p}_4) \delta\left(\frac{p^2}{2m} + \frac{p_2^2}{2m} - \frac{p_3^2}{2m} - \frac{p_4^2}{2m}\right) \times \left[f(\mathbf{r}, \mathbf{p}_3, t) f(\mathbf{r}, \mathbf{p}_4, t) - f(\mathbf{r}, \mathbf{p}, t) f(\mathbf{r}, \mathbf{p}_2, t)\right] . \tag{4.3}$$

We recover this result from the theory of cumulants in Sec. 4.7. The derivation of the Boltzmann equation assumes that the de Broglie wavelength of the particles is much smaller than the interparticle separation. It is also assumed that the momenta of particles at any point in space are uncorrelated. The Boltzmann equation is valid for the case of a thermal gas where the average population of each quantum state is much smaller than 1. Quantum mechanically, the effects of Bose and Fermi statistics must be included. This

leads to the quantum Boltzmann equation [155], where the collision term takes the form

$$\frac{\partial}{\partial t} f_{\rm coll}(\mathbf{r},\mathbf{p},t) = \frac{a^2}{m^2(2\pi\hbar)^3}\int d\mathbf{p}_2 d\mathbf{p}_3 d\mathbf{p}_4 \delta(\mathbf{p}+\mathbf{p}_2-\mathbf{p}_3-\mathbf{p}_4)\delta\left(\frac{p^2}{2m}+\frac{p_2^2}{2m}-\frac{p_3^2}{2m}-\frac{p_4^2}{2m}\right)$$
$$\times\Big\{f(\mathbf{r},\mathbf{p}_3,t)f(\mathbf{r},\mathbf{p}_4,t)\left[1\pm f(\mathbf{r},\mathbf{p},t)\right]\left[1\pm f(\mathbf{r},\mathbf{p}_2,t)\right]$$
$$-f(\mathbf{r},\mathbf{p},t)f(\mathbf{r},\mathbf{p}_2,t)\left[1\pm f(\mathbf{r},\mathbf{p}_3,t)\right]\left[1\pm f(\mathbf{r},\mathbf{p}_4,t)\right]\Big\}. \tag{4.4}$$

Here, the positive and negative signs refer to Bose and Fermi statistics, respectively. In the limit of small occupation numbers, $[1 \pm f(\mathbf{r},\mathbf{p},t)] \approx 1$, and Eq. (4.3) is recovered.

In the context of ultracold gases, the Boltzmann equation has been used to study effects such as collisional relaxation in thermal Bose gases [30], and the lifetime, damping, and instabilities of spin-waves in a two-component, one-dimensional gas of bosonic atoms [156, 157]. Holland *et al.* developed a stochastic implementation of the Boltzmann equation [158], making the ergodic approximation (i.e. that the population of a state depends only on its energy). They were able to apply this to the equilibration of thermal gases. A linearised Boltzmann equation, including a mean-field as a modification to the drift terms on the left-hand side of Eq. (4.1), has been used to study the frequency and damping of collective modes in resonantly interacting Fermi gases [159]. Applications of kinetic theory to ultracold gases have, however, been primarily concerned with the formation and behaviour of Bose-Einstein condensates.

After the achievement of BEC of dilute gases in 1995, significant theoretical insight into condensate dynamics was gained from studies of the Gross-Pitaevskii equation (GPE) [32, 33, 160, 161, 162, 163, 164]. The GPE was able to explain effects such as condensate expansion after release from a trap [162], interference of condensates [164, 165], and their excitation spectra [163]. The GPE is valid for condensates well below the critical temperature, for which thermal and quantum depletion are negligible. It is also necessary that the gas be dilute, i.e. $n|a|^3 \ll 1$, where a is the s-wave scattering length. Finally, the length and time scales of the interactions must be smaller than all others that are characteristic of the gas. The excitation spectrum of a BEC at zero temperature is given by Bogoliubov's theory of weakly interacting Bose gases [29]. Here we give a brief summary of this theory and the Hartree-Fock and Popov approximations, which allow its extension to nonzero temperature. At the temperatures and densities typical of experiments with cold and ultracold gases, the atomic interactions are predominantly pairwise. The general Hamiltonian for a gas of bosonic atoms inter-

acting pairwise via a potential V is given by

$$H = \sum_{lm} a_l^\dagger \langle l|H_{1\mathrm{B}}|m\rangle a_m + \frac{1}{2}\sum_{\substack{m_1 m_2 \\ m_3 m_4}} \langle m_1 m_2|V|m_3 m_4\rangle a_{m_1}^\dagger a_{m_2}^\dagger a_{m_3} a_{m_4}\,. \tag{4.5}$$

Here, the indices refer to an arbitrary set of basis states, and the field operators have the usual bosonic commutation relations:

$$[a_i, a_j^\dagger] = \delta_{ij}\,, \tag{4.6}$$

$$[a_i, a_j] = 0\,. \tag{4.7}$$

For a homogeneous gas in a box of volume $\mathcal{V}$, the basis states are interpreted as box states, satisfying $e^{i\mathbf{k}\cdot\mathbf{x}}/\sqrt{\mathcal{V}}$, with $\mathbf{k}$ taking the full range of values that give the wavefunction nodes at the boundaries of the box. All of the calculations in this thesis use either the hard core + van der Waals tail potential of Sec. 2.4.1 or the separable potential of Sec. 2.4.2. To illustrate the fundamental principles, however, in this introduction we consider particles interacting via a contact interaction of strength $U_0 = 4\pi\hbar^2 a/m$. The Bogoliubov approximation consists of replacing a_0 and $a_0^\dagger$ by $\sqrt{N_0}$ [29], where the zero momentum mode population N_0 is assumed to be macroscopically large. Assuming that the fluctuations are small and retaining terms up to second order in the fluctuations leads to the Bogoliubov Hamiltonian:

$$H = \frac{N_0^2 U_0}{2\mathcal{V}} + \sum_{\mathbf{k}(\mathbf{k}\neq 0)} (\epsilon_k^0 + 2n_0 U_0) a_{\mathbf{k}}^\dagger a_{\mathbf{k}} + \frac{n_0 U_0}{2} \sum_{\mathbf{k}(\mathbf{k}\neq 0)} (a_{\mathbf{k}}^\dagger a_{-\mathbf{k}}^\dagger + a_{\mathbf{k}} a_{-\mathbf{k}})\,. \tag{4.8}$$

Here, n_0 is the condensate density, and $\epsilon_k^0 = \hbar^2 k^2/2m$. The first summation has terms corresponding to independent excitations of momentum $\hbar\mathbf{k}$, and the atoms in the condensate. The second summation, involving pairs of creation or annihilation operators, corresponds to pairs of atoms scattered into and out of the condensate, respectively, and is referred to as the anomalous term. Diagonalising Eq. (4.8) by converting to a quasi-particle basis leads to the Bogoliubov spectrum for a homogeneous gas at zero temperature [30],

$$\epsilon_k = \sqrt{2nU_0\epsilon_k^0 + (\epsilon_k^0)^2}\,. \tag{4.9}$$

This dispersion relation is quadratic (particle-like) for short-wavelength excitations, and linear (wave-like) for long, which is a key property of superfluids.

At non-zero temperatures, the expectation value of the interaction term in Eq. (4.5) can be calculated using Hartree-Fock theory [30]. The lowest order Hartree-Fock approximation gives a theory in which an excitation corresponds simply to adding a particle of nonzero momentum and removing one from the condensate. It therefore neglects the interaction of the excitations with each other. This has a spectrum $\epsilon_k = \epsilon_k^0 + 2nU_0$, valid for $n_0U_0 \ll \epsilon_k^0$. The simplest theory which produces a gapless spectrum, as is the case in reality for an infinite homogeneous gas, is the Popov approximation in which the terms linear in $a_{\mathbf{k}}a_{-\mathbf{k}}$ and $a_{\mathbf{k}}^\dagger a_{-\mathbf{k}}^\dagger$ are retained in Eq. (4.8), but the effect of the thermal excitations on them is neglected [30, 166]. This leads to an excitation spectrum consistent with Eq. (4.9), with the thermally depleted condensate density determined self-consistently. In both the Hartree-Fock and Popov approximations, the effect of interactions is to provide static mean fields that couple to the density of particles, or create and destroy pairs of particles. The HFB-Popov approach has been successful in describing condensates up to approximately 60% of the critical temperature [167]. Morgan developed a number-conserving approach which includes higher order terms using first and second order perturbative corrections to a quadratic Hamiltonian [168]. The validity of this approach is limited by the size of the higher order terms, which become more significant with increasing temperature, condensate depletion, and interaction strength.

Several beyond mean-field approaches have been developed with the aim of relaxing the assumptions underlying the derivation of the GPE, in order to study processes such as condensate growth, thermalisation, and vortex nucleation in condensed gases at nonzero temperatures [169]. One group of approaches utilise techniques from quantum optics, dividing the Bose field operator into highly occupied modes, which may in general be treated as classical fields, and little-occupied modes which are treated as a thermal bath. This technique was pioneered by Gardiner and Zoller [170]. Different levels of approximation are used to treat the thermal bath. In the ZNG approach [171], the bath is considered to be always in thermal equilibrium and collisions are assumed to be frequent enough that a hydrodynamic description of the condensed and noncondensed fractions is valid. This theory has been applied to several situations, including the dynamics of the scissors [172] and breathing modes [173], and vortex nucleation [174]. Davis and co-workers developed an approach in which the highly occupied modes are described by classical field equations, and the thermal bath is described by a quantum Boltzmann equation [175, 176]. Such a finite-temperature GPE requires each mode in the classical region to have a large number of atoms. Neglecting the bath leads to the

projected GPE [177, 178], which takes account of all the Bose-enhancement but none of the spontaneous processes. Applications of the PGPE have included evaporative cooling and the calculation of critical temperatures [179, 180], vortex dynamics [181], and thermalisation [176, 177]. Holland *et al.* extended their stochastic approach to the Boltzmann equation for a classical gas [162] to include the macroscopic occupation of a single mode, modelling evaporative cooling and finite-temperature BEC dynamics [182, 183].

Phase-space approaches are based on the principle of expanding the density matrix in a basis suitable for dynamical simulations. Expressing the master equation in terms of a Wigner function leads to a functional partial differential equation with first and third order derivatives. The third order derivatives are small when the occupation numbers are large, and neglecting them leads to the truncated Wigner approach [184]. The differential equation that remains coincides with the GPE, however the effects of quantum noise are retained in the initial conditions, which are chosen to sample the initial Wigner function. Expectation values are obtained by averaging over several trajectories. The truncated Wigner approach is valid provided that the number of particles is larger than the number of modes, and that the maximum energy of the Bogoliubov excitations is not too high [185]. It has been applied to phenomena such as vortex nucleation [186], Beliaev-Landau damping [185], the loading and dynamics of gases in optical lattices [187, 188], and atom laser statistics [189]. Expanding the density matrix in terms of coherent state projectors leads to a stochastic differential equation which provides a technique known as the positive-P approach [190]. This method is in principle precise, however the distribution of trajectories that must be averaged over to calculate an expectation value can become very wide, making convergence difficult. This issue limits the length of time over which strong interactions can be modelled. The positive-P technique has been applied to evaporative cooling [191], and has also recently been applied to calculations of molecule dissociation and quadrature squeezing of the resulting atom pairs [192, 193].

In recent years significant attention has also been paid to strong interactions in ultracold gases. Theoretical treatments of this regime have inherited a lot of their formalism from condensed matter and nuclear physics. The two-particle irreducible effective action technique calculates quantum dynamics from the variation of an effective action, expanding it in terms of the inverse of the number of field components, and has been applied to dynamical studies in one-dimensional gases [194, 195] and optical lattices [196, 197]. Stoof developed a quantum field theoretic approach in which a Hartree-

Fock approximation is used to calculate the many-body T-matrix [198]. The resulting dynamical equation is, however, difficult to solve and is typically reduced to a stochastic differential equation in which the damping and noise terms are calculated from the Keldysh self-energy [198, 199]. Applications of this approach have included condensate growth [199], and quasicondensate growth [200] and phase fluctuations [201] in one-dimensional gases. A similar 'stochastic GPE' may be derived from a Wigner function representation of the master equation, using the ideas of the finite-temperature GPE and quantum kinetic theory [202, 203]. Both of these approaches to the stochastic GPE assume the thermal cloud to be in equilibrium.

The dynamics of molecule formation from zero-temperature condensates and thermal gases has been studied in both two- and single-channel approaches, using a range of potential models. For isolated pairs of atoms in an optical lattice, the conversion may be accurately calculated from two-body physics [126, 139]. Zero-temperature condensates have been considered in a two-level mean-field approach using contact interactions [125, 204, 205, 206], and microscopic quantum dynamics approaches [117, 128, 134, 207]. Mean-field approaches require the interactions to occur on a timescale much faster than the condensate evolution, and are inherently two-level. Microscopic quantum dynamics approaches are more general, however the calculations are correspondingly more difficult. The dynamics of molecule formation from a partially condensed gas with a significant thermal fraction, for which strong interactions and nonzero temperatures must be included, remains an open problem. Molecule formation in loosely trapped thermal gases has been studied by assuming the trap to approximate a continuum, and summing over the two-body transition amplitudes [117, 208, 209]. Such approaches neglect the depletion and rethermalisation of the continuum of unbound states. The quantum kinetics of molecule formation has been studied by Williams *et al.* [115, 210], who used the Keldysh non-equilibrium Green's function formalism [211] to derive generalised Boltzmann equations for the resonance level and unbound pairs. We further discuss the kinetics of molecule formation, and the resulting predictions for the saturation of this process, in Chapter 6.

In this chapter we explain in detail the theory of cumulants (see, e.g., Ref. [212]) and its application to the production of molecules from ultracold gases. The results derived here form the basis of the calculations presented in the following chapters. Our approach, like that of Ref. [115], is motivated by kinetic theory, but further relaxes the assumptions

regarding the number of collisions during the ramp and equilibrium of the gas. We give an overview of the theory of cumulants in the next section. In Sec. 4.3 we use the theory of cumulants to derive the non-Markovian, nonlinear Schrödinger equation for the dynamics of the mean field in a condensate that is initially at zero temperature. The non-Markovian Boltzmann equation, giving the evolution of the one-body density matrix of a thermal gas, is derived in Sec. 4.4. We then show how these two equations lead to predictions of the molecule production efficiency, considering condensed and thermal gases in Secs. 4.5 and 4.6, respectively. In Sec. 4.6.1, we discuss molecule production from thermal gases in the limit of short times, for which the conversion may be calculated more simply by thermally averaging over the two-body transition probability density. In Sec. 4.7 we consider the limit of long times, for which the conversion efficiency should reach saturation. We show how the non-Markovian Boltzmann equation of Sec. 4.4 then reduces to the normal Boltzmann equation, provided the limit of stationary interactions is also taken. This shows the relation between our approach and conventional kinetic theory, and shows that our approach has the correct behaviour in the limit of long times.

4.2 Theory of cumulants

The dynamical equation for the expectation value of an operator θ at time t, $\langle\theta\rangle_t$, is given by

$$i\hbar\frac{\partial}{\partial t}\langle\theta\rangle_t = \langle[\theta, H]\rangle_t \,. \tag{4.10}$$

The form of the general Hamiltonian in Eq. (4.5) shows that calculating the dynamics for the expectation value of an operator produces an infinite recursion of products of higher numbers of operators. A method of truncation is therefore required. The simplest method is to neglect all expectation values with more than a certain number of operators, however this has no guarantee that the higher order terms are of a size that can be safely neglected. In fact, in some cases the size of the terms can grow as the order increases. The method of cumulants has been applied to calculations of the dynamics of many-body quantum systems in terms of correlation functions [145, 213, 214]. The approach we use here [145] provides a truncation scheme in which the nth order theory includes the exact evolution of expectation values of n or less operators, plus the free evolution of products of $n + 1$ and $n + 2$ operators. For a set of bosonic field operators a_i, cumulants may be defined recursively in terms of expectation values [215]. The first three of these

are

$$\langle a_1 \rangle = \langle a_1 \rangle^c \,, \tag{4.11}$$

$$\langle a_1 a_2 \rangle = \langle a_1 a_2 \rangle^c + \langle a_1 \rangle^c \langle a_2 \rangle^c \,, \tag{4.12}$$

$$\langle a_1 a_2 a_3 \rangle = \langle a_1 a_2 a_3 \rangle^c + \langle a_1 \rangle^c \langle a_2 a_3 \rangle^c + \langle a_2 \rangle^c \langle a_1 a_3 \rangle^c + \langle a_3 \rangle^c \langle a_1 a_2 \rangle^c + \langle a_1 \rangle^c \langle a_2 \rangle^c \langle a_3 \rangle^c \,. \tag{4.13}$$

In the thermal equilibrium of a grand canonical ensemble, all cumulants of order greater than 2 vanish for an ideal gas [213]. These can therefore act as a measure of the deviation of the system from its interaction-free equilibrium. Each cumulant of order n adds the nth order interactions around the interaction-free evolution already included in the $(n-1)$th order. Cumulants therefore get smaller as n increases. For this reason, a system that stays reasonably close to an equilibrium which is changing in time should be well described by a cumulant expansion of order n for a longer time than it would be by a perturbative expansion to nth order, for which the higher order terms are in general important. In the context of ultracold gases, the theory of cumulants has been applied to colliding condensates [145], the dynamics of quantum accelerator modes [216], and spin-squeezing in two-component BECs [217]. It has been applied to a range of problems related to Feshbach molecules, including their dissociation [218], and their production by linear ramps [128], the Ramsey fringe experiments of Wieman's group [134, 207], and resonantly modulated magnetic fields ([117], as detailed in Chapter 5). The theory of cumulants has also been applied to the production of cold molecules by photoassociation [219].

In this thesis, we follow the notation of [145], making the following definitions:

$$\Psi_m(t) = \langle a_m \rangle_t^c \,, \tag{4.14}$$

$$\Phi_{lm}(t) = \langle a_m a_l \rangle_t^c \,, \tag{4.15}$$

$$\Gamma_{lm}(t) = \langle a_m^\dagger a_l \rangle_t^c \,. \tag{4.16}$$

These quantities are referred to as the mean field, the pair function, and the one-body density matrix of the non-condensed fraction, respectively. Higher order cumulants are denoted

$$\Gamma^{(m,n)}_{k_1 k_2 \cdots k_m; l_1 l_2 \cdots l_n}(t) = \langle a_{l_1}^\dagger a_{l_2}^\dagger \cdots a_{l_n}^\dagger a_{k_1} a_{k_2} \cdots a_{k_m} \rangle_t^c \,. \tag{4.17}$$

Our formulation of the theory of cumulants allows us to use exact calculations of the two-body dynamics as inputs to the many-body equations. It therefore incorporates the

full time variation of the two-body interactions, as well as simplifying the subsequent calculation of many-body dynamics. We consider the production of molecules from condensed gases, and thermal gases in the short-time limit, in Chapter 5. Application of the theory of cumulants to the dynamics of the one-body density matrix provides a beyond mean-field approach which includes fluctuations and realistic, time-varying interactions. This enables studies of the many-body effects leading to the saturation of molecule production, which we present in Chapter 6.

4.3 Mean-field evolution

In this section we use the first order cumulant approach to derive the non-Markovian, nonlinear Schrödinger equation governing the evolution of the mean field in a condensate that is initially at zero temperature. The exact evolution of the expectation value of a field operator a_i is given by

$$\begin{aligned} i\hbar\frac{\partial}{\partial t}\Psi_i(t) &= \langle [a_i, H]\rangle_t \\ &= \sum_{lm}\langle l|H_{1\mathrm{B}}|m\rangle\left[\langle a_i a_l^\dagger a_m\rangle_t - \langle a_l^\dagger a_m a_i\rangle_t\right] \\ &+ \frac{1}{2}\sum_{\substack{m_1 m_2\\ m_3 m_4}}\langle m_1 m_2|V|m_3 m_4\rangle\left[\langle a_i a_{m_1}^\dagger a_{m_2}^\dagger a_{m_3} a_{m_4}\rangle_t - \langle a_{m_1}^\dagger a_{m_2}^\dagger a_{m_3} a_{m_4} a_i\rangle_t\right]. \end{aligned} \tag{4.18}$$

Here, H is the general Hamiltonian of Eq. (4.5). Using the commutation relations of Eqs. (4.6)-(4.7) to normal-order the expectation values of this equation gives

$$\begin{aligned} i\hbar\frac{\partial}{\partial t}\Psi_i(t) = \sum_m\langle i|H_{1\mathrm{B}}|m\rangle\langle a_m\rangle_t + \frac{1}{2}\sum_{m_1 m_3 m_4}\langle m_1 i|V|m_3 m_4\rangle\langle a_{m_1}^\dagger a_{m_3} a_{m_4}\rangle_t \\ + \frac{1}{2}\sum_{m_2 m_3 m_4}\langle i m_2|V|m_3 m_4\rangle\langle a_{m_2}^\dagger a_{m_3} a_{m_4}\rangle_t . \end{aligned} \tag{4.19}$$

The potential matrix element is left unchanged after exchange of the first two indices, and so the last two summations are identical after a relabelling of indices. Performing the cumulant expansion of the expectation values using Eqs. (4.11)-(4.13) then gives

$$\begin{aligned} i\hbar\frac{\partial}{\partial t}\Psi_i(t) = \sum_m\langle i|H_{1\mathrm{B}}|m\rangle\Psi_m(t) + \sum_{m_1 m_3 m_4}\langle m_1 i|V|m_3 m_4\rangle\Big[\Gamma^{(2,1)}_{m_3 m_4; m_1}(t) \\ + \Psi^*_{m_1}(t)\Phi_{m_3 m_4}(t) + \Gamma_{m_3 m_1}(t)\Psi_{m_4}(t) + \Gamma_{m_4 m_1}(t)\Psi_{m_3}(t) + \Psi^*_{m_1}(t)\Psi_{m_3}(t)\Psi_{m_4}(t)\Big]. \end{aligned} \tag{4.20}$$

Here, $\Gamma^{(2,1)}_{m_3m_4;m_1}(t)$ is defined by Eq. (4.17).

We now change to a position basis to show the effect of the separation of length scales between the de Broglie wavelength of the atoms and the characteristic length scale of the interatomic potential. The field operators are written in the form $\psi_\alpha(\mathbf{x})$ to refer to a particle annihilated at $\mathbf{x}$ in the Zeeman state α. The Hamiltonian of Eq. (4.5) now takes the form [220]:

$$H = \sum_\alpha \int d\mathbf{x}\, \psi^\dagger_\alpha(\mathbf{x})\Big[-\frac{\hbar^2}{2m}\nabla^2 + E^{\rm a}_\alpha(B) + V_\alpha(\mathbf{x})\Big]\psi_\alpha(\mathbf{x}) + H_{\rm int}\,, \tag{4.21}$$

where $E^{\rm a}_\alpha(B)$ is the Zeeman energy of spin state α, $V_\alpha(\mathbf{x})$ is the trapping potential, and the interaction Hamiltonian is given by

$$H_{\rm int} = \frac{1}{2}\sum_{\alpha\beta\alpha'\beta'} \int d\mathbf{x} d\mathbf{y} V_{\alpha\beta,\alpha'\beta'}(\mathbf{r})\psi^\dagger_\alpha(\mathbf{x})\psi^\dagger_\beta(\mathbf{y})\psi_{\beta'}(\mathbf{y})\psi_{\alpha'}(\mathbf{x})\,. \tag{4.22}$$

Here, $\mathbf{r} = \mathbf{x} - \mathbf{y}$ is the relative coordinate of the atom pair. We make the approximation that the pair function and one-body density matrix are initially zero. Neglecting the pair function at the initial time corresponds to assuming that no pairwise correlations exist in the BEC. Neglecting the one-body density matrix corresponds to neglecting the influence of noncondensed atoms on the condensate, which limits the range of situations able to be considered to those in which the condensate is nearly pure. The first order cumulant approach includes the precise evolution of the expectation value of one operator, and the free evolution of products of two or three operators. Consequently, to this level of approximation the one-body density matrix then remains zero at all times, and the condensate evolution given by Eq. (4.20) becomes

$$i\hbar\frac{\partial}{\partial t}\Psi_\alpha(\mathbf{x},t) = H^\alpha_{\rm 1B}\Psi_\alpha(\mathbf{x},t) + \sum_{\beta\alpha'\beta'}\int d\mathbf{y} V_{\alpha\beta\alpha'\beta'}(\mathbf{r})\Psi^*_\beta(\mathbf{y},t)\big[\Phi_{\alpha'\beta'}(\mathbf{x},\mathbf{y},t) + \Psi_{\alpha'}(\mathbf{x},t)\Psi_{\beta'}(\mathbf{y},t)\big]\,. \tag{4.23}$$

The formal solution of the pair function at this level of approximation is

$$\begin{aligned}\Phi_{\alpha\beta}(\mathbf{x},\mathbf{y},t) = \sum_{\alpha'\beta'}\int d\mathbf{x}' d\mathbf{y}'\Big(&\langle \mathbf{x},\mathbf{y},\alpha\beta|U_{\rm 2B}(t,t_{\rm i})|\mathbf{x}',\mathbf{y}',\alpha'\beta'\rangle\Phi_{\alpha'\beta'}(\mathbf{x}',\mathbf{y}',t_{\rm i})\\ &+\frac{1}{i\hbar}\int_{t_{\rm i}}^t dt'\langle \mathbf{x},\mathbf{y},\alpha\beta|U_{\rm 2B}(t,t')|\mathbf{x}',\mathbf{y}',\alpha'\beta'\rangle V_{\alpha'\beta'}(\mathbf{x}'-\mathbf{y}')\Psi_{\alpha'}(\mathbf{x}',t')\Psi_{\beta'}(\mathbf{y}',t')\Big).\end{aligned} \tag{4.24}$$

Neglecting the pair function at the initial time $t_{\rm i}$ and transforming to centre of mass and

relative coordinates leaves

$$\Phi_{\alpha\beta}(\mathbf{R},\mathbf{r},t) = \frac{1}{i\hbar}\sum_{\alpha'\beta'}\int d\mathbf{R}'d\mathbf{r}'\int_{t_\mathrm{i}}^{t} dt'\langle\mathbf{R},\mathbf{r},\alpha\beta|U_{2\mathrm{B}}(t,t')|\mathbf{R}',\mathbf{r}',\alpha'\beta'\rangle V_{\alpha'\beta'}(\mathbf{r}') \times \Psi_{\alpha'}(\mathbf{R}'+\mathbf{r}'/2,t')\Psi_{\beta'}(\mathbf{R}'-\mathbf{r}'/2,t')\,. \tag{4.25}$$

We use the fact that the de Broglie wavelength of the atoms is much larger than the range of the interactions, and that the atomic wavefunction is therefore slowly varying by comparison with the potential, to write $\Psi(\mathbf{R}\pm\mathbf{r}/2)V(\mathbf{r}) \approx \Psi(\mathbf{R})V(\mathbf{r})$. Expressing the potential in terms of the derivative of $U_{2\mathrm{B}}(t,t')$ with respect to t', and writing the zero momentum plane wave as $|0\rangle = (2\pi\hbar)^{-3/2}\int d\mathbf{r}|\mathbf{r}\rangle$, the pair function then becomes

$$\Phi_{\alpha\beta}(\mathbf{R},\mathbf{r},t) \approx -(2\pi\hbar)^{3/2}\int_{t_\mathrm{i}}^{t} dt'\Psi_\alpha(\mathbf{R},t')\Psi_\beta(\mathbf{R},t')\frac{\partial}{\partial t'}\langle\mathbf{r}|U_{2\mathrm{B}}^{\alpha\beta}(t,t')|0\rangle\,. \tag{4.26}$$

Substituting this into Eq. (4.23) and again using the fact that the de Broglie wavelength is much greater than the length scale of the interactions gives

$$i\hbar\frac{\partial}{\partial t}\Psi_\alpha(\mathbf{x},t) = H_{1\mathrm{B}}^{\alpha}\Psi_\alpha(\mathbf{x},t) + (2\pi\hbar)^{3/2}\sum_{\beta\alpha'\beta'}\Psi_\beta^*(\mathbf{x},t)\int_{t_\mathrm{i}}^{t} dt'\Psi_{\alpha'}(\mathbf{x},t')\Psi_{\beta'}(\mathbf{x},t') \times\frac{\partial}{\partial t'}[\theta(t-t')\int d\mathbf{y}V_{\alpha\beta\alpha'\beta'}(\mathbf{r})\langle\mathbf{r}|U_{2\mathrm{B}}^{\alpha'\beta'}(t,t')|0\rangle]\,. \tag{4.27}$$

Here, the derivative of the step function $\theta(t-\tau)$ accounts for the mean-field terms at time t. For a homogeneous gas, this leads to the non-Markovian, nonlinear equation

$$i\hbar\frac{\partial}{\partial t}\Psi_\alpha(t) = H_{1\mathrm{B}}^{\alpha}\Psi_\alpha(t) + \sum_{\beta\alpha'\beta'}\Psi_\beta^*(t)\int_{t_\mathrm{i}}^{t} dt'\Psi_{\alpha'}(t')\Psi_{\beta'}(t')\frac{\partial}{\partial t'}h^{\alpha\beta\alpha'\beta'}(t,t')\,, \tag{4.28}$$

where the memory function $h^{\alpha\beta\alpha'\beta'}(t,t')$ is given by

$$h^{\alpha\beta\alpha'\beta'}(t,t') = (2\pi\hbar)^3\theta(t-t')\langle 0|V_{\alpha\beta\alpha'\beta'}U_{2\mathrm{B}}^{\alpha'\beta'}(t,t')|0\rangle\,. \tag{4.29}$$

The memory function provides a precise representation of the two-body physics, which is then used as an input to the many-body equation Eq. (4.28), and is so-called because it contains the non-Markovian effects. For the single-channel case, which we consider in Chapter 5, this simplifies to

$$i\hbar\frac{\partial}{\partial t}\Psi(t) = H_{1\mathrm{B}}\Psi(t) - \Psi^*(t)\int_0^{\infty} dt'\Psi^2(t')\frac{\partial}{\partial t'}h(t,t')\,, \tag{4.30}$$

where the memory function $h(t,t')$ is given by

$$h(t,t') = (2\pi\hbar)^3\langle 0|V(t)U_{2\mathrm{B}}(t,t')|0\rangle\theta(t-t')\,. \tag{4.31}$$

We find $h(t,t')$ by solving a Volterra equation. The Lippman-Schwinger equation provides two equations for the two-body evolution operator:

$$U_{2\mathrm{B}}(t,t') = U_0(t-t') + \frac{1}{i\hbar}\int_{t'}^{t} d\tau U_{2\mathrm{B}}(t,\tau)V(\tau)U_0(\tau-t')\,, \tag{4.32}$$

$$U_{2\mathrm{B}}(t,t') = U_0(t-t') + \frac{1}{i\hbar}\int_{t'}^{t} d\tau U_0(t-\tau)V(\tau)U_{2\mathrm{B}}(\tau,t')\,. \tag{4.33}$$

The form of the separable potential in Eq. (2.85) shows that the memory function may be calculated from the matrix element $\langle\chi|U_{2\mathrm{B}}(t,t')|0\rangle$. Projecting Eq. (4.32) onto $\langle\chi|$ on the left and $|0\rangle$ on the right gives the equation

$$\langle\chi|U_{2\mathrm{B}}(t,t')|0\rangle = \langle\chi|0\rangle + \frac{1}{i\hbar}\langle\chi|0\rangle\int_{t'}^{t} d\tau\langle\chi|U_{2\mathrm{B}}(t,\tau)|\chi\rangle\xi(\tau)\,. \tag{4.34}$$

Projecting Eq. (4.33) onto $|\chi\rangle$ on the left and right gives a closed integral equation which can be used to calculate $\langle\chi|U_{2\mathrm{B}}(t,t')|\chi\rangle$. The numerical technique used to solve this equation is detailed in Appendix D.

4.4 One-body density matrix evolution: The non-Markovian Boltzmann equation

From the Schrödinger equation with the general Hamiltonian of Eq. (4.5), and the cumulant expansion of Eq. (4.12), the precise evolution of the one-body density matrix is given by

$$\begin{aligned}
i\hbar\frac{\partial}{\partial t}\Gamma_{ij}(t) &= \langle[a_j^\dagger a_i, H]\rangle_t - \Psi_i(t)\langle[a_j^\dagger, H]\rangle_t - \Psi_j^*(t)\langle[a_i, H]\rangle_t \\
&= \sum_{lm}\langle l|H_{1\mathrm{B}}|m\rangle\{\langle a_j^\dagger a_i a_l^\dagger a_m\rangle_t - \langle a_l^\dagger a_m a_j^\dagger a_i\rangle_t\} \\
&+ \frac{1}{2}\sum_{\substack{m_1 m_2\\ m_3 m_4}}\langle m_1 m_2|V|m_3 m_4\rangle\{\langle a_j^\dagger a_i a_{m_1}^\dagger a_{m_2}^\dagger a_{m_3} a_{m_4}\rangle_t - \langle a_{m_1}^\dagger a_{m_2}^\dagger a_{m_3} a_{m_4} a_j^\dagger a_i\rangle_t\} \\
&- i\hbar\Psi_i(t)\frac{\partial}{\partial t}\Psi_j^*(t) - i\hbar\Psi_j^*(t)\frac{\partial}{\partial t}\Psi_i(t)\,.
\end{aligned} \tag{4.35}$$

Normal-ordering the expectation values of six operators that occur in this expression gives additional terms with an expectation value of four operators and a delta function, e.g.:

$$\langle a_j^\dagger a_i a_{m_1}^\dagger a_{m_2}^\dagger a_{m_3} a_{m_4}\rangle_t = \langle a_j^\dagger a_{m_1}^\dagger a_{m_2}^\dagger a_i a_{m_3} a_{m_4}\rangle_t + \delta_{im_2}\langle a_j^\dagger a_{m_1}^\dagger a_{m_3} a_{m_4}\rangle_t + \delta_{im_1}\langle a_j^\dagger a_{m_2}^\dagger a_{m_3} a_{m_4}\rangle_t\,. \tag{4.36}$$

After normal-ordering the expectation values in Eq. (4.35), we perform the cumulant expansion for each term. Neglecting the non-number conserving terms, which give zero for a thermal gas, leaves

$$\begin{aligned} i\hbar\frac{\partial}{\partial t}\Gamma_{ij}(t) = &\sum_{l}\Big(\langle i|H_{1\mathrm{B}}|l\rangle\Gamma_{lj}(t) - \langle l|H_{1\mathrm{B}}|j\rangle\Gamma_{il}(t)\Big) \\ &+ \sum_{m_1m_2m_3}\langle im_1|V|m_2m_3\rangle\Big(\Gamma^{(2,2)}_{m_2m_3;jm_1}(t) + \Gamma_{m_2j}(t)\Gamma_{m_3m_1}(t) + \Gamma_{m_3j}(t)\Gamma_{m_2m_1}(t)\Big) \\ &- \sum_{m_1m_2m_3}\langle m_1m_2|V|jm_3\rangle\Big(\Gamma^{(2,2)}_{m_3i;m_1m_2}(t) + \Gamma_{m_3m_1}(t)\Gamma_{im_2}(t) + \Gamma_{im_1}(t)\Gamma_{m_3m_2}(t)\Big)\,. \end{aligned} \tag{4.37}$$

Here, $\Gamma^{(2,2)}_{m_2m_3;jm_1}(t)$ is the two-body density matrix defined in Eq. (4.17).

We define the density matrices in the interaction picture by

$$\Gamma^{\mathrm{I}}_{ij}(t) = \sum_{kl}\langle i|U^{\dagger}_{1\mathrm{B}}(t-t_0)|k\rangle\Gamma_{kl}(t)\langle l|U_{1\mathrm{B}}(t-t_0)|j\rangle\,, \tag{4.38}$$

$$\begin{aligned} \Gamma^{(2,2)\mathrm{I}}_{k_4i;k_1k_2}(t) = &\sum_{\substack{r_1r_2\\r_3r_4}}\langle k_4|U^{\dagger}_{1\mathrm{B}}(t-t_0)|r_1\rangle\langle i|U^{\dagger}_{1\mathrm{B}}(t-t_0)|r_2\rangle\Gamma^{(2,2)}_{r_1r_2;r_3r_4}(t)\langle r_3|U_{1\mathrm{B}}(t-t_0)|k_1\rangle \\ &\times\langle r_4|U_{1\mathrm{B}}(t-t_0)|k_2\rangle\,. \end{aligned} \tag{4.39}$$

Here, t_0 is the (arbitrary) time at which the transformation to the interaction picture is made. In calculations, we typically set this to be equal to the initial time, t_{i}. We also note that the potential is given in the interaction picture by

$$V_{\mathrm{I}}(t) = U^{\dagger}_0(t-t_0)V(t)U_0(t-t_0)\,, \tag{4.40}$$

and the two-body evolution operator is given by

$$U^{\mathrm{I}}_{2\mathrm{B}}(t,t') = U^{\dagger}_0(t-t_0)U_{2\mathrm{B}}(t,t')U_0(t'-t_0)\,. \tag{4.41}$$

Here, $U_0(t-t_0) = \exp(-iH_0(t-t_0)/\hbar)$ is the evolution operator associated with the free Hamiltonian. Differentiating Eq. (4.38) and using Eq. (4.37) gives the dynamical equation for the one-body density matrix in the interaction picture:

$$\begin{aligned} i\hbar\frac{\partial}{\partial t}\Gamma^{\mathrm{I}}_{ij}(t) = &\sum_{k_2k_3k_4}\langle ik_2|V_{\mathrm{I}}(t)|k_3k_4\rangle\Big[\Gamma^{(2,2)\mathrm{I}}_{k_3k_4;k_2j}(t) + \Gamma^{\mathrm{I}}_{k_3k_2}(t)\Gamma^{\mathrm{I}}_{k_4j}(t) + \Gamma^{\mathrm{I}}_{k_3j}(t)\Gamma^{\mathrm{I}}_{k_4k_2}(t)\Big] \\ &- \sum_{k_1k_2k_4}\langle k_1k_2|V_{\mathrm{I}}(t)|jk_4\rangle\Big[\Gamma^{(2,2)\mathrm{I}}_{k_4i;k_1k_2}(t) + \Gamma^{\mathrm{I}}_{k_4k_1}(t)\Gamma^{\mathrm{I}}_{ik_2}(t) + \Gamma^{\mathrm{I}}_{k_4k_2}(t)\Gamma^{\mathrm{I}}_{ik_1}(t)\Big]\,. \end{aligned} \tag{4.42}$$

The second order cumulant approach includes the precise evolution of one and products of two operators, and the free evolution of products of three and four operators.

Products of three operators have already been eliminated, since terms which are not number conserving do not appear for a thermal gas. We are therefore left requiring only the free evolution of $\Gamma^{(2,2)}_{m_2 m_3; j m_1}(t)$ to close the equation. In Appendix C.1 we show how this may be calculated, converted to the interaction picture, and substituted into Eq. (4.42). In this thesis, we apply the technique discussed here to the case of a homogeneous gas. In Appendix C.2, we apply the requirement of translational invariance to the one-body density matrix, taking the limit of an infinitely large box. The two-body density matrix at t_i is neglected, corresponding to the initial two-body correlations in the gas being zero. This gives the following equation:

$$\begin{aligned}
\frac{\partial}{\partial t}\Gamma(p,t) = {} & \frac{4}{\hbar}\Gamma(p,t_\mathrm{i}) \int d\mathbf{q}\Gamma(q,t_\mathrm{i})\mathrm{Im}\left[\langle \mathbf{q}_\mathrm{r}|V_\mathrm{I}(t)U^\mathrm{I}_{2\mathrm{B}}(t,t_\mathrm{i})|\mathbf{q}_\mathrm{r}\rangle\right] \\
& + \frac{4}{\hbar}\int d\mathbf{p}_1 d\mathbf{p}_2 \Gamma(p_1,t_\mathrm{i})\Gamma(p_2,t_\mathrm{i}) \\
& \times \mathrm{Im}[\langle \mathbf{p}_\mathrm{cm}|V_\mathrm{I}(t)U^\mathrm{I}_{2\mathrm{B}}(t,t_\mathrm{i})|\mathbf{p}_\mathrm{r}\rangle\langle \mathbf{p}_\mathrm{r}|[U^\mathrm{I}_{2\mathrm{B}}(t,t_\mathrm{i})-1]^\dagger|\mathbf{p}_\mathrm{cm}\rangle] \\
& + \frac{4}{\hbar}\int_{t_\mathrm{i}}^{t} dt' \int d\mathbf{q}\mathrm{Im}\left[\langle \mathbf{q}_\mathrm{r}|V_\mathrm{I}(t)U^\mathrm{I}_{2\mathrm{B}}(t,t')|\mathbf{q}_\mathrm{r}\rangle\right]\frac{\partial}{\partial t'}\left(\Gamma(p,t')\Gamma(q,t')\right) \\
& + \frac{4}{\hbar}\int_{t_\mathrm{i}}^{t} dt' \int d\mathbf{p}_1 d\mathbf{p}_2 \mathrm{Im}[\langle \mathbf{p}_\mathrm{cm}|V_\mathrm{I}(t)U^\mathrm{I}_{2\mathrm{B}}(t,t')|\mathbf{p}_\mathrm{r}\rangle\langle \mathbf{p}_\mathrm{r}|[U^\mathrm{I}_{2\mathrm{B}}(t,t')-1]^\dagger|\mathbf{p}_\mathrm{cm}\rangle] \\
& \times \frac{\partial}{\partial t'}\left(\Gamma(p_1,t')\Gamma(p_2,t')\right) . \qquad (4.43)
\end{aligned}$$

We refer to this as the non-Markovian Boltzmann equation. Here, we have made the definitions $\mathbf{q}_\mathrm{r} = (\mathbf{p}-\mathbf{q})/2$, $\mathbf{p}_\mathrm{r} = (\mathbf{p}_1-\mathbf{p}_2)/2$, and $\mathbf{p}_\mathrm{cm} = \mathbf{p}-(\mathbf{p}_1+\mathbf{p}_2)/2$. These definitions are simply for notational convenience – note that we cannot use a coordinate transformation to evaluate the integrals because the simplification gained in the matrix elements would be compensated for by the appearance of angular integrals in the density matrices. Consequently, the evaluation of the momentum integrals requires us to integrate over the relative angles between $\mathbf{p}$, $\mathbf{p}_1$ and $\mathbf{p}_2$. We discuss the evaluation of these angular integrals in Chapter 6. The reduced one-body density matrix in Eq. (4.43) is defined by

$$\Gamma(\mathbf{p},\mathbf{q},t) = \delta(\mathbf{p}-\mathbf{q})\Gamma(p,t). \qquad (4.44)$$

We note that after translational invariance is imposed, the phases given by Eq. (4.38) cancel out, and so we have $\Gamma^\mathrm{I}(p,t) = \Gamma(p,t)$. Consequently, we write it without the superscript.

The matrix element of $[U^\mathrm{I}_{2\mathrm{B}}(t,t')-1]$ that occurs in Eq. (4.43) can be rewritten using

Eq. (C.25):

$$\langle \mathbf{p}_{\rm cm}|[U^{\rm I}_{\rm 2B}(t,t')-1]|\mathbf{p}_{\rm r}\rangle = \frac{1}{i\hbar}\int_{t'}^{t} d\tau e^{i\frac{p^2_{\rm cm}}{m\hbar}(\tau-t_0)}e^{-i\frac{p^2_{\rm r}}{m\hbar}(t'-t_0)}\langle \mathbf{p}_{\rm cm}|V(\tau)U_{\rm 2B}(\tau,t')|\mathbf{p}_{\rm r}\rangle\,, \quad (4.45)$$

where we have taken out the interaction picture phases. We can then write

$$\begin{aligned}\langle \mathbf{p}_{\rm cm}|V_{\rm I}(t)U^{\rm I}_{\rm 2B}(t,t')|\mathbf{p}_{\rm r}\rangle\langle \mathbf{p}_{\rm r}|[U^{\rm I}_{\rm 2B}(t,t')-1]^{\dagger}|\mathbf{p}_{\rm cm}\rangle &= -\frac{1}{i\hbar}\langle \mathbf{p}_{\rm cm}|V(t)U_{\rm 2B}(t,t')|\mathbf{p}_{\rm r}\rangle \\ &\times\int_{t'}^{t} d\tau e^{i\frac{p^2_{\rm cm}}{m\hbar}(t-\tau)}\langle \mathbf{p}_{\rm r}|U^{\dagger}_{\rm 2B}(\tau,t')V(\tau)|\mathbf{p}_{\rm cm}\rangle\,.\end{aligned} \quad (4.46)$$

The matrix element outside the integral is the conjugate of the derivative of the integral itself with respect to t. The imaginary part of this can be expressed as

$$\begin{aligned}&2{\rm Im}\left\{\langle \mathbf{p}_{\rm cm}|V_{\rm I}(t)U^{\rm I}_{\rm 2B}(t,t')|\mathbf{p}_{\rm r}\rangle\langle \mathbf{p}_{\rm r}|[U^{\rm I}_{\rm 2B}(t,t')-1]^{\dagger}|\mathbf{p}_{\rm cm}\rangle\right\} \\ &\quad=\frac{1}{\hbar}\frac{\partial}{\partial t}\left|\int_{t'}^{t} d\tau e^{i\frac{p^2_{\rm cm}}{m\hbar}(\tau-t')}\langle \mathbf{p}_{\rm cm}|V(\tau)U_{\rm 2B}(\tau,t')|\mathbf{p}_{\rm r}\rangle\right|^2\,.\end{aligned} \quad (4.47)$$

Using the form of the separable potential in Eq. (2.61), we see that this term may be calculated from the Fourier transform of the matrix element $\langle\chi|U_{\rm 2B}(t,t')|\mathbf{p}_{\rm r}\rangle$. Substituting Eq. (4.47) into Eq. (4.43) gives

$$\begin{aligned}\frac{\partial}{\partial t}\Gamma^{\rm I}(p,t) &= \frac{4}{\hbar}\Gamma(p,t_{\rm i})\int d\mathbf{q}\Gamma(q,t_{\rm i}){\rm Im}\left[\langle \mathbf{q}_{\rm r}|V_{\rm I}(t)U^{\rm I}_{\rm 2B}(t,t_{\rm i})|\mathbf{q}_{\rm r}\rangle\right] \\ &+2\int d\mathbf{p}_1 d\mathbf{p}_2\Gamma(p_1,t_{\rm i})\Gamma(p_2,t_{\rm i})\frac{\partial}{\partial t}\left|\frac{1}{\hbar}\int_{t_{\rm i}}^{t} d\tau e^{i\frac{p^2_{\rm cm}}{m\hbar}(\tau-t_{\rm i})}\langle \mathbf{p}_{\rm cm}|V(\tau)U_{\rm 2B}(\tau,t_{\rm i})|\mathbf{p}_{\rm r}\rangle\right|^2 \\ &+\frac{4}{\hbar}\int_{t_{\rm i}}^{t} dt'\int d\mathbf{q}{\rm Im}\left[\langle \mathbf{q}_{\rm r}|V_{\rm I}(t)U^{\rm I}_{\rm 2B}(t,t')|\mathbf{q}_{\rm r}\rangle\right]\frac{\partial}{\partial t'}\left(\Gamma(p,t')\Gamma(q,t')\right) \\ &+2\int_{t_{\rm i}}^{t} dt'\int d\mathbf{p}_1 d\mathbf{p}_2\frac{\partial}{\partial t}\left|\frac{1}{\hbar}\int_{t'}^{t} d\tau e^{i\frac{p^2_{\rm cm}}{m\hbar}(\tau-t')}\langle \mathbf{p}_{\rm cm}|V(\tau)U_{\rm 2B}(\tau,t')|\mathbf{p}_{\rm r}\rangle\right|^2 \\ &\times\frac{\partial}{\partial t'}\left(\Gamma(p_1,t')\Gamma(p_2,t')\right)\,.\end{aligned} \quad (4.48)$$

We refer to the terms with two momentum integrals as the cross-section terms, and those with one momentum integral as the imaginary terms. The cross-section terms represent the coupling into the element of momentum space surrounding $\mathbf{p}$. The imaginary terms correspond to the total coupling out of the same element. Equation (4.48) is the form in which we implement the solution of the non-Markovian Boltzmann equation, which we discuss in Chapter 6. In the Sec. 4.7, we show how this equation reduces to the normal Boltzmann equation in the Markov limit for the interactions, and the limit of long times.

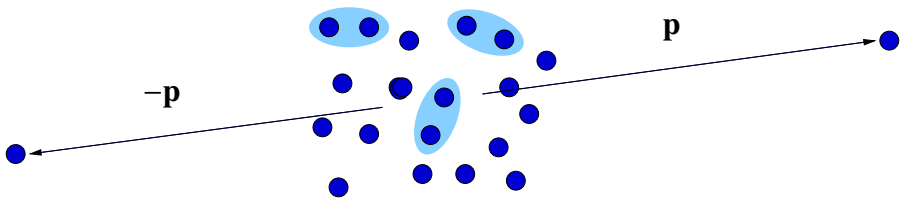

Figure 4.2: Schematic of the production of molecules from a BEC, which also results in the production of a burst fraction of atoms in noncondensate modes.

4.5 Production of molecules from pure condensates

In this section we show from first principles how the evolution of the mean field given by Eq. (4.30) can be used to calculate the number of Feshbach molecules formed from a condensed Bose gas by magnetic field variation. We have sketched the result of a magnetic field pulse in Fig. 4.2. As well as producing molecules, the pulse excites pairs of atoms into the continuum of noncondensate modes, which we discuss in Sec. 4.5.1.

We consider a bosonic gas in a box of volume $\mathcal{V}$. For a pair of atoms, the quantum mechanical observable for the bound state $\phi_{\rm b}(\mathbf{r})$, where $\mathbf{r}$ is the relative position coordinate, is

$$\theta = \int d\mathbf{R} |\phi_{\rm b}, \mathbf{R}\rangle\langle\phi_{\rm b}, \mathbf{R}| \,, \tag{4.49}$$

where $\mathbf{R}$ is the centre of mass coordinate. To find the second-quantised operator we expand this in terms of the box states $|\mathbf{k}\rangle$, satisfying $\langle\mathbf{x}|\mathbf{k}\rangle = e^{i\mathbf{k}\cdot\mathbf{x}}/\sqrt{\mathcal{V}}$. This gives

$$\begin{aligned}\langle\mathbf{k}_1\mathbf{k}_2|\theta|\mathbf{k}_3\mathbf{k}_4\rangle = \frac{1}{\mathcal{V}}\sum_{\alpha\beta\alpha'\beta'}\int d\mathbf{r}_1 \int d\mathbf{r}_2\, \delta(\mathbf{k}_1+\mathbf{k}_2-\mathbf{k}_3-\mathbf{k}_4)\langle\mathbf{r}_1,\alpha\beta|\phi_{\rm b}\rangle\langle\phi_{\rm b}|\mathbf{r}_2,\alpha'\beta'\rangle \\ \times \exp\left(-\frac{i}{2}\mathbf{r}_1\cdot(\mathbf{k}_1-\mathbf{k}_2)\right)\exp\left(\frac{i}{2}\mathbf{r}_2\cdot(\mathbf{k}_3-\mathbf{k}_4)\right) .\end{aligned} \tag{4.50}$$

Here, the Greek subscripts refer to the different Zeeman states of the atoms. We use the Fourier transform $\langle\mathbf{k}|\phi_{\rm b}\rangle = \frac{1}{\sqrt{\mathcal{V}}}\int d\mathbf{r} e^{-i\mathbf{k}\cdot\mathbf{r}}\langle\mathbf{r}|\phi_{\rm b}\rangle$ to write this as

$$\langle\mathbf{k}_1\mathbf{k}_2|\theta|\mathbf{k}_3\mathbf{k}_4\rangle = \sum_{\alpha\beta\alpha'\beta'}\delta(\mathbf{k}_1+\mathbf{k}_2-\mathbf{k}_3-\mathbf{k}_4)\langle(\mathbf{k}_1-\mathbf{k}_2)/2,\alpha\beta|\phi_{\rm b}\rangle\langle\phi_{\rm b}|(\mathbf{k}_3-\mathbf{k}_4)/2,\alpha'\beta'\rangle\,. \tag{4.51}$$

The second-quantised operator is then given by

$$\begin{aligned}N_{\rm mol} = \frac{1}{2}\sum_{\mathbf{k}_1\mathbf{k}_2\mathbf{k}_3\mathbf{k}_4}\sum_{\alpha\beta\alpha'\beta'}\delta(\mathbf{k}_1+\mathbf{k}_2-\mathbf{k}_3-\mathbf{k}_4)\langle(\mathbf{k}_1-\mathbf{k}_2)/2,\alpha\beta|\phi_{\rm b}\rangle\langle\phi_{\rm b}|(\mathbf{k}_3-\mathbf{k}_4)/2,\alpha'\beta'\rangle \\ \times a^\dagger_{\mathbf{k}_1\alpha}a^\dagger_{\mathbf{k}_2\beta}a_{\mathbf{k}_3\alpha'}a_{\mathbf{k}_4\beta'}\,,\end{aligned} \tag{4.52}$$

where the bosonic field operators are defined in Eqs. (4.6)-(4.7), and the factor of $1/2$ prevents double counting of pairs. Consequently, the expectation value of $N_{\rm mol}$ at time t, $\langle N_{\rm mol}\rangle_t$, can be found by calculating $\langle a^\dagger_{\mathbf{k}_1\alpha} a^\dagger_{\mathbf{k}_2\beta} a_{\mathbf{k}_3\alpha'} a_{\mathbf{k}_4\beta'}\rangle_t$. Converting this to position space, the number of molecules at time t is given by

$$\langle N_{\rm mol}\rangle_t = \frac{1}{2}\sum_{\alpha\beta\alpha'\beta'}\int d\mathbf{R}d\mathbf{r}d\mathbf{r}'\phi_{\rm b}^{\alpha\beta}(\mathbf{r})[\phi_{\rm b}^{\alpha'\beta'}(\mathbf{r}')]^*\langle\psi^\dagger_\alpha(\mathbf{x})\psi^\dagger_\beta(\mathbf{y})\psi_{\beta'}(\mathbf{y}')\psi_{\alpha'}(\mathbf{x}')\rangle_t\,. \tag{4.53}$$

Here, $\mathbf{R} = (\mathbf{x}+\mathbf{y})/2$, $\mathbf{r} = \mathbf{x}-\mathbf{y}$, and $\mathbf{r}' = \mathbf{x}'-\mathbf{y}'$.

Provided the gas is not too far from equilibrium, we are able to use Wick's theorem [220] to calculate the expectation value in Eq. (4.53). This leads to

$$\langle\psi^\dagger_\alpha(\mathbf{x})\psi^\dagger_\beta(\mathbf{y})\psi_{\beta'}(\mathbf{y}')\psi_{\alpha'}(\mathbf{x}')\rangle_t = \langle\psi^\dagger_\alpha(\mathbf{x})\psi^\dagger_\beta(\mathbf{y})\rangle_t\langle\psi_{\beta'}(\mathbf{y}')\psi_{\alpha'}(\mathbf{x}')\rangle_t\,. \tag{4.54}$$

Here, we have neglected the products of one-body density matrices, as in Sec. 4.3. Summing over spins, we can then write $\langle N_{\rm mol}\rangle_t = \int d\mathbf{R}|\Psi_{\rm b}(\mathbf{R},t)|^2$, where the mean field is given by

$$\Psi_{\rm b}(\mathbf{R},t) = \frac{1}{\sqrt{2}}\int d\mathbf{r}\phi^*_{\rm b}(\mathbf{r})\big[\Phi(\mathbf{R},\mathbf{r},t) + \Psi(\mathbf{R}+\mathbf{r}/2,t)\Psi(\mathbf{R}-\mathbf{r}/2,t)\big]\,. \tag{4.55}$$

Using the solution to the pair function evolution of Eq. (4.26) gives

$$\Psi_{\rm b}(\mathbf{R},t) = -\frac{(2\pi\hbar)^{3/2}}{\sqrt{2}}\int d\mathbf{r}\phi^*_{\rm b}(\mathbf{r})\int_{t_{\rm i}}^t d\tau\Psi^2(\mathbf{R},\tau)\frac{\partial}{\partial\tau}[\theta(t-\tau)\langle\mathbf{r}|U_{\rm 2B}(t,\tau)|0\rangle]\,. \tag{4.56}$$

Reversing the order of integration then gives, for a homogeneous gas,

$$\Psi_{\rm b}(t) = -\frac{1}{\sqrt{2}}\int_{t_{\rm i}}^t d\tau\Psi^2(\tau)\frac{\partial}{\partial\tau}h_{\rm b}(t,\tau)\,, \tag{4.57}$$

where the bound state coupling function is given by

$$h_{\rm b}(t,\tau) = (2\pi\hbar)^{3/2}\langle\phi_{\rm b}|U_{\rm 2B}(t,\tau)|0\rangle\theta(t-\tau)\,. \tag{4.58}$$

The bound state coupling function is calculated in an analogous manner to $h(t,\tau)$, by projecting Eq. (4.32) onto $\langle\phi_{\rm b}|$ on the left and $|\chi\rangle$ on the right. This gives a closed equation for $\langle\phi_{\rm b}|U_{\rm 2B}(t,\tau)|\chi\rangle$, which may then used to calculate $\langle\phi_{\rm b}|U_{\rm 2B}(t,\tau)|0\rangle$ in the same manner as Eq. (4.34) for $\langle\chi|U_{\rm 2B}(t,\tau)|0\rangle$.

4.5.1 Continuum fraction

The density of atom pairs with relative momentum **p** is calculated in an analogous manner to the bound state component, with an integral over all momenta giving the total continuum fraction. The continuum mode of a pair of atoms of relative momentum **p** has an amplitude at time t given by

$$\Psi_{\mathbf{p}}(t) = \frac{-1}{\sqrt{2}} \int_{t_\mathrm{i}}^{t} d\tau \Psi^2(\tau) \frac{\partial}{\partial \tau} h_p(t,\tau)\,, \tag{4.59}$$

where

$$h_p(t,\tau) = (2\pi\hbar)^3 \langle \phi_{\mathbf{p}}^{(+)} | U_{2\mathrm{B}}(t,\tau)|0\rangle\,. \tag{4.60}$$

The continuum coupling function $h_{\mathbf{p}}(t,\tau)$ may be calculated from Eq. (4.33):

$$\langle \phi_{\mathbf{p}}^{(+)} | U_{2\mathrm{B}}(t,\tau)|0\rangle = \langle \phi_{\mathbf{p}}^{(+)}|0\rangle + \frac{1}{i\hbar}\int_{\tau}^{t} d\tau' \langle \phi_{\mathbf{p}}^{(+)} | U_0(t-\tau')V(\tau')U_{2\mathrm{B}}(\tau',\tau)|0\rangle\,. \tag{4.61}$$

We drop the constant term, which corresponds to the approximation that there is no overlap between a burst pair of atoms and the condensate. We can then write $h_{\mathbf{p}}(t,\tau)$ in terms of $h(t,\tau)$ as

$$h_{\mathbf{p}}(t,\tau) = \int_{\tau}^{t} d\tau' \frac{\langle \phi_{\mathbf{p}}^{(+)} | G_0(t-\tau')|\chi\rangle h(\tau',\tau)}{\langle 0|\chi\rangle}\,. \tag{4.62}$$

4.6 Production of molecules from thermal gases

In this section we show how the one-body density matrix may be used to calculate the number of molecules formed from a thermal Bose gas by magnetic field variation. For a non-condensed gas, the expectation value in Eq. (4.52) may be expressed in terms of cumulants using the definitions of Eqs. (4.11) - (4.13):

$$\langle a^\dagger_{\mathbf{k}_1\alpha} a^\dagger_{\mathbf{k}_2\beta} a_{\mathbf{k}_3\alpha'} a_{\mathbf{k}_4\beta'}\rangle_t = \Gamma^{(2,2)}_{\mathbf{k}_3\alpha'\mathbf{k}_4\beta';\mathbf{k}_1\alpha\mathbf{k}_2\beta}(t) + \Gamma^{\beta'\alpha}_{\mathbf{k}_4\mathbf{k}_1}(t)\Gamma^{\alpha'\beta}_{\mathbf{k}_3\mathbf{k}_2}(t) + \Gamma^{\beta'\beta}_{\mathbf{k}_4\mathbf{k}_2}(t)\Gamma^{\alpha'\alpha}_{\mathbf{k}_3\mathbf{k}_1}(t)\,. \tag{4.63}$$

The second order cumulant approach includes the free evolution of the two-body density matrix, $\Gamma^{(2,2)}_{\mathbf{k}_3\alpha'\mathbf{k}_4\beta';\mathbf{k}_1\alpha\mathbf{k}_2\beta}(t)$, which we derive in Appendix C.1. We make the approximation that $\Gamma^{(2,2)}_{\mathbf{k}_3\alpha'\mathbf{k}_4\beta';\mathbf{k}_1\alpha\mathbf{k}_2\beta}(t_\mathrm{i}) = 0$, i.e. that there are initially no two-body correlations in the gas. Substituting the result of Eq. (C.6) into the above equation, we next take the

homogeneous gas limit. The box states are then transformed to plane waves, according to

$$|\mathbf{k}\rangle \to \sqrt{\frac{(2\pi\hbar)^3}{\mathcal{V}}}|\mathbf{p}\rangle\,, \tag{4.64}$$

where $\mathbf{p} = \hbar\mathbf{k}$. The one-body density matrix takes the form

$$\Gamma^{\alpha\alpha'}_{k_3k_1}(t) \to \Gamma^{\alpha\alpha'}(|(\mathbf{p}_1+\mathbf{p}_3)/2|,t)\delta(\mathbf{p}_1-\mathbf{p}_3)\,. \tag{4.65}$$

Here, we have defined the reduced one-body density matrix, derived in Appendix C.2, to have a normalisation of $\int d\mathbf{p}\Gamma(p,t) = (2\pi\hbar)^3 n$, where n is the density of the gas. Using these results, the expectation value of the molecular number operator becomes

$$\begin{aligned}
\langle N_{\mathrm{mol}}\rangle_t = \frac{\mathcal{V}}{(2\pi\hbar)^3}\sum_{\alpha\beta\alpha'\beta'}\sum_{\alpha_1\beta_1,\alpha_1'\beta_1'}\int d\mathbf{p}_1 d\mathbf{p}_2 d\mathbf{p}_3 d\mathbf{q}\langle(\mathbf{p}_1-\mathbf{p}_2)/2,\alpha\beta|\phi_{\mathrm{b}}\rangle \\
\times\langle\phi_{\mathrm{b}}|\mathbf{p}_3-(\mathbf{p}_1+\mathbf{p}_2)/2,\alpha'\beta'\rangle\Gamma^{\alpha_1\alpha_1'}(|\mathbf{p}_1+\mathbf{p}_2-\mathbf{q}|,t_{\mathrm{i}})\Gamma^{\beta_1\beta_1'}(q,t_{\mathrm{i}}) \\
\times\langle\mathbf{p}_3-(\mathbf{p}_1+\mathbf{p}_2)/2,\alpha'\beta'|U^{\mathrm{I}}_{2\mathrm{B}}(t,t_{\mathrm{i}})|(\mathbf{p}_1+\mathbf{p}_2)/2-\mathbf{q},\alpha_1\beta_1\rangle \\
\times\langle(\mathbf{p}_1+\mathbf{p}_2)/2-\mathbf{q},\alpha_1'\beta_1'|[U^{\mathrm{I}}_{2\mathrm{B}}(t,t_{\mathrm{i}})]^{\dagger}|(\mathbf{p}_1-\mathbf{p}_2)/2,\alpha\beta\rangle \\
+\frac{\mathcal{V}}{(2\pi\hbar)^3}\sum_{\alpha\beta\alpha'\beta'}\sum_{\alpha_1\beta_1,\alpha_1'\beta_1'}\int d\mathbf{p}_1 d\mathbf{p}_2 d\mathbf{p}_3 d\mathbf{q}\int_{t_{\mathrm{i}}}^{t}dt'\langle\phi_{\mathrm{b}}|\mathbf{p}_3-(\mathbf{p}_1+\mathbf{p}_2)/2,\alpha'\beta'\rangle \\
\times\langle\mathbf{p}_3-(\mathbf{p}_1+\mathbf{p}_2)/2,\alpha'\beta'|U^{\mathrm{I}}_{2\mathrm{B}}(t,t')|(\mathbf{p}_1+\mathbf{p}_2)/2-\mathbf{q},\alpha_1\beta_1\rangle \\
\times\langle(\mathbf{p}_1+\mathbf{p}_2)/2-\mathbf{q},\alpha_1'\beta_1'|[U^{\mathrm{I}}_{2\mathrm{B}}(t,t')]^{\dagger}|(\mathbf{p}_1-\mathbf{p}_2)/2,\alpha\beta\rangle\langle(\mathbf{p}_1-\mathbf{p}_2)/2,\alpha\beta|\phi_{\mathrm{b}}\rangle \\
\times\frac{\partial}{\partial t'}\left(\Gamma^{\alpha_1\alpha_1'}(|\mathbf{p}_1+\mathbf{p}_2-\mathbf{q}|,t')\Gamma^{\beta_1\beta_1'}(q,t')\right)\,.
\end{aligned} \tag{4.66}$$

Evaluating the sum over spins and changing variables, this reduces to

$$\begin{aligned}
n_{\mathrm{mol}} = \frac{1}{(2\pi\hbar)^3}\int d\mathbf{p}_1 d\mathbf{p}_2\Gamma(p_1,t_{\mathrm{i}})\Gamma(p_2,t_{\mathrm{i}})|\langle\phi_{\mathrm{b}}|U_{2\mathrm{B}}(t,t_{\mathrm{i}})|(\mathbf{p}_1-\mathbf{p}_2)/2\rangle|^2 \\
+\frac{1}{(2\pi\hbar)^3}\int d\mathbf{p}_1 d\mathbf{p}_2\int_{t_{\mathrm{i}}}^{t}dt'|\langle\phi_{\mathrm{b}}|U_{2\mathrm{B}}(t,t')|(\mathbf{p}_1-\mathbf{p}_2)/2\rangle|^2\frac{\partial}{\partial t'}\left(\Gamma(p_1,t')\Gamma(p_2,t')\right)\,.
\end{aligned} \tag{4.67}$$

Here, n_{mol} is the density of molecules. This shows that, for a thermal gas, knowing the one-body density matrix for all times during a magnetic field variation sequence is sufficient for calculating the molecular production efficiency. In Chapter 6 we solve the non-Markovian Boltzmann equation of Sec. 4.4 and use the results to study the role of many-body effects in determining the molecule production efficiency.

4.6.1 Short-time limit

As can be seen from Eq. (4.52), the expectation value of N_{mol} can be found by calculating the expectation value of $a^\dagger_{\mathbf{k}_1\alpha}a^\dagger_{\mathbf{k}_2\beta}a_{\mathbf{k}_3\alpha'}a_{\mathbf{k}_4\beta'}$. At short times, the evolution of this quantity from its value at the initial time t_i is primarily due to two-body dynamics. For sufficiently small t, we can therefore make the approximation

$$\langle a^\dagger_{\mathbf{k}_1\alpha}a^\dagger_{\mathbf{k}_2\beta}a_{\mathbf{k}_3\alpha'}a_{\mathbf{k}_4\beta'}\rangle_t \approx \sum_{\mathbf{k}_5\mathbf{k}_6\mathbf{k}_7\mathbf{k}_8}\sum_{\alpha_1\beta_1,\alpha'_1\beta'_1}\langle \mathbf{k}_3\mathbf{k}_4,\alpha'\beta'|U_{2\mathrm{B}}(t,t_\mathrm{i})|\mathbf{k}_5\mathbf{k}_6,\alpha_1\beta_1\rangle \times \langle a^\dagger_{\mathbf{k}_5\alpha_1}a^\dagger_{\mathbf{k}_6\beta_1}a_{\mathbf{k}_7\alpha'_1}a_{\mathbf{k}_8\beta'_1}\rangle_{t_\mathrm{i}}\langle \mathbf{k}_7\mathbf{k}_8,\alpha'_1\beta'_1|U^\dagger_{2\mathrm{B}}(t,t_\mathrm{i})|\mathbf{k}_1\mathbf{k}_2,\alpha\beta\rangle\,. \tag{4.68}$$

Assuming the gas to be close to the non-interacting equilibrium before the magnetic field variation, we can use Wick's theorem to decompose the expectation value into products of the expectation values of two operators. Taking the homogeneous limit and evaluating the sum over spins then gives the following formula for the molecule production efficiency:

$$n_{\mathrm{mol}} = \frac{1}{(2\pi\hbar)^3}\int d\mathbf{p}d\mathbf{q}|\langle\phi_\mathrm{b}|U_{2\mathrm{B}}(t,t_\mathrm{i})|\phi_\mathbf{p}\rangle|^2\Gamma(|\mathbf{p}+\mathbf{q}/2|,t_\mathrm{i})\Gamma(|\mathbf{p}-\mathbf{q}/2|,t_\mathrm{i})\,. \tag{4.69}$$

Here, we have used the interacting scattering state $|\phi_\mathbf{p}\rangle$ rather than the plane wave $|\mathbf{p}\rangle$. This is to account for the interactions that, in reality, occur before the start of the magnetic field variation. Plane waves correspond to the case of an ideal gas. The molecular and scattering state wavefunctions are evaluated at the final and initial magnetic fields, respectively. The difference in the molecule production efficiencies predicted by the scattering states and plane waves are only significant for fields sufficiently close to the resonance, and for sufficiently short times. For $t = t_\mathrm{i}$, the result should be zero. This is reproduced by using the scattering state transition amplitudes, as the scattering and bound states are orthogonal, however this is not the case for plane waves. For far off-resonant fields, or if the magnetic field variation is long enough for correlations to build up, the results are not significantly different. This is shown for the example of a linear ramp across the 155 G resonance of ^{85}Rb in Fig. 4.3. Holding the ramp rate constant, the difference between the two results reduces as the initial field is taken further from resonance. We note that Eq. (4.69) is equivalent to the first line of Eq. (4.67). The correction given by the many-body approach is represented by the second line of Eq. (4.67), which in the limit of short times or small depletions becomes small. Consequently, the many-body approach reduces to the two-body approach in these limits.

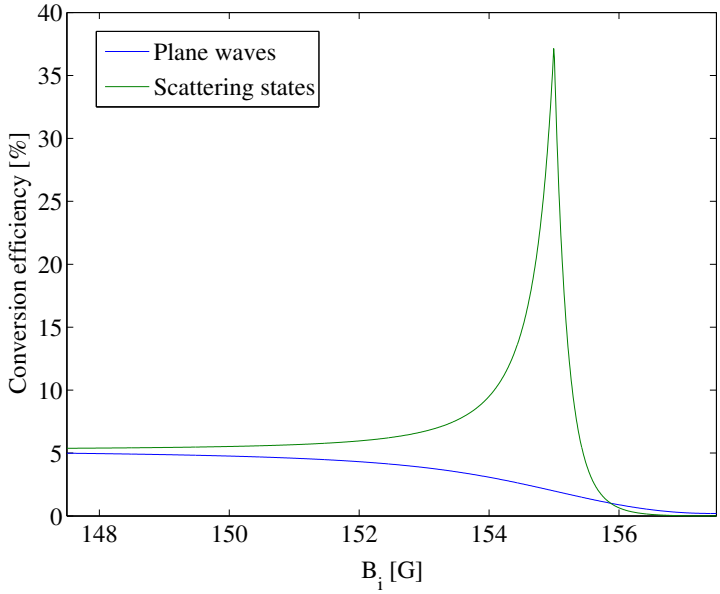

Figure 4.3: Conversion efficiency from a thermal gas of ^{85}Rb after 50 G/ms ramp across the 155 G resonance ending at $B_\mathrm{f} = 157.5$ G, as a function of the initial magnetic field B_i. Here, the single-channel approach of Sec. 2.3 is used, and the temperature and density of the gas are given by $T = 20$ nK and $n = 10^{11}\,\mathrm{cm}^{-3}$. Both lines are obtained using the thermal average of Eq. (4.76), however the plane wave result substitutes the plane wave $|\mathbf{p}\rangle$ for the scattering state $|\phi_\mathbf{p}^{(+)}\rangle$ in Eq. (4.79). For initial fields close to the resonance, the two-body correlations contained in the interacting scattering states significantly increase the prediction from the result obtained by assuming a non-interacting gas, as in the plane wave result. As the initial field is taken further from resonance, the initial correlations become less significant, and the two predictions converge.

At thermal equilibrium, the average total number of particles in a box, $\langle N\rangle$, is given in the grand canonical ensemble by

$$\langle N\rangle = \sum_\mathbf{k}\langle N_\mathbf{k}\rangle\,, \tag{4.70}$$

where the average number of particles of momentum $\hbar\mathbf{k}$ is given by the Bose-Einstein distribution, $\langle N_\mathbf{k}\rangle = \left(\exp\left[\beta\left(\frac{(\hbar k)^2}{2m}-\mu\right)\right]-1\right)^{-1}$, where $\beta = (k_\mathrm{B}T)^{-1}$ and the chemical potential μ ensures that Eq. (4.70) is satisfied. In the homogeneous limit, the one-body density matrix at the initial time is given by

$$\Gamma(p,t_\mathrm{i}) = \frac{1}{\exp\left[\beta\left(\frac{p^2}{2m}-\mu\right)\right]-1}\,, \tag{4.71}$$

which gives the required normalisation of $(2\pi\hbar)^3 n$, where n is the density of atoms. Substituting this into Eq. (4.69) gives

$$n_\mathrm{mol} = \int d\mathbf{p}|\langle\phi_\mathrm{b}|U_\mathrm{2B}(t,t_\mathrm{i})|\phi_\mathbf{p}\rangle|^2 f(p)\,. \tag{4.72}$$

Here, the function $f(p)$ is found by evaluating the integral over the angle θ between $\mathbf{p}$ and $\mathbf{q}$, and the integral over q:

$$f(p) = \frac{2\pi}{(2\pi\hbar)^3}\int_0^\infty dqq^2\int_0^\pi d\theta\sin\theta\frac{1}{\left(\exp\left[\beta\left(\frac{|\mathbf{p}+\mathbf{q}/2|^2}{2m}-\mu\right)\right]-1\right)\left(\exp\left[\beta\left(\frac{|\mathbf{p}-\mathbf{q}/2|^2}{2m}-\mu\right)\right]-1\right)}. \tag{4.73}$$

In the limit of high temperatures, the Bose-Einstein distribution reduces to the classical Maxwell-Boltzmann distribution. In the homogeneous limit we consider here, this gives the following result for the density matrices at the initial time:

$$\Gamma(p,t_\mathrm{i}) = (2\pi\hbar)^3 n\frac{\exp\left(-\beta\frac{p^2}{2m}\right)}{\left(\frac{2\pi m}{\beta}\right)^{3/2}}. \tag{4.74}$$

Substituting this into Eq. (4.69) gives

$$n_\mathrm{mol} = (2\pi\hbar)^3 n^2\left(\frac{\beta}{\pi m}\right)^{3/2}\int d\mathbf{p}|\langle\phi_\mathrm{b}|U_\mathrm{2B}(t,t_\mathrm{i})|\phi_\mathbf{p}\rangle|^2\exp\left(-\beta\frac{p^2}{m}\right). \tag{4.75}$$

The final fraction of atoms converted to molecules can then be written in the form

$$\frac{2N_\mathrm{mol}}{N} = 2n(2\pi\hbar)^3\left(\frac{\beta}{\pi m}\right)^{3/2}\int d\mathbf{p}\exp\left(-\beta\frac{p^2}{m}\right)\rho(p,t) \tag{4.76}$$

$$= 4\sqrt{2}\bar{\omega}\int d\mathbf{p}\exp\left(-\beta\frac{p^2}{m}\right)\rho(p,t). \tag{4.77}$$

In Eq. (4.77), we have written the molecule production efficiency in terms of the phase space density of the initial gas, $\bar{\omega} = n\lambda_\mathrm{T}^3$, where λ_T is the thermal de Broglie wavelength. The transition probability density between a pair of atoms of relative momentum $\mathbf{p}$ and the Feshbach molecule is given by

$$\rho(p,t) = |T(p,t)|^2 . \tag{4.78}$$

Here,

$$T(p,t) = \langle\phi_\mathrm{b}|U_\mathrm{2B}(t,t_\mathrm{i})|\phi_\mathbf{p}\rangle \tag{4.79}$$

is the transition amplitude, analogous to that given in Eq. (3.4) for a dissociation sweep. The transition amplitude for association given in Eq. (4.79) corresponds to the overlap of the wavefunction of a pair of atoms initially in the state $\phi_\mathbf{p}$ with the Feshbach molecular state, after the magnetic field variation. Consequently, Eq. (4.76) may be interpreted as the weighted average of the transition probability density, where the weighting is given by the population of pairs of each momentum in a thermal gas.

4.7 Derivation of the Markovian Boltzmann equation from the theory of cumulants

In this section we show that the non-Markovian Boltzmann equation of Eq. (4.48) reduces to the normal Boltzmann equation in the limit of long times and Markovian interactions, in which the interactions are assumed to happen on a timescale much faster than any other that is relevant. This establishes the relation between our approach and conventional kinetic theory. Returning to the general form of the equation in Eq. (C.8), we neglect the correlations in the gas at the initial time. This leaves

$$i\hbar\frac{\partial}{\partial t}\Gamma^{\mathrm{I}}_{ij}(t) = \sum_{k_1k_2l_1l_2}\int_{t_\mathrm{i}}^{\infty} dt' \left[\Gamma^{\mathrm{I}}_{k_1l_1}(t')\Gamma^{\mathrm{I}}_{k_2l_2}(t') + \Gamma^{\mathrm{I}}_{k_2l_1}(t')\Gamma^{\mathrm{I}}_{k_1l_2}(t')\right]\mathcal{K}^{k_1k_2l_1l_2}_{\mathrm{I},ij}(t,t')\,, \tag{4.80}$$

where $\mathcal{K}^{k_1k_2l_1l_2}_{\mathrm{I},ij}(t,t')$ is the kernel of the non-Markovian Boltzmann equation, given by Eq. (C.9). We assume that the one-body density matrix varies much more slowly than the kernel, which we assume to be peaked around $t' = t$. Consequently, we can make the Markov approximation, evaluating the one-body density matrices on the right side of Eq. (4.80) at time t. This leaves the kernel as the only quantity inside the integral over t'. Evaluating this integral then gives

$$\begin{aligned}\int_{t_\mathrm{i}}^{\infty} dt'\mathcal{K}^{k_1k_2l_1l_2}_{\mathrm{I},ij}(t,t') = \sum_l \Big[&\langle il|V_\mathrm{I}(t)U^{\mathrm{I}}_{2\mathrm{B}}(t,t_\mathrm{i})|k_1k_2\rangle\langle l_1l_2|[U^{\mathrm{I}}_{2\mathrm{B}}(t,t_\mathrm{i})]^\dagger|jl\rangle \\ &- \langle il|U^{\mathrm{I}}_{2\mathrm{B}}(t,t_\mathrm{i})|k_1k_2\rangle\langle l_1l_2|[V_\mathrm{I}(t)U^{\mathrm{I}}_{2\mathrm{B}}(t,t_\mathrm{i})]^\dagger|jl\rangle\Big]\,.\end{aligned} \tag{4.81}$$

After converting this back to the Schrödinger picture, we take the time limit of $t \to \infty$ inside the matrix elements in Eq. (4.81), which gives the Møller operators of Eq. (2.9). Additional exponential factors containing energy terms are cancelled out by conjugate factors arising from the conversion of the one-body density matrices in Eq. (4.80) to the Schrödinger picture. Having made the Markov approximation for the one-body density matrices, and taken the limit of $t \to \infty$, we are left with

$$\begin{aligned}i\hbar\frac{\partial}{\partial t}\Gamma_{ij}(t) = (E_i - E_j)\Gamma_{ij}(t) + \sum_{k_1k_2l_1l_2}\Big\{&\left[\Gamma_{k_1l_1}(t)\Gamma_{k_2l_2}(t) + \Gamma_{k_2l_1}(t)\Gamma_{k_1l_2}(t)\right] \\ &\times\sum_l\left(\langle il|V\Omega^{(+)}|k_1l_2\rangle\langle l_1l_2|[\Omega^{(+)}]^\dagger|jl\rangle - \langle il|\Omega^{(+)}|k_1l_2\rangle\langle l_1l_2|[\Omega^{(+)}]^\dagger V|jl\rangle\right)\Big\}\,.\end{aligned} \tag{4.82}$$

Here, $\Omega^{(+)}$ is the Møller operator, defined in Eq. (2.9).

We will now show this Markovian equation to be equivalent to the normal Boltzmann equation of Eq. (4.1) by converting to the momentum representation and calculating the Wigner transform of the one-body density matrix. In the momentum basis, the above equation becomes

$$\begin{aligned} i\hbar\frac{\partial}{\partial t}\Gamma(\mathbf{p},\mathbf{q},t) = &\int d\mathbf{p}'\langle\mathbf{p}|H_{1\mathrm{B}}|\mathbf{p}'\rangle\Gamma(\mathbf{p}',\mathbf{q},t) - \int d\mathbf{q}'\langle\mathbf{q}'|H_{1\mathrm{B}}|\mathbf{q}\rangle\Gamma(\mathbf{p},\mathbf{q}',t)\,, \\ &+ \int d\mathbf{p}_1 d\mathbf{p}_2 d\mathbf{q}_1 d\mathbf{q}_2\left[\Gamma(\mathbf{p}_1,\mathbf{q}_1,t)\Gamma(\mathbf{p}_2,\mathbf{q}_2,t) + \Gamma(\mathbf{p}_2,\mathbf{q}_1,t)\Gamma(\mathbf{p}_1,\mathbf{q}_2,t)\right] \\ &\times\mathcal{K}_{\mathrm{m}}(\mathbf{p},\mathbf{q};\mathbf{p}_1,\mathbf{p}_2;\mathbf{q}_1,\mathbf{q}_2)\,. \end{aligned} \tag{4.83}$$

Here, we have written the kernel in the momentum basis as

$$\begin{aligned} &\mathcal{K}_{\mathrm{m}}(\mathbf{p},\mathbf{q};\mathbf{p}_1,\mathbf{p}_2;\mathbf{q}_1,\mathbf{q}_2) \\ &= \int d\mathbf{p}'\left\{\langle\mathbf{p}\mathbf{p}'|V\Omega^{(+)}|\mathbf{p}_1\mathbf{p}_2\rangle\langle\mathbf{q}_1\mathbf{q}_2|[\Omega^{(+)}]^\dagger|\mathbf{q}\mathbf{p}'\rangle - \langle\mathbf{p}\mathbf{p}'|\Omega^{(+)}|\mathbf{p}_1\mathbf{p}_2\rangle\langle\mathbf{q}_1\mathbf{q}_2|[V\Omega^{(+)}]^\dagger|\mathbf{q}\mathbf{p}'\rangle\right\} \\ &= \int d\mathbf{p}'\delta(\mathbf{p}+\mathbf{p}'-\mathbf{p}_1-\mathbf{p}_2)\delta(\mathbf{q}_1+\mathbf{q}_2-\mathbf{p}'-\mathbf{q}) \\ &\times\left[\left\langle\frac{\mathbf{p}-\mathbf{p}'}{2}\middle|V\middle|\frac{\mathbf{p}_1-\mathbf{p}_2}{2},+\right\rangle\left\langle\frac{\mathbf{q}_1-\mathbf{q}_2}{2},+\middle|\frac{\mathbf{q}-\mathbf{p}'}{2}\right\rangle\right. \\ &\left.-\left\langle\frac{\mathbf{p}-\mathbf{p}'}{2}\middle|\frac{\mathbf{p}_1-\mathbf{p}_2}{2},+\right\rangle\left\langle\frac{\mathbf{q}_1-\mathbf{q}_2}{2},+\middle|V\middle|\frac{\mathbf{q}-\mathbf{p}'}{2}\right\rangle\right]. \end{aligned} \tag{4.84}$$

Here, '+' indicates an outgoing scattering wave as produced by the Møller operator and defined in Eq. (2.32). We have separated out the relative and centre of mass motion, the latter of which gives the delta functions in momentum. Using Eq. (2.32), together with the identity of Eq. (2.62), we can write this as

$$\begin{aligned} \mathcal{K}_m(\mathbf{p},\mathbf{q};\mathbf{p}_1,\mathbf{p}_2;\mathbf{q}_1,\mathbf{q}_2) = &\int d\mathbf{p}'\delta(\mathbf{p}+\mathbf{p}'-\mathbf{p}_1-\mathbf{p}_2)\delta(\mathbf{q}_1+\mathbf{q}_2-\mathbf{p}'-\mathbf{q}) \\ &\times\left[t\left(\frac{\mathbf{p}-\mathbf{p}'}{2},\frac{\mathbf{p}_1-\mathbf{p}_2}{2}\right)\delta\left(\frac{\mathbf{q}_1-\mathbf{q}_2}{2}-\frac{\mathbf{q}-\mathbf{p}}{2}\right) - \delta\left(\frac{\mathbf{p}-\mathbf{p}'}{2}-\frac{\mathbf{p}_1-\mathbf{p}_2}{2}\right)t^*\left(\frac{\mathbf{q}-\mathbf{p}}{2},\frac{\mathbf{q}_1-\mathbf{q}_2}{2}\right)\right. \\ &\left.+ m\frac{t\left(\frac{\mathbf{p}-\mathbf{p}'}{2},\frac{\mathbf{p}_1-\mathbf{p}_2}{2}\right)t^*\left(\frac{\mathbf{q}-\mathbf{p}'}{2},\frac{\mathbf{q}_1-\mathbf{q}_2}{2}\right)}{\left|\frac{\mathbf{q}_1-\mathbf{q}_2}{2}\right|^2-\left|\frac{\mathbf{q}-\mathbf{p}}{2}\right|^2-i0} - m\frac{t(\frac{\mathbf{p}-\mathbf{p}'}{2},\frac{\mathbf{p}_1-\mathbf{p}_2}{2})t^*(\frac{\mathbf{q}-\mathbf{p}'}{2},\frac{\mathbf{q}_1-\mathbf{q}_2}{2})}{\left|\frac{\mathbf{p}_1-\mathbf{p}_2}{2}\right|^2-\left|\frac{\mathbf{p}-\mathbf{p}'}{2}\right|^2+i0}\right]. \end{aligned} \tag{4.85}$$

Here, we have made the definition $t(\mathbf{p},\mathbf{q}) = \langle\mathbf{p}|T(\frac{q^2}{m}+i0)|\mathbf{q}\rangle$.

The Wigner transform of the one-body density matrix, giving the joint probability amplitude for $\mathbf{r}$ and $\mathbf{p}$, is defined by the following:

$$f(\mathbf{r},\mathbf{p},t) = \int d\mathbf{q}e^{i\mathbf{q}\cdot\mathbf{r}/\hbar}\Gamma(\mathbf{p}+\mathbf{q}/2,\mathbf{p}-\mathbf{q}/2,t)\,, \tag{4.86}$$

$$\Gamma(\mathbf{p},\mathbf{q},t) = \int\frac{d\mathbf{r}}{(2\pi\hbar)^3}e^{-i(\mathbf{p}-\mathbf{q})\cdot\mathbf{r}/\hbar}f(\mathbf{r},(\mathbf{p}+\mathbf{q})/2,t)\,. \tag{4.87}$$

The Wigner function $f(\mathbf{r},\mathbf{p},t)$ has the property that integrating over one of the coordinates yields the probability density in the other, i.e. $\int d\mathbf{p} f(\mathbf{r},\mathbf{p},t) = (2\pi\hbar)^3 n(\mathbf{r},t)$, and $\int d\mathbf{r} f(\mathbf{r},\mathbf{p},t) = (2\pi\hbar)^3 n(\mathbf{p},t)$. In the following we will also need the Wigner transform of a convolution of two functions. It can be shown [156] that this is given in the gradient approximation by

$$\int d\mathbf{q} e^{i\mathbf{q}\cdot\mathbf{r}/\hbar} \int d\mathbf{q}' H(\mathbf{p}+\mathbf{q}/2,\mathbf{q}') F(\mathbf{q}',\mathbf{p}-\mathbf{q}/2) \approx h(\mathbf{r},\mathbf{p}) f(\mathbf{r},\mathbf{p}) + \frac{i\hbar}{2}\left[\nabla_{\mathbf{r}} h(\mathbf{r},\mathbf{p})\cdot\nabla_{\mathbf{p}} f(\mathbf{r},\mathbf{p}) - \nabla_{\mathbf{p}} h(\mathbf{r},\mathbf{p})\cdot\nabla_{\mathbf{r}} f(\mathbf{r},\mathbf{p})\right], \quad (4.88)$$

where h and f are the Wigner transforms of the functions H and F respectively. We also note that

$$\int d\mathbf{q} e^{i\mathbf{q}\cdot\mathbf{r}/\hbar} \int d\mathbf{q}' F(\mathbf{p}+\mathbf{q}/2,\mathbf{q}') H(\mathbf{q}',\mathbf{p}-\mathbf{q}/2) = \left[\int d\mathbf{q} e^{i\mathbf{q}\cdot\mathbf{r}/\hbar} \int d\mathbf{q}' H(\mathbf{p}+\mathbf{q}/2,\mathbf{q}') F(\mathbf{q}',\mathbf{p}-\mathbf{q}/2)\right]^*, \quad (4.89)$$

which can be seen by interchanging variables. The one body Hamiltonians in Eq. (4.83) can be written in the form

$$\langle\mathbf{p}|H_{1\mathrm{B}}|\mathbf{q}\rangle = \frac{p^2}{2m}\delta(\mathbf{p}-\mathbf{q}) + \langle\mathbf{p}|V_{\mathrm{trap}}|\mathbf{q}\rangle, \quad (4.90)$$

of which the Wigner transform is simply $h(\mathbf{r},\mathbf{p}) = \frac{p^2}{2m} + V_{\mathrm{trap}}(\mathbf{r})$. Using this, the Wigner transform of the free terms of Eq. (4.83) is

$$\int d\mathbf{q}\, e^{i\mathbf{q}\cdot\mathbf{r}/\hbar} \int d\mathbf{q}' \left[\langle\mathbf{p}+\mathbf{q}/2|H_{1\mathrm{B}}|\mathbf{q}'\rangle\Gamma(\mathbf{q}',\mathbf{p}+\mathbf{q}/2,t) - \Gamma(\mathbf{p}+\mathbf{q}/2,\mathbf{q}',t)\langle\mathbf{q}'|H_{1\mathrm{B}}|\mathbf{p}-\mathbf{q}/2\rangle\right] = -i\hbar\left[\frac{\mathbf{p}}{m}\cdot\nabla_{\mathbf{r}} f(\mathbf{r},\mathbf{p},t) - \nabla_{\mathbf{r}}\left(V_{\mathrm{trap}}(\mathbf{r})\right)\cdot\nabla_{\mathbf{p}} f(\mathbf{r},\mathbf{p},t)\right]. \quad (4.91)$$

This enables us to write Eq. (4.83) in the form of the Boltzmann equation of Eq. (4.1):

$$\frac{\partial}{\partial t} f(\mathbf{r},\mathbf{p},t) = -\frac{\mathbf{p}}{m}\cdot\nabla_{\mathbf{r}} f(\mathbf{r},\mathbf{p},t) + \left(\nabla_{\mathbf{r}} V_{\mathrm{trap}}(\mathbf{r})\right)\cdot\nabla_{\mathbf{p}} f(\mathbf{r},\mathbf{p},t) + \frac{\partial}{\partial t} f_{\mathrm{coll}}(\mathbf{r},\mathbf{p},t). \quad (4.92)$$

Here, the collision term $\frac{\partial}{\partial t} f_{\mathrm{coll}}(\mathbf{r},\mathbf{p},t)$ is given by

$$\begin{aligned}\frac{\partial}{\partial t} f_{\mathrm{coll}}(\mathbf{r},\mathbf{p},t) = \frac{1}{i\hbar}\int & d\mathbf{p}_1 d\mathbf{p}_2 d\mathbf{q}_1 d\mathbf{q}_2 d\mathbf{p}' d\mathbf{q}' e^{i\mathbf{q}'\cdot\mathbf{r}/\hbar} \\ & \times \delta\left(\mathbf{p}+\tfrac{1}{2}\mathbf{q}'+\mathbf{p}'-\mathbf{p}_1-\mathbf{p}_2\right)\delta\left(\mathbf{p}-\tfrac{1}{2}\mathbf{q}'+\mathbf{p}'-\mathbf{q}_1-\mathbf{q}_2\right) \\ & \times \left[\Gamma(\mathbf{p}_1,\mathbf{q}_1,t)\Gamma(\mathbf{p}_2,\mathbf{q}_2,t) + \Gamma(\mathbf{p}_2,\mathbf{q}_1,t)\Gamma(\mathbf{p}_1,\mathbf{q}_2,t)\right] \\ & \times \Big[t(\tfrac{1}{2}(\mathbf{p}+\tfrac{1}{2}\mathbf{q}'-\mathbf{p}'),\tfrac{1}{2}(\mathbf{p}_1-\mathbf{p}_2))\langle\tfrac{1}{2}(\mathbf{q}_1-\mathbf{q}_2),+\big|\tfrac{1}{2}(\mathbf{p}-\tfrac{1}{2}\mathbf{q}'-\mathbf{p}')\rangle \\ & - \langle\tfrac{1}{2}(\mathbf{p}+\tfrac{1}{2}\mathbf{q}'-\mathbf{p}')\big|\tfrac{1}{2}(\mathbf{p}_1-\mathbf{p}_2),+\rangle t^*(\tfrac{1}{2}(\mathbf{p}-\tfrac{1}{2}\mathbf{q}'-\mathbf{p}'),\tfrac{1}{2}(\mathbf{q}_1-\mathbf{q}_2))\Big]. \end{aligned} \quad (4.93)$$

We will now show that the collision term given here reduces to that in Eq. (4.3) in the limits of low-energy collisions and contact interactions. The integral of the second term in the last brackets of Eq. (4.93) is just the conjugate of that of the first, as can be seen by letting $\mathbf{p}_1 \leftrightarrow \mathbf{q}_1$, $\mathbf{p}_2 \leftrightarrow \mathbf{q}_2$ and $\mathbf{q}' \leftrightarrow -\mathbf{q}'$. Also, the brackets containing the one-body density matrices can be simplified by letting $\mathbf{p}_1 \leftrightarrow \mathbf{p}_2$. We use these together with the result of Eq. (4.89), then evaluate the delta functions in $\mathbf{p}'$ and $\mathbf{q}'$. Converting to relative and centre of mass coordinates, the collision term becomes

$$\begin{aligned}\frac{\partial}{\partial t}f_{\rm coll}(\mathbf{r},\mathbf{p},t) = \frac{2}{\hbar}\mathrm{Im}\Big\{ \int d\mathbf{P}'d\mathbf{p}'d\mathbf{Q}'e^{i(\mathbf{P}'-\mathbf{Q}')\cdot\mathbf{r}/\hbar}\Gamma(\tfrac{1}{2}\mathbf{P}'+\mathbf{p}',\tfrac{1}{2}(\mathbf{Q}'-\mathbf{P}')+\mathbf{p},t) \\ \times\Gamma(\tfrac{1}{2}\mathbf{P}'-\mathbf{p}',\tfrac{1}{2}(\mathbf{Q}'+\mathbf{P}')-\mathbf{p},t)\left[t(\mathbf{p},\mathbf{p}')+t(\mathbf{p},-\mathbf{p}')\right]\Big\} \qquad (4.94a) \\ + \frac{2}{\hbar}\mathrm{Im}\Big\{ \int d\mathbf{P}'d\mathbf{p}'d\mathbf{Q}'d\mathbf{q}'e^{i(\mathbf{P}'-\mathbf{Q}')\cdot\mathbf{r}/\hbar} \\ \times\Gamma(\tfrac{1}{2}\mathbf{P}'+\mathbf{p}',\tfrac{1}{2}\mathbf{Q}'+\mathbf{q}',t)\Gamma(\tfrac{1}{2}\mathbf{P}'-\mathbf{p}',\tfrac{1}{2}\mathbf{Q}'-\mathbf{q}',t) \\ \times\left[t(\mathbf{p}-\tfrac{1}{2}\mathbf{P}',\mathbf{p}')+t(\mathbf{p}+\tfrac{1}{2}\mathbf{P}',-\mathbf{p}')\right]m\frac{t^*(\mathbf{p}-\frac{1}{2}\mathbf{P}',\mathbf{q}')}{q'^2-\left|\mathbf{p}-\frac{1}{2}\mathbf{P}'\right|^2-i0}\Big\}. \qquad (4.94b)\end{aligned}$$

From this equation, we can identify the terms giving the scattering in and out of the phase-space element surrounding $(\mathbf{r},\mathbf{p})$, in analogy to Eq. (4.3). The term representing the scattering out of the phase space element is given by the integral over the centre of mass coordinates in Eq. (4.94a):

$$\int d\mathbf{P}'d\mathbf{Q}'e^{i(\mathbf{P}'-\mathbf{Q}')\cdot\mathbf{r}/\hbar}\Gamma(\tfrac{1}{2}\mathbf{P}'+\mathbf{p}',\tfrac{1}{2}(\mathbf{Q}'-\mathbf{P}')+\mathbf{p},t)\Gamma(\tfrac{1}{2}\mathbf{P}'-\mathbf{p}',\tfrac{1}{2}(\mathbf{Q}'+\mathbf{P}')-\mathbf{p},t)\,. \qquad (4.95)$$

We can write the product of one-body density matrices in terms of Wigner functions using the definition of Eq. (4.87). Assuming the Wigner functions are slowly varying in space, we can take them outside the integrals, evaluating them at $\mathbf{r}$. Equation (4.95) then becomes

$$\begin{aligned}&\int d\mathbf{P}'d\mathbf{Q}'f\left(\mathbf{r},\tfrac{1}{2}(\tfrac{1}{2}\mathbf{Q}'+\mathbf{P}'+\mathbf{p}),t\right)f\left(\mathbf{r},\tfrac{1}{2}(\tfrac{1}{2}\mathbf{Q}'+\mathbf{P}'-\mathbf{p}-\mathbf{p}'),t\right)\exp\left(i(\mathbf{P}'-\mathbf{Q}')\cdot\mathbf{r}/\hbar\right) \\ &\times\int\frac{d\mathbf{y}_1d\mathbf{y}_2}{(2\pi\hbar)^6}\exp\left(i(\tfrac{1}{2}\mathbf{Q}'-\mathbf{P}'+\mathbf{p}-\mathbf{p}')\cdot\mathbf{y}_1/\hbar\right)\exp\left(i(\mathbf{P}'+\tfrac{1}{2}\mathbf{Q}'-\mathbf{p})\cdot\mathbf{y}_2/\hbar\right) \\ &= 8f(\mathbf{r},\mathbf{p},t)f(\mathbf{r},\mathbf{p}-2\mathbf{p}',t)\,. \qquad (4.96)\end{aligned}$$

Here, the spatial integrals provide us with delta functions in momentum which we use to evaluate the momentum integrals. From Eq. (4.94b), the term representing scattering

into the phase-space element is

$$\int d\mathbf{Q}' d\mathbf{p}' e^{i(\mathbf{P}'-\mathbf{Q}')\cdot\mathbf{r}/\hbar}\Gamma(\tfrac{1}{2}\mathbf{P}'+\mathbf{p}',\tfrac{1}{2}\mathbf{Q}'+\mathbf{q},t)\Gamma(\tfrac{1}{2}\mathbf{P}'-\mathbf{p}',\tfrac{1}{2}\mathbf{Q}'-\mathbf{q}',t)$$
$$\approx f(\mathbf{r},\mathbf{p}'+\mathbf{p}+\mathbf{q}',t)f(\mathbf{r},\mathbf{p}'+\mathbf{p}-\mathbf{q}',t)\,. \tag{4.97}$$

The second line of this equation is obtained using the same process that led from Eq. (4.95) to Eq. (4.96). Substituting Eq. (4.96) and Eq. (4.97) into Eq. (4.94) and noting that the Wigner transforms are real gives

$$\begin{aligned}\frac{\partial}{\partial t}f_{\rm coll}(\mathbf{r},\mathbf{p},t) \approx \frac{16}{\hbar}\int d\mathbf{p}' f(\mathbf{r},\mathbf{p},t)f(\mathbf{r},\mathbf{p}-2\mathbf{p}',t)\mathrm{Im}\left[t(\mathbf{p},\mathbf{p}')+t(\mathbf{p},-\mathbf{p}')\right]\\ +\frac{16m}{\hbar}\int d\mathbf{p}'d\mathbf{q}' f(\mathbf{r},\mathbf{p}'+\mathbf{p}+\mathbf{q}',t)f(\mathbf{r},\mathbf{p}'+\mathbf{p}-\mathbf{q}',t)\\ \times\mathrm{Im}\left(\frac{[t(-\mathbf{p}',\mathbf{q}')+t(-\mathbf{p}',-\mathbf{q}')]t^*(-\mathbf{p}',\mathbf{q}')}{q'^2-p'^2-i0}\right).\end{aligned} \tag{4.98}$$

Finally, using the result of Eq. (C.28), the collision term in the limit of low collision energy is

$$\begin{aligned}\frac{\partial}{\partial t}f_{\rm coll}(\mathbf{r},\mathbf{p},t) = \frac{a^2}{m^2(2\pi\hbar)^3}\int d\mathbf{p}_2 d\mathbf{p}_3 d\mathbf{p}_4\delta(\mathbf{p}+\mathbf{p}_2-\mathbf{p}_3-\mathbf{p}_4)\delta\left(\frac{p^2}{m}+\frac{p_2^2}{m}-\frac{p_3^2}{m}-\frac{p_4^2}{m}\right)\\ \times\left[f(\mathbf{r},\mathbf{p}_3,t)f(\mathbf{r},\mathbf{p}_4,t)-f(\mathbf{r},\mathbf{p},t)f(\mathbf{r},\mathbf{p}_2,t)\right],\end{aligned} \tag{4.99}$$

which recovers Eq. (4.3). This shows that the second order cumulant approach correctly recovers the normal Boltzmann equation in the limit of long times and Markovian interactions, and establishes the relation between our approach and conventional kinetic theory.

Chapter 5

Association of Feshbach molecules using a resonantly modulated magnetic field

In this chapter we study the process of associating molecules from atomic gases using a magnetic field modulation that is resonant with the molecular bound state energy. We show that maximal conversion is obtained by optimising the amplitude and frequency of the modulation for the particular temperature and density of the gas. For small modulation amplitudes, resonant coupling of an unbound atom pair to a molecule occurs at a modulation frequency corresponding to the sum of the absolute value of the molecular bound state energy and the relative kinetic energy of the atom pair. An atom pair with an off-resonant energy has a probability of association which oscillates with a frequency and time-varying amplitude which are primarily dependent on its detuning. Increasing the amplitude of the modulation tends to result in less energetic atom pairs being resonantly coupled to the molecular state, and also alters the dynamics of the transfer from continuum states with off-resonant energies. This leads to maxima and minima in the total conversion from the gas as a function of the modulation amplitude. Increasing the temperature of the gas leads to an increase in the modulation frequency providing the best fit to the thermal distribution, and weakens the resonant frequency dependence of the conversion. Mean-field effects can alter the optimal modulation frequency and lead to the excitation of higher modes. Our simulations predict that resonant association can be effective for bound state energies of order $-h \times 1$ MHz. The work of this chapter is published in Ref. [117].

5.1 Introduction

In recent experiments, dimers of $^{85}Rb_2$ [89], ^{85}Rb-^{87}Rb [81], $^{133}Cs_2$ [221] and p-wave Feshbach molecules of $^{40}K_2$ [80] were associated from cold atomic gases by applying a magnetic field modulation resonant with the molecular bound state energy. This technique eliminates the need for the magnetic field to spend time in the near-resonant, strongly interacting region. It therefore reduces the unwanted effect of heating [89, 111]

during the production of molecules. The narrow Fourier spectrum of the pulse accurately targets the molecular state, minimising the coupling to deeper bound states and highly energetic continuum states. In a direct comparison to a linear ramp using the same apparatus, Thompson *et al.* reported more efficient conversion using resonant association [89]. This technique has also been used as an accurate probe of molecular bound state energy [81, 89].

In this chapter we study the resonant association of molecules from thermal and condensed gases. Our approach precisely accounts for the continuum of states in a gas. The transition amplitude from a pair of unbound atoms to the bound molecular state depends on the relative kinetic energy of the atom pair. A resonant continuum energy exists, at which the transition amplitude to the molecular state increases linearly with time. At small modulation amplitudes, the resonant continuum energy is given by the difference between the energy corresponding to the modulation frequency, and the absolute value of the bound state energy. The distribution of atoms in different continuum states, all contributing to the production of molecules, gives the total conversion a dependence on temperature. The width of the thermal distribution increases with the temperature of the gas, weakening the resonant behaviour of the molecule production. The continuum distinguishes the current case from the association of atom pairs held in optical lattices, where the resonant modulation couples the discrete ground state of the tightly confining potential to the molecular bound state [222, 223].

We find damped oscillations in the number of molecules produced in the short-time limit, as observed in Ref. [89]. The damping is caused by the dephasing of the transition amplitudes from states across the continuum. After the damping out of the initial oscillations, the conversion increases at a rate which displays resonant dependence on the modulation frequency. Maximal conversion is achieved when the frequency and amplitude of the magnetic field modulation are together optimised for the temperature and density of the gas. The modulation amplitude required depends on the sensitivity of the molecular state to the magnetic field. As the modulation amplitude increases, states of lower continuum energy are resonantly coupled, until the zero-energy continuum state is reached. Beyond this point all continuum states are coupled in a non-resonant manner. There remain some modulation amplitudes where, for momenta close to the peak of the thermal distribution, the transition amplitude is large enough to lead to a revival in conversion efficiency. Our calculations of molecule production for bound state ener-

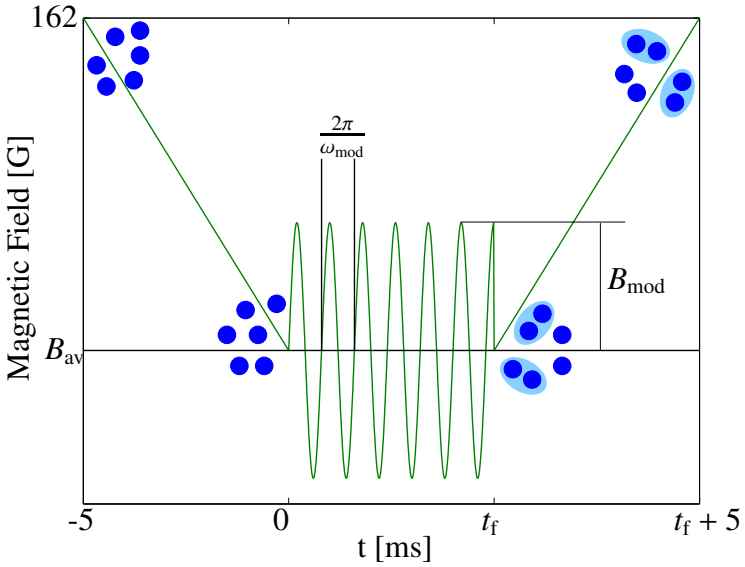

Figure 5.1: A schematic of the magnetic field sequence used in Ref. [89]. The ramps before and after the resonant pulse were shown not to create molecules. We assume a jump in $B(t)$ at $t_{\rm f}$ when $B(t_{\rm f}) \neq B_{\rm av}$.

gies ranging from $-h \times 5$ kHz to $-h \times 1$ MHz predict that resonant association can be effective over this range. We also examine short pulses in pure condensates, where the mean-field shift and the decay of the condensate into higher modes alter the dynamics. In condensates, the damping of oscillations in conversion due to dephasing of the transition amplitudes from different continuum states is suppressed.

In Sec. 5.2 we introduce the magnetic field profile used for resonant association, and also set up the notation used in our calculations. We then discuss the dynamics of the transition amplitude for a pair of atoms to a molecule, and the dependence this has on the continuum, in Sec. 5.3. In Sec. 5.4 we examine in turn the effects of altering the duration, frequency and amplitude of the modulation on the efficiency of the molecule production. We also discuss the dependence of the conversion efficiency on the temperature and density of the atomic gas. In each section we discuss the results of Thompson *et al.* [89], which formed the original motivation for our studies, and then consider resonant association under a broader range of conditions. We conclude in Sec. 5.5.

5.2 Magnetic field sequence

A schematic of the magnetic field sequence used in the experiments of Thompson *et al.* [89] is shown in Fig. 5.1, which also summarises our notation. Gases of ^{85}Rb atoms in the ($f = 2$, $m_f = -2$) excited Zeeman state were prepared at 162 G. Experiments were performed using thermal gases of temperature $T = 20 - 80$ nK, as well as partially and wholly condensed gases. Following a 5 ms ramp to an average field in the range $156 - 157$ G, a sinusoidal magnetic field pulse was applied for a duration of up to 38 ms in order to couple unbound pairs to the Feshbach molecular state. The magnetic field was then ramped back to 162 G in 5 ms, and the gas held until all molecules were lost due to inelastic spin relaxation [89, 98, 99]. Absorption imaging before and after this sequence showed the depletion of the atomic gas.

In our calculations of molecular conversion from thermal gases we neglect the 5 ms ramps on either side of the magnetic field pulse, which were found in Ref. [89] not to lead to molecule production. We have verified that including the ramps causes only a negligible difference to the final result. The magnetic field pulse is taken to have the form $B(t) = B_{\rm av} + B_{\rm mod}\sin(\omega_{\rm mod}t)$, where $B_{\rm mod}$ and $\omega_{\rm mod}$ are the amplitude and angular frequency of the modulation, as shown in Fig. 5.1. $B(t)$ is assumed to satisfy $B(0) = B(t_{\rm f}) = B_{\rm av}$. Where $B(t_{\rm f}) \neq B_{\rm av}$, a sudden jump at $t_{\rm f}$ returning to $B_{\rm av}$ is assumed, as illustrated in Fig. 5.1. Consequently, we analyse the initial and final states in terms of the eigenstates of the Hamiltonian at $B_{\rm av}$. The local density approximation is valid for weakly confining traps such as that used by Thompson *et al.* [18, 89], and for simplicity we assume a homogeneous gas.

Our calculations of molecule production from thermal gases use the two-channel approach detailed in Sec. 2.2. We start from the two-channel, two-body Hamiltonian in the single-resonance approximation, as given by Eqs. (2.20) and (2.22). The Feshbach molecular state and the scattering states at the average field $B_{\rm av}$ are given by Eqs. (2.25) and (2.29) and denoted $\phi_{\rm b}^{\rm av} = \phi_{\rm b}(B_{\rm av})$ and $\phi_{\mathbf{p}}^{\rm av} = \phi_{\mathbf{p}}(B_{\rm av})$, respectively. We also denote the molecular bound state energy at the average field as $E_{\rm b}^{\rm av}$. Using this notation, the transition amplitude of Eq. (4.79) becomes

$$T(p, t_{\rm f}) = \langle \phi_{\rm b}^{\rm av} | U_{\rm 2B}(t_{\rm f}, 0) | \phi_{\mathbf{p}}^{\rm av} \rangle \,. \tag{5.1}$$

Splitting the closed-channel Hamiltonian of Eq. (2.22) into its constant and time depen-

dent parts gives

$$H_{\rm cl}(B(t)) \;=\; |\phi_{\rm res}\rangle \left[E_{\rm res}^{\rm av} + E_{\rm res}^{\rm mod}(t)\right] \langle \phi_{\rm res}| \,. \tag{5.2}$$

Here $E_{\rm res}^{\rm av} = \mu_{\rm res}(B_{\rm av} - B_{\rm res})$, $E_{\rm res}^{\rm mod}(t) = \mu_{\rm res}(B(t) - B_{\rm av})$.

We use the separable potential detailed in Sec. 2.4.2. The comparatively deeply bound states of the entrance-channel potential are neglected. The resonance parameters used are summarised in Tables 2.1 and 2.2. The approach taken to calculating the dynamics is to calculate $U_{\rm 2B}(t_{\rm f}, 0)$ by backwards integration. The Feshbach molecular state $|\phi_{\rm b}^{\rm av}\rangle$ is expanded in terms of the bare scattering states for the entrance channel, and the resonance level for the closed channel. Conjugating Eq. (2.57) - (2.59) gives the following:

$$i\hbar \frac{\partial}{\partial(-t)} C_{-1}^*(t) = E_{-1} C_{-1}^*(t) + \langle \phi_{\rm res}|W|\phi_{-1}\rangle C_{\rm res}^*(t) \,, \tag{5.3}$$

$$i\hbar \frac{\partial}{\partial(-t)} C_{p}^*(t) = \frac{p^2}{m} C_{p}^*(t) + \langle \phi_{\rm res}|W|\phi_{\mathbf{p}}^{(+)}\rangle C_{\rm res}^*(t) \,, \tag{5.4}$$

$$i\hbar \frac{\partial}{\partial(-t)} C_{\rm res}^*(t) = E_{\rm res}(t) C_{\rm res}^*(t) + \int d\mathbf{p} \langle \phi_{\mathbf{p}}^{(+)}|W|\phi_{\rm res}\rangle C_{p}^*(t) + \langle \phi_{-1}|W|\phi_{\rm res}\rangle C_{-1}^*(t) \,. \tag{5.5}$$

These equations are solved numerically using a Runge-Kutta algorithm [224] with adaptive step size. Although not included in our ^{85}Rb calculations, the bare entrance-channel bound state ϕ_{-1} plays a role for many resonances, and is included in these equations for generality. This state is included, for example, in the calculations for ^{133}Cs presented in Sec. 5.4.2. We then have the bare state amplitudes $C_p(t), C_{\rm res}(t), C_{-1}(t)$, which are converted to dressed state amplitudes using the method of Sec. 2.4.2.

5.3 Dynamics of an atom pair

In this section we discuss the dynamics of a pair of atoms in the presence of a continuum, due to the magnetic field pulse introduced in Sec. 5.2. The transition probability density gives the dynamics of only one state in the continuum. This is to be distinguished from the conversion itself, which includes the contributions of all the continuum states. The transition probability density calculated using the approach of the previous section is shown in Fig. 5.2. The fastest growth in the transition probability density $\rho(p,t)$ of Eq. (4.78) for small $B_{\rm mod}$ occurs for the resonant continuum energy $p_{\rm res}^2/m$, which satisfies

$$E_{\rm b}^{\rm av} + \hbar\omega_{\rm mod} - \frac{p_{\rm res}^2}{m} = 0 \,. \tag{5.6}$$

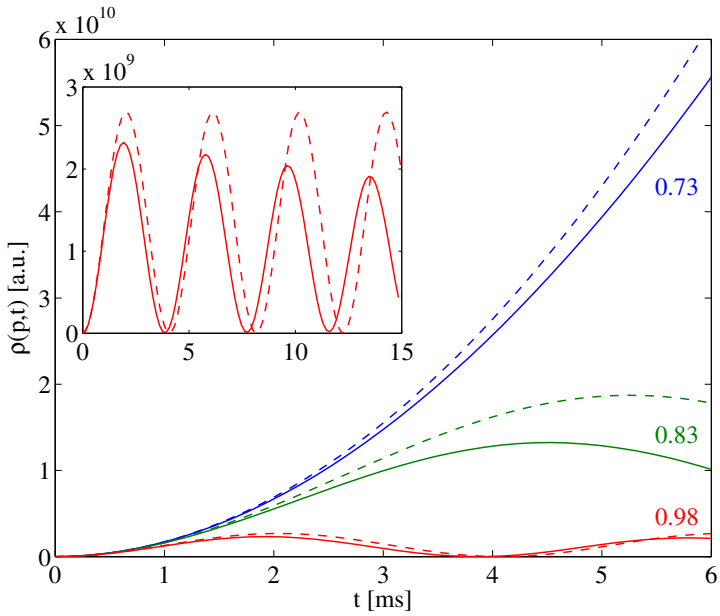

Figure 5.2: Evolution of the transition probability density $\rho(p,t)$ in a ^{85}Rb gas for near-resonant continuum energies. The resonance condition of Eq. (5.6) is fulfilled at $p^2/m = h \times 0.73\,\mathrm{kHz}$. The solid lines show the numerical results, and the dashed lines show the perturbative estimate of Eq. (5.8). The transition probability densities shown are labelled with the energy of the continuum state in $h \times \mathrm{kHz}$. The inset shows the evolution of $\rho(p,t)$ for the 0.98 kHz continuum state at longer times. Here, $B_{\mathrm{av}} = 156.45\,\mathrm{G}$, $B_{\mathrm{mod}} = 0.065\,\mathrm{G}$, $E_{\mathrm{b}}^{\mathrm{av}}/h = -5.77\,\mathrm{kHz}$, and $\omega_{\mathrm{mod}}/2\pi = 6.5\,\mathrm{kHz}$.

This corresponds to the difference between the relative kinetic energy of the unbound atom pair and the molecular bound state energy $E_{\mathrm{b}}^{\mathrm{av}}$ being exactly matched by the modulation frequency. As shown in Fig. 5.2, the growth in the transition probability density $\rho(p,t)$ for $\frac{p^2}{mh} = 0.73\,\mathrm{kHz}$ is quadratic. This corresponds to the transition amplitude of Eq. (5.1) having a linearly increasing amplitude, similar to a resonantly driven harmonic oscillator. At sufficiently short times, $\rho(p,t)$ also grows quadratically for states detuned from the resonant continuum energy. As shown in Fig. 5.2, $\rho(p,t)$ displays behaviour different to $\rho(p_{\mathrm{res}},t)$ after a time of order $\hbar/(|p^2 - p_{\mathrm{res}}^2|/m)$. The inset of Fig. 5.2 shows the oscillatory nature of $\rho(p,t)$. The numerical approach, accounting precisely for the continuum of states, yields an envelope in the oscillation amplitude. The thermal gases measured in Ref. [89] had temperatures in the range 20 - 80 nK. The energy $k_{\mathrm{B}} \times 50\,\mathrm{nK}$ corresponds to $h \times 1\,\mathrm{kHz}$. Consequently, the phase difference between the continuum states spread over the thermal distribution becomes significant after times of order milliseconds.

5.3.1 Perturbative estimate of the two-body evolution

In the limit of short times and a small modulation amplitude, $U_{2B}(t_f, 0)$ may be approximated using time dependent perturbation theory. Treating the oscillating component of the Hamiltonian of Eq. (5.2) as a perturbation to H_{2B}^{av} gives the first order approximation to the two-body evolution operator:

$$U_{2B}^{(1)}(t_f, 0) \approx U_{2B}^{av}(t_f) + \frac{1}{i\hbar}\int_0^{t_f} dt\, U_{2B}^{av}(t_f - t)|\phi_{res}\rangle E_{res}^{mod}(t)\langle\phi_{res}|U_{2B}^{av}(t)\,. \tag{5.7}$$

Here, the two-body evolution operator at B_{av} is given by $U_{2B}^{av}(t) = \exp[-iH_{2B}^{av}t/\hbar]$. Projecting the estimate of Eq. (5.7) onto $\langle\phi_b^{av}|$ on the left and $|\phi_{\mathbf{p}}^{av}\rangle$ on the right gives an approximation to the transition amplitude:

$$T^{(1)}(p, t_f) = -\frac{1}{2\hbar}\mu_{res}B_{mod}e^{-iE_b^{av}t_f/\hbar}C(p)\left[e^{i\omega_+ t_f}\frac{\sin(\omega_+ t_f)}{\omega_+} - e^{i\omega_- t_f}\frac{\sin(\omega_- t_f)}{\omega_-}\right]. \tag{5.8}$$

Here,

$$\omega_\pm = \frac{1}{2\hbar}\left(E_b^{av} \pm \hbar\omega_{mod} - \frac{p^2}{m}\right), \tag{5.9}$$

and $C(p) = \langle\phi_b^{av}|\phi_{res}\rangle\langle\phi_{res}|\phi_{\mathbf{p}}^{av}\rangle$ is the product of the overlaps of the resonance state with the bound and scattering states at B_{av}. The resonance condition of Eq. (5.6) corresponds to $\omega_+ = 0$. However, since E_b^{av}, $\hbar\omega_{mod}$, and p^2/m can all be of the same order of magnitude, it is not in general possible to make the rotating wave approximation and neglect the ω_- term in Eq. (5.8). The quadratic growth of the resonant mode, and the oscillations of off-resonant modes, are reproduced at short times by the analytic estimate of Eq. (5.8), as shown in Fig. 5.2. At longer times, a difference in the frequency of the oscillations in the precise and perturbative approaches becomes apparent. A variation in amplitude of the oscillations, produced only by the precise approach, also becomes significant. The perturbative estimate is therefore valid only at sufficiently short times. As we will show in the following section, the analytic estimate also breaks down as the modulation amplitude becomes too large.

5.4 Experimental parameters affecting the conversion efficiency

In this section we study the variation of the molecule production with the duration, frequency and amplitude of the magnetic field modulation, and the temperature and density of a thermal or fully condensed gas. We refer to the fraction of atoms converted to

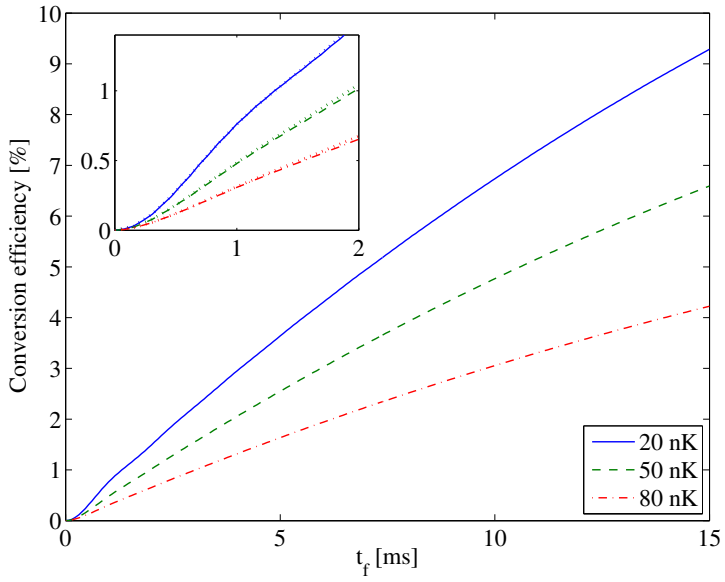

Figure 5.3: Conversion efficiency from a thermal ^{85}Rb gas as a function of pulse duration, for a density of $n = 10^{11}$ cm^{-3}. All other parameters are the same as those of the data represented in Fig. 5.2, which has been thermally averaged according to Eq. (4.76) to give the conversion efficiency. The inset shows damped oscillations in the conversion efficiency, visible for $T = 20$ nK but washed out for 50 nK by the dephasing of the transition amplitudes from different continuum states. The dotted lines show the results given by thermally averaging the perturbative estimate of Eq. (5.8).

molecules as the conversion efficiency. In the limit of small depletion of a thermal atomic gas, this is given by a weighted average of the transition probability density $\rho(p, t_f)$ over a Maxwell-Boltzmann distribution, as given by Eq. (4.76). In this limit the conversion efficiency is proportional to the density of the atomic gas. We note that this approach does not lead to saturation of the conversion efficiency, which requires the inclusion of genuinely many-body effects. This requires the solution of non-Markovian Boltzmann-like equations, whose Markov limit has previously been used to study the special case of saturation of molecule production from magnetic field ramps [115]. We study this problem in Chapter 6.

5.4.1 Pulse duration

Thermal gas

We first consider the conversion efficiency from a thermal gas. The averaging of Eq. (4.76) gives a contribution from $\rho(p, t)$ for each p, weighted according to the thermal distribu-

tion. Figure 5.3 shows the resulting conversion efficiency for gases of 20, 50 and 80 nK as a function of pulse duration. The resonance condition of Eq. (5.6) is fulfilled at a continuum energy of $h \times 0.73\,\mathrm{kHz}$, which corresponds to 37 nK. Of the gas temperatures quoted in Ref. [89], 20 nK gives the highest conversion efficiency because the most atom pairs have energies close to the resonant continuum energy.

In the experiments of Ref. [89], damped oscillations in the conversion efficiency as a function of time were observed over the first few milliseconds. In our calculations, damped oscillations are visible over approximately 2 ms for a temperature of 20 nK. We have verified for several values of B_{av} and ω_{mod} that the frequency of the damped oscillations, f_{conv}, for the thermal gas case is close to $p_{\mathrm{res}}^2/(mh)$. This is the value of $\omega_+/2\pi$ for $p = 0$ in Eq. (5.9), corresponding to the detuning of the zero momentum state from the resonant continuum energy. Increasing the temperature causes a negative shift in the frequency of the damped oscillations, together with faster damping. For 50 and 80 nK gases our calculations do not predict damped oscillations large enough to be observed. The main cause of damping is the variation in the oscillation frequency of $\rho(p,t)$ with p, as shown in Fig. 5.2 and discussed in Sec. 5.3. A wider thermal distribution corresponds to a wider spread in momentum of the atom pairs contributing to the conversion efficiency, and so the initial coherence in $\rho(p,t)$ across the distribution is destroyed more quickly.

Condensed gas

We now consider the case of resonant association from a Bose-Einstein condensate. The critical temperature reported in Ref. [89] is 14 nK, with average densities of order $10^{11}\,\mathrm{cm}^{-3}$. For a density of $10^{11}\,\mathrm{cm}^{-3}$, which we use in our thermal gas calculations, and a magnetic field of 156.45 G, the dilute gas parameter $\sqrt{na^3}$ is 0.02. For such gases, which are close to condensation or partially condensed, there will be a mean-field shift in the frequency of the oscillations in conversion efficiency. We have analysed this effect for the case of a pure, homogeneous condensate. For our studies of condensed gases we use the first order cumulant approach detailed in Sec. 4.3. We solve the non-Markovian, nonlinear Schrödinger equation of Eq. (4.30), and calculate the molecular conversion efficiency from Eq. (4.57). The magnetic fields used in this calculation are within the range for which single-channel approaches have been shown to be valid for the 155 G resonance of ^{85}Rb [218].

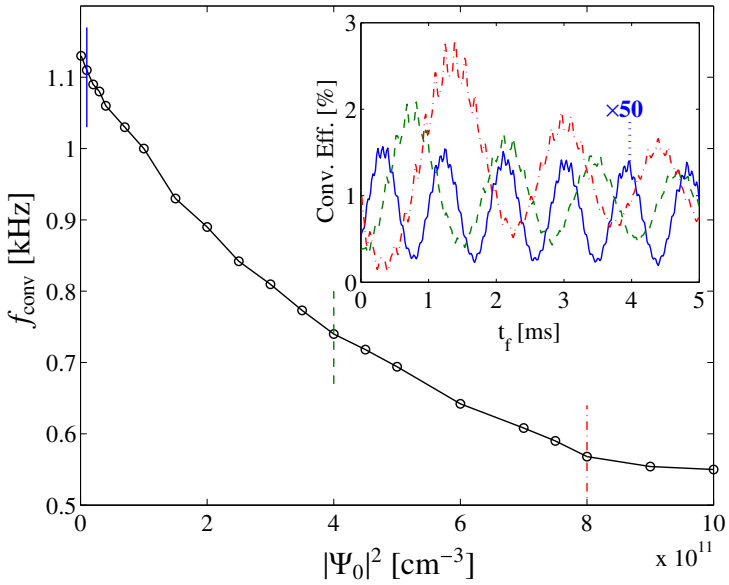

Figure 5.4: Frequency of the oscillations in conversion efficiency at short times for a pure ^{85}Rb condensate as a function of the initial density. The mean-field shift lowers the frequency of the oscillations in conversion efficiency from that given by the two-body approach, which is recovered in the limit of low density. The oscillations are, however, much clearer than those in a thermal gas due to the suppression of the contributions of different continuum states to the production of molecules. The inset shows the variation in time of the conversion efficiency for densities of 10^{10} (×50 for clarity), 4×10^{11} and 8×10^{11} cm^{-3}. The 0.5 ms ramp from 157.45 G to B_{av} = 156.45 G, not shown here, gives a density dependent initial phase to the oscillations. Here B_{mod} = 0.065 G, $E_b^{av}/h = -5.86$ kHz and $\omega_{mod}/2\pi$ = 7 kHz. Because a single-channel approach is used in the condensed gas case, the bound state energy is slightly different to that given by the two-channel, thermal gas calculations above.

The oscillation frequency of the conversion efficiency at short times, f_{conv}, has a mean-field shift, as shown in Fig. 5.4. In the low-density limit, the value of f_{conv} expected from the two-body picture is recovered. The oscillations in conversion efficiency are clearer and have weaker damping than those in thermal gases, as shown in the inset of Fig. 5.4. This is due to suppression of the dephasing between the transition amplitudes from different continuum states. The main cause of damping in this case is the decay of the condensate and molecular populations into the continuum of noncondensate modes. In these calculations we have included a 0.5 ms ramp from B_{av} + 1 G to B_{av}, in analogy to the ramp shown in Fig. 5.1. Neglecting the ramp and simulating only the pulse corresponds to instantly turning on the interactions at the beginning of the pulse. For the parameters used here, this results in strong excitation of higher modes. The ramp reduces but does not completely eliminate the excitations, which are visible in the inset of Fig. 5.4 as high frequency oscillations whose amplitude increases with conden-

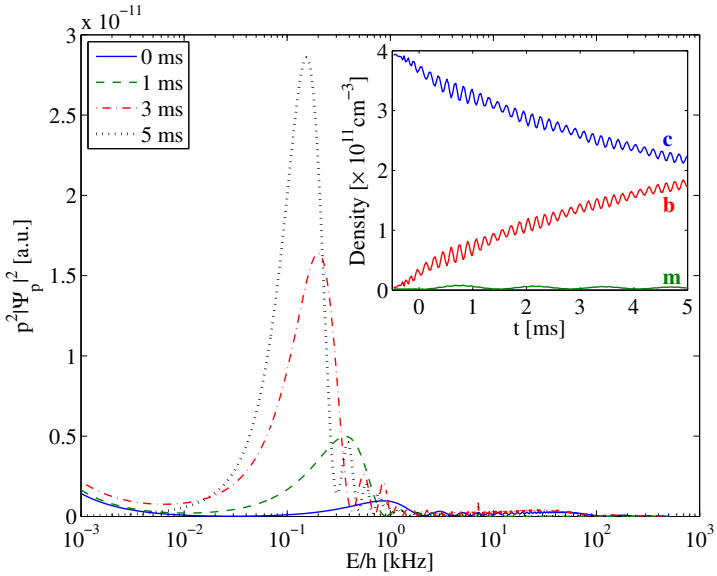

Figure 5.5: Decay of a pure ^{85}Rb BEC into the continuum due to a 7 kHz modulation, showing the burst spectrum at four different times during the 5 ms pulse. A narrow peak at 7 kHz, corresponding to the modulation frequency, is visible, however most of the decay is into low energy modes. The spectrum for 0 ms is due to the effects of the ramp, and the neglect of the initial effect of the continuum on the condensate, as discussed in the text. The inset shows the density of atoms in each of the three components: condensate (c), burst (b) and molecules (m). Here, $B_{\rm av} = 156.45$ G, $B_{\rm mod} = 0.065$ G and $E_{\rm b}^{\rm av}/h = -5.86$ kHz.

sate density. We have extracted the frequency of the damped oscillations using the fit procedure of Claussen *et al.* [225], which includes exponential damping of the oscillations and a linear decay. Strong decay of the condensate into the continuum at higher densities makes the fit less reliable and meaningful, and we have therefore limited the analysis using this technique to densities below 10^{12} cm^{-3}. The decay of the condensate into the continuum is shown in Fig. 5.5. A small peak occurs at the continuum energy corresponding to the modulation frequency, however most of the decay is into modes of lower energy. The detuning of the modulation frequency from the molecular bound state energy leads to excess energy being added to the condensate, which is shared between many atom pairs resulting in the production of pairs of low energy.

The frequency of the oscillations in conversion efficiency shown in Fig. 5.4 plateaus close to 0.5 kHz. For higher initial densities, the condensate decays into the continuum fast enough that the mean field shift changes substantially with time. Fig. 5.6 shows a similar calculation with a modulation frequency of 6.5 kHz. At short times, resonant coupling including the mean-field shift occurs for a density of approximately 1.5×10^{12} cm^{-3}.

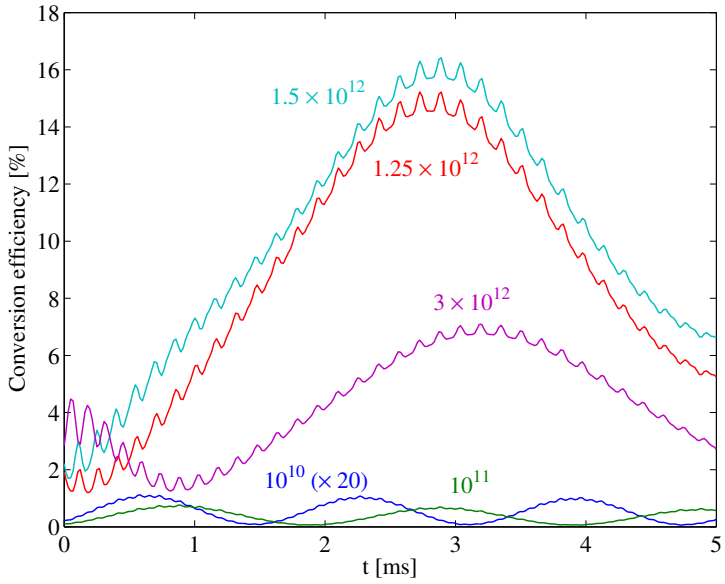

Figure 5.6: Conversion from a pure ^{85}Rb BEC due to a 6.5 kHz modulation for different initial condensate densities, labelled in cm^{-3}. The role of the mean-field shift in bringing the energy gap between a free atom pair and a Feshbach molecule close to the modulation frequency is clear from the conversion efficiency, which peaks at approximately 17% for $\rho = 1.5 \times 10^{12}\,\mathrm{cm}^{-3}$. The result for $n = 10^{10}\,\mathrm{cm}^{-3}$ is multiplied by 20 for clarity. Here, $B_{\mathrm{av}} = 156.45\,\mathrm{G}$, $B_{\mathrm{mod}} = 0.065\,\mathrm{G}$ and $E_{\mathrm{b}}^{\mathrm{av}}/h = -5.86\,\mathrm{kHz}$.

A maximum conversion of 17 % is found, at which point the lower density of atoms due to conversion and decay into the continuum leads to off-resonant behaviour. Comparison of the curves for densities of $1.5 \times 10^{12}\,\mathrm{cm}^{-3}$ and $1.25 \times 10^{12}\,\mathrm{cm}^{-3}$ shows different behaviour at small times, but similar dynamics after the first few milliseconds due to faster decay into the continuum for the higher density condensate. Varying the modulation frequency with time to account for the changing mean-field shift could be used to achieve an optimal production efficiency.

5.4.2 Modulation frequency

Resonant behaviour was observed in Ref. [89] in the strong variation of the conversion efficiency with modulation frequency, which is reproduced by our calculations. The conversion efficiency from a thermal gas due to a pulse of fixed duration and varying frequency is shown in Fig. 5.7. For the resonance curve representing 6 ms pulses, the full-width at half-maximum is 0.75 kHz. The 6 ms pulse in Fig. 1 of Ref. [89] has a width of 0.82(14) kHz. At longer times many-body effects may lead to the production of

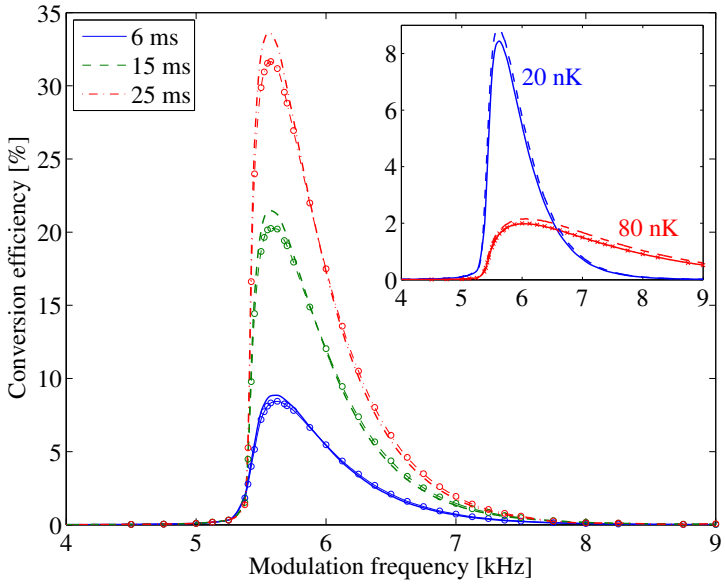

Figure 5.7: Resonance curve of conversion efficiency vs modulation frequency for different pulse durations, for a thermal ^{85}Rb gas. Here $B_{\mathrm{av}} = 156.41\,\mathrm{G}$, $E_{\mathrm{b}}^{\mathrm{av}}/h = -5.39\,\mathrm{kHz}$, $B_{\mathrm{mod}} = 0.065\,\mathrm{G}$, $T = 20\,\mathrm{nK}$ and $n = 10^{11}\,\mathrm{cm}^{-3}$. The lines with circles are averaged according to a Maxwell-Boltzmann distribution, as in Eq. (4.76), while those without circles are averaged according to a Bose-Einstein distribution, as in Eq. (4.72). The difference between the two starts to become significant at longer times and higher depletions. Inset: Conversion efficiency after a 6 ms pulse with $T = 20\,\mathrm{nK}$ and $T = 80\,\mathrm{nK}$, showing its weaker dependence on modulation frequency at higher temperatures. The dashed curves are thermal averages of the perturbative estimate of Eq. (5.8) for 6 ms pulses. The conversion efficiency obtained for 80 nK by averaging using a Bose-Einstein distribution is also shown, marked by red crosses. The difference between the two distributions at this temperature is negligible.

molecules by thermalisation. This could lead, for example, to production of molecules for modulation frequencies smaller than $|E_{\mathrm{b}}^{\mathrm{av}}|/h$, and so increase the width of the resonance curve. The inset of Fig. 5.7 shows estimates of the conversion efficiency using the perturbative estimate of the transition amplitude in Eq. (5.8). The agreement with the numerical result is significantly better than that of the transition probability density, shown in Fig. 5.2, due to the effect of thermally averaging over all of the continuum states. We have also performed the thermal average using a Bose-Einstein distribution, as in Eq. (4.72). This results in a distribution which, for the same temperature, has more atom pairs at lower relative kinetic energies. Consequently, the maximum of the resonance curve is slightly higher, and the high-frequency wing of the curve goes below the Maxwell-Boltzmann result. For a 20 nK gas, the difference becomes significant for the longest timescales shown in Fig. 5.7. However, for the shorter pulses we consider in the rest of this chapter the difference is small, and we use the Maxwell-Boltzmann

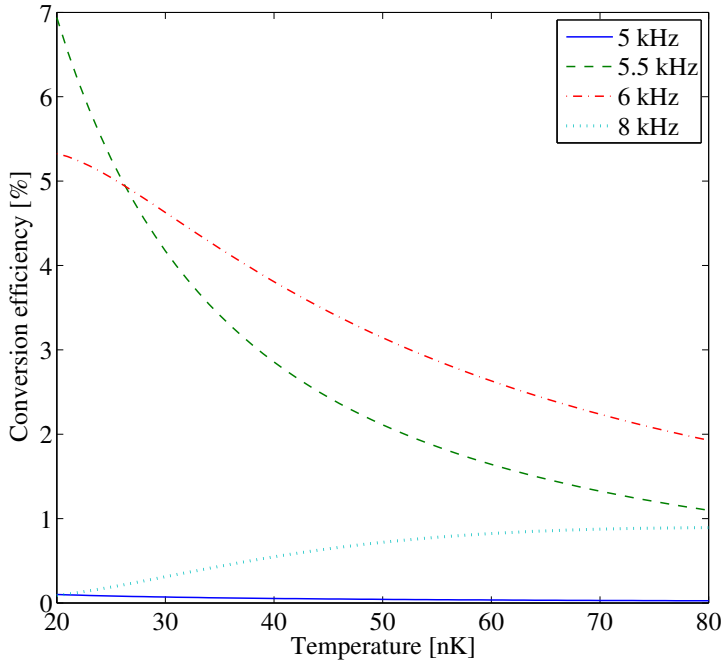

Figure 5.8: Conversion efficiency vs temperature for 6 ms pulses of different modulation frequencies, for a thermal ^{85}Rb gas. For a modulation frequency of 5 kHz, less than the frequency corresponding to the molecular bound state energy, the conversion efficiency remains low at all temperatures. For frequencies higher than that corresponding to the molecular bound state energy, the conversion peaks at the temperature best corresponding to the thermal distribution. Here $B_{\mathrm{av}} = 156.41$ G, $E_{\mathrm{b}}^{\mathrm{av}}/h = -5.39$ kHz, $B_{\mathrm{mod}} = 0.065$ G, $T = 20$ nK and $n = 10^{11}$ cm^{-3}.

distribution. For an 80 nK gas, as shown in the inset of Fig. 5.7, the difference between the Bose-Einstein and Maxwell-Boltzmann results is not noticeable.

The maximum of a thermal distribution is at a higher energy in a warmer gas, and so the optimal modulation frequency increases with temperature. An example of this is shown in Fig. 5.8. A 5.5 kHz modulation gives a better conversion efficiency than 6 kHz below approximately 26 nK, above which the higher frequency is better. However, the dependence of the conversion efficiency on modulation frequency weakens at higher temperatures, as shown in the inset of Fig. 5.7. This is caused by the changes in the thermal distribution of the gas, which has a decreasing maximum and an increasing width as the temperature rises. The decreasing maximum of the distribution leads to less being gained by optimising the modulation frequency $\omega_{\mathrm{mod}}/2\pi$. Conversely, the increasing width means that a wider range of ω_{mod} have a significant population of atoms close to the resonant continuum energy $p_{\mathrm{res}}^2/m = E_{\mathrm{b}}^{\mathrm{av}} + \hbar\omega_{\mathrm{mod}}$. In general, the stronger resonant behaviour in colder gases allows more efficient conversion, as shown in Fig. 5.8.

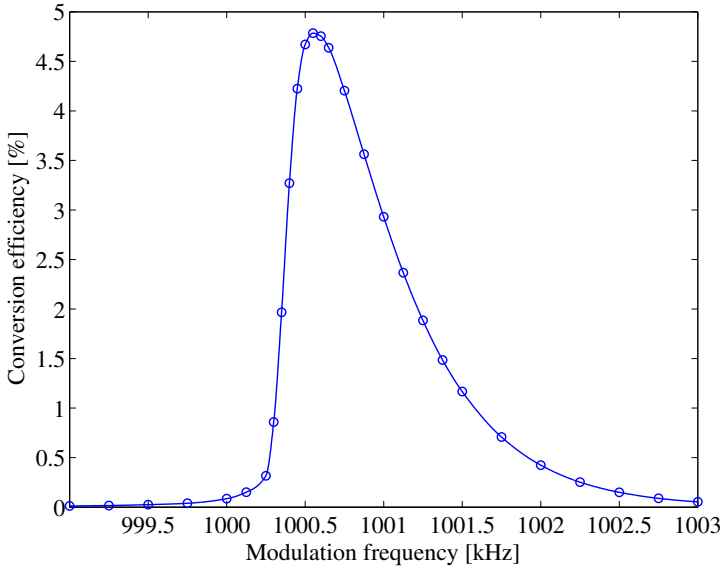

Figure 5.9: Conversion efficiency vs modulation frequency for a thermal ^{133}Cs gas, from a 6 ms pulse. The gas density and modulation amplitude are identical to the ^{85}Rb curve shown in Fig. 5.7. Here $T = 20\,\mathrm{nK}$, $n = 1 \times 10^{11}\,\mathrm{cm}^{-3}$, $B_{\mathrm{av}} = 21.37\,\mathrm{G}$, $B_{\mathrm{mod}} = 0.065\,\mathrm{G}$, and $E_{\mathrm{b}}^{\mathrm{av}}/h = -1\,\mathrm{MHz}$.

We have studied the conversion efficiency as a function of frequency for molecular bound state energies of $-h \times 100\,\mathrm{kHz}$, and found that it leads to a resonance curve of similar width and maximum to that for the bound state energies examined above. $^{85}Rb_2$, though, is unstable with respect to inelastic spin relaxation [98, 99]. We have therefore also performed the calculation for ^{133}Cs atoms in the $(f = 3, m_{\mathrm{f}} = 3)$ Zeeman ground state for a molecular bound state energy of $-h \times 1\,\mathrm{MHz}$. The resonance parameters we have used are summarised in Tables 2.1 and 2.2. A similar resonance curve is obtained, as shown in Fig. 5.9. It is broader and has a lower maximum than the comparable calculations for 6 ms pulses in ^{85}Rb, which had an identical modulation amplitude and gas density. Despite the deeper bound state energy, the conversion efficiency grows at a similar rate. The evolution of the transition probability density for a continuum state depends primarily upon its detuning from the resonant continuum energy. Consequently, the pulse duration necessary for association is largely independent of the bound state energy. Our calculations indicate that resonant association can be efficient for bound state energies ranging from $-h \times 5\,\mathrm{kHz}$ to $-h \times 1\,\mathrm{MHz}$.

Efficient conversion is therefore possible, in principle, for a wide range of bound state energies. It is necessary, however, that the molecular bound state energy be sensitive to variations in the magnetic field. If this is not the case, the magnetic field modulation has

little or no effect on the diatomic level spectrum, and so significant transitions between the continuum states and the molecular bound state do not occur. Such a weak dependence on the magnetic field can occur due to an avoided crossing with another bound state, as occurs for $^{133}Cs_2$ at some bound state energies [113]. In some cases, it may be possible to compensate for this by using a larger modulation amplitude. An example of this is shown for $^{133}Cs_2$ at $B_{av} = 157\,G$ in Fig. 5.10. A lack of variation in the bound state energy with magnetic field implies a high admixture of the Feshbach molecular state in the entrance-channel spin configuration. In the opposite limit of closed-channel dominance, the Feshbach molecular state has a high admixture in the resonance level. This corresponds to a lack of coupling between the channels. The low efficiency of resonant association when the admixture in one of the channels is too great can be understood in terms of the perturbative estimate of Eq. (5.8). The factor $C(p)$ is the product of the closed-channel admixtures of the scattering and Feshbach molecular states at B_{av}. If the Feshbach molecular state is highly entrance-channel dominated, $C(p)$ is correspondingly small, and so the transition amplitude grows slowly. On the other hand, if the Feshbach molecular state is highly closed-channel dominated, the scattering states have a high admixture in the entrance channel, and so $C(p)$ is again small. We have numerically confirmed this low efficiency by performing simulations for ^{87}Rb atoms in the vicinity of the 1007.4 G resonance.

5.4.3 Modulation amplitude

In the experiments of Thompson *et al.*, increasing the modulation amplitude B_{mod} with a fixed frequency and pulse duration gave a point of maximum conversion, and after reaching a minimum a partial revival was observed [226]. Examining the transition probability density of Eq. (4.78) for different B_{mod} shows that as B_{mod} is increased, the resonant growth of $\rho(p_{res}, t)$ is at first amplified, as shown in Fig. 5.11a. The faster resonant growth is also reflected in the proportionality of the analytic estimate of $T(p, t)$ in Eq. (5.8) to B_{mod}. For $B_{mod} = 0.35\,G$, there is no longer resonant growth in $\rho(p_{res}, t)$ over a 1 ms pulse duration, although this modulation amplitude does maximise $\rho(p_{res}, 1\,ms)$. The changing amplitude and position of the maximum as B_{mod} varies alters the quality of the fit to the thermal distribution, and consequently the conversion efficiency. For $B_{mod} < 0.9\,G$, resonant growth is still observed, however the continuum energy of the state with resonantly growing population is negatively shifted from that predicted by

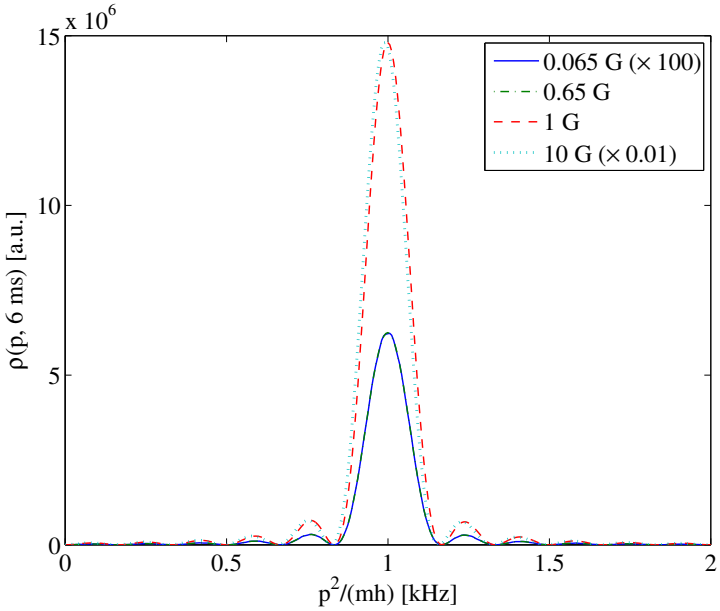

Figure 5.10: The distribution of transition probability density for ^{133}Cs at a field $B_{\mathrm{av}} = 157\,\mathrm{G}$. The weak dependence on magnetic field of the two-body states is compensated for by a large modulation amplitude. The shift in peak energy of the distribution from the low modulation amplitude limit is just discernible for a modulation amplitude of 10 G. Here $|E_{\mathrm{b}}^{\mathrm{av}}|/h = 15\,\mathrm{kHz}$ and $\omega_{\mathrm{mod}}/2\pi = 16\,\mathrm{kHz}$.

Eq. (5.6). As shown in Fig. 5.11b, $\rho(p, 1\,\mathrm{ms})$ has a peak in momentum which, as B_{mod} is increased, at first grows in amplitude and retains its width and position, before being shifted towards $p = 0$. Fully destructive interference for continuum energies up to a few kHz occurs when $B_{\mathrm{mod}} \approx 1.0\,\mathrm{G}$ and so a minimum in conversion efficiency is produced, as reflected in Fig. 5.12. Beyond this modulation amplitude, there is no continuum energy for which quadratic growth of $\rho(p, t)$ is observed. Figure 5.11b also shows two bands of constructive interference in $\rho(p, t)$. These bands have a peak energy which is also dependent on B_{mod}. Consequently, at the modulation amplitudes for which these peaks coincide with the thermal distribution, a revival of the conversion efficiency occurs.

The dependence of the shift in peak energy of $\rho(p, t)$ on modulation amplitude can be different for each species and bound state energy. In the example of $^{133}Cs_2$ dimers at 157 G, modulation amplitudes of up to 10 G do not substantially change the shape of the distribution of $\rho(p, t)$, as shown in Fig. 5.10. This is because the bound state energy of the Cs dimers discussed above varies very weakly with magnetic field, and the weaker sensitivity to the magnetic field also reduces this shift. This may also be understood

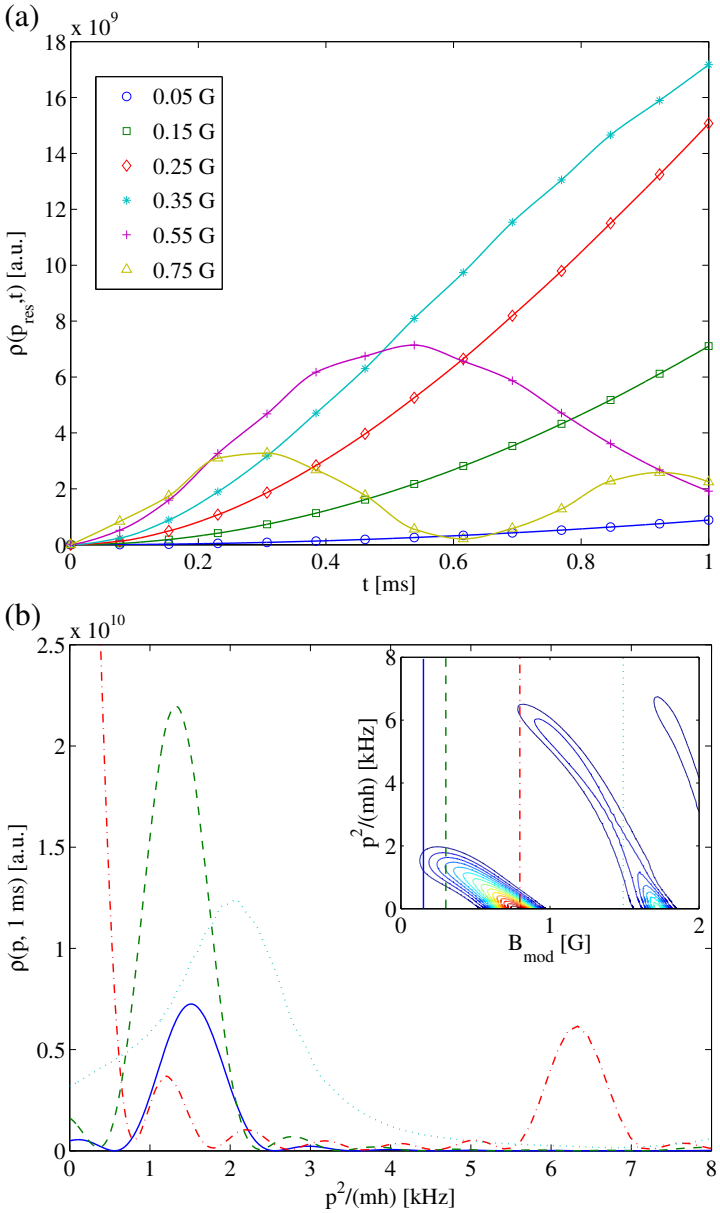

Figure 5.11: The transition probability density $\rho(p,t)$ in a ^{85}Rb gas for different values of $B_{\rm mod}$. Here $B_{\rm av} = 156.352\,$G, $\omega_{\rm mod}/2\pi = 6.5\,$kHz, and $E_{\rm b}^{\rm av}/h = -4.88\,$kHz. (a) The evolution of $\rho(p,t)$ for the continuum state of energy satisfying the resonance condition of Eq. (5.6). Quadratic growth ceases to be observed when the modulation amplitude becomes too great. (b) The transition probability density distribution $\rho(p, 1\,{\rm ms})$ for $B_{\rm mod} = 0.15$, 0.3, 0.8 and 1.5 G, as indicated in the contour plot shown in the inset. For each $B_{\rm mod} < 0.9\,$G, the peak in energy of $\rho(p,t)$ grows resonantly on a timescale of 1 ms. The continuum energy of the maximal $\rho(p, 1\,{\rm ms})$ is negatively shifted from $p_{\rm res}^2/m$ with increasing $B_{\rm mod}$. Two bands of revival in $\rho(p,t)$ can be seen in the inset, as well as in the distributions of $\rho(p,t)$ for $B_{\rm mod} = 0.8$ and 1.5 G.

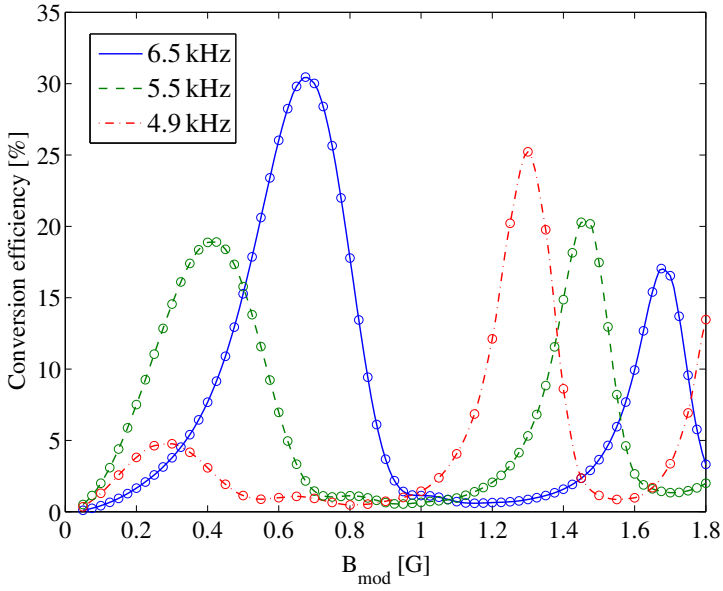

Figure 5.12: Conversion efficiency from a thermal ^{85}Rb gas as a function of modulation amplitude for $B_{\rm av} = 156.352$ G, $n = 10^{11}$ cm^{-3}, $T = 20$ nK and $\omega_{\rm mod}/2\pi = 4.9$, 5.5 and 6.5 kHz. The solid line ($\omega_{\rm mod}/2\pi = 6.5$ kHz) is a thermal average of the data shown in Fig. 5.11. The variation in conversion efficiency with $B_{\rm mod}$ is caused by the changes in the distribution of $\rho(p,t)$, as shown in Fig. 5.11b. The revivals are caused by the regions of constructive interference, shown in Fig. 5.11b, coinciding with the thermal distribution.

in terms of the perturbative estimate of Eq. (5.8): this estimate is only valid when the predicted transition amplitude is small, and so is valid over a wider range of $B_{\rm mod}$ if the factor $C(p)$ is small. The factor $C(p)$ represents the closed-channel admixture of the molecular and scattering states, and therefore also the sensitivity of the two-body energy spectrum to magnetic field.

The maximum, minimum and revival in conversion efficiency are shown for three different modulation frequencies in Fig. 5.12. The absolute conversion efficiency at the maximum is strongly temperature dependent, as shown for $B_{\rm mod} = 0.065$ G in Fig. 5.7, however the modulation amplitude giving the maximum conversion has a weak variation with temperature above 20 nK. The continuum energy for which the state is resonantly coupled varies with the modulation amplitude, and so both frequency and amplitude should be matched to the temperature of the gas for maximum conversion. Of the plots shown in Fig. 5.12, for example, the best conversion is achieved for $B_{\rm mod} = 0.7$ G and $\omega_{\rm mod}/(2\pi) = 6.5$ kHz. The revival in conversion efficiency for larger modulation amplitudes occurs in a peak that is narrower, and is due to the constructive interference shown in the inset of Fig. 5.11b. We note that for $B_{\rm mod} > 1.352$ G the resonance position B_0

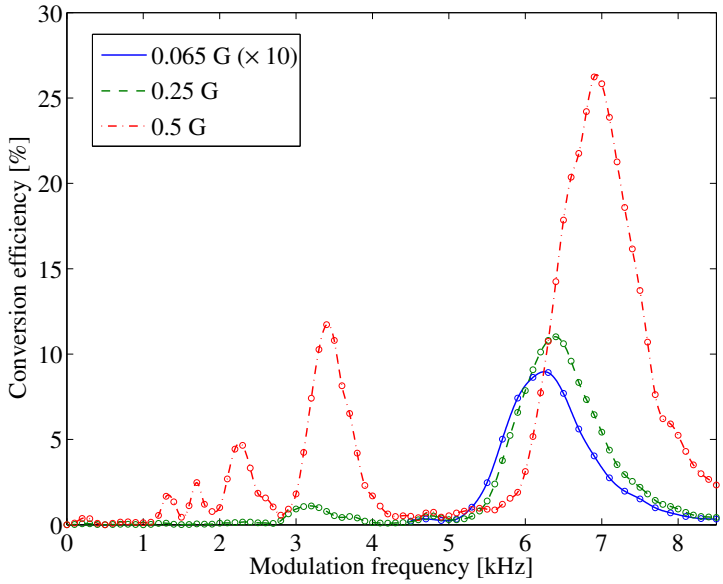

Figure 5.13: Conversion efficiency from a thermal ^{85}Rb gas as a function of modulation frequency, for different modulation amplitudes. A modulation amplitude of 0.065 G (blue line) corresponds to that used in Figs. 5.2-5.8. For higher modulation amplitudes, the peak is shifted upward in modulation frequency, a manifestation of the modulation amplitude dependent shift discussed above. The line-shape also changes. Harmonics of integer divisions of the peak frequency are visible for $B_{\mathrm{mod}} = 0.5$ G (red dot-dashed line).

is being crossed during the pulse. The conversion efficiency as a function of frequency is shown for a variety of modulation amplitudes in Fig. 5.13. The location of the peak of conversion efficiency is the same as in Fig. 5.7 for the same modulation amplitude. As the modulation amplitude is increased, the frequency shift shown in Fig. 5.11 moves the peak upwards in energy. The lineshape also alters as the dynamics of the evolution of individual modes changes with modulation amplitude. Harmonics become visible, as shown for $B_{\mathrm{mod}} = 0.5$ G. This may be interpreted as the resonance condition of Eq. (5.6) also being a harmonic of lower frequencies of which integer multiples equal the resonant frequency. The second harmonic was observed experimentally, as was the linewidth of this feature being narrower than the main peak [227].

5.5 Conclusions

Resonant association has been experimentally shown to be an effective technique of producing molecules [80, 81, 89]. Here we have studied the dependence of the conversion efficiency on the duration, frequency and amplitude of the pulse, and the density and

temperature of the gas. We have shown that for a homogeneous gas, the continuum shapes the dynamics of the association in such a way that it is unlike a two-level system, in contrast to the case of resonant association in strongly confining optical lattices. The presence of other continuum states around that resonantly coupled to the Feshbach molecule leads to the requirement of optimising the properties of the pulse for the gas in question. Maximum conversion requires the amplitude and frequency of the modulation to together be optimised for the density and temperature of the gas. Colder gases have narrower thermal distributions and so display stronger resonant behaviour. The width of the thermal distribution also leads to the dephasing of the oscillations in conversion efficiency observed at short times in Ref. [89]. An increase in temperature causes a positive shift in the optimal frequency for association, but also lowers the maximum possible conversion efficiency.

The amplitude of the modulation and mean-field shifts lead to the resonant coupling of continuum states of different energy, and thus also affect the conversion efficiency. A higher modulation amplitude causes a less energetic continuum state to be resonantly coupled. Beyond a certain amplitude, no resonant growth in transition probability density occurs, however for the parameters of Ref. [89] a revival in conversion efficiency is seen due to a region of constructive interference between the different continuum states. A weak dependence of the molecular bound state energy on magnetic field limits the effectiveness of resonant association, although this can sometimes be compensated for by an increase in the modulation amplitude. The evolution of the transfer probability density from a state is primarily determined by its detuning from the resonant continuum energy. Consequently, the pulse duration necessary for association does not vary significantly with the molecular bound state energy. We have simulated the resonant association of molecules for bound state energies ranging from $-h \times 5$ kHz to $-h \times 1$ MHz, and predict that resonant association can be effective over this range.

Chapter 6

Many-body effects in the production of Feshbach molecules from thermal gases

In this chapter we study the production of Feshbach molecules from ultracold thermal gases from a many-body perspective. We discuss the technique we have implemented for solving the non-Markovian Boltzmann equation (NMBE), the most computationally intensive part of which is the calculation of the kernel. We apply the NMBE to the case of a linear ramp of the magnetic field across a zero-energy resonance. In the limit of small depletion, this approach reproduces results obtained by thermally averaging the two-body transition probability density, as was done in Chapter 5. Many-body effects become more significant as the conversion efficiency increases, which can be achieved by considering a higher initial density of the atomic gas. Our approach predicts the molecule production efficiency to fall below the two-body prediction as the density of the gas increases. We have therefore shown that our approach is practicable, and is applicable to the production of molecules in regimes where only a many-body approach is valid.

6.1 Introduction

Linear ramps across zero-energy resonances for molecule production are often slow in order to maximise the conversion efficiency. For two isolated atoms in the ground state of a trap, a sufficiently slow ramp adiabatically maps the atom pair onto a Feshbach molecule as the resonance is crossed. Calculations on the basis of two-body physics using approaches such as that detailed in Sec. 2.2 predict that this process can in principle have perfect efficiency. Experimentally, the production of molecules from atom pairs in a strong optical lattice, for which the tunnelling rate between sites is low, has been observed to have an efficiency up to approximately 95% [110]. The lack of tunnelling ensures good agreement with the two-body prediction. For the saturation of the production of molecules in bulk gases, however, many-body effects are of relevance. The highest production efficiencies achieved from loosely trapped atomic gases are 88% in ^{40}K [84],

and 85% in ^{6}Li [74]. The latter experiments were performed with ramps sufficiently slow for thermal equilibrium to be assumed throughout the ramp, whereas relaxation losses in the experiments of [84] placed a lower limit on the ramp speed. For slow ramps such as the ones used in these experiments, each atom can undergo several collisions, and so a many-body approach is required. Hodby *et al.* [111] studied molecule production from slow ramps in gases of bosonic ^{85}Rb and fermionic ^{40}K. They analysed their data in terms of a model assuming that the likelihood of a pair forming a molecule depends only on the proximity of the two atoms in phase-space. Two atoms were assumed to form a molecule if their proximity in phase-space was smaller than a constant which was varied to find optimal agreement with experimental data. The values of this constant providing the best fit for each of the two cases agreed to within experimental uncertainty, supporting the idea that phase-space proximity is the main factor affecting the maximum production efficiency.

For the case of an asymptotically slow ramp, the saturation of molecule production can be calculated by assuming thermal equilibrium during the ramp [112, 113]. The molecular state is then treated as one of the two-body states, with a population determined by the appropriate Boltzmann factor. Using a mean-field approach, Szymańska *et al.* showed that the Feshbach molecular state creates a minimum in the many-particle action [114]. Thus, for a ramp slow enough that the gas is always close to thermal equilibrium, or even for a static field, molecules should be formed as the gas relaxes to the state of lowest free energy. A weaker condition than the assumption of thermal equilibrium is to consider the regime in which each atom undergoes many collisions during the ramp, as used by Williams *et al.* [115]. The molecular formation process and its saturation is calculated from the limits of coupled Boltzmann equations for separated atom pairs and pairs in the resonance state, and the variation of the coupling with the varying energy of the resonance state. This treatment qualitatively agrees with the data of [111], as well as giving a kinetic and thermodynamic motivation for the phase-space proximity model used in that paper.

In this chapter we apply the non-Markovian Boltzmann equation (NMBE) derived in Chapter 4 to the problem of many-body effects in the production of Feshbach molecules, and the saturation of this process. The NMBE enables us to perform calculations of molecule formation from ultracold gases including the full time variation of the interactions, as well as the depletion and rethermalisation of the continuum of atomic states.

This enables us to go beyond the calculations of Chapter 5 and study the saturation of molecule production due to many-body effects. Obtaining the kernel is the most computationally intensive component of the implementation. We discuss this in Sec. 6.2, detailing the calculation of the kernel for the terms with two momentum integrals in Sec. 6.2.1, and for the terms with one momentum integral in Sec. 6.2.2. In Sec. 6.3 we apply the NMBE to the case of a linear ramp across a zero-energy resonance. In the limit of small depletions we recover the result predicted by thermally averaging the two-body transition probability density, as was done in Chapter 5. As gases of increasing density are considered, many-body effects become more significant. This leads to the many-body prediction for the conversion efficiency being lower than the two-body result, which is proportional to the initial density of the gas. We have therefore shown that our approach gives the correct result in the low-density limit, and the correct qualitative behaviour as the density is increased. Lastly, we discuss the prospects for extending our approach to situations where only a many-body approach is valid.

6.2 The kernel of the non-Markovian Boltzmann equation

We have implemented the non-Markovian Boltzmann equation using a single-channel approach. As in Chapter 5, we assume a homogeneous gas. This provides a good approximation to experiments performed in loose magnetic traps. Starting from the non-Markovian Boltzmann equation of Eq. (4.48), we separate out the kernel for each of the terms:

$$\frac{\partial}{\partial t}\Gamma(p,t) = \frac{4}{\hbar}\Gamma(p,t_\mathrm{i})\int_0^\infty dq q^2\,\Gamma(q,t_\mathrm{i})\mathcal{K}_1(p,q,t,t_\mathrm{i}) \tag{6.1a}$$

$$+\,2\int_0^\infty dp_1\int_0^\infty dp_2 p_1^2 p_2^2\,\Gamma(p_1,t_\mathrm{i})\Gamma(p_2,t_\mathrm{i})\mathcal{K}(p,p_1,p_2,t,t_\mathrm{i}) \tag{6.1b}$$

$$+\,\frac{4}{\hbar}\int_{t_\mathrm{i}}^t dt'\int_0^\infty dq q^2\,\mathcal{K}_1(p,q,t,t')\frac{\partial}{\partial t'}(\Gamma(p,t')\Gamma(q,t')) \tag{6.1c}$$

$$+\,2\int_{t_\mathrm{i}}^t dt'\int_0^\infty dp_1\int_0^\infty dp_2 p_1^2 p_2^2\,\mathcal{K}(p,p_1,p_2,t,t')\frac{\partial}{\partial t'}(\Gamma(p_1,t')\Gamma(p_2,t'))\ . \tag{6.1d}$$

Here, the kernel for the cross-section terms of Eqs. (6.1b) and (6.1d) is given by

$$\mathcal{K}(p,p_1,p_2,t,t') = 2\pi \int_0^\pi d\theta_{p_2} \sin\theta_{p_2} \int_0^\pi d\theta_p \sin\theta_p \int_0^{2\pi} d\phi_p \times \frac{\partial}{\partial t}\left|\frac{1}{\hbar}\int_{t'}^{t} d\tau \exp\left(\frac{ip_{\rm cm}^2}{m\hbar}(\tau - t')\right)\langle \mathbf{p}_{\rm cm}|V(\tau)U_{\rm 2B}(\tau,t')|\mathbf{p}_{\rm r}\rangle\right|^2 . \quad (6.2)$$

Here, $\mathbf{p}_{\rm cm} = \mathbf{p} - (\mathbf{p}_1 + \mathbf{p}_2)/2$, $\mathbf{p}_{\rm r} = (\mathbf{p}_1 - \mathbf{p}_2)/2$. The kernel for the imaginary terms of Eqs. (6.1a) and (6.1c) is given by

$$\mathcal{K}_1(p,q,t,t') = \int d\Omega_{\mathbf{q}} {\rm Im}\left[\langle \mathbf{q}_{\rm r}|\, V_{\rm I}(t)U_{\rm 2B}^{\rm I}(t,t')\,|\mathbf{q}_{\rm r}\rangle\right] , \quad (6.3)$$

where $\mathbf{q}_{\rm r} = (\mathbf{p} - \mathbf{q})/2$. We are therefore able to perform all the angular integrals in advance and store the kernels $\mathcal{K}(p,p_1,p_2,t,t')$ and $\mathcal{K}_1(p,q,t,t')$, leaving only the integrals over time and the moduli of the momenta to be performed during the calculation. This represents a substantial speedup over doing all of the integrals at each time-step. Once the kernel has been calculated for a given magnetic field variation sequence, it can be used for several different input values of the temperature and density of the gas.

6.2.1 The kernel of the cross-section terms

The kernel of the cross-section terms is a function of three momenta and two times. In the kernel, $\mathbf{p}_1$ and $\mathbf{p}_2$ only appear in the form of relative or centre of mass coordinates. We are prevented from transforming the coordinates by the need to integrate over $\Gamma(p_1,t)\Gamma(p_2,t)$ in the dynamical code. The kernel does however have the symmetry

$$\mathcal{K}(p,p_1,p_2,t,t') = \mathcal{K}(p,p_2,p_1,t,t') , \quad (6.4)$$

reducing the effort involved in its calculation. Also, in the dynamical simulation the p_1 and p_2 integrals are evaluated over the kernel multiplied by the density matrices, which have a much narrower range in momentum than the kernel itself. The density matrix therefore defines the maximum required momenta in the integrations. This allows the evaluation of the kernel for the highest momenta to be approximate, as the contribution to the integrals will be small. The derivative with respect to t of the cross-section terms

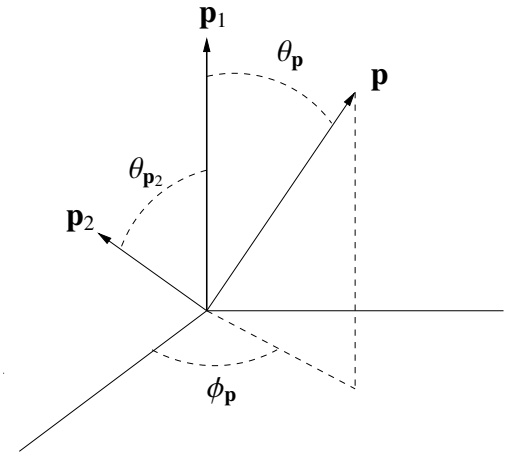

Figure 6.1: Schematic of the angular integration of Eq. (6.2). Translational invariance reduces the number of angular integrals from 6 to 3. We fix $\mathbf{p}_1$ at $(\theta = 0, \phi = 0)$ and $\mathbf{p}_2$ at $(\phi = 0)$, and evaluate the other 3 integrals.

in Eq. (6.2) can be written

$$\begin{aligned}
&\frac{\partial}{\partial t}\left|\frac{1}{\hbar}\int_{t'}^{t} d\tau \exp\left(\frac{ip_{\rm cm}^2}{m\hbar}(\tau - t')\right)\langle \mathbf{p}_{\rm cm}|V(\tau)U_{\rm 2B}(\tau,t')|\mathbf{p}_{\rm r}\rangle\right|^2 \\
&= \frac{2}{\hbar^2}|\langle\chi|\mathbf{p}_{\rm cm}\rangle|^2 {\rm Re}\Bigg[\exp\left(\frac{ip_{\rm cm}^2}{m\hbar}(t - t')\right)\xi(t)\langle\chi|U_{\rm 2B}(t,t')|\mathbf{p}_{\rm r}\rangle \\
&\times\left(\int_{t'}^{t} d\tau \exp\left(\frac{ip_{\rm cm}^2}{m\hbar}(\tau - t')\right)\xi(\tau)\langle\chi|U_{\rm 2B}(\tau,t')|\mathbf{p}_{\rm r}\rangle\right)^*\Bigg]. \qquad (6.5)
\end{aligned}$$

Here, we have used the form of the separable potential in Eq. (2.85). We therefore need, as a function of $(p_{\rm r}, t, t')$, the matrix element $\langle\chi|U_{\rm 2B}(t,t')|\mathbf{p}_{\rm r}\rangle$. We also need, as a function of $(p_{\rm cm}, p_{\rm r}, t, t')$, the Fourier transform of its product with $\xi(t)$:

$$\int_{t'}^{t} d\tau \exp\left(i\frac{p_{\rm cm}^2}{m\hbar}(\tau - t')\right)\xi(\tau)\langle\chi|U_{\rm 2B}(\tau,t')|\mathbf{p}_{\rm r}\rangle\,. \qquad (6.6)$$

The method of calculating these matrix elements and their Fourier transforms is detailed in Appendix D. We spline these functions to the required values of $p_{\rm cm}$ and $p_{\rm r}$ to evaluate the angular integrals in Eq. (6.2). A schematic of the manner in which we do the integration is given in Fig. 6.1. There are 3 momenta, giving a total of 6 angles. Translational invariance reduces this number to 3. It is simplest to fix $\mathbf{p}_1$, and evaluate an integral over both angular variables of $\mathbf{p}$, which only appears in one of the two moduli.

Calculating the kernel for the cross-section term requires approximately 1500 hours of processor time for the 5 G, 0.1 ms ramp we consider in Sec. 6.3. We use a maximum energy of $h\times 500$ kHz, and a grid of 100 p, 50 p_1 and p_2, and 40 t and t'. The calculation

may be naturally divided up according to t', as we calculate the Fourier transform of Eq. (6.6) separately for each. For each t', the angular integrals must then be evaluated for all (p, p_1, p_2, t). This can be divided into as many jobs as is appropriate for the available number of processors. The kernel is shown in Fig. 6.2 for $t' = 0$, and a few representative p and t.

6.2.2 The kernel of the imaginary terms

It is possible to calculate the angular integral of Eq. (6.3) analytically. To do so, we first use the integral equation for $\langle\chi|U_{2B}(t,t')|\mathbf{p}\rangle$ of Eq. (D.11). After including the phase due to the interaction picture in Eq. (6.3), the imaginary part of the free term is 0, which leaves

$$\mathcal{K}_1(p,q,t,t') = \frac{\xi(t)}{\hbar}\int d\Omega_{\mathbf{q}}\,|\langle\chi|\mathbf{q}_r\rangle|^2\,\mathrm{Im}\left[-i\int_{t'}^{t} d\tau\langle\chi|U_{2B}(t,\tau)|\chi\rangle\xi(\tau)\exp\left(\frac{iq_r^2}{m\hbar}(t-\tau)\right)\right]. \tag{6.7}$$

Here, we have again used the form of the separable potential in Eq. (2.85). Expanding the modulus, $q_r^2 = |\mathbf{p}-\mathbf{q}|^2/4 = (p^2+q^2-2pq\cos\theta)/4$, with θ the angle between $\mathbf{p}$ and $\mathbf{q}$, we then have

$$\begin{aligned}\mathcal{K}_1(p,q,t,t') = \frac{\xi(t)}{\hbar}\frac{1}{4\pi^2\hbar^3}\mathrm{Im}\Big[-i\int_{t'}^{t} d\tau\langle\chi|U_{2B}(t,\tau)|\chi\rangle\xi(\tau)\\ \times\int_0^{\pi} d\theta\sin\theta\exp\Big(-\frac{p^2+q^2-2pq\cos\theta}{4m\hbar}[\eta-i(t-\tau)]\Big)\Big].\end{aligned} \tag{6.8}$$

Here, $\eta = m\sigma^2/\hbar$, where σ is the range of the potential defined in Eq. (2.85). The integral over θ can be simply evaluated, leaving

$$\begin{aligned}\mathcal{K}_1(p,q,t,t') = \frac{m\xi(t)}{2\pi^2\hbar^3 pq}\mathrm{Re}\Big\{\int_{t'}^{t} d\tau\langle\chi|U_{2B}(t,\tau)|\chi\rangle\xi(\tau)\\ \times\frac{\exp\left(-\frac{(p+q)^2}{4m\hbar}[\eta-i(t-\tau)]\right)-\exp\left(-\frac{(p-q)^2}{4m\hbar}[\eta-i(t-\tau)]\right)}{\eta-i(t-\tau)}\Big\}.\end{aligned} \tag{6.9}$$

This result allows us to calculate the kernel for the single integral terms from a Fourier transform of the function $\langle\chi|U_{2B}(t,t')|\chi\rangle$. Because the momenta p and q only appear in the form $(p \pm q)$, Eq. (6.9) can be written in the form

$$\mathcal{K}_1(p,q,t,t') = \frac{1}{pq}\left(r((p+q)/2,t,t') - r((p-q)/2,t,t')\right), \tag{6.10}$$

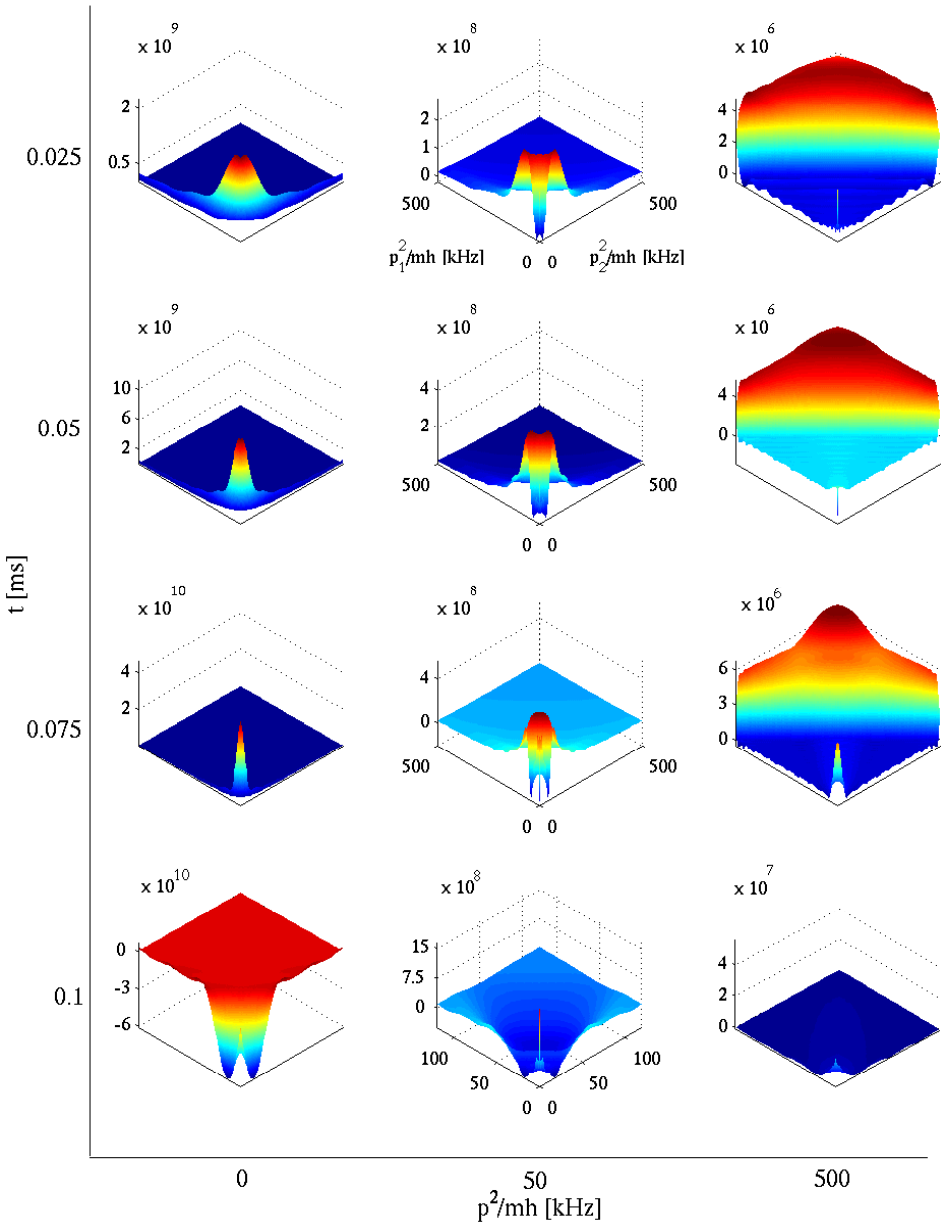

Figure 6.2: Kernel of the cross-section term, $\mathcal{K}(p, p_1, p_2, t, t')$, for a 0.1 ms ramp with $B_\mathrm{i} = 152.5\,\mathrm{G}$, and $B_\mathrm{f} = 157.5\,\mathrm{G}$, for $t' = 0$, and for various p and t, as a function of p_1^2/mh and p_2^2/mh. The limits of p_1^2/mh and p_2^2/mh are the same across each row. For large p, the kernel is small at low $p_{1,2}$, indicating that there is little coupling into these states from the from the low-energy region.

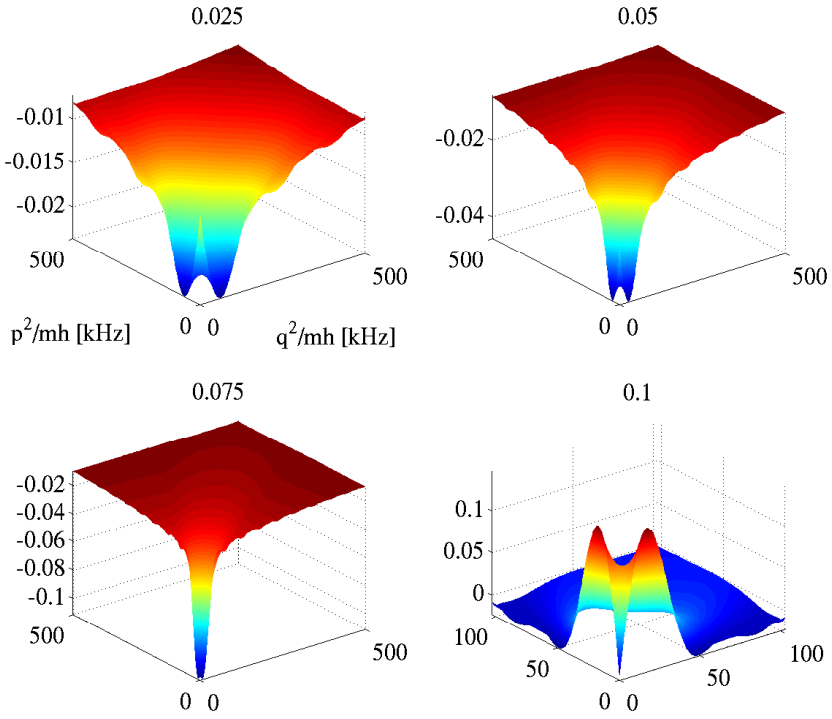

Figure 6.3: The kernel of the imaginary term, $\mathcal{K}_1(p, q, t, t')$, for $t' = 0$ and various values of t, as labelled in ms. The properties of the ramp are the same as in Fig. 6.2.

where

$$r((p \pm q)/2, t, t') = \frac{m\xi(t)}{2\pi^2\hbar^3} \exp\left(-\frac{(p \pm q)^2}{4m\hbar}\eta\right) \times \mathrm{Re} \int_{t'}^{t} d\tau \frac{\langle\chi|U_{2B}(t,\tau)|\chi\rangle\xi(\tau) \exp\left(i\frac{(p\pm q)^2}{4m\hbar}(t-\tau)\right)}{\eta - i(t-\tau)}. \quad (6.11)$$

For the kernel of the imaginary terms, we evaluate $r(p, t, t')$ for a sufficiently fine mesh of times and momentum p, and spline to the required values during the dynamical simulation. The kernel of the imaginary terms is illustrated in Fig. 6.3.

6.3 Comparison of many-body and two-body approaches

We have implemented the non-Markovian Boltzmann equation for a gas of ^{85}Rb in the vicinity of the 155 G resonance, using a 0.1 ms ramp with $B_i = 152.5$ G and $B_f = 157.5$ G. This ramp was chosen for a first demonstration of our approach because, for a low density gas, many-body effects are insignificant. This allows us to make a direct comparison

with the approach of Chapter 5, in which the conversion efficiency is calculated from a thermal average of the two-body transition probability density. However, this ramp is also long enough that by considering higher density gases, which lead to higher molecule production efficiencies, many-body effects are noticeable.

We consider a thermal gas with a temperature of 20 nK and a density of 10^{11} - 10^{12} cm^{-3}. We assume a Maxwell-Boltzmann distribution for the initial state of the gas. We have verified that assuming a Bose-Einstein distribution instead has only a small effect on the final conversion efficiency. Our initial conditions give the non-interacting equilibrium of the system, and so at small times some transient dynamics occur, similar to those shown in Fig. 5.4, though they are less significant here due to the lower phase-space density. We calculate the evolution of the one-body density matrix using the Runge-Kutta technique [224], with adaptive stepsize. The values of $\Gamma(p,t)$ and $\frac{\partial}{\partial t}\Gamma(p,t)$ are stored as a function of momentum and time. For evaluating the integral over time, the value of the derivative at time t, which is not yet known, is approximated by assuming $\Gamma(p,t)$ to be linear over the last time interval defined by the mesh. The full dynamical simulation takes $30-60$ hours of processor time, depending on the input parameters, and is parallelised using an Open-MP architecture. This kind of parallelisation allows several processors to access the same memory, and so avoids the issues of synchronisation and data transfer that hinder a distributed approach.

The evolution of the one-body density matrix is shown in Fig. 6.4. As the resonance is crossed, the population of the low-lying continuum modes begins to decrease as atoms are coupled to higher energy modes, corresponding to the emergence of the Feshbach molecular state. The nonlinearity of the NMBE makes the changes in the one-body density matrix larger for higher densities, and excites more atoms to higher momenta. The maximum energy that is required to be included in the simulations is set by the temperature and density of the gas, and the timescale of the variation in magnetic field. The maximum energy must be such that the population of the highest modes is always insignificant. The maximum energy included in the simulations presented here is 500 kHz. For the highest densities considered, the highest energy states start to play a role. Consequently, higher energies may need to be included in some situations to be considered in future, with a corresponding increase in the difficulty of evaluating the kernel.

The form of Eq. (4.67) for the conversion efficiency shows that in the limit of small

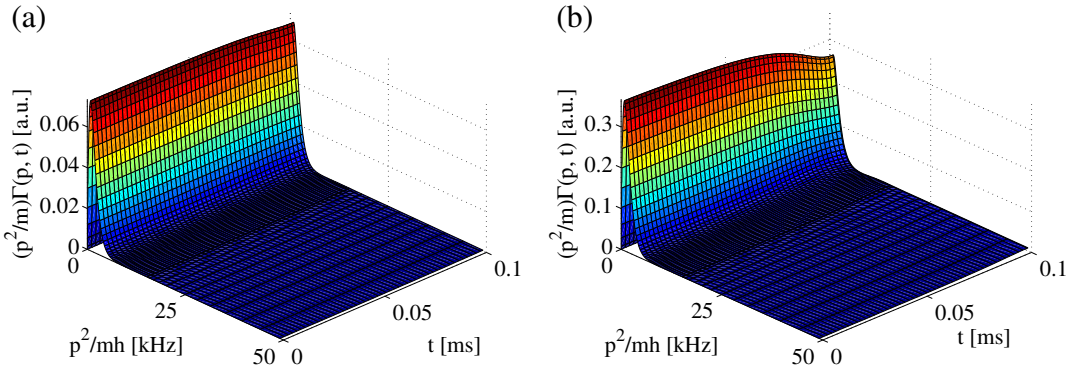

Figure 6.4: Evolution of the one-body density matrix for densities of (a) $10^{11}\,\mathrm{cm}^{-3}$ and (b) $5 \times 10^{11}\,\mathrm{cm}^{-3}$. The depletion of the low-energy continuum modes as the resonance is crossed corresponds to the emergence of the molecular bound state. For higher densities this effect becomes more significant, as does the rethermalisation of the gas. The maximum energy included in the simulations is 500 kHz, however for clarity we only show energies up to 50 kHz.

depletion, when the changes in the one-body density matrix are small, the prediction of the many-body approach reduces to that given by a thermal average of the two-body transition probability density, as was used in Chapter 5. To see the size of the correction due to many-body effects, we compare the results predicted by the NMBE to that calculated with a single-channel implementation of the two-body approach. In this case, the conversion efficiency is predicted to be

$$\frac{2N_{\mathrm{mol}}}{N} = 2n(2\pi\hbar)^3 \left(\frac{\beta}{\pi m}\right)^{3/2} \int d\mathbf{p} \exp\left(-\beta\frac{p^2}{m}\right) |\langle\phi_{\mathrm{b}}^{\mathrm{f}}|U_{2\mathrm{B}}(t_{\mathrm{f}},0)|\mathbf{p}\rangle|^2 \,. \tag{6.12}$$

Here, $\phi_{\mathrm{b}}^{\mathrm{f}}$ is the Feshbach molecular state evaluated at the final magnetic field. We have used plane waves instead of the scattering states which were used in the thermal averages of Chapter 5. This ensures consistency with the one-body density matrix, which is expanded in terms of plane waves. For the range of fields used here, the initial correlations which are included in the scattering states change the predicted conversion efficiency, as shown in Fig. 4.3, but do not change the physical trends. This difference diminishes for wider ramps, in which the initial state is closer to the non-interacting equilibrium, or for longer ramps in which sufficient thermalisation occurs at the beginning of the ramp.

The conversion efficiency predicted by the non-Markovian Boltzmann equation is shown in Fig. 6.5. The molecular fraction is calculated from Eq. (4.67). For a density of $10^{11}\,\mathrm{cm}^{-3}$, the two-body and many-body approaches predict 4.11 % and 4.06 %, respectively. The two-body approach gives a conversion efficiency proportional to density, which is unphysical at large conversion efficiencies. The NMBE approach gives a

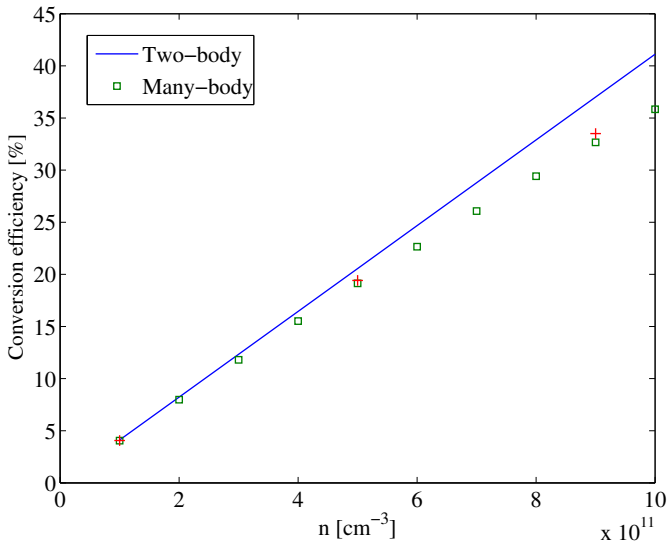

Figure 6.5: The conversion efficiency predicted by thermally averaging the two-body transition probability density (blue line), and the many-body non-Markovian Boltzmann equation (green squares). Here, we have considered a 0.1 ms ramp with $B_{\mathrm{i}} = 152.5$ G and $B_{\mathrm{f}} = 157.5$ G, and a gas of temperature $T = 20$ nK. At low densities, the two approaches agree. As the density increases, the depletion and rethermalisation of the continuum become significant, reducing the efficiency predicted by the many-body approach. Only a small difference in the conversion efficiency is found between a Maxwell-Boltzmann distribution and a Bose-Einstein distribution (red '+').

smaller prediction, with the deviation from the two-body result becoming more significant as the conversion efficiency increases, as shown in Fig. 6.5. The NMBE is therefore correct in the small depletion limit and gives the expected behaviour as the conversion efficiency increases.

Although we have only considered a short ramp for which the thermal averaging technique of Chapter 5 is sufficient for normal experimental parameters, our results here show that the NMBE approach is practicable, and should be able to be extended to consider longer magnetic field variation sequences, where only a many-body approach is valid. As the present calculation is well within current capabilities, we envisage being able to do simulations of millisecond lengths. Our approach is not limited to linear ramps, and can be applied to arbitrary magnetic field variations, such as the resonant association experiments of Chapter 5.

6.4 Conclusions

The non-Markovian Boltzmann equation provides a many-body implementation of the dynamics of Feshbach molecule formation from ultracold atomic gases. The precise time-variation of the interactions is included, as are the depletion and rethermalisation of the continuum. The calculation of the dynamics of the one-body density matrix is made possible by calculating the kernel for the non-Markovian Boltzmann equation in advance. We have applied this approach to a 5 G, 0.1 ms ramp, showing that it produces the correct result in the limit of small depletions. As the density of the gas increases, many-body effects become more significant, leading to the predicted molecule production efficiency being lower than that obtained from a thermal average of the two-body transition probability density. We have therefore shown that the non-Markovian Boltzmann equation is a practicable and useful approach, which we anticipate being able to extend to consider magnetic field variations of millisecond lengths, and correspondingly high molecule production efficiencies.

Chapter 7

Conclusions and outlook

This thesis has focused on the dynamics of the production of Feshbach molecules from ultracold gases, examining the role of both two- and many-body effects. In both cases we have studied the role of the continuum of states from which molecules are associated. We have formulated and implemented the non-Markovian Boltzmann equation, allowing beyond mean-field calculations with realistic, time-varying interactions. In this chapter we summarise the work of this thesis and briefly discuss further planned applications and developments of this work.

In Chapter 3 we considered the dissociation of Feshbach molecules, and the conclusions that may be drawn about the nature of a zero-energy resonance from the shape of dissociation spectra. In particular, a zero-energy resonance dominated by the closed channel can produce a dissociation spectrum with a sharp peak close to the final resonance energy, provided that the ramp is fast enough. We showed that currently achievable ramp speeds may be interpreted to be in this 'sudden jump' regime, and discussed instances where such a jump can also lead to the transfer of molecules into the next deeper bound vibrational state. We studied the transition from sudden jumps to asymptotically wide, linear ramps, rigorously deriving the form of the spectrum that has been inferred previously from Fermi's golden rule. Consequently, our work shows the independence of the spectrum produced by such a ramp on the implementation of the two-body physics, provided that the near-resonant scattering properties are correctly reproduced.

In Chapter 4 we detailed the theory of cumulants and applied it to the production of Feshbach molecules from both thermal and condensed gases. A key element of this approach is the inclusion of the precise, time-varying two-body interactions as an input

to the many-body equations. We showed that the molecule production can be calculated from the one-body density matrix for the case of a thermal gas. We then derived a non-Markovian Boltzmann equation governing the evolution of the one-body density matrix, and showed that in the limits of stationary interactions and long times it reduces to the normal Boltzmann equation.

Our calculations of the association of Feshbach molecules using a magnetic field modulation that is near resonant with the molecular bound state energy were presented in Chapter 5. We examined in depth the two-body physics of the transition, showing how the dephasing between continuum modes in a thermal gas washes out the oscillations in conversion efficiency at short times, and produces a smooth increase in the number of molecules produced as the pulse lengthens. We also characterised the shift in the resonant modulation frequency due to the amplitude of the modulation, the temperature of the gas, and mean-field shifts. The temperature of the gas also influences the width of the distribution of conversion efficiency as a function of frequency, the resonant behaviour being stronger in a cooler gas because of the narrower distribution of significantly populated continuum modes. Because the evolution of an atom pair depends primarily on the detuning from the energy that is resonantly coupled to the molecular state, the conversion efficiency is not significantly dependent on bound state energy. However, reasonably strong variation in the two-body energy levels with magnetic field is necessary. For the case of a condensed gas, which we studied using a first order cumulant approach, the oscillations in conversion efficiency at short times are longer lived, and mean-field effects contribute a further change to the resonant modulation frequency.

In Chapter 6 we discussed the implementation of the non-Markovian Boltzmann equation derived in Chapter 4. This approach allows the calculation of beyond mean-field dynamics with realistic interactions. We have implemented a technique for calculating the kernel, the two-body evolution which is used as an input to the many-body equation, and the dynamical code. Applying this to a linear ramp across a zero-energy resonance, we obtained a molecule production efficiency that agrees with the thermal averaging technique of Chapter 5 in the limit of small depletion. As the density of the gas is increased, leading to a higher production efficiency, the prediction of this approach falls below the thermal averaging prediction due to the onset of many-body effects.

Both the dissociation calculations of Chapter 3 and the resonant association calculations of Chapter 5 can be applied to the case of molecules formed from a p-wave

resonance [80]. The presence of a centrifugal barrier makes the Feshbach molecular state closed-channel dominated even at threshold. At positive energies the molecules decay by tunnelling through the barrier. Resonant association was used to produce p-wave molecules in Ref. [80]. Calculations analogous to those of Chapter 3 will allow investigation of the lifetime of the molecular state, and the behaviour of the dissociation spectrum under different ramp parameters.

The non-Markovian Boltzmann equation approach will allow studies of a range of situations. One application will be to re-examine the resonant association calculations of Chapter 5. Including the effects of the depletion and rethermalisation of the continuum will allow us to extend our previous work to look at the saturation of molecule production and the onset of many-body effects as the pulse duration increases, and as other properties such as the modulation amplitude are varied. The role of many-body effects in shaping the low-frequency side of the resonance curve in Fig. 5.7 is another unresolved question. Applying our second order cumulant approach to a partially condensed Bose gas would be difficult, as in this case there would be coupled equations for the mean field, one-body density matrix and pair function. At the present time, we are limited to the first order cumulant approach of Secs. 4.3 and 5.4 for zero-temperature condensates, and the second order approach of Sec. 4.4 and Chapter 6 for thermal Bose gases with no degeneracy. It is, however, possible to extend our technique to study the growth of pairing in a two-component Fermi gas during a BCS-BEC ramp. Previous calculations [228] suggest that the ramps of Jin's experiments [37] might have had pairing develop during the ramp, rather than reflecting only the pairing present in the initial state. For the case of a two-component Fermi gas, the mean field is still zero, however the pair function of Eq. (4.15) must be included, which leads to coupled equations for the pair function and one-body density matrix. Our non-Markovian Boltzmann equation approach can also be applied to optical Feshbach resonances and the photoassociation of molecules. The work of this thesis therefore lays a foundation for several studies in beyond mean-field dynamics in ultracold gases including realistic interactions and many-body effects.

Appendix A

Transformed grid for hard core + van der Waals potential

In this appendix we detail the transformed grid method we have implemented for our calculations using the hard core + van der Waals potential of Sec. 2.4.1. The transformed grid used in these calculations allows good resolution of both short and long range properties with a lower number of mesh points than would be required in a uniform grid. The transformation we use, appropriate for a van der Waals interaction, is [229]

$$y(r) = \frac{1}{2}\left(\frac{R_0}{r + R_s}\right)^2 . \tag{A.1}$$

Here, $R_0 = 2l_{\mathrm{vdW}} = (mC_6/\hbar^2)^{1/4}$ and R_s is a free parameter which can be used to set how non-uniform the grid is (for $R_s \to \infty$ the grid is uniform). Using a transformed grid changes the kinetic energy operator in the Hamiltonian, which for the transformation of Eq. (A.1) becomes

$$K = \frac{-\hbar^2}{mR_0^2}\left[8y^{3/2}\frac{d^2}{dy^2}y^{3/2} + \frac{3}{2}y\right] . \tag{A.2}$$

We solve for $\phi(y)$, given by

$$\phi(y) = \psi(r)\sqrt{\frac{-dR(y)}{dy}} , \tag{A.3}$$

where $R(y) = r$ is the inverse transformation, and the minus sign arises because $r_{\mathrm{min}} \leftrightarrow y_{\mathrm{max}}$ and $r_{\mathrm{max}} \leftrightarrow y_{\mathrm{min}}$. The definition Eq. (A.3) ensures that $\int dr|\psi(r)|^2 = \int dy|\phi(y)|^2$.

To find the Feshbach molecular state, we first expand the bare entrance-channel potential of Eq. (2.50) using a sine basis, due to the boundary conditions that the wavefunction vanish at the hard core and for $r \to \infty$. Diagonalising this allows us to find the

energy and wavefunction of the highest vibrational bound state of the entrance channel. We then use this energy as the shift between the potential of the entrance channel and that of the closed channel, which is given by Eq. (2.53). Using the form of the interchannel coupling in Eq. (2.54), we are then able to expand the full two-channel Hamiltonian of Eq. (2.20) in the same sine basis. The highest bound state of the Hamiltonian is the Feshbach molecular state. This calculation is done in a spherical box, which is permissible since the initial wavefunction, the Feshbach molecular state, is well localised. The same property of the bound states of the bare potentials allow them to be found in a box.

The sine-expansion of the Hamiltonian can be used for dynamical simulations. A faster approach, however, is to use the basis set expansion of Eqs. (2.57) - (2.59), expanding the Hamiltonian in terms of the eigenstates of the bare potentials. Having made the single-resonance approximation of Eq. (2.22), the description of the closed channel is determined by using the highest vibrational bound state of the entrance channel. In free space, a complete basis for the entrance channel is given by the bound states of the bare potential and the bare scattering states $|\phi_{\mathbf{p}}^{(+)}\rangle$ of Eq. (2.32). A numerical approximation to the continuous set $\{|\phi_{\mathbf{p}}^{(+)}\rangle\}$ is made by choosing a set of momenta with fine enough resolution that the wavefunctions of successive basis states are not significantly different, and that the amplitudes of adjacent states do not become significantly different during the simulation. In finding the scattering states we follow the approach of Taylor [119], modified for our non-uniform grid. For our case of a hard sphere potential of radius R_c and low-energy s-wave scattering, the Green's function is given by

$$G_E^0(r, r') = -\frac{1}{p}\sin(p(r_< - R_c)/\hbar)\exp(ip(r_> - R_c)/\hbar)\,, \tag{A.4}$$

where $r_{<,>}$ are the smaller and larger respectively of r, r'. The scattering wavefunction is then given by

$$\langle \mathbf{r}|\phi_{\mathbf{p}}^{(+)}\rangle = \frac{1}{(2\pi\hbar)^{3/2} pr}\psi_p(r)\,. \tag{A.5}$$

Here, $\psi_p(r)$ is given by the Lippman-Schwinger equation,

$$\psi_p(r) = \psi_0(r) + \int dr' G_E^0(r, r')U(r')\psi_p(r')\,. \tag{A.6}$$

For a hard core + van der Waals potential, we have $\psi_0(r) = \sin(p(r - R_c)/\hbar)$, and $U(r) = mV_{bg}(r)/\hbar^2$. Because the scattering states are not localised and we want to solve on a finite grid we actually solve for $\sqrt{|U(r)|}\psi_p(r)$, which is localised. Multiplying Eq. (A.6) through by $\sqrt{|U(r)|}$ gives a closed equation for $\sqrt{|U(r)|}\psi_p(r)$ which can be

converted to the transformed grid using Eq. (A.3) to give

$$\sqrt{|U(r)|}\phi(y) = \sqrt{|U(r)|}\psi_0(r)\sqrt{-R'(y)} + \int dy' \sqrt{-R'(y)}\sqrt{|U(r)|}G_E^0(r,r')\sqrt{|U(r')|}\mathrm{sign}(U(r'))\sqrt{-R'(y')}\sqrt{|U(r')|}\phi(y')\,, \tag{A.7}$$

where we now reinterpret r, r' as $R(y)$ and $R(y')$. To solve Eq. (A.7) we perform a two-dimensional sine expansion of the integrand with respect to y and y', and a one-dimensional sine expansion of $\sqrt{|U(r')|}\phi(y')$ and $\sqrt{|U(r)|}\psi_0(r)\sqrt{-R'(y)}$. We write these as the matrix $\{f_{ij}\}$ and the vectors $[v_i]$ and $[j_i]$ respectively. Having done this we are left with a matrix equation to invert:

$$[v_i] = \left[I - \{f_{ij}\}\right]^{-1}[j_i]\,, \tag{A.8}$$

where I is the identity matrix. For accuracy at the grid boundaries we then put $\sqrt{|U(r)|}\phi(y)$ back into the LS equation, this time not multiplying through by $\sqrt{|U(r)|}$:

$$\phi(y) = \psi_0(r)\sqrt{-R'(y)} + \int dy' \sqrt{-R'(y)}G_E^0(r,r')\sqrt{|U(r')|}\mathrm{sign}(U(r'))\sqrt{-R'(y')}\left(\sqrt{|U(r')|}\phi(y')\right)\,. \tag{A.9}$$

The scattering wavefunction is then found by putting $\psi_p(r)$ into Eq. (A.5). This enables us to calculate the initial admixtures of the Feshbach molecular state in each scattering state, and the coupling matrix elements $\langle\phi_{\mathbf{p}}^{(+)}|W|\phi_{\mathrm{res}}\rangle$.

Appendix B

Time evolution operator for a linear ramp

In this appendix we derive an exact expression for the time evolution operator for a linear ramp, and evaluate it in the limit of an asymptotically wide ramp to recover the result of Eq. (3.15). In Sec. B.1, we derive the exact time evolution operator for a linear ramp in the two channel, single resonance approach. In the following section, we use this result to evaluate the transition amplitude for the case of an asymptotic ramp, which provides a rigorous derivation of the corresponding dissociation spectrum of Eq. (3.15). Lastly, in Sec. B.3, we show that this spectrum can also be derived from a single-channel approach.

B.1 Two-channel time evolution operator

We calculate the transition amplitude in terms of the retarded Green's function $G^{(+)}_{\mathrm{2B}}(t,t')$, related to the time evolution operator $U_{\mathrm{2B}}(t,t')$ of Eq. (2.79) by

$$G^{(+)}_{\mathrm{2B}}(t,t') = \frac{1}{i\hbar}\theta(t-t')U_{\mathrm{2B}}(t,t')\,. \tag{B.1}$$

We separate the constant and time dependent parts of the Hamiltonian as in Eq. (3.11). The stationary Hamiltonian H_{stat} in Eq. (3.11) has an associated retarded Green's function given by

$$G^{(+)}_{\mathrm{stat}}(t-t') = \frac{1}{i\hbar}\theta(t-t')\exp[-iH_{\mathrm{stat}}(t-t')/\hbar]\,. \tag{B.2}$$

The separation of $H_{\mathrm{2B}}(B)$ into stationary and time dependent parts then gives two equivalent integral equations for the full retarded Green's function, which are referred to as

the preform and postform, respectively:

$$G^{(+)}_{2\mathrm{B}}(t,t') = G^{(+)}_{\mathrm{stat}}(t-t') + \int d\tau\, G^{(+)}_{2\mathrm{B}}(t,\tau) H_{\mathrm{cl}}(\tau) G^{(+)}_{\mathrm{stat}}(\tau - t')\,, \tag{B.3}$$

$$G^{(+)}_{2\mathrm{B}}(t,t') = G^{(+)}_{\mathrm{stat}}(t-t') + \int d\tau\, G^{(+)}_{\mathrm{stat}}(t-\tau) H_{\mathrm{cl}}(\tau) G^{(+)}_{2\mathrm{B}}(\tau,t')\,. \tag{B.4}$$

Differentiating either form of the integral equation with respect to t and using Eq. (B.1) recovers Eq. (2.79) defining $U_{2\mathrm{B}}(t,t')$. Substituting Eq. (B.3) into Eq. (B.4) and using the form of $H_{\mathrm{cl}}(t)$ in Eq. (2.22) gives the following general expression for the two-body time dependent Green's function:

$$G^{(+)}_{2\mathrm{B}}(t_{\mathrm{f}},t_{\mathrm{i}}) = G^{(+)}_{\mathrm{stat}}(t_{\mathrm{f}}-t_{\mathrm{i}}) + \int d\tau\, G^{(+)}_{\mathrm{stat}}(t_{\mathrm{f}}-\tau)|\phi_{\mathrm{res}},\mathrm{cl}\rangle E_{\mathrm{res}}(\tau)\Big[\langle\phi_{\mathrm{res}},\mathrm{cl}|G^{(+)}_{\mathrm{stat}}(\tau-t_{\mathrm{i}}) + \\ + \int d\tau'\, g^{(+)}_{2\mathrm{B}}(\tau,\tau') E_{\mathrm{res}}(\tau')\langle\phi_{\mathrm{res}},\mathrm{cl}|G^{(+)}_{\mathrm{stat}}(\tau'-t_{\mathrm{i}})\Big]. \tag{B.5}$$

Here, $g^{(+)}_{2\mathrm{B}}(t,t')$ is given in Eq. (3.12). Throughout these appendices we use the notation of a lower-case g to refer to the closed-channel matrix element of the corresponding Green's function.

The explicit form of $G^{(+)}_{2\mathrm{B}}(t_{\mathrm{f}},t_{\mathrm{i}})$ in Eq. (B.5) shows that obtaining its closed-channel matrix element $g^{(+)}_{2\mathrm{B}}(t,t')$ is sufficient for fully determining the time evolution. To this end, we project Eq. (B.4) onto $|\phi_{\mathrm{res}},\mathrm{cl}\rangle$ from the left and right, and again use the definition of $H_{\mathrm{cl}}(t)$ to yield

$$g^{(+)}_{2\mathrm{B}}(t,t') = g^{(+)}_{\mathrm{stat}}(t-t') + \int d\tau\, g^{(+)}_{\mathrm{stat}}(t-\tau) E_{\mathrm{res}}(\tau) g^{(+)}_{2\mathrm{B}}(\tau,t')\,. \tag{B.6}$$

Performing a Fourier transform of both sides of Eq. (B.6) with respect to t leads to the time dependence of $E_{\mathrm{res}}(t)$, given in Eq. (3.2), being converted into a derivative with respect to energy, yielding the following ordinary differential equation:

$$i\hbar\frac{\partial}{\partial E} g_{2\mathrm{B}}(z,t') = \hbar\left[\frac{\partial}{\partial E}\varphi(z,t')\right] g_{2\mathrm{B}}(z,t') + 1/\dot{E}_{\mathrm{res}}\,. \tag{B.7}$$

Here the energy and time dependent matrix element $g_{2\mathrm{B}}(z,t')$ is given by a Fourier transform with respect to time, $g_{2\mathrm{B}}(z,t') = \int dt\, e^{iz(t-t')/\hbar} g^{(+)}_{2\mathrm{B}}(t,t')$, where $z = E + i0$. The energy and time dependent phase $\varphi(z,t')$ is given by

$$\varphi(z,t') = \frac{E(t'-t_{\mathrm{res}})}{\hbar} - \frac{1}{\hbar\dot{E}_{\mathrm{res}}}\int_0^E \frac{dE'}{g_{\mathrm{stat}}(z')}\,, \tag{B.8}$$

where $z' = E' + i0$, and $g_{\mathrm{stat}}(z) = \int dt\, e^{iz(t-t')/\hbar} g^{(+)}_{\mathrm{stat}}(t-t')$.

A solution of Equation (B.7) can be inferred from the derivative with respect to energy of $e^{i\varphi(z,t')}g_{2\mathrm{B}}(z,t')$. Calculating the inverse Fourier transform of the relation for $g_{2\mathrm{B}}(z,t')$ thus obtained gives Eq. (3.13). Substituting $g_{2\mathrm{B}}(t,t')$ into Eq. (B.5) leaves the resonance energy and the phase terms as the only explicitly time dependent quantities. The time dependence due to the resonance energy may be eliminated by writing

$$(t-t_{\mathrm{res}})e^{i\varphi(z,t)} = -i\hbar e^{i\varphi(z,t_{\mathrm{res}})}\frac{\partial}{\partial E}e^{iE(t-t_{\mathrm{res}})/\hbar}\,, \tag{B.9}$$

and calculating the partial integrals with respect to energy. The time integrals in Eq. (B.5) may then be expressed as Fourier transforms, reducing the general expression for the two-body retarded Green's function to

$$G^{(+)}_{2\mathrm{B}}(t_{\mathrm{f}},t_{\mathrm{i}}) = \int\frac{dE}{2\pi\hbar}G_{\mathrm{stat}}(z)\Bigg\{e^{-iE(t_{\mathrm{f}}-t_{\mathrm{i}})/\hbar}\Big[1-|\phi_{\mathrm{res}},\mathrm{cl}\rangle\frac{1}{g_{\mathrm{stat}}(z)}\langle\phi_{\mathrm{res}},\mathrm{cl}|G_{\mathrm{stat}}(z)\Big]+ \\ +\int_{-\infty}^{E}dE'|\phi_{\mathrm{res}},\mathrm{cl}\rangle\frac{e^{-i[\varphi(z,t_{\mathrm{f}})-\varphi(z',t_{\mathrm{i}})]}}{g_{\mathrm{stat}}(z)i\hbar\dot{E}_{\mathrm{res}}g_{\mathrm{stat}}(z')}\langle\phi_{\mathrm{res}},\mathrm{cl}|G_{\mathrm{stat}}(z')\Bigg\}\,. \tag{B.10}$$

This Green's function represents the exact evolution of the two-body system in the two channel, single resonance approach. The separable form of the closed-channel potential and the linear time dependence of the resonance energy allow the dynamics to be calculated from the known Green's function $G_{\mathrm{stat}}(z)$ associated with the stationary Hamiltonian H_{stat} and its closed-channel component.

B.2 Asymptotic ramp limit

We will now evaluate the transition amplitude $T_{\mathrm{diss}}(p)$ of Eq. (3.4) for the case of an asymptotic ramp, which allows the integrals contained in Eq. (B.10) to be calculated analytically. In the limit of $t_{\mathrm{i}}\to-\infty$, $E_{\mathrm{res}}(t_{\mathrm{i}})$ is large and negative, and so we can write

$$\begin{aligned}&G_{\mathrm{stat}}(z)\Big[1-|\phi_{\mathrm{res}},\mathrm{cl}\rangle\frac{1}{g_{\mathrm{stat}}(z)}\langle\phi_{\mathrm{res}},\mathrm{cl}|G_{\mathrm{stat}}(z)\Big]\\ &\underset{t_{\mathrm{i}}\to-\infty}{\sim}G_{\mathrm{stat}}(z)\Big[1+|\phi_{\mathrm{res}},\mathrm{cl}\rangle\frac{E_{\mathrm{res}}(t_{\mathrm{i}})}{1-E_{\mathrm{res}}(t_{\mathrm{i}})g_{\mathrm{stat}}(z)}\langle\phi_{\mathrm{res}},\mathrm{cl}|G_{\mathrm{stat}}(z)\Big]\\ &=G_{2\mathrm{B}}(B_{\mathrm{i}},z)\,.\end{aligned} \tag{B.11}$$

The energy dependent Green's function $G_{2\mathrm{B}}(B_{\mathrm{i}},z)$ is associated with $H_{2\mathrm{B}}(B_{\mathrm{i}})$. We note that the singularities of $G_{2\mathrm{B}}(B,z)$ determine the two-body energy spectrum, in accordance with the relation

$$E_{\mathrm{res}}(B)g_{\mathrm{stat}}(E_{\mathrm{b}}(B)) = 1\,, \tag{B.12}$$

which is equivalent to Eq. (2.27). The contribution given by Eq. (B.11) to the transition amplitude from the initial bound state $\phi_{\mathrm{b}}^{\mathrm{i}}$ to the final continuum state $\phi_{\mathbf{p}}^{\mathrm{f}}$ is then

$$i\hbar \int \frac{dE}{2\pi\hbar} e^{-iE(t_{\mathrm{f}}-t_{\mathrm{i}})/\hbar} \langle \phi_{\mathbf{p}}^{\mathrm{f}} | G_{2\mathrm{B}}(B_{\mathrm{i}}, z) | \phi_{\mathrm{b}}^{\mathrm{i}} \rangle = e^{-iE_{\mathrm{b}}(B_{\mathrm{i}})(t_{\mathrm{f}}-t_{\mathrm{i}})/\hbar} \langle \phi_{\mathbf{p}}^{\mathrm{f}} | \phi_{\mathrm{b}}^{\mathrm{i}} \rangle \,. \tag{B.13}$$

In the asymptotic limit of $t_{\mathrm{i}} \to -\infty$ and $t_{\mathrm{f}} \to +\infty$, the interchannel coupling becomes negligible at the initial and final fields. The initial Feshbach molecular state $\phi_{\mathrm{b}}^{\mathrm{i}}$ and the final continuum state $\phi_{\mathbf{p}}^{\mathrm{f}}$ are then orthogonal, and the contribution of Eq. (B.11) to $T_{\mathrm{diss}}(p)$ vanishes.

The remaining term in Eq. (B.10) contains the rapidly varying phase terms $\varphi(z', t_{\mathrm{i}})$ and $\varphi(z, t_{\mathrm{f}})$, which we evaluate using the stationary phase method [61]. First we evaluate the matrix elements that appear in the integrals over E and E'. The point of stationary phase for the term $\varphi(z', t_{\mathrm{i}})$ occurs at $z' = E_{\mathrm{b}}(B_{\mathrm{i}})$. Using the definition of the Feshbach molecular state in Eq. (2.25), and Eqs. (2.26) and (B.8) we find that

$$\begin{aligned} \frac{\langle \phi_{\mathrm{res}}, \mathrm{cl} | G_{\mathrm{stat}}(z') | \phi_{\mathrm{b}}^{\mathrm{i}} \rangle}{g_{\mathrm{stat}}(z')} &\underset{z' \to E_{\mathrm{b}}^{\mathrm{i}}}{\sim} \mathcal{N}_{\mathrm{b}}(B_{\mathrm{i}}) \\ &= \sqrt{-\hbar \dot{E}_{\mathrm{res}} \varphi''(E_{\mathrm{b}}^{\mathrm{i}}, t_{\mathrm{i}})} \,. \end{aligned} \tag{B.14}$$

Here we have also made use of the following representation of $G_{\mathrm{stat}}(z)$ in terms of the entrance-channel Green's function $G_{\mathrm{bg}}(z)$ and the coupling W:

$$\begin{aligned} G_{\mathrm{stat}}(z) = {} & |\mathrm{bg}\rangle G_{\mathrm{bg}}(z) \langle \mathrm{bg}| + |\phi_{\mathrm{res}}, \mathrm{cl}\rangle \frac{1}{z} \langle \phi_{\mathrm{res}}, \mathrm{cl}| + G_{\mathrm{bg}}(z) W |\phi_{\mathrm{res}}, \mathrm{bg}\rangle \langle \phi_{\mathrm{res}}, \mathrm{cl}| \\ & + |\phi_{\mathrm{res}}, \mathrm{cl}\rangle \frac{1}{z} \langle \phi_{\mathrm{res}}, \mathrm{bg}| W G_{\mathrm{bg}}(z) + |\phi_{\mathrm{res}}, \mathrm{cl}\rangle \frac{1}{z} \langle \phi_{\mathrm{res}}| W G_{\mathrm{bg}}(z) W |\phi_{\mathrm{res}}\rangle \langle \phi_{\mathrm{res}}, \mathrm{cl}| G_{\mathrm{stat}}(z) \,. \end{aligned} \tag{B.15}$$

Using the definition of the scattering states in Eq. (2.29) we also find, in the asymptotic limit of $t_{\mathrm{f}} \to +\infty$ where the interchannel coupling can be neglected,

$$\frac{\langle \phi_{\mathbf{p}}^{\mathrm{f}} | G_{\mathrm{stat}}(z) | \phi_{\mathrm{res}}, \mathrm{cl}\rangle}{g_{\mathrm{stat}}(z)} \underset{t_{\mathrm{f}} \to +\infty}{\sim} \frac{\langle \phi_{\mathbf{p}}^{(+)} | W | \phi_{\mathrm{res}}\rangle}{z - p^2/m} \,. \tag{B.16}$$

The results of Eqs. (B.14) and (B.16) then give the transition amplitude to be

$$T_{\mathrm{diss}}(p) = -\frac{\langle \phi_{\mathbf{p}}^{(+)} | W | \phi_{\mathrm{res}}\rangle \mathcal{N}_{\mathrm{b}}(B_{\mathrm{i}})}{2\pi\hbar \dot{E}_{\mathrm{res}}} e^{i\varphi(E_{\mathrm{b}}^{\mathrm{i}}, t_{\mathrm{i}})} \int dE \frac{e^{-i\varphi(z, t_{\mathrm{f}})}}{z - p^2/m} \int_{-\infty}^{E_{\mathrm{b}}^{\mathrm{i}}} dE' \, e^{-\frac{1}{2} i |\varphi''(E_{\mathrm{b}}^{\mathrm{i}}, t_{\mathrm{i}})| (E' - E_{\mathrm{b}}^{\mathrm{i}})^2} \,. \tag{B.17}$$

Reversing the order of integration, the energy integrals can be evaluated in the limit of $t_\mathrm{i} \to -\infty$, giving

$$T_\mathrm{diss}(p) = -\sqrt{\frac{2\pi}{\hbar|\dot{E}_\mathrm{res}|}}\langle\phi_\mathbf{p}^{(+)}|W|\phi_\mathrm{res}\rangle \exp\left(i[\varphi(E_\mathrm{b}(B_\mathrm{i}), t_\mathrm{i}) - \varphi((p^2/m) + i0, t_\mathrm{f}) + \pi/4]\right) . \tag{B.18}$$

The imaginary part of the phase difference will give a real damping factor when we calculate $|T_\mathrm{diss}(p)|^2$, and is therefore the quantity of interest. Using the spectral decomposition of $G_\mathrm{bg}(z)$ to evaluate the imaginary part of the phase factor in Eq. (B.18) then gives the result of Eq. (3.14) which leads to Eq. (3.15) for energies in the Wigner threshold law regime. We note that the accuracy of Eq. (3.15) depends on the quality of the asymptotic evaluation of the phase integral in Eq. (B.18). For a given resonance and initial and final magnetic field strengths, the associated conditions are easier to fulfil for slower magnetic field ramps. The asymptotic spectrum is therefore approached as the ramp speed goes to zero for fixed initial and final fields, or as the initial and final fields become infinitely far from the resonance for a fixed ramp rate.

B.3 Asymptotic dissociation spectrum in the single-channel approach

In this section we show that the asymptotic dissociation spectrum of Eq. (3.15) can also be calculated within a single-channel approach, using the separable potential of Eq. (2.85). Given the resonance-enhanced behaviour of the scattering length of Eq. (2.18), Eq. (2.86) in general implies a nonlinear dependence of $\xi(B)$ on the magnetic field strength B. However, if B varies linearly with time, it can be shown that in the close vicinity of the singularity of the scattering length at $B = B_0$, the amplitude of the separable potential $\xi(B)$ follows the linear dependence given by

$$\xi(t) = \xi_0 + \dot{\xi}(t - t_0) . \tag{B.19}$$

Here $1/\xi_0 = \langle\chi_\mathrm{bg}|G_0(0)|\chi_\mathrm{bg}\rangle$, t_0 denotes the time when the zero-energy resonance is crossed, and

$$\dot{\xi} = \frac{m\dot{B}(2\pi\hbar)^3|\langle\chi|0\rangle|^2}{4\pi\hbar^2 a_\mathrm{bg}\Delta B|\langle\chi|G_0(0)|\chi\rangle|^2} . \tag{B.20}$$

In the following, we will assume that the linear form of Eq. (B.19) applies throughout the whole dissociation ramp. It can be shown that the final result is independent of the precise time dependence of $\xi(t)$ outside the near-resonant region. We have confirmed numerically that this is a valid approximation for the cases considered here. Given the linear time dependence of Eq. (B.19) and the separable form of the interaction potential in Eq. (2.85), the effective single-channel Hamiltonian is similar to the two-channel Hamiltonian of Eq. (3.11). Consequently, the analytic determination of the evolution operator for the single-channel Hamiltonian of Eq. (2.46) proceeds along the lines of Sec. B.1 by noting the following substitutions: H_{stat} is replaced by H_0, $E_{\mathrm{res}}(t)$ by $\xi(t)$, and $|\phi_{\mathrm{res}}, \mathrm{cl}\rangle$ by $|\chi\rangle$. A similar substitution is applied to the respective Green's functions and their matrix elements.

We will now evaluate the general expression of Eq. (3.4) for the dissociation transition amplitude in the asymptotic limit of $t_{\mathrm{i}} \to -\infty$ and $t_{\mathrm{f}} \to +\infty$ for the single-channel Hamiltonian. Applying the above substitutions, the contribution of Eq. (B.11) to $T_{\mathrm{diss}}(p)$ vanishes for the same reasons as in the two-channel case. The first phase integral of the remaining term in Eq. (B.11) is analogous to the two-channel case, and is given by Eq. (B.14) with the appropriate substitution. The second phase integral (corresponding to Eq. (B.16) in the two-channel case) takes the form

$$\int_{E_{\mathrm{b}}(B_{\mathrm{i}})}^{\infty} \frac{dE}{2\pi\hbar}\, e^{-i\varphi(z,t_{\mathrm{f}})} \frac{\langle \phi_{\mathbf{p}}^{(+)} | G_0(z) | \chi \rangle}{g_0(z)} \underset{t_{\mathrm{f}}\to\infty}{\sim} -\frac{i}{\hbar} e^{-i\varphi(z_p,t_{\mathrm{f}})} \frac{\langle \mathbf{p}|\chi\rangle}{g_0(z_p)} \,. \tag{B.21}$$

Here, $z_p = (p^2/m) + i0$. This leads to the following result for $T_{\mathrm{diss}}(p)$:

$$T_{\mathrm{diss}}(p) = -\sqrt{\frac{2\pi}{\hbar|\dot{\xi}|}} \frac{\langle \mathbf{p}|\chi\rangle}{g_0(z_p)} \exp\left(i[\varphi(E_{\mathrm{b}}(B_{\mathrm{i}}), t_{\mathrm{i}}) - \varphi(z_p, t_{\mathrm{f}}) + \pi/4]\right) . \tag{B.22}$$

To calculate the imaginary part of the phase difference we use the definition of $\varphi(E,t)$ of Eq. (B.8), yielding

$$\mathrm{Im}[\varphi(E_{\mathrm{b}}(B_{\mathrm{i}}), t_{\mathrm{i}}) - \varphi(z_p, t_{\mathrm{f}})] = \frac{1}{\hbar\dot{\xi}} \mathrm{Im} \int_0^{p^2/m} \frac{dE}{g_0(z)} \,. \tag{B.23}$$

Multiplying the numerator and denominator of the integrand by $-\xi(t_{\mathrm{f}})$, we then take the asymptotic limit of $t_{\mathrm{f}} \to +\infty$, in which case $\xi(t_{\mathrm{f}})$ is large and we can write

$$\mathrm{Im}[\varphi(E_{\mathrm{b}}(B_{\mathrm{i}}), t_{\mathrm{i}}) - \varphi(z_p, t_{\mathrm{f}})] \underset{t_{\mathrm{f}}\to\infty}{\sim} \frac{1}{\hbar\dot{\xi} g_0(0)} \mathrm{Im} \int_0^{\frac{p^2}{m}} dE \frac{1 - \xi(t_{\mathrm{f}}) g_0(0)}{1 - \xi(t_{\mathrm{f}}) g_0(z)} \,. \tag{B.24}$$

We then make use of Eq. (2.60) to rewrite this in terms of the T-matrix. Using the explicit expression for $\dot{\xi}$ given in Eq. (B.20) and the low-energy expansion of the T-matrix gives, in the Wigner threshold law regime,

$$\mathrm{Im}\left[\varphi(E_\mathrm{b}(B_\mathrm{i}), t_\mathrm{i}) - \varphi(z_p, t_\mathrm{f})\right] = \frac{2}{3}\frac{a_\mathrm{bg}\Delta B}{\hbar^2 m\dot{B}}p^3 \,. \tag{B.25}$$

By evaluating the remaining prefactors in Eq. (B.22) in the zero-momentum limit, we arrive at the final formula for the dissociation transition probability density:

$$|T_\mathrm{diss}(p)|^2 = \frac{|a_\mathrm{bg}\Delta B|}{\pi\hbar^2 m|\dot{B}|}\exp\left(-\frac{4}{3}\frac{a_\mathrm{bg}\Delta B}{\hbar^2 m\dot{B}}p^3\right), \tag{B.26}$$

which recovers Eq. (3.15).

Appendix C

Derivation of the non-Markovian Boltzmann equation

This appendix contains parts of the derivation of the non-Markovian Boltzmann equation in Sec. 4.4 and of the Markovian Boltzmann equation in Sec. 4.7 which were omitted for reasons of brevity. We first derive the free evolution of the two-body density matrix and show how it is substituted into Eq. (4.42) for the dynamics of the one-body density matrix. In the following section, we derive the simplifications to the dynamical equations due to translational invariance. This leads to the result of Eq. (4.43). Finally, in Sec. C.3 we derive a relation for the imaginary part of the T-matrix element which we use in Sec. 4.7.

C.1 Free evolution of the two-body density matrix

We solve for the free evolution of the two-body density matrix, $\Gamma^{(2,2)}_{m_2 m_3; j m_1}(t)$, by calculating its full dynamics and then neglecting all cumulants involving a product of more than four operators. The evolution of the expectation value $\langle a^\dagger_{j_1} a^\dagger_{j_2} a_{i_1} a_{i_2}\rangle_t$ is given by

$$\begin{aligned} i\hbar\frac{\partial}{\partial t}\langle a^\dagger_{j_1} a^\dagger_{j_2} a_{i_1} a_{i_2}\rangle_t &= \langle [a^\dagger_{j_1} a^\dagger_{j_2} a_{i_1} a_{i_2}, H]\rangle_t \\ &= i\hbar\frac{\partial}{\partial t}\left[\Gamma^{(2,2)}_{i_1 i_2; j_1 j_2}(t) + \Gamma_{i_1 j_1}(t)\Gamma_{i_2 j_2}(t) + \Gamma_{i_2 j_1}(t)\Gamma_{i_1 j_2}(t)\right] . \end{aligned} \tag{C.1}$$

Here, the second line has been obtained using the cumulant expansion of Eqs. (4.11)-(4.13), again neglecting non-number conserving terms. We then have

$$\begin{aligned} i\hbar\frac{\partial}{\partial t}\Gamma^{(2,2)}_{i_1i_2;j_1j_2}(t) &= \sum_{lm}\langle l|H_{1\mathrm{B}}|m\rangle\left\{\langle a^\dagger_{j_1}a^\dagger_{j_2}a_{i_1}a_{i_2}a^\dagger_l a_m\rangle_t - \langle a^\dagger_l a_m a^\dagger_{j_1}a^\dagger_{j_2}a_{i_1}a_{i_2}\rangle_t\right\} \\ &+ \frac{1}{2}\sum_{\substack{l_1l_2\\m_1m_2}}\langle l_1l_2|V|m_1m_2\rangle\left\{\langle a^\dagger_{j_1}a^\dagger_{j_2}a_{i_1}a_{i_2}a^\dagger_{l_1}a^\dagger_{l_2}a_{m_1}a_{m_2}\rangle_t - \langle a^\dagger_{l_1}a^\dagger_{l_2}a_{m_1}a_{m_2}a^\dagger_{j_1}a^\dagger_{j_2}a_{i_1}a_{i_2}\rangle_t\right\} \\ &- i\hbar\left[\Gamma_{i_1j_1}(t)\dot\Gamma_{i_2j_2}(t) + \dot\Gamma_{i_1j_1}(t)\Gamma_{i_2j_2}(t) + \Gamma_{i_2j_1}(t)\dot\Gamma_{i_1j_2}(t) + \dot\Gamma_{i_2j_1}(t)\Gamma_{i_1j_2}(t)\right]. \end{aligned} \tag{C.2}$$

Here, $\dot\Gamma_{i_1j_1}(t) = \frac{\partial}{\partial t}\Gamma_{i_1j_1}(t)$. The normal-ordering of the expectation values and taking out of the resulting delta functions then leaves only products of four and two operators:

$$\begin{aligned} i\hbar\frac{\partial}{\partial t}\Gamma^{(2,2)}_{i_1i_2;j_1j_2}(t) &= \sum_m\left[\langle i_2|H_{1\mathrm{B}}|m\rangle\langle a^\dagger_{j_1}a^\dagger_{j_2}a_{i_1}a_m\rangle_t + \langle i_1|H_{1\mathrm{B}}|m\rangle\langle a^\dagger_{j_1}a^\dagger_{j_2}a_{i_2}a_m\rangle_t\right] \\ &- \sum_l\left[\langle l|H_{1\mathrm{B}}|j_1\rangle\langle a^\dagger_l a^\dagger_{j_2}a_{i_1}a_{i_2}\rangle_t + \langle l|H_{1\mathrm{B}}|j_2\rangle\langle a^\dagger_l a^\dagger_{j_1}a_{i_1}a_{i_2}\rangle_t\right] \\ &+ \sum_{m_1m_2}\langle i_1i_2|V|m_1m_2\rangle\langle a^\dagger_{j_1}a^\dagger_{j_2}a_{m_1}a_{m_2}\rangle_t - \sum_{l_1l_2}\langle l_1l_2|V|j_1j_2\rangle\langle a^\dagger_{l_1}a^\dagger_{l_2}a_{i_1}a_{i_2}\rangle_t \\ &- i\hbar\left[\Gamma_{i_1j_1}(t)\Gamma'_{i_2j_2}(t) + \Gamma'_{i_1j_1}(t)\Gamma_{i_2j_2}(t) + \Gamma_{i_2j_1}(t)\Gamma'_{i_1j_2}(t) + \Gamma'_{i_2j_1}(t)\Gamma_{i_1j_2}(t)\right]. \end{aligned} \tag{C.3}$$

We next substitute for the dynamics of the one-body density matrix using Eq. (4.37). The free evolution of the one-body density matrices cancels out and we neglect the products of six operators that arise, having the form $\Gamma(t)\Gamma^{(2,2)}(t)$ or $\Gamma(t)\Gamma(t)\Gamma(t)$. The free evolution of $\Gamma^{(2,2)}_{i_1i_2;j_1j_2}(t)$ is then given by

$$\begin{aligned} i\hbar\frac{\partial}{\partial t}\Gamma^{(2,2)}_{i_1i_2;j_1j_2}(t) &= \sum_{m_1m_2}\langle i_1i_2|H_{2\mathrm{B}}|m_1m_2\rangle\Gamma^{(2,2)}_{m_1m_2;j_1j_2}(t) - \sum_{l_1l_2}\langle l_1l_2|H_{2\mathrm{B}}|j_1j_2\rangle\Gamma^{(2,2)}_{i_1i_2;l_1l_2}(t) \\ &+ \sum_{m_1m_2}\langle i_1i_2|V|m_1m_2\rangle\left[\Gamma_{m_1j_1}(t)\Gamma_{m_2j_2}(t) + \Gamma_{m_2j_1}(t)\Gamma_{m_1j_2}(t)\right] \\ &- \sum_{l_1l_2}\langle l_1l_2|V|j_1j_2\rangle\left[\Gamma_{i_1l_1}(t)\Gamma_{i_2l_2}(t) + \Gamma_{i_2l_1}(t)\Gamma_{i_1l_2}(t)\right]. \end{aligned} \tag{C.4}$$

The formal solution to this is the following:

$$\begin{aligned}\Gamma^{(2,2)}_{i_1 i_2; j_1 j_2}(t) = &\sum_{\substack{k_1 k_2 \\ k_3 k_4}} \langle i_1 i_2 | U_{2\mathrm{B}}(t, t_\mathrm{i}) | k_1 k_2 \rangle \Gamma^{(2,2)}_{k_1 k_2; k_3 k_4}(t_\mathrm{i}) \langle k_3 k_4 | U^\dagger_{2\mathrm{B}}(t, t_\mathrm{i}) | j_1 j_2 \rangle \\ &+ \frac{1}{i\hbar} \int_{t_\mathrm{i}}^{t} dt' \sum_{\substack{k_1 k_2 \\ k_3 k_4}} \left[\Gamma_{k_1 k_3}(t') \Gamma_{k_2 k_4}(t') + \Gamma_{k_1 k_4}(t') \Gamma_{k_2 k_3}(t') \right] \\ &\times \Big\{ \langle i_1 i_2 | U_{2\mathrm{B}}(t, t') V(t') | k_1 k_2 \rangle \langle k_3 k_4 | U^\dagger_{2\mathrm{B}}(t, t') | j_1 j_2 \rangle \\ &- \langle i_1 i_2 | U_{2\mathrm{B}}(t, t') | k_1 k_2 \rangle \langle k_3 k_4 | [U_{2\mathrm{B}}(t, t') V(t')]^\dagger | j_1 j_2 \rangle \Big\} . \end{aligned} \tag{C.5}$$

Converting this expression to the interaction picture using the definitions of Eqs. (4.38) - (4.41), we are able to replace the potentials $V_\mathrm{I}(t')$ with derivatives. This leads to

$$\begin{aligned}\Gamma^{(2,2)\mathrm{I}}_{i_1 i_2; j_1 j_2}(t) = &\sum_{\substack{k_1 k_2 \\ k_3 k_4}} \langle i_1 i_2 | U^\mathrm{I}_{2\mathrm{B}}(t, t_\mathrm{i}) | k_1 k_2 \rangle \Gamma^{(2,2)\mathrm{I}}_{k_1 k_2; k_3 k_4}(t_\mathrm{i}) \langle k_3 k_4 | [U^\mathrm{I}_{2\mathrm{B}}(t, t_\mathrm{i})]^\dagger | j_1 j_2 \rangle \\ &- \int_{t_\mathrm{i}}^{t} dt' \sum_{\substack{k_1 k_2 \\ k_3 k_4}} \left[\Gamma^\mathrm{I}_{k_1 k_3}(t') \Gamma^\mathrm{I}_{k_2 k_4}(t') + \Gamma^\mathrm{I}_{k_1 k_4}(t') \Gamma^\mathrm{I}_{k_2 k_3}(t') \right] \\ &\times \frac{\partial}{\partial t'} \left\{ \langle i_1 i_2 | U^\mathrm{I}_{2\mathrm{B}}(t, t') | k_1 k_2 \rangle \langle k_3 k_4 | [U^\mathrm{I}_{2\mathrm{B}}(t, t')]^\dagger | j_1 j_2 \rangle \right\} . \end{aligned} \tag{C.6}$$

Substituting the formal solution for the two-body density matrix into Eq. (4.42) gives the following result in the interaction picture:

$$
\begin{aligned}
i\hbar\frac{\partial}{\partial t}\Gamma^{\mathrm{I}}_{ij}(t) = &\sum_{lm_1m_2}\langle il|V_{\mathrm{I}}(t)|m_1m_2\rangle\left[\Gamma^{\mathrm{I}}_{m_1l}(t)\Gamma^{\mathrm{I}}_{m_2j}(t)+\Gamma^{\mathrm{I}}_{m_1j}(t)\Gamma^{\mathrm{I}}_{m_2l}(t)\right]\\
&-\sum_{l_1l_2m}\langle l_1l_2|V_{\mathrm{I}}(t)|jm\rangle\left[\Gamma^{\mathrm{I}}_{ml_1}(t)\Gamma^{\mathrm{I}}_{il_2}(t)+\Gamma^{\mathrm{I}}_{ml_2}(t)\Gamma^{\mathrm{I}}_{il_1}(t)\right]\\
&+\sum_{\substack{k_1k_2\\k_3k_4}}\sum_{l}\langle il|V_{\mathrm{I}}(t)U^{\mathrm{I}}_{2\mathrm{B}}(t,t_{\mathrm{i}})|k_1k_2\rangle\Gamma^{(2,2)\mathrm{I}}_{k_1k_2;k_3k_4}(t_{\mathrm{i}})\langle k_3k_4|[U^{\mathrm{I}}_{2\mathrm{B}}(t,t_{\mathrm{i}})]^{\dagger}|lj\rangle\\
&-\sum_{\substack{k_1k_2\\k_3k_4}}\sum_{m}\langle mi|U^{\mathrm{I}}_{2\mathrm{B}}(t,t_{\mathrm{i}})|k_1k_2\rangle\Gamma^{(2,2)\mathrm{I}}_{k_1k_2;k_3k_4}(t_{\mathrm{i}})\langle k_3k_4|[V_{\mathrm{I}}(t)U^{\mathrm{I}}_{2\mathrm{B}}(t,t_{\mathrm{i}})]^{\dagger}|jm\rangle\\
&-\int_{t_{\mathrm{i}}}^{t}dt'\sum_{\substack{k_1k_2\\k_3k_4}}\sum_{l}\left[\Gamma^{\mathrm{I}}_{k_1k_3}(t')\Gamma^{\mathrm{I}}_{k_2k_4}(t')+\Gamma^{\mathrm{I}}_{k_1k_4}(t')\Gamma^{\mathrm{I}}_{k_2k_3}(t')\right]\\
&\times\frac{\partial}{\partial t'}\left(\langle il|V_{\mathrm{I}}(t)U^{\mathrm{I}}_{2\mathrm{B}}(t,t')|k_1k_2\rangle\langle k_3k_4|[U^{\mathrm{I}}_{2\mathrm{B}}(t,t')]^{\dagger}|lj\rangle\right)\\
&+\int_{t_{\mathrm{i}}}^{t}dt'\sum_{\substack{k_1k_2\\k_3k_4}}\sum_{m}\left[\Gamma^{\mathrm{I}}_{k_1k_3}(t')\Gamma^{\mathrm{I}}_{k_2k_4}(t')+\Gamma^{\mathrm{I}}_{k_1k_4}(t')\Gamma^{\mathrm{I}}_{k_2k_3}(t')\right]\\
&\times\frac{\partial}{\partial t'}\left(\langle im|U^{\mathrm{I}}_{2\mathrm{B}}(t,t')|k_1k_2\rangle\langle k_3k_4|[V_{\mathrm{I}}(t)U^{\mathrm{I}}_{2\mathrm{B}}(t,t')]^{\dagger}|mj\rangle\right). \qquad \text{(C.7)}
\end{aligned}
$$

Replacing the potential $V_{\mathrm{I}}(t)$ with a time derivative, and separating out the kernel of the integral equation, we have

$$
\begin{aligned}
i\hbar\frac{\partial}{\partial t}\Gamma^{\mathrm{I}}_{ij}(t) = &\, i\hbar\frac{\partial}{\partial t}\Bigg(\sum_{\substack{k_1k_2\\k_3k_4}}\sum_{l}\langle il|U^{\mathrm{I}}_{2\mathrm{B}}(t,t_{\mathrm{i}})|k_1k_2\rangle\Gamma^{(2,2)\mathrm{I}}_{k_1k_2;k_3k_4}(t_{\mathrm{i}})\langle k_3k_4|[U^{\mathrm{I}}_{2\mathrm{B}}(t,t_{\mathrm{i}})]^{\dagger}|lj\rangle\Bigg)\\
&+\int_{t_{\mathrm{i}}}^{\infty}dt'\sum_{\substack{k_1k_2\\k_3k_4}}\left[\Gamma^{\mathrm{I}}_{k_1k_3}(t')\Gamma^{\mathrm{I}}_{k_2k_4}(t')+\Gamma^{\mathrm{I}}_{k_1k_4}(t')\Gamma^{\mathrm{I}}_{k_2k_3}(t')\right]\mathcal{K}^{ij}_{k_1k_2k_3k_4}(t,t'). \qquad \text{(C.8)}
\end{aligned}
$$

Here, the kernel is given by

$$
\mathcal{K}^{ij}_{k_1k_2k_3k_4}(t,t') = -i\hbar\frac{\partial}{\partial t'}\Bigg[\theta(t-t')\frac{\partial}{\partial t}\sum_{l}\left\{\langle il|U^{\mathrm{I}}_{2\mathrm{B}}(t,t')|k_1k_2\rangle\langle k_3k_4|[U^{\mathrm{I}}_{2\mathrm{B}}(t,t')]^{\dagger}|lj\rangle\right\}\Bigg]. \qquad \text{(C.9)}
$$

C.2 Translational invariance of the one-body density matrix

Translational invariance implies the following relation for the density matrix [220]:

$$
e^{-i\hat{\mathbf{p}}\cdot\mathbf{a}/\hbar}\rho(t)e^{i\hat{\mathbf{p}}\cdot\mathbf{a}/\hbar} = \rho(t). \qquad \text{(C.10)}
$$

where the exponentials act to displace an operator by $\mathbf{a}$ in position space. The momentum operator $\hat{\mathbf{p}}$ is given in the second-quantised formalism by

$$\hat{\mathbf{p}} = \int d\mathbf{x}\psi^\dagger(\mathbf{x})(-i\hbar\nabla_{\mathbf{x}})\psi(\mathbf{x})\,. \tag{C.11}$$

An expectation value in momentum space can be written as a Fourier transform:

$$\begin{aligned}\langle a^\dagger_{\mathbf{p}_1}\cdots a^\dagger_{\mathbf{p}_n}a_{\mathbf{q}_n}\cdots a_{\mathbf{q}_1}\rangle = (2\pi\hbar)^{-3n}\int d\mathbf{x}_1\cdots d\mathbf{x}_n d\mathbf{y}_n\cdots d\mathbf{y}_1\langle\psi^\dagger(\mathbf{x}_1)\cdots\psi^\dagger(\mathbf{x}_n)\psi(\mathbf{y}_n)\cdots\psi(\mathbf{y}_1)\rangle \\ \times\exp\left(-\frac{i}{\hbar}[\mathbf{q}_1\cdot\mathbf{y}_1+\cdots+\mathbf{q}_n\cdot\mathbf{y}_n-\mathbf{p}_n\cdot\mathbf{x}_n-\cdots-\mathbf{p}_1\cdot\mathbf{x}_1]\right)\,.\end{aligned} \tag{C.12}$$

Using the result of Eq. (C.10), and applying translation operators to the field operators in position space, we have

$$\begin{aligned}\langle\psi^\dagger(\mathbf{x}_1)\cdots\psi^\dagger(\mathbf{x}_n)\psi(\mathbf{y}_n)\cdots\psi(\mathbf{y}_1)\rangle &= \mathrm{Tr}\left(\psi^\dagger(\mathbf{x}_1)\cdots\psi(\mathbf{y}_1)\rho(t)\right)\\ &= \mathrm{Tr}\left(\psi^\dagger(\mathbf{x}_1)\cdots\psi(\mathbf{y}_1)e^{-i\hat{\mathbf{p}}\cdot\mathbf{a}/\hbar}\rho(t)e^{i\hat{\mathbf{p}}\cdot\mathbf{a}/\hbar}\right)\\ &= \mathrm{Tr}\left(e^{i\hat{\mathbf{p}}\cdot\mathbf{a}/\hbar}\psi^\dagger(\mathbf{x}_1)e^{-i\hat{\mathbf{p}}\cdot\mathbf{a}/\hbar}e^{i\hat{\mathbf{p}}\cdot\mathbf{a}/\hbar}\cdots e^{-i\hat{\mathbf{p}}\cdot\mathbf{a}/\hbar}e^{i\hat{\mathbf{p}}\cdot\mathbf{a}/\hbar}\psi(\mathbf{y}_1)e^{-i\hat{\mathbf{p}}\cdot\mathbf{a}/\hbar}\rho(t)\right)\\ &= \langle\psi^\dagger(\mathbf{x}_1-\mathbf{a})\cdots\psi(\mathbf{y}_1-\mathbf{a})\rangle\,.\end{aligned} \tag{C.13}$$

Here, we have also used the cyclic property of the trace operation. Substituting this into Eq. (C.12) and transforming the coordinates gives

$$\langle a^\dagger_{\mathbf{p}_1}\cdots a^\dagger_{\mathbf{p}_n}a_{\mathbf{q}_n}\cdots a_{\mathbf{q}_1}\rangle = \exp\left(\frac{i}{\hbar}\mathbf{a}\cdot(\mathbf{p}_1+\cdots\mathbf{p}_n-\mathbf{q}_n-\cdots-\mathbf{q}_1)\right)\langle a^\dagger_{\mathbf{p}_1}\cdots a^\dagger_{\mathbf{p}_n}a_{\mathbf{q}_n}\cdots a_{\mathbf{q}_1}\rangle\,, \tag{C.14}$$

which is true for all $\mathbf{a}$ if and only if $\mathbf{p}_1+\cdots+\mathbf{p}_n-\mathbf{q}_n-\cdots-\mathbf{q}_1=0$.

We now show how the imposition of translational invariance changes the one-body density matrix. In position space, translational invariance leads the one-body density matrix to depend only on the difference of coordinate:

$$\Gamma(\mathbf{x},\mathbf{y},t) = \bar{\Gamma}(|\mathbf{x}-\mathbf{y}|,t)\,. \tag{C.15}$$

Here, we have defined the reduced one-body density matrix $\bar{\Gamma}(|\mathbf{x}-\mathbf{y}|,t)$ such that

$$\bar{\Gamma}(0,t) = \Gamma(\mathbf{x},\mathbf{x},t) = n\,, \tag{C.16}$$

where n is the density of the gas. The one-body density matrix in momentum space may be written as a Fourier transform,

$$\Gamma(\mathbf{p},\mathbf{q},t) = \frac{1}{(2\pi\hbar)^3}\int d\mathbf{x}d\mathbf{y}\exp[i(\mathbf{p}\cdot\mathbf{x}-\mathbf{q}\cdot\mathbf{y})/\hbar]\Gamma(\mathbf{x},\mathbf{y},t)\,. \tag{C.17}$$

Substituting Eq. (C.15) into this relation, and defining $\mathbf{z} = \mathbf{x} - \mathbf{y}$ gives

$$\Gamma(\mathbf{p}, \mathbf{q}, t) = \delta(\mathbf{p} - \mathbf{q}) \int d\mathbf{z} e^{i\mathbf{p}\cdot\mathbf{z}} \bar{\Gamma}(z, t) \tag{C.18}$$

$$= \sqrt{(2\pi\hbar)^3}\delta(\mathbf{p} - \mathbf{q})\bar{\Gamma}(p, t)\,. \tag{C.19}$$

For notational convenience, we absorb the factor $\sqrt{(2\pi\hbar)^3}$ into the reduced one-body density matrix, making it dimensionless, and write it as $\Gamma(p, t)$. In terms of the full one-body density matrix, it is then given by Eq. (4.44). With this definition, the reduced density matrix has the normalisation

$$\int d\mathbf{p}\Gamma(p, t) = (2\pi\hbar)^3 n\,. \tag{C.20}$$

We now apply the requirement of translational invariance to Eq. (C.8), taking the homogeneous gas limit at the same time. The box states are transformed according to Eq. (4.64). The matrix elements of the two-body evolution operator become

$$\langle il|U^{\mathrm{I}}_{2\mathrm{B}}(t, t')|k_1 k_2\rangle \to \delta(\mathbf{p} + \mathbf{q} - \mathbf{p}_1 - \mathbf{p}_2)\langle(\mathbf{p} - \mathbf{q}_1)/2|U^{\mathrm{I}}_{2\mathrm{B}}(t, t')|(\mathbf{p}_1 - \mathbf{p}_2)/2\rangle \left[\frac{(2\pi\hbar)^3}{\mathcal{V}}\right]^2, \tag{C.21}$$

where $\mathcal{V}$ is the volume of the box, and we have separated out the relative and centre of mass coordinates. Neglecting the initial two-body correlations then gives

$$\begin{aligned}\frac{\partial}{\partial t}\Gamma^{\mathrm{I}}(p, t) = -\frac{2}{i\hbar}\int_{t_{\mathrm{i}}}^{\infty} dt' \int d\mathbf{p}_1 d\mathbf{p}_2 \Gamma^{\mathrm{I}}(p_1, t')\Gamma^{\mathrm{I}}(p_2, t') \\ \times \frac{\partial}{\partial t'}\Big(\theta(t - t')[\langle\mathbf{p}_{\mathrm{cm}}|V_{\mathrm{I}}(t)U^{\mathrm{I}}_{2\mathrm{B}}(t, t')|\mathbf{p}_{\mathrm{r}}\rangle\langle\mathbf{p}_{\mathrm{r}}|[U^{\mathrm{I}}_{2\mathrm{B}}(t, t')]^\dagger|\mathbf{p}_{\mathrm{cm}}\rangle \\ - \langle\mathbf{p}_{\mathrm{cm}}|U^{\mathrm{I}}_{2\mathrm{B}}(t, t')|\mathbf{p}_{\mathrm{r}}\rangle\langle\mathbf{p}_{\mathrm{r}}|[V_{\mathrm{I}}(t)U^{\mathrm{I}}_{2\mathrm{B}}(t, t')]^\dagger|\mathbf{p}_{\mathrm{cm}}\rangle]\Big)\,.\end{aligned} \tag{C.22}$$

Here, $\mathbf{p}_{\mathrm{r}} = (\mathbf{p}_1 - \mathbf{p}_2)/2$, and $\mathbf{p}_{\mathrm{cm}} = \mathbf{p} - (\mathbf{p}_1 + \mathbf{p}_2)/2$. We perform the integration by parts with respect to t', and note that the second term of the square brackets is the complex conjugate of the first. This gives

$$\begin{aligned}\frac{\partial}{\partial t}\Gamma^{\mathrm{I}}(p, t) = \frac{4}{\hbar}\int d\mathbf{p}_1 d\mathbf{p}_2 \Gamma^{\mathrm{I}}(p_1, t_{\mathrm{i}})\Gamma^{\mathrm{I}}(p_2, t_{\mathrm{i}})\mathrm{Im}[\langle\mathbf{p}_{\mathrm{cm}}|V_{\mathrm{I}}(t)U^{\mathrm{I}}_{2\mathrm{B}}(t, t_{\mathrm{i}})|\mathbf{p}_{\mathrm{r}}\rangle\langle\mathbf{p}_{\mathrm{r}}|[U^{\mathrm{I}}_{2\mathrm{B}}(t, t_{\mathrm{i}})]^\dagger|\mathbf{p}_{\mathrm{cm}}\rangle] \\ + \frac{4}{\hbar}\int_{t_{\mathrm{i}}}^{t} dt' \int d\mathbf{p}_1 d\mathbf{p}_2 \mathrm{Im}[\langle\mathbf{p}_{\mathrm{cm}}|V_{\mathrm{I}}(t)U^{\mathrm{I}}_{2\mathrm{B}}(t, t')|\mathbf{p}_{\mathrm{r}}\rangle\langle\mathbf{p}_{\mathrm{r}}|[U^{\mathrm{I}}_{2\mathrm{B}}(t, t')]^\dagger|\mathbf{p}_{\mathrm{cm}}\rangle] \\ \times \frac{\partial}{\partial t'}(\Gamma^{\mathrm{I}}(p_1, t')\Gamma^{\mathrm{I}}(p_2, t'))\,.\end{aligned} \tag{C.23}$$

In the interaction picture, the integral equation for the two-body evolution operator of Eq. (4.32) becomes

$$U^{\mathrm{I}}_{2\mathrm{B}}(t,t') = 1 + \frac{1}{i\hbar}\int_{t'}^{t} d\tau U^{\mathrm{I}}_{2\mathrm{B}}(t,\tau)V_{\mathrm{I}}(\tau) \tag{C.24}$$

$$= 1 + \frac{1}{i\hbar}\int_{t'}^{t} d\tau V_{\mathrm{I}}(\tau)U^{\mathrm{I}}_{2\mathrm{B}}(\tau,t')\,. \tag{C.25}$$

From these equations it is clear that matrix elements of the form $\langle \mathbf{q}|U^{\mathrm{I}}_{2\mathrm{B}}(t,t')|\mathbf{p}\rangle$ have a delta function component in momentum. We can remove these from Eq. (C.23), which leaves the non-Markovian Boltzmann equation of Eq. (4.43).

C.3 Optical theorem

From the definition of $t(\mathbf{p},\mathbf{p}')$ in Eq. (4.85), we can write

$$\mathrm{Im}t(\mathbf{p},\mathbf{p}') = -\frac{1}{2i}\langle \mathbf{p}|[T((p'^2/m)-i0) - T((p'^2/m)+i0)]|\mathbf{p}'\rangle\,. \tag{C.26}$$

From the identity of Eq. (2.62), it may be shown that $T^{-1}(z) = V^{-1} - G_0(z)$, and consequently that

$$T(z) - T(z^*) = T(z^*)\left[G_0(z) - G_0(z^*)\right]T(z)\,. \tag{C.27}$$

Substituting this into Eq. (C.26) and performing a spectral decomposition gives

$$\begin{aligned}\mathrm{Im}t(\mathbf{p},\mathbf{p}') = &-\frac{1}{2i}\int d\mathbf{q}\langle \mathbf{p}|T((p'^2/m)-i0)|\mathbf{q}\rangle\left(\left[\tfrac{p'^2}{m}-\tfrac{q^2}{m}-i0\right]^{-1} - \left[\tfrac{p'^2}{m}-\tfrac{q^2}{m}+i0\right]^{-1}\right)\\ &\times\langle \mathbf{q}|T((p'^2/m)+i0)|\mathbf{p}'\rangle\\ = &-\pi\int d\mathbf{q}\,\delta\left(\frac{p'^2}{m}-\frac{q^2}{m}\right)\langle \mathbf{p}|T((p'^2/m)-i0)|\mathbf{q}\rangle\langle \mathbf{q}|T((p'^2/m)+i0)|\mathbf{p}'\rangle\,.\end{aligned} \tag{C.28}$$

Appendix D

Matrix elements for the kernel of the non-Markovian Boltzmann equation

D.1 Calculation of $\langle\chi|U_{\mathbf{2B}}(t,t')|\chi\rangle$

In this section we detail the calculation of $f(t,t') = \langle\chi|U_{2\mathrm{B}}(t,t')|\chi\rangle$, where $|\chi\rangle$ is the form factor of the single-channel potential of Eq. (2.85). The Lippman-Schwinger equation of Eq. (4.32) may be closed by $|\chi\rangle$ on each side to give a Volterra equation:

$$f(t,t') = f_0(t-t') + \frac{1}{i\hbar}\int_{t'}^{t} d\tau f(t,\tau)\xi(\tau)f_0(\tau-t')\,. \tag{D.1}$$

Here, $f_0(t-t') = \langle\chi|U_0(t-t')|\chi\rangle$ is the matrix element of the free evolution operator. We make the following definitions for the matrix element of the free Green's function and its anti-derivatives:

$$k(\tau-t') = \langle\chi|G_0(\tau-t')|\chi\rangle\,, \tag{D.2}$$

$$K(\tau-t') = -\int d\tau k(\tau-t')\,, \tag{D.3}$$

$$\kappa(\tau-t') = -\int d\tau K(\tau-t')\,. \tag{D.4}$$

Here, $G_0(\tau-t') = \frac{1}{i\hbar}\theta(\tau-t')U_0(\tau-t')$ is the free Green's function. The function $f_0(t-t')$ can be calculated from a spectral decomposition:

$$f_0(t-t') = \frac{1}{8\pi^{3/2}\hbar^3\left(\frac{\sigma^2}{\hbar^2} + \frac{i(t-t')}{m\hbar}\right)^{3/2}}\,. \tag{D.5}$$

Here, σ is the range of the potential, defined in Eq. (2.63). From Eq. (D.2), we see that Eq. (D.5) also gives $k(t-t')$. The anti-derivatives of this can also be calculated analytically, providing $K(t-t')$ and $\kappa(t-t')$.

For the numerical solution of Eq. (D.1), we define a grid of $(n+1)$ points τ_i from $\tau_0 = t'$ to $\tau_n = t$. We then have:

$$f(t,\tau_i) = f_0(t-\tau_i) - \int_{\tau_i}^{t} d\tau' f(t,\tau')\xi(\tau')\frac{\partial}{\partial\tau'}K(\tau'-\tau_i)\,. \tag{D.6}$$

Starting at τ_n, for which $f(t,t) = f_0(0)$, we propagate this backwards in the second time variable to τ_0. We evaluate the integral in Eq. (D.6) using integration by parts, and then splitting the integral into the intervals defined by the mesh:

$$\begin{aligned}\int_{\tau_i}^{t} d\tau' f(t,\tau')\xi(\tau')\frac{\partial}{\partial\tau'}K(\tau'-\tau_i) = f(t,t)\xi(t)K(t-\tau_i) - f(t,\tau_i)\xi(\tau_i)K(0)\\ - \sum_{j=i+1}^{n}\int_{\tau_{j-1}}^{\tau_j} d\tau' K(\tau'-\tau_i)\frac{\partial}{\partial\tau'}\left[f(t,\tau')\xi(\tau')\right]\,.\end{aligned} \tag{D.7}$$

We approximate $f(t,\tau')\xi(\tau')$ to be piecewise linear over the mesh. Then, substituting Eq. (D.7) into Eq. (D.6) and rearranging gives

$$f(t,\tau_i) = N_i/D_i\,, \tag{D.8}$$

where

$$N_i = f_0(t-\tau_i) - f(t,t)\xi(t)K(t-\tau_i) - \sum_{j=i+2}^{n}\gamma_j[\kappa(\tau_j-\tau_i) - \kappa(\tau_{j-1}-\tau_i)]\,, \tag{D.9}$$

$$D_i = 1 - \xi(\tau_i)K(0) - \xi(\tau_i)\frac{\kappa(\tau_{i+1}-\tau_i)-\kappa(0)}{\tau_{i+1}-\tau_i}\,. \tag{D.10}$$

Here, $\gamma_j = [f(t,\tau_j)\xi(\tau_j) - f(t,\tau_{j-1})\xi(\tau_{j-1})]/[\tau_j - \tau_{j-1}]$. By applying this method for a suitable range of t, we obtain $f(t,t')$ as a function of (t,t'). An analogous method can be applied to solve the Volterra equation for $f(t,\tau)$ in the forward direction, i.e. as a function of the first time variable. From $f(t,t')$ we can calculate the memory function $h(t,t')$ of Eq. (4.31). $f(t,t')$ is also used in the calculation of the kernel for the single-integral term of the non-Markovian Boltzmann equation, as discussed in Chapter 6. In the following sections we discuss the calculation of the other matrix elements required for calculating the kernel of this equation.

D.2 Calculation of $\langle\chi|U_{2\mathrm{B}}(t,t')|\mathbf{p}\rangle$

The integral equation for $U_{2\mathrm{B}}(t,t')$ in Eq. (4.32), referred to as the pre-form, and the associated post-form of Eq. (4.33), may be closed by $\langle\chi|$ and $|\mathbf{p}\rangle$ to give

$$\langle\chi|U_{2\mathrm{B}}(t,t')|\mathbf{p}\rangle = \langle\chi|U_0(t-t')|\mathbf{p}\rangle + \frac{1}{i\hbar}\int_{t'}^{t} d\tau f(t,\tau)\xi(\tau)\langle\chi|U_0(\tau-t')|\mathbf{p}\rangle\,. \tag{D.11}$$

$$\langle\chi|U_{2\mathrm{B}}(t,t')|\mathbf{p}\rangle = \langle\chi|U_0(t-t')|\mathbf{p}\rangle + \frac{1}{i\hbar}\int_{t'}^{t} d\tau f_0(t-\tau)\xi(\tau)\langle\chi|U_{2\mathrm{B}}(\tau,t')|\mathbf{p}\rangle\,, \tag{D.12}$$

Here, $f(t,\tau)$ and $f_0(t-\tau)$ are as defined in the previous section. As these equations show, it is only possible to obtain a closed integral equation for $\langle\chi|U_{2\mathrm{B}}(t,t')|\mathbf{p}\rangle$ as a function of the first time variable. For this case, it may be calculated with the same method as in the previous section. To obtain $\langle\chi|U_{2\mathrm{B}}(t,t')|\mathbf{p}\rangle$ as a function of the second variable, we calculate it from $f(t,t')$. Using Eq. (D.11), we have

$$\langle\chi|U_{2\mathrm{B}}(t,t')|\mathbf{p}\rangle - \langle\chi|U_0(t-t')|\mathbf{p}\rangle = \frac{\langle\chi|\mathbf{p}\rangle}{i\hbar}\int_{t'}^{t} d\tau f(t,\tau)\xi(\tau)\exp\left(-i\frac{p^2}{m\hbar}(\tau-t')\right)\,. \tag{D.13}$$

We now define a grid transformation,

$$u = -(\varphi_\mathrm{b}(t)-\varphi_\mathrm{b}(\tau)) + (p^2/m+\Delta E)(t-\tau)/\hbar\,. \tag{D.14}$$

Here, $\varphi_\mathrm{b}(t') = \varphi(E_\mathrm{b}(t'),t')$ is the bound state phase of Eq. (B.8). We add a small energy shift ΔE so that this transformation is well defined for the case where $\tau < t_0$ (where $\varphi_\mathrm{b}(\tau) = 0$) and $p^2/m = 0$. For evaluating the phase at the bound state energy for a linear ramp which ends on the positive scattering length side of the resonance, we can rewrite Eq. (B.8) as

$$\varphi_\mathrm{b}(t') = \varphi(E_\mathrm{b}(t'),t') = \frac{E_\mathrm{b}(t')(t'-t_\mathrm{res})}{\hbar} - \frac{1}{\hbar\dot{E}_\mathrm{res}}\int_{t_0}^{t'} d\tau\dot{E}_\mathrm{b}(B(\tau))E_\mathrm{res}(B(\tau))\,. \tag{D.15}$$

Here, we have used the condition that the magnetic field dependent energy of the molecular bound state is constrained by Eq. (B.12). The time t_0 is that at which the resonance is crossed, i.e. $B(t_0) = B_0$. Integrating by parts then gives the result

$$\varphi_\mathrm{b}(t') = \frac{1}{\hbar}\int_{t_0}^{t'} d\tau E_\mathrm{b}(B(\tau))\,. \tag{D.16}$$

Making the substitution of Eq. (D.14) allows us to evaluate an integral over time of the function $e^{i(\varphi_\mathrm{b}(t)-\varphi_\mathrm{b}(t'))}f(t,t')$, which is slowly varying by comparison to $f(t,t')$. The right-hand side of Eq. (D.13) then becomes

$$\frac{\langle\chi|\mathbf{p}\rangle}{i\hbar}e^{-i\frac{p^2}{m\hbar}(t-t')}\int_{u_\mathrm{i}}^{u_\mathrm{f}} du F(u)e^{iu}\,, \tag{D.17}$$

where $u_\mathrm{i} = u(t')$, $u_\mathrm{f} = u(t)$, and

$$F(u) = \left.\frac{\hbar e^{i(\varphi_\mathrm{b}(t)-\varphi_\mathrm{b}(\tau))}e^{-i\Delta E(t-\tau)}f(t,\tau)\xi(\tau)}{E_\mathrm{b}(\tau) - (p^2/m + \Delta E)}\right|_{\tau=t(u)}. \tag{D.18}$$

We split the range of integration up into small regions defined by mesh-points u_j, with $u_0 = u_\mathrm{i}$ and $u_\mathrm{N} = u_\mathrm{f}$, on which $F(u)$ is approximately linear, i.e. $F(u) \approx F_j + \alpha_j(u' - u_j)$, with $\alpha_j = (F_{j+1} - F_j)/(u_{j+1} - u_j)$. We then have

$$\langle\chi|U_\mathrm{2B}(t,t')|\mathbf{p}\rangle - \langle\chi|U_0(t-t')|\mathbf{p}\rangle = \frac{\langle\chi|\mathbf{p}\rangle}{i\hbar}e^{-i\frac{p^2}{m\hbar}(t-t')}\sum_{j=0}^{N-1}\int_{u_j}^{u_{j+1}} du[F_j + \alpha_j(u-u_j)]e^{iu} \tag{D.19}$$

$$= -\frac{\langle\chi|\mathbf{p}\rangle}{\hbar}e^{-i\frac{p^2}{m\hbar}(t-t')}\left\{e^{iu_\mathrm{f}}F(u_\mathrm{f}) - e^{iu_\mathrm{i}}F(u_\mathrm{i}) + i\sum_{j=0}^{N-1}\alpha_j(e^{iu_{j+1}} - e^{iu_j})\right\}. \tag{D.20}$$

Here, we have evaluated the integrals, and then the summation to reach Eq. (D.20).

D.3 Fourier transform of $\langle\chi|U_\mathrm{2B}(t,t')|\mathbf{p}\rangle$

To make storage of $\langle\chi|U_\mathrm{2B}(t,t')|\mathbf{p}\rangle$ and the subsequent Fourier transform easier, we take out the phases due to the bound state and continuum states. The Fourier transform of Eq. (6.6) can then be written as

$$\int_{t'}^{t} d\tau \exp\left(i\frac{q^2-p^2}{m\hbar}(\tau-t') - i(\varphi_\mathrm{b}(\tau) - \varphi_\mathrm{b}(t'))\right)$$
$$\times\left[\exp\left(i\frac{p^2}{m\hbar}(\tau-t') + i(\varphi_\mathrm{b}(\tau) - \varphi_\mathrm{b}(t'))\right)\xi(t)\langle\chi|U_\mathrm{2B}(\tau,t')|\mathbf{p}\rangle\right]. \tag{D.21}$$

We calculate $\langle\chi|U_\mathrm{2B}(\tau,t')|\mathbf{p}\rangle$ as a function of the first variable from Eq. (D.12), using a technique similar to that described in Sec. D.1. We then store the quantity in the square brackets in Eq. (D.21). For calculating the Fourier integral, we define the grid transformation

$$u = \frac{q^2-p^2}{m\hbar}(\tau-t') - [\varphi_\mathrm{b}(\tau) - \varphi_\mathrm{b}(t')]. \tag{D.22}$$

This transformation is only well-defined when $((q^2 - p^2)/m - E_\mathrm{b}(\tau) > 0)$ throughout the ramp, as otherwise there can be a point at which $\frac{du}{d\tau} = 0$. When this condition is not fulfilled, we take out just the bound state phase, and use the transformation $u = \Delta E(\tau - t') - (\varphi_\mathrm{b}(\tau) - \varphi_\mathrm{b}(t'))$. Having made the change of variables, the integral can be evaluated using a method similar to that of Sec. D.2.

Bibliography

[1] S. N. Bose, *Z. Phys.* **26**, 178 (1924), English translation by O. Theimer and B. Ram: Am. J. Phys. **44**, 1056 (1976).* {1}

[2] A. Einstein, *Sitzungsber. Preuss. Akad. Wiss., Phys. Math. Kl.* **22**, 261 (1924). {1}

[3] A. Einstein, *Sitzungsber. Preuss. Akad. Wiss., Phys. Math. Kl.* **1**, 3 (1925), available online at 'http://www.lorentz.leidenuniv.nl/history/Einstein_archive/Einstein_1925_publication/'. {1}

[4] F. London, *Nature (London)* **141**, 643 (1938). {1}

[5] F. London, *Phys. Rev.* **54**, 947 (1938). {1}

[6] E. Fermi, *Rend. R. Accad. Lincei* **3**, 145 (1926). {1}

[7] E. Fermi, *Z. Phys.* **36**, 902 (1926). {1}

[8] P. A. M. Dirac, *Proc. Roy. Soc. London A* **112**, 661 (1926). {1}

[9] W. Pauli, *Z. Phys.* **31**, 765 (1925), available online at 'http://home.tiscali.nl/physis/HistoricPaper/Pauli/The%20Fourth%20Quantum%20Number.htm'. {1}

[10] R. K. Pathria, *Statistical Mechanics* (Pergamon Press, Oxford, 1972). {1}

[11] W. Pauli, *Phys. Rev.* **58**, 716 (1940). {1}

[12] H. J. Metcalf and P. van der Straaten, *Laser cooling and trapping* (Springer, New York, 1999). {2}

[13] M. H. Anderson, J. R. Ensher, M. R. Matthews, C. E. Wieman, and E. A. Cornell, *Science* **269**, 198 (1995). {2}

[14] K. B. Davis, M. O. Mewes, M. R. Andrews, N. J. van Druten, D. S. Durfee, D. M. Kurn, and W. Ketterle, *Phys. Rev. Lett.* **75**, 3969 (1995). {2}

*The number(s) in braces indicate the page(s) on which each citation occurs.

[15] C. C. Bradley, C. A. Sackett, J. J. Tollett, and R. G. Hulet, *Phys. Rev. Lett.* **75**, 1687 (1995). {2}

[16] C. C. Bradley, C. A. Sackett, and R. G. Hulet, *Phys. Rev. Lett.* **78**, 985 (1997). {2}

[17] D. G. Fried, T. C. Killian, L. Willmann, D. Landhuis, S. C. Moss, D. Kleppner, and T. J. Greytak, *Phys. Rev. Lett.* **81**, 3811 (1998). {2}

[18] S. L. Cornish, N. R. Claussen, J. L. Roberts, E. A. Cornell, and C. E. Wieman, *Phys. Rev. Lett.* **85**, 1795 (2000). {2, 4, 76}

[19] A. Robert, O. Sirjean, A. Browaeys, J. Poupard, S. Nowak, D. Boiron, C. I. Westbrook, and A. Aspect, *Science* **292**, 461 (2001). {2}

[20] F. Pereira Dos Santos, J. Léonard, J. Wang, C. J. Barrelet, F. Perales, E. Rasel, C. S. Unnikrishnan, M. Leduc, and C. Cohen-Tannoudji, *Phys. Rev. Lett.* **86**, 3459 (2001). {2}

[21] G. Modugno, G. Ferrari, G. Roati, R. J. Brecha, A. Simoni, and M. Inguscio, *Science* **294**, 1320 (2001). {2, 6}

[22] T. Weber, J. Herbig, M. Mark, H.-C. Nägerl, and R. Grimm, *Science* **299**, 232 (2003). {2, 4}

[23] Y. Takasu, K. Maki, K. Komori, T. Takano, K. Honda, M. Kumakura, T. Yabuzaki, and Y. Takahashi, *Phys. Rev. Lett.* **91**, 040404 (2003). {2, 3}

[24] A. Griesmaier, J. Werner, S. Hensler, J. Stuhler, and T. Pfau, *Phys. Rev. Lett.* **94**, 160401 (2005). {2, 4}

[25] G. Roati, M. Zaccanti, C. D'Errico, J. Catani, M. Modugno, A. Simoni, M. Inguscio, and G. Modugno, *Phys. Rev. Lett.* **99**, 010403 (2007). {2}

[26] M. R. Matthews, B. P. Anderson, P. C. Haljan, D. S. Hall, C. E. Wieman, and E. A. Cornell, *Phys. Rev. Lett.* **83**, 2498 (1999). {2}

[27] C. Raman, M. Köhl, R. Onofrio, D. S. Durfee, C. E. Kuklewicz, Z. Hadzibabic, and W. Ketterle, *Phys. Rev. Lett.* **83**, 2502 (1999). {2}

[28] M. R. Andrews, C. G. Townsend, H.-J. Miesner, D. S. Durfee, D. M. Kurn, and W. Ketterle, *Science* **275**, 637 (1997). {2}

[29] N. Bogoliubov, *J. Phys. USSR* **11**, 23 (1947). {2, 47, 48}

[30] C. J. Pethick and H. Smith, *Bose-Einstein condensation in dilute gases* (Cambridge University Press, Cambridge, 2002). {2, 47, 48, 49}

[31] L. Pitaevskii and S. Stringari, *Bose-Einstein condensation* (Oxford University Press, Oxford, 2003). {2}

[32] E. P. Gross, *Nuovo Cimento* **20**, 454 (1961). {2, 47}

[33] L. P. Pitaevskii, *Zh. Eksp. Teor. Fys.* **40**, 646 [*Sov. Phys. JETP* **13**, 451] (1961). {2, 47}

[34] C. J. Myatt, E. A. Burt, R. W. Ghrist, E. A. Cornell, and C. E. Wieman, *Phys. Rev. Lett.* **78**, 586 (1997). {2}

[35] B. DeMarco and D. S. Jin, *Science* **285**, 1703 (1999). {2}

[36] A. G. Truscott, K. E. Strecker, W. I. McAlexander, G. B. Partridge, and R. G. Hulet, *Science* **291**, 2570 (2001). {2}

[37] C. A. Regal, M. Greiner, and D. S. Jin, *Phys. Rev. Lett.* **92**, 040403 (2004). {2, 6, 109}

[38] M. W. Zwierlein, C. A. Stan, C. H. Schunck, S. M. F. Raupach, A. J. Kerman, and W. Ketterle, *Phys. Rev. Lett.* **92**, 120403 (2004). {2, 6}

[39] M. Greiner, O. Mandel, T. Esslinger, T. W. Hänsch, and I. Bloch, *Nature (London)* **415**, 39 (2002). {2}

[40] D. Jaksch, C. Bruder, J. I. Cirac, C. W. Gardiner, and P. Zoller, *Phys. Rev. Lett.* **81**, 3108 (1998). {2}

[41] D. Jaksch and P. Zoller, *Ann. Phys.* **315**, 52 (2005). {2}

[42] F. Schreck, L. Khaykovich, K. L. Corwin, G. Ferrari, T. Bourdel, J. Cubizolles, and C. Salomon, *Phys. Rev. Lett.* **87**, 080403 (2001). {2, 6}

[43] A. Görlitz, J. M. Vogels, A. E. Leanhardt, C. Raman, T. L. Gustavson, J. R. Abo-Shaeer, A. P. Chikkatur, S. Gupta, S. Inouye, T. Rosenband, and W. Ketterle, *Phys. Rev. Lett.* **87**, 130402 (2001). {2}

[44] T. Jeltes, J. M. McNamara, W. Hogervorst, W. Vassen, V. Krachmalnicoff, M. Schellekens, A. Perrin, H. Chang, D. Boiron, A. Aspect, and C. I. Westbrook, *Nature (London)* **445**, 402 (2007). {2}

[45] U. Fano, *Nuovo Cimento* **12**, 154 (1935), translation into English by G. Pupillo, A. Zannoni, and C. W. Clark available at arXiv:cond-mat/0502210. {3}

[46] U. Fano, *Phys. Rev.* **124**, 1866 (1961). {3}

[47] H. Feshbach, *Ann. Phys.* **5**, 357 (1958). {3}

[48] H. Feshbach, *Ann. Phys.* **19**, 287 (1962). {3}

[49] O. K. Rice, *J. Chem. Phys.* **1**, 375 (1933). {3}

[50] W. C. Stwalley, *Phys. Rev. Lett.* **37**, 1628 (1976). {3}

[51] E. Tiesinga, B. J. Verhaar, and H. T. C. Stoof, *Phys. Rev. A* **47**, 4114 (1993). {3}

[52] E. Timmermans, P. Tommasini, M. Hussein, and A. Kerman, *Phys. Rep.* **315**, 199 (1999). {3, 17}

[53] S. Inouye, M. R. Andrews, J. Stenger, H.-J. Miesner, D. M. Stamper-Kurn, and W. Ketterle, *Nature (London)* **392**, 151 (1998). {3}

[54] P. Courteille, R. S. Freeland, D. J. Heinzen, F. A. van Abeelen, and B. J. Verhaar, *Phys. Rev. Lett.* **81**, 69 (1998). {3}

[55] J. L. Roberts, N. R. Claussen, J. P. Burke, C. H. Greene, E. A. Cornell, and C. E. Wieman, *Phys. Rev. Lett.* **81**, 5109 (1998). {3}

[56] V. Vuletić, A. J. Kerman, C. Chin, and S. Chu, *Phys. Rev. Lett.* **82**, 1406 (1999). {3}

[57] T. Lahaye, T. Koch, B. Fröhlich, M. Fattori, J. Metz, A. Griesmaier, S. Giovanazzi, and T. Pfau, *Nature (London)* **448**, 672 (2007). {4}

[58] K. Góral, K. Rzążewski, and T. Pfau, *Phys. Rev. A* **61**, 051601 (2000). {4}

[59] K. Góral, L. Santos, and M. Lewenstein, *Phys. Rev. Lett.* **88**, 170406 (2002). {4}

[60] J. Doyle, B. Friedrich, R. V. Krems, and F. Masnou-Seeuws, *Eur. Phys. J. D* **31**, 149 (2004). {4}

[61] T. Köhler, K. Góral, and P. S. Julienne, *Rev. Mod. Phys.* **78**, 1311 (2006). {4, 5, 6, 11, 12, 20, 22, 24, 34, 35, 40, 42, 118}

[62] R. deCarvalho, J. M. Doyle, B. Friedrich, T. Guillet, J. Kim, D. Patterson, and J. D. Weinstein, *Eur. Phys. J. D* **7**, 289 (1999). {4}

[63] J. Kim, B. Friedrich, D. P. Katz, D. Patterson, J. D. Weinstein, R. DeCarvalho, and J. M. Doyle, *Phys. Rev. Lett.* **78**, 3665 (1997). {4}

[64] J. D. Weinstein, R. deCarvalho, T. Guillet, B. Friedrich, and J. M. Doyle, *Nature (London)* **395**, 148 (1998). {4}

[65] H. R. Thorsheim, J. Weiner, and P. S. Julienne, *Phys. Rev. Lett.* **58**, 2420 (1987). {4}

[66] P. D. Lett, K. Helmerson, W. D. Phillips, L. P. Ratliff, S. L. Rolston, and M. E. Wagshul, *Phys. Rev. Lett.* **71**, 2200 (1993). {4}

[67] J. D. Miller, R. A. Cline, and D. J. Heinzen, *Phys. Rev. Lett.* **71**, 2204 (1993). {4}

[68] A. Fioretti, D. Comparat, A. Crubellier, O. Dulieu, F. Masnou-Seeuws, and P. Pillet, *Phys. Rev. Lett.* **80**, 4402 (1998). {4}

[69] T. Takekoshi, B. M. Patterson, and R. J. Knize, *Phys. Rev. A* **59**, R5 (1999). {4}

[70] A. N. Nikolov, E. E. Eyler, X. T. Wang, J. Li, H. Wang, W. C. Stwalley, and P. L. Gould, *Phys. Rev. Lett.* **82**, 703 (1999). {4}

[71] R. Wynar, R. S. Freeland, D. J. Han, C. Ryu, and D. J. Heinzen, *Science* **287**, 1016 (2000). {4}

[72] E. A. Donley, N. R. Claussen, S. T. Thompson, and C. E. Wieman, *Nature (London)* **417**, 529 (2002). {4, 5, 6, 33}

[73] J. Herbig, T. Kraemer, M. Mark, T. Weber, C. Chin, H.-C. Nägerl, and R. Grimm, *Science* **301**, 1510 (2003). {4, 5, 33}

[74] J. Cubizolles, T. Bourdel, S. J. J. M. F. Kokkelmans, G. V. Shlyapnikov, and C. Salomon, *Phys. Rev. Lett.* **91**, 240401 (2003). {4, 5, 7, 33, 96}

[75] S. Jochim, M. Bartenstein, A. Altmeyer, G. Hendl, C. Chin, J. Hecker Denschlag, and R. Grimm, *Phys. Rev. Lett.* **91**, 240402 (2003). {4, 5, 33}

[76] K. E. Strecker, G. B. Partridge, and R. G. Hulet, *Phys. Rev. Lett.* **91**, 080406 (2003). {4, 5, 33}

[77] K. Xu, T. Mukaiyama, J. R. Abo-Shaeer, J. K. Chin, D. E. Miller, and W. Ketterle, *Phys. Rev. Lett.* **91**, 210402 (2003). {4, 5, 6, 33}

[78] S. Dürr, T. Volz, A. Marte, and G. Rempe, *Phys. Rev. Lett.* **92**, 020406 (2004). {4, 5, 33}

[79] C. A. Regal, C. Ticknor, J. L. Bohn, and D. S. Jin, *Nature (London)* **424**, 47 (2003). {4, 5, 33}

[80] J. P. Gaebler, J. T. Stewart, J. L. Bohn, and D. S. Jin, *Phys. Rev. Lett.* **98**, 200403 (2007). {4, 5, 73, 92, 109}

[81] S. B. Papp and C. E. Wieman, *Phys. Rev. Lett.* **97**, 180404 (2006). {5, 6, 8, 73, 74, 92}

[82] C. Ospelkaus, S. Ospelkaus, L. Humbert, P. Ernst, K. Sengstock, and K. Bongs, *Phys. Rev. Lett.* **97**, 120402 (2006). {5, 6}

[83] J. J. Zirbel, K.-K. Ni, S. Ospelkaus, T. L. Nicholson, M. L. Olsen, C. E. Wieman, J. Ye, D. S. Jin, and P. S. Julienne, arXiv:0712.3889 [cond-mat.other] (2007). {5, 6}

[84] M. Greiner, C. A. Regal, and D. S. Jin, *Nature (London)* **426**, 537 (2003). {5, 6, 7, 33, 95, 96}

[85] C. Chin, A. J. Kerman, V. Vuletić, and S. Chu, *Phys. Rev. Lett.* **90**, 033201 (2003). {5, 33}

[86] T. Mukaiyama, J. R. Abo-Shaeer, K. Xu, J. K. Chin, and W. Ketterle, *Phys. Rev. Lett.* **92**, 180402 (2004). {5, 33, 34, 35, 43}

[87] S. Dürr, T. Volz, and G. Rempe, *Phys. Rev. A* **70**, 031601R (2004). {5, 24, 33, 34, 35, 38, 39, 40, 42, 43}

[88] T. Volz, S. Dürr, N. Syassen, G. Rempe, E. van Kempen, and S. Kokkelmans, *Phys. Rev. A* **72**, 010704R (2005). {5, 33}

[89] S. T. Thompson, E. Hodby, and C. E. Wieman, *Phys. Rev. Lett.* **95**, 190404 (2005). {5, 8, 33, 73, 74, 75, 76, 78, 81, 84, 92, 93}

[90] S. Jochim, M. Bartenstein, A. Altmeyer, G. Hendl, S. Riedel, C. Chin, J. Hecker Denschlag, and R. Grimm, *Science* **302**, 2101 (2003). {5, 6, 33}

[91] M. Mark, T. Kraemer, J. Herbig, C. Chin, H.-C. Nägerl, and R. Grimm, *Europhys. Lett.* **69**, 706 (2005). {5, 33}

[92] H. Moritz, T. Stöferle, K. Günter, M. Köhl, and T. Esslinger, *Phys. Rev. Lett.* **94**, 210401 (2005). {5}

[93] K. Winkler, G. Thalhammer, F. Lang, R. Grimm, J. Hecker Denschlag, A. J. Daley, A. Kantian, H. P. Büchler, and P. Zoller, *Nature (London)* **441**, 853 (2006). {5}

[94] F. Lang, P. v. d. Straten, B. Brandstätter, G. Thalhammer, K. Winkler, P. S. Julienne, R. Grimm, and J. H. Denschlag, arXiv:0708.3958 [quant-ph] (2007). {5}

[95] T. Köhler, T. Gasenzer, P. S. Julienne, and K. Burnett, *Phys. Rev. Lett.* **91**, 230401 (2003). {5, 22, 24, 26, 32}

[96] A. S. Jensen, K. Riisager, D. V. Fedorov, and E. Garrido, *Rev. Mod. Phys.* **76**, 215 (2004). {5, 22}

[97] M. Bartenstein, A. Altmeyer, S. Riedl, R. Geursen, S. Jochim, C. Chin, J. Hecker Denschlag, R. Grimm, A. Simoni, E. Tiesinga, C. J. Williams, and P. S. Julienne, *Phys. Rev. Lett.* **94**, 103201 (2005). {5}

[98] S. T. Thompson, E. Hodby, and C. E. Wieman, *Phys. Rev. Lett.* **94**, 020401 (2005). {5, 76, 87}

[99] T. Köhler, E. Tiesinga, and P. Julienne, *Phys. Rev. Lett.* **94**, 020402 (2005). {5, 76, 87}

[100] D. S. Petrov, *Phys. Rev. Lett.* **93**, 143201 (2004). {5, 37}

[101] D. S. Petrov, C. Salomon, and G. V. Shlyapnikov, *Phys. Rev. A* **71**, 012708 (2005). {5}

[102] M. W. Zwierlein, C. A. Stan, C. H. Schunck, S. M. F. Raupach, S. Gupta, Z. Hadzibabic, and W. Ketterle, *Phys. Rev. Lett.* **91**, 250401 (2003). {6}

[103] J. M. McNamara, T. Jeltes, A. S. Tychkov, W. Hogervorst, and W. Vassen, *Phys. Rev. Lett.* **97**, 080404 (2006). {6}

[104] J. J. Hudson, B. E. Sauer, M. R. Tarbutt, and E. A. Hinds, *Phys. Rev. Lett.* **89**, 023003 (2002). {6}

[105] D. DeMille, *Phys. Rev. Lett.* **88**, 067901 (2002). {6}

[106] C. Chin, T. Kraemer, M. Mark, J. Herbig, P. Waldburger, H.-C. Nägerl, and R. Grimm, *Phys. Rev. Lett.* **94**, 123201 (2005). {6}

[107] T. Kraemer, M. Mark, P. Waldburger, J. G. Danzl, C. Chin, B. Engeser, A. D. Lange, K. Pilch, A. Jaakkola, H.-C. Nägerl, and R. Grimm, *Nature (London)* **440**, 315 (2006). {6}

[108] M. D. Lee, T. Köhler, and P. S. Julienne, *Phys. Rev. A* **76**, 012720 (2007). {6}

[109] J. von Stecher and C. H. Greene, *Phys. Rev. Lett.* **99**, 090402 (2007). {6, 25}

[110] G. Thalhammer, K. Winkler, F. Lang, S. Schmid, R. Grimm, and J. Hecker Denschlag, *Phys. Rev. Lett.* **96**, 050402 (2006). {6, 95}

[111] E. Hodby, S. T. Thompson, C. A. Regal, M. Greiner, A. C. Wilson, D. S. Jin, E. A. Cornell, and C. E. Wieman, *Phys. Rev. Lett.* **94**, 120402 (2005). {7, 73, 96}

[112] S. J. J. M. F. Kokkelmans, G. V. Shlyapnikov, and C. Salomon, *Phys. Rev. A* **69**, 031602R (2004). {7, 96}

[113] C. Chin, V. Vuletić, A. J. Kerman, S. Chu, E. Tiesinga, P. J. Leo, and C. J. Williams, *Phys. Rev. A* **70**, 032701 (2004). {7, 88, 96}

[114] M. H. Szymańska, K. Góral, T. Köhler, and K. Burnett, *Phys. Rev. A* **72**, 013610 (2005). {7, 22, 28, 96}

[115] J. E. Williams, N. Nygaard, and C. W. Clark, *New J. Phys.* **8**, 150 (2006). {7, 51, 80, 96}

[116] T. M. Hanna, K. Góral, E. Witkowska, and T. Köhler, *Phys. Rev. A* **74**, 023618 (2006). {7, 28, 33}

[117] T. M. Hanna, T. Köhler, and K. Burnett, *Phys. Rev. A* **75**, 013606 (2007). {8, 28, 51, 53, 73}

[118] H. T. C. Stoof, J. M. V. A. Koelman, and B. J. Verhaar, *Phys. Rev. B* **38**, 4688 (1988). {12, 16}

[119] J. Taylor, *Scattering theory: the quantum theory on nonrelativistic collisions* (John Wiley & Sons, New York, 1972). {13, 20, 112}

[120] A. J. Moerdijk, B. J. Verhaar, and A. Axelsson, *Phys. Rev. A* **51**, 4852 (1995). {14, 17}

[121] H. A. Bethe, *Phys. Rev.* **76**, 38 (1949), and references therein to the work of Schwinger (1947). {16}

[122] F. H. Mies, C. J. Williams, P. S. Julienne, and M. Krauss, *J. Res. Natl. Inst. Stand. Technol.* **101**, 521 (1996). {16}

[123] P. J. Leo, C. J. Williams, and P. S. Julienne, *Phys. Rev. Lett.* **85**, 2721 (2000). {16}

[124] M. S. Child, *Molecular Collision Theory* (Academic, London, 1974). {17}

[125] P. D. Drummond, K. V. Kheruntsyan, and H. He, *Phys. Rev. Lett.* **81**, 3055 (1998). {17, 51}

[126] F. H. Mies, E. Tiesinga, and P. S. Julienne, *Phys. Rev. A* **61**, 022721 (2000). {17, 24, 26, 51}

[127] N. Nygaard, B. I. Schneider, and P. S. Julienne, *Phys. Rev. A* **73**, 042705 (2006). {17, 24}

[128] K. Góral, T. Köhler, S. A. Gardiner, E. Tiesinga, and P. S. Julienne, *J. Phys. B.* **37**, 3457 (2004). {18, 19, 22, 25, 27, 28, 34, 35, 37, 43, 51, 53}

[129] P. Julienne and B. Gao, arXiv:physics/0609013 (2006). {21}

[130] B. Marcelis, E. G. M. van Kempen, B. J. Verhaar, and S. J. J. M. F. Kokkelmans, *Phys. Rev. A* **70**, 012701 (2004). {21}

[131] G. B. Partridge, K. E. Strecker, R. I. Kamar, M. W. Jack, and R. G. Hulet, *Phys. Rev. Lett.* **95**, 020404 (2005). {22}

[132] E. P. Wigner, *Phys. Rev.* **73**, 1002 (1948). {22, 37}

[133] G. F. Gribakin and V. V. Flambaum, *Phys. Rev. A* **48**, 546 (1993). {23, 25}

[134] T. Köhler, T. Gasenzer, and K. Burnett, *Phys. Rev. A* **67**, 013601 (2003). {23, 28, 51, 53}

[135] H. A. Bethe, *Phys. Rev.* **47**, 747 (1935). {23}

[136] P. S. Julienne and F. H. Mies, *J. Opt. Soc. Am. B* **6**, 2257 (1989). {23, 24}

[137] F. H. Mies and M. Raoult, *Phys. Rev. A* **62**, 012708 (2000). {23, 24}

[138] M. Raoult and F. H. Mies, *Phys. Rev. A* **70**, 012710 (2004). {23, 24}

[139] P. S. Julienne, E. Tiesinga, and T. Köhler, *J. Mod. Opt* **51**, 1787 (2004). {24, 51}

[140] M. D. Lee, private communication (2006). {24}

[141] P. S. Julienne, private communication (2005). {24}

[142] R. A. Duine and H. T. C. Stoof, *Phys. Rep.* **396**, 115 (2004). {25}

[143] C. Chin, arXiv:cond–mat/0506313 (2005). {25}

[144] C. Lovelace, *Phys. Rev.* **135**, B1225 (1964). {27}

[145] T. Köhler and K. Burnett, *Phys. Rev. A* **65**, 033601 (2002). {28, 52, 53}

[146] K. Huang, *Statistical Mechanics* (Wiley, New York, 1987). {28, 46}

[147] S. Dürr, T. Volz, N. Syassen, G. Rempe, E. van Kempen, S. Kokkelmans, B. Verhaar, and H. Friedrich, *Phys. Rev. A* **72**, 052707 (2005). {33}

[148] M. Haque and H. T. C. Stoof, *Phys. Rev. A* **71**, 063603 (2005). {34}

[149] S. Brouard and J. Plata, *Phys. Rev. A* **72**, 023620 (2005). {34}

[150] M. Stoll and T. Köhler, *Phys. Rev. A* **72**, 022714 (2005). {37}

[151] S. Dürr, *Private communication* (2006). {39, 40}

[152] Y. N. Demkov and V. I. Osherov, *Sov. Phys. JETP* **26**, 916 (1968). {42}

[153] J. H. Macek and M. J. Cavagnero, *Phys. Rev. A* **58**, 348 (1998). {42}

[154] L. Boltzmann, *Sitzungsber. Akad. Wiss.* **66**, 275 (1872), reproduced in S. G. Brush (ed.), *Kinetic Theory (Vol. 2)*, Pergamon Press, Oxford, 1966. {45}

[155] E. A. Uehling and G. E. Uhlenbeck, *Phys. Rev.* **43**, 552 (1933). {47}

[156] J. N. Fuchs, D. M. Gangardt, and F. Laloë, *Eur. Phys. J. D* **25**, 57 (2003). {47, 70}

[157] J. N. Fuchs, O. Prévoté, and D. M. Gangardt, *Eur. Phys. J. D* **25**, 167 (2003). {47}

[158] M. Holland, J. Williams, K. Coakley, and J. Cooper, *Quantum Semiclass. Opt.* **8**, 571 (1996). {47}

[159] P. Massignan, G. M. Bruun, and H. Smith, *Phys. Rev. A* **71**, 033607 (2005). {47}

[160] G. Baym and C. J. Pethick, *Phys. Rev. Lett.* **76**, 6 (1996). {47}

[161] M. Edwards, R. J. Dodd, C. W. Clark, P. A. Ruprecht, and K. Burnett, *Phys. Rev. A* **53**, R1950 (1996). {47}

[162] M. Holland and J. Cooper, *Phys. Rev. A* **53**, R1954 (1996). {47, 50}

[163] M. Edwards, P. A. Ruprecht, K. Burnett, R. J. Dodd, and C. W. Clark, *Phys. Rev. Lett.* **77**, 1671 (1996). {47}

[164] W. Hoston and L. You, *Phys. Rev. A* **53**, 4254 (1996). {47}

[165] A. Röhrl, M. Naraschewski, A. Schenzle, and H. Wallis, *Phys. Rev. Lett.* **78**, 4143 (1997). {47}

[166] V. N. Popov, *Functional integrals and collective excitations* (Cambridge University Press, Cambridge, 1987). {49}

[167] R. J. Dodd, M. Edwards, C. W. Clark, and K. Burnett, *Phys. Rev. A* **57**, R32 (1998). {49}

[168] S. A. Morgan, *J. Phys. B* **33**, 3847 (2000). {49}

[169] N. P. Proukakis, arXiv:0706.3541 [cond–mat.other] (2007). {49}

[170] C. W. Gardiner and P. Zoller, *Quantum noise* (Springer-Verlag, Berlin, 2000), 2nd edn. {49}

[171] E. Zaremba, T. Nikuni, and A. Griffin, *J. Low Temp. Phys.* **116**, 277 (1999). {49}

[172] B. Jackson and E. Zaremba, *Phys. Rev. Lett.* **87**, 100404 (2001). {49}

[173] B. Jackson and E. Zaremba, *Phys. Rev. Lett.* **89**, 150402 (2002). {49}

[174] J. E. Williams, E. Zaremba, B. Jackson, T. Nikuni, and A. Griffin, *Phys. Rev. Lett.* **88**, 070401 (2002). {49}

[175] M. J. Davis, *Dynamics of Bose-Einstein Condensation*, D. Phil. thesis, University of Oxford (2001). {49}

[176] M. J. Davis, R. J. Ballagh, and K. Burnett, *J. Phys. B* **34**, 4487 (2001). {49, 50}

[177] M. J. Davis, S. A. Morgan, and K. Burnett, *Phys. Rev. Lett.* **87**, 160402 (2001). {50}

[178] M. Brewczyk, M. Gajda, and K. Rzążewski, *J. Phys. B* **40**, R1 (2007). {50}

[179] P. B. Blakie and M. J. Davis, *Phys. Rev. A* **72**, 063608 (2005). {50}

[180] M. J. Davis and P. B. Blakie, *Phys. Rev. Lett.* **96**, 060404 (2006). {50}

[181] H. Schmidt, K. Góral, F. Floegel, M. Gajda, and K. Rzążewski, *J. Opt. B* **5**, S96 (2003). {50}

[182] M. Holland, J. Williams, and J. Cooper, *Phys. Rev. A* **55**, 3670 (1997). {50}

[183] R. Walser, J. Williams, J. Cooper, and M. Holland, *Phys. Rev. A* **59**, 3878 (1999). {50}

[184] M. J. Steel, M. K. Olsen, L. I. Plimak, P. D. Drummond, S. M. Tan, M. J. Collett, D. F. Walls, and R. Graham, *Phys. Rev. A* **58**, 4824 (1998). {50}

[185] A. Sinatra, C. Lobo, and Y. Castin, *J. Phys. B* **35**, 3599 (2002). {50}

[186] C. Lobo, A. Sinatra, and Y. Castin, *Phys. Rev. Lett.* **92**, 020403 (2004). {50}

[187] A. Polkovnikov and D.-W. Wang, *Phys. Rev. Lett.* **93**, 070401 (2004). {50}

[188] L. Isella and J. Ruostekoski, *Phys. Rev. A* **72**, 011601 (2005). {50}

[189] M. T. Johnsson and J. J. Hope, *Phys. Rev. A* **75**, 043619 (2007). {50}

[190] P. D. Drummond and C. W. Gardiner, *J. Phys. A* **13**, 2353 (1980). {50}

[191] P. D. Drummond and J. F. Corney, *Phys. Rev. A* **60**, R2661 (1999). {50}

[192] K. V. Kheruntsyan and P. D. Drummond, *Phys. Rev. A* **66**, 031602(R) (2002). {50}

[193] C. M. Savage, P. E. Schwenn, and K. V. Kheruntsyan, *Phys. Rev. A* **74**, 033620 (2006). {50}

[194] T. Gasenzer, J. Berges, M. G. Schmidt, and M. Seco, *Phys. Rev. A* **72**, 063604 (2005). {50}

[195] J. Berges and T. Gasenzer, *Phys. Rev. A* **76**, 033604 (2007). {50}

[196] A. M. Rey, B. L. Hu, E. Calzetta, A. Roura, and C. W. Clark, *Phys. Rev. A* **69**, 033610 (2004). {50}

[197] A. M. Rey, B. L. Hu, E. Calzetta, and C. W. Clark, *Phys. Rev. A* **72**, 023604 (2005). {50}

[198] H. T. C. Stoof, *J. Low Temp. Phys.* **114**, 11 (1999). {51}

[199] H. T. C. Stoof and N. J. Bijlsma, *J. Low Temp. Phys.* **124**, 431 (2001). {51}

[200] N. P. Proukakis, J. Schmiedmayer, and H. T. C. Stoof, *Phys. Rev. A* **73**, 053603 (2006). {51}

[201] U. Al Khawaja, J. O. Andersen, N. P. Proukakis, and H. T. C. Stoof, *Phys. Rev. A* **66**, 013615 (2002). {51}

[202] C. W. Gardiner, J. R. Anglin, and T. I. A. Fudge, *J. Phys. B* **35**, 1555 (2002). {51}

[203] C. W. Gardiner and M. J. Davis, *J. Phys. B* **36**, 4731 (2003). {51}

[204] E. Timmermans, P. Tommasini, R. Côté, M. Hussein, and A. Kerman, *Phys. Rev. Lett.* **83**, 2691 (1999). {51}

[205] F. A. van Abeelen and B. J. Verhaar, *Phys. Rev. Lett.* **83**, 1550 (1999). {51}

[206] K. Góral, M. Gajda, and K. Rzążewski, *Phys. Rev. Lett.* **86**, 1397 (2001). {51}

[207] K. Góral, T. Köhler, and K. Burnett, *Phys. Rev. A* **71**, 023603 (2005). {51, 53}

[208] J. Chwedeńczuk, K. Góral, T. Köhler, and P. S. Julienne, *Phys. Rev. Lett.* **93**, 260403 (2004). {51}

[209] J. Javanainen, *Phys. Rev. A* **73**, 061605(R) (2006). {51}

[210] J. E. Williams, T. Nikuni, N. Nygaard, and C. W. Clark, *J. Phys. B* **37**, L351 (2004). {51}

[211] L. P. Kadanoff and G. Baym, *Quantum Statistical Mechanics* (W. A. Benjamin, Menlo Park, 1962). {51}

[212] S. Weinberg, *The quantum theory of fields* (Cambridge University Press, Cambridge, 1996). {51}

[213] J. Fricke, *Ann. Phys.* **252**, 479 (1996). {52, 53}

[214] N. P. Proukakis and K. Burnett, *J. Res. Natl. Inst. Stand. Technol.* **101**, 457 (1996). {52}

[215] H. Schoeller, *Ann. Phys.* **229**, 273 (1994). {52}

[216] R. Bach, K. Burnett, M. B. d'Arcy, and S. A. Gardiner, *Phys. Rev. A* **71**, 033417 (2005). {53}

[217] S. Thanvanthri and Z. Dutton, *Phys. Rev. A* **75**, 023618 (2007). {53}

[218] T. Köhler, K. Góral, and T. Gasenzer, *Phys. Rev. A* **70**, 023613 (2004). {53, 81}

[219] P. Naidon and F. Masnou-Seeuws, *Phys. Rev. A* **73**, 043611 (2006). {53}

[220] A. L. Fetter and J. D. Walecka, *Quantum theory of many-particle systems* (Dover, New York, 2003). {55, 62, 126}

[221] H.-C. Nägerl, private communication (2006). {73}

[222] J. F. Bertelsen and K. Mølmer, *Phys. Rev. A* **73**, 013811 (2006). {74}

[223] J. F. Bertelsen and K. Mølmer, *Phys. Rev. A* **76**, 043615 (2007). {74}

[224] C. Runge, *Math. Ann.* **46**, 167 (1895), and W. Kutta, *Zeitschr. Math. Phys.* **46**, 435 (1901). Parts of these are reproduced in J. C. Butcher and G. Wanner, *App. Num. Math.* **22**, 113 (1996). {77, 103}

[225] N. R. Claussen, S. J. J. M. F. Kokkelmans, S. T. Thompson, E. A. Donley, E. Hodby, and C. E. Wieman, *Phys. Rev. A* **67**, 060701(R) (2003). {83}

[226] S. T. Thompson, private communication (2006). {88}

[227] S. B. Papp, private communication (2007). {92}

[228] K. Góral, private communication (2006). {109}

[229] E. Tiesinga, C. J. Williams, and P. S. Julienne, *Phys. Rev. A* **57**, 4257 (1998). {111}